

High Resolution Field Imaging with Atomic Vapor Cells

Inauguraldissertation

zur
Erlangung der Würde eines Doktors der Philosophie
vorgelegt der
Philosophisch-Naturwissenschaftlichen Fakultät
der Universität Basel

von

Andrew Horsley
aus Australien



Basel, 2015

The original document is saved on the university of Basel document server
<http://edoc.unibas.ch>



This work is licensed under a Creative Commons
Attribution-NonCommercial-NoDerivatives 4.0 International License.

The complete text may be reviewed here:
<http://creativecommons.org/licenses/by-nc-nd/4.0/>

Genehmigt von der Philosophisch-Naturwissenschaftlichen Fakultät
auf Antrag von
Prof. Dr. Philipp Treutlein
Prof. Dr. Dmitry Budker

Basel, den 15. September 2015

Prof. Dr. Jörg Schibler
Dekan



Creative Commons License Deed

Attribution-NonCommercial-NoDerivatives 4.0 International

This is a human-readable summary of (and not a substitute for) the license.

You are free to:



Share — copy and redistribute the material in any medium or format

The licensor cannot revoke these freedoms as long as you follow the license terms.

Under the following terms:



Attribution — You must give appropriate credit, provide a link to the license, and indicate if changes were made. You may do so in any reasonable manner, but not in any way that suggests the licensor endorses you or your use.



NonCommercial — You may not use the material for commercial purposes.



NoDerivatives — If you remix, transform, or build upon the material, you may not distribute the modified material.

No additional restrictions — You may not apply legal terms or technological measures that legally restrict others from doing anything the license permits.

Notices:

You do not have to comply with the license for elements of the material in the public domain or where your use is permitted by an applicable exception or limitation.

No warranties are given. The license may not give you all of the permissions necessary for your intended use. For example, other rights such as publicity, privacy, or moral rights may limit how you use the material.

Abstract

In this thesis, I report on the development of imaging techniques in atomic vapor cells. This is a relatively unexplored area, despite the ubiquitous use of imaging in experiments with ultracold atoms. Our main focus is in high resolution imaging of microwave near fields, for which there is currently no satisfactory established technique. We detect microwave fields through Rabi oscillations driven by the microwave on atomic hyperfine transitions. The technique can be easily modified to also image dc magnetic fields. In addition, we have developed techniques to image vapor cell processes such as atomic T_1 and T_2 relaxation. These provide a new window into vapor cell physics, which we have used to obtain spatially resolved information on Rb interactions with the cell walls, and to estimate the Rb relaxation probability in a collision with the cell wall.

As a first application of our imaging techniques, we imaged the dc and microwave magnetic fields inside a state-of-the-art vapor cell atomic clock. This new clock characterisation technique should lead to real improvements in clock performance, and is in the process of being adopted by the atomic clock community.

We have developed a widefield, high resolution imaging setup using a microfabricated vapor cell, which we have used to image microwave and dc magnetic vector fields. With the addition of a 480 nm laser, the setup can be configured to image microwave electric fields. Our camera-based imaging system records 2D images with a $6 \times 6 \text{ mm}^2$ field of view at a rate of 10 Hz. It provides up to $50 \mu\text{m}$ spatial resolution, and allows imaging of fields as close as $150 \mu\text{m}$ above structures, through the use of extremely thin external cell walls. This is crucial in allowing us to take practical advantage of the high spatial resolution, as feature sizes in near-fields are on the order of the distance from their source, and represents an order of magnitude improvement in surface-feature resolution compared to previous vapor cell experiments. We demonstrate a microwave magnetic field sensitivity of $1.4 \mu\text{T Hz}^{-1/2}$ per $50 \times 50 \times 140 \mu\text{m}^3$ voxel, at present limited by the speed of our imaging system. Since we image 120×120 voxels in parallel, a single scanned sensor would require a sensitivity of at least $12 \text{ nT Hz}^{-1/2}$ to produce images with the same sensitivity.

The spatial resolution, distance of approach, and sensitivity of our high resolution setup are sufficient for characterising 6.8 GHz microwave fields above a range of real world devices. However, frequency tunability is essential for wider applications of our imaging technique. Industry is particularly interested in techniques for imaging high frequency microwaves, above 18 GHz, where simulations become increasingly

unreliable. I have shown that our technique can be extended to image microwaves of any frequency, in principle from dc to 100s of GHz, by using a large dc magnetic field to Zeeman shift the hyperfine ground state transitions to the desired frequency. I present results from a proof-of-principle setup, where we have used a 0.8 T solenoid to detect and image microwaves from 2.3 GHz to 26.4 GHz.

Acknowledgements

Firstly, thank you to my PhD supervisor, Philipp Treutlein. I have thoroughly enjoyed working with Philipp, who was patient with my transition to atomic physics, generous with conference opportunities, and provided a stimulating and welcoming lab environment. I also thank Guan-Xiang Du, who worked for two years as a postdoc on the project, particularly for his fabrication and modelling of the demonstration microwave structures.

Thanks to the other members of our research group, both past and present, who provided excellent company, advice, and help in the lab when my own experience or lack of extra hands were not enough: Andreas Jöckel, Aline Faber, Tobias Kamp-schulte, Thomas Karg, Lucas Beguin, Roman Schmied, Baptiste Allard, Matteo Fadel, Caspar Ockeloen, Maria Korppi, Matt Rakher, and Thomas Lauber.

Thanks to our friends and collaborators in Neuchâtel: Matthieu Pellaton, The-jesh Bandi, Christoph Affolderbach, and Gaetano Mileti. I gained a huge amount out of our work together. The Neuchâtel team provided me with vapor cells and other precious and essential equipment, helped me with my struggles in vapor cell physics, and introduced me to the atomic clock and precision measurement community.

From the vapor cell and atomic clock communities, thanks to the Adams/Hughes group in Durham, UK, especially Lee Weller and Mark Zentile for your generous help with ElecSus. Thanks to the Pfau group in Stuttgart, Germany, especially Harald Kübler, for sharing your knowledge on vapor cell construction and microwave electrometry. Thanks to Jim Camparo and John Kitching, who were always generous with their time and advice, inspired solutions to lab problems such as cell heating, and from whom I learnt a great deal about vapor cells.

From the ANU, thanks to Nick Robins, who got me over here in the first place, and to my supervisors in nuclear physics, David Hinde and Mahananda Dasgupta, whose voices I still have in my head every time I prepare a new presentation.

Thank you to my family, who have supported me both from Australia and the UK: Horsleys, Carvers, McCarrons, and Lees. Thanks especially to mum, who is wonderful, and who flies all the way to Europe to replenish my vegemite supply. Thanks to my mate Gábor Fábíán, who I've been lucky enough to share the PhD struggles with. Finally, thank you to my girlfriend Clara, who has transformed my life in Basel. Thank you for all of your love and support. I'm not sure I would have made it through without you.

Contents

Abstract	i
Acknowledgements	iii
Contents	viii
1 Introduction	1
2 Atomic Physics in Vapor Cells	11
2.1 Rb Atomic Structure	11
2.2 Rb Vapor Pressure and Atomic Density	13
2.3 Optical Density and Absorption Profile	14
2.4 Optical Pumping	17
2.4.1 Modelling Optical Pumping	18
2.4.2 Radiation Trapping and Quenching	23
2.5 Hyperfine Relaxation	24
2.6 Broadening and Line Shifts	26
2.6.1 Doppler Broadening	26
2.6.2 Dicke Narrowing	27
2.6.3 Optical Broadening and Line Shift	27
2.6.4 Hyperfine Broadening and Line Shift	27
2.7 Collisional Processes	28
2.7.1 Collision Rates	28
2.7.2 Rb - Rb Collisions	29
2.7.3 Rb - Buffer Gas Collisions	33
2.7.4 Diffusion and Rb - Wall Collisions	38
2.8 Antirelaxation Coatings	44
2.9 Conclusions	45
3 Imaging Techniques using Atoms	49
3.1 Microwave Field Reconstruction	49
3.1.1 ^{87}Rb Hamiltonian in a DC Magnetic Field	50
3.1.2 Hyperfine (Microwave) Transitions	52
3.1.3 Rabi Frequencies	53

3.1.4	Microwave Amplitude	54
3.1.5	Microwave Phase	54
3.1.6	Power Broadening and Off-Resonant Microwaves	54
3.2	Experiment Sequences	55
3.2.1	Double-Resonance Spectra	56
3.2.2	Franzen Sequence	56
3.2.3	Ramsey Sequence	58
3.2.4	Rabi Sequence	60
3.2.5	Fitting in Chapters 7 and 8	61
3.2.6	Alternative Techniques	61
3.3	Absorption Imaging	61
3.3.1	Pixel Binning	64
3.3.2	Measurements of the Absolute OD	64
3.3.3	Vibrations	64
3.4	Field Sensitivity and Spatial and Temporal Resolution	65
3.4.1	Atomic Projection Noise	65
3.4.2	Photon Shot Noise	65
3.4.3	Spatial Resolution and Sensor Size	67
3.4.4	Parallel Measurements (Imaging vs. Scanning)	67
3.4.5	Temporal Resolution	67
3.4.6	OD Image Streaming	68
3.5	Equipment	68
3.5.1	Experiment Control	68
3.5.2	Lasers	69
3.5.3	Microwave Generation	70
3.5.4	Detectors	71
4	Relaxation Imaging	73
4.1	Experiment Setup	73
4.2	Temperature Dependence	75
4.3	Imaging Relaxation in the Cell	77
4.4	Modelling Relaxation in the Cell	79
4.4.1	Depolarisation Probability of Rb-Wall Collisions	80
4.4.2	T_1 Relaxation: 2D Model	81
4.5	Outlook	82
5	Clock Characterisation	85
5.1	Clock C-Field	87
5.2	Clock Microwave Magnetic Field	88
5.3	Conclusions	90

6	Ultrathin Vapor Cells and the Cell Filling Station	91
6.1	Equipment and Setup	93
6.1.1	Ultrathin Vapor Cells	93
6.1.2	Temperature Control	94
6.1.3	Imaging Setup	95
6.1.4	Vacuum System	96
6.1.5	Coils	96
6.2	Controlling the Rb Vapor Density, and Vapor Cell Curing	96
6.2.1	Rb Transport	97
6.2.2	Cell Walls as a Rb Source	98
6.2.3	Cell Walls as a Rb Loss Mechanism	99
6.3	Exploring the Parameter Space	102
6.3.1	Relaxation	103
6.3.2	Optical Response	105
6.3.3	Sensitivity and Spatial Resolution	108
6.4	Optical Pumping and Relaxation	110
6.4.1	Modelling Optical Pumping and Relaxation with the Diffusion Equation	110
6.4.2	Characterisation of Optical Pumping	112
6.4.3	Optical Pumping During Imaging Experiments	116
6.5	Discussion of Setup and Possible Improvements	118
6.5.1	Cell Valve Leak	118
6.5.2	White Residue	118
6.5.3	Mechanical Noise	119
6.5.4	Oven and DUT Heating	119
6.5.5	Buffer Gas Filling	120
6.5.6	Isotopically Pure ^{87}Rb	120
6.5.7	Antirelaxation Coated Cells	121
6.5.8	Other Notes	122
7	Imaging Microwave and DC Magnetic Fields with $< 100\mu\text{m}$ Spatial Resolution	125
7.1	Experiment Parameters	125
7.2	OD_{mw} Images	126
7.3	Imaging Microwave Fields Above Test Structures	126
7.3.1	CPW	128
7.3.2	Zigzag Chip	130
7.3.3	Split-Ring Resonator	132
7.4	Vector Imaging of a DC Magnetic Field	133
7.5	Sensitivity	134
7.6	Effect of the Cell on the Microwave Field	140
7.7	Imaging both B_{mw} and E_{mw}	142

8	Frequency Tunable Imaging	145
8.1	Hyperfine Transitions in an Arbitrary DC Magnetic Field	145
8.1.1	Hyperfine Transitions for Microwave Sensing	151
8.2	Reconstruction of Microwave Fields of Arbitrary Frequency	153
8.2.1	Microwave Amplitude	153
8.2.2	Microwave Phase	155
8.3	Experiment Setup	156
8.3.1	Solenoid	158
8.3.2	Temperature Control by Laser Heating	159
8.4	Optical Transitions in an Arbitrary Magnetic Field	160
8.5	Double-Resonance Microwave Detection	163
8.6	Microwave and DC Magnetic Field Imaging	165
8.7	Atomic Relaxation	169
8.8	Conclusions	170
9	Outlook	173
A	Constants and Rb Data	179
B	Lineshape Functions	181
C	Angular Momentum Matrices	183
D	Hyperfine Transitions for Microwave Sensing	185
E	Filling Station Operation	189
E.1	Ultrathin Cell Preparation	189
E.2	Vacuum System	191
E.3	Rb Transfer	191
E.4	Buffer Gas Filling	196
E.5	General Operation	196
E.6	Valve Damage	197
F	Cell Cleaning	199
G	How to see Rabi Oscillations	203
H	S-Parameter Characterisations of the Demonstration Microwave Devices	205
	Bibliography	207

Chapter 1

Introduction

This is a thesis exploring imaging techniques in atomic vapor cells, which is an area that has received relatively little investigation, despite the ubiquitous use of imaging in experiments with ultracold atoms. The main motivation was to develop techniques for imaging microwave magnetic fields. This could transform how we design, characterise, and debug microwave devices, as there are currently no widely used or completely satisfactory microwave imaging techniques. We also worked closely with the Mileti group, at the Laboratoire Temps-Fréquence, Université de Neuchâtel, Switzerland, to develop techniques for characterising and debugging vapor cell atomic clocks. This resulted in imaging techniques for dc magnetic fields and relaxation processes in vapor cells.

As shown in Figure 1.1.a, a vapor cell is essentially a glass box which is used to confine Rb (or other alkali) atoms. In addition to Rb, the cell is also typically filled with some inert buffer gas, which acts to localise the Rb atoms. This gives us longer atomic lifetimes, as the atoms collide with the cell walls less frequently, and gives us better spatial resolution for imaging. In contrast to experiments with ultracold atoms, vapor cells are small, low cost, low power, and simple. This makes vapor cells ideal for practical applications. The price paid is in precise quantum control over the atomic states, and relatively ‘messy’ physics compared to the pure quantum systems achievable with ultracold atoms.

Vapor cells have been a workhorse of atomic physics for decades, with experiments dating back to the 1960s and earlier [1, 2]. Much of the early research was driven by applications in vapor cell atomic clocks [3–6], which at one stage were used as a primary frequency standard. The portability and low power requirements of vapor cell clocks ensure their continuing importance as secondary frequency standards, for example, as the on-board clocks in GPS and Galileo satellites [7, 8]. Recent years have seen significant advances in vapor cell and clock miniaturisation, with micro-fabricated cells on the mm or even 100 μm scale [9–11], further improving clock portability and power consumption, and with a view to integrating atomic clocks into an ever wider range of applications.

There is also a growing interest in applying new techniques to vapor cells, in

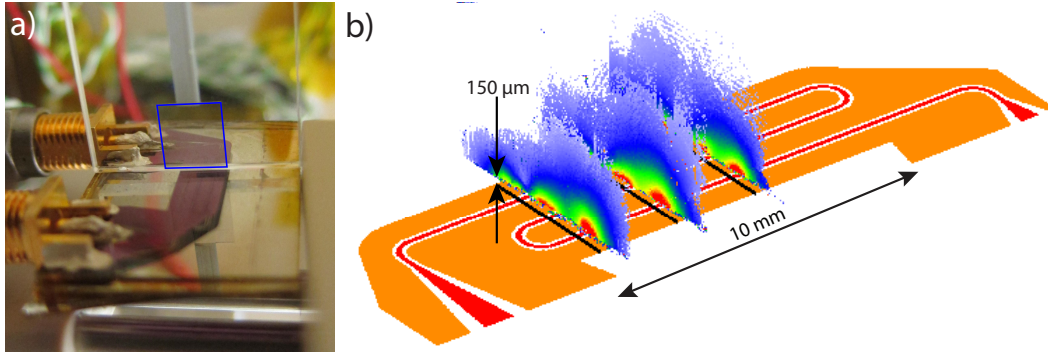


Figure 1.1: Microwave near field imaging using vapor cells: a) photo of an ultrathin vapor cell (inner volume outlined in blue), in position for imaging the microwave field above a test device; b) images of the amplitude of the microwave field above the device. The field is shown in three different planes: by scanning the position of the vapor cell, we are able to build up a 3D image of the field above a device. See Chapter 7 for more information on this measurement.

part taking advantage of advances in our understanding and control of atoms and quantum physics gained in ultracold atom experiments. The largest number of applications to date have been in sensing electromagnetic fields, for which vapor cells have proven themselves to be excellently suited [12–14]. Magnetometers measuring both dc [15–18] and radio-frequency [19] fields, have demonstrated sensitivities as low as $\delta B_{dc} = 0.16 \text{ fT Hz}^{-1/2}$ in a 0.45 cm^3 volume [20], and are used as gyroscopes [21], in explosives detection [22], magnetic nanoparticle detection [23–25], materials characterization [26, 27], in MRI for both medical [28–30] and microfluidics applications [31, 32], and for magnetic imaging of the human heart [33, 34] and brain [35–38]. Vapor cells have also been used to create optical isolators [39] and extremely narrow-band optical filters [40, 41], and are used in quantum memories [42–45].

In the above sensing techniques, the vapor cell is generally used as a single-channel sensor, with measurements performed on the cell bulk, and images of fields obtained either by scanning the single sensor, or by using an array of vapor cells. It is also possible, however, to perform imaging using a single vapor cell, where an array of sensors is formed by groups of atoms at different positions across the cell. All of the sensors are measured in parallel, translating to improvements in imaging speed, sensitivity, and temporal resolution, when compared to creating an image by scanning a single sensor. Compared to obtaining an image using an array of sensors formed by multiple vapor cells, single-cell imaging allows maximally close packing of sensors, and (except in the case of an array of exceptionally small vapor cells) will generally provide better spatial resolution and a simpler setup (e.g. imaging using only a single laser beam instead of one for each sensor). In this way, vapor cells have been used to image dc magnetic scalar potentials with 1 mm^3 spatial resolution and a field resolution corresponding to $\Delta B_{dc} = 2 \text{ nT}$ [46]. Atoms in Rydberg states have

been used to detect and image microwave electric fields with $66\ \mu\text{m} \times 66\ \mu\text{m} \times 3\ \text{cm}$ spatial resolution, and a sensitivity of $\delta E_{mw} = 30\ \mu\text{V cm}^{-1}\ \text{Hz}^{-1/2}$ [47–49], and our group has demonstrated microwave magnetic field imaging with $50\ \mu\text{m} \times 50\ \mu\text{m} \times 140\ \mu\text{m}$ spatial resolution, and a sensitivity of $\delta B_{mw} \approx 1\ \mu\text{T Hz}^{-1/2}$ [50–53]. We have also demonstrated imaging of vapor cell parameters such as T_1 and T_2 atomic relaxation times, with a similar spatial resolution [51, 52].

Microwave Sensing

Motivation

The initial drive for the microwave imaging project in our group came during the development of an atom chip, which uses microwave near fields to trap and manipulate ultracold atoms. There was no satisfactory technique available for characterising the microwave fields above the chip, and so our group developed a new technique, where Rabi oscillations driven on Rb hyperfine transitions are used to image the microwave magnetic field. The technique was first developed with ultracold atoms [54]. This is impractical for debugging during the design phase however, due to the need to place the chip inside an ultrahigh vacuum, and a proof of principle setup for microwave imaging using a vapor cell was constructed [50]. A major component of this thesis was then developing a practical setup capable of imaging microwave near fields above real world devices. I also performed a proof of principle demonstration of microwave imaging at arbitrary microwave frequencies, from 2.3 GHz to 26.4 GHz, rather than the fixed 6.8 GHz splitting of the ^{87}Rb ground state.

In addition to scientific applications, microwave devices play a broad and critical role in modern technology, particularly in telecommunications and defence [55]. In industry, the trend towards miniaturisation requires ever more tightly packed components, with reduced size and thus higher operating frequency. Sophisticated microwave simulation programs are available, but direct measurements of devices are still necessary, particularly for non-linear devices and for devices operating at higher frequencies, above say 18 GHz [56]. Simulation can also become impractical for particularly large or complicated circuits. Our microwave imaging technique is applicable to microwave devices of all types. It has seen success in characterising the magnetron cavities at the heart of vapor cell atomic clocks [51, 52, 57], and we are working with a major microwave company to characterise non-linear devices, such as microwave amplifiers.

The basic characterisation of microwave devices is usually performed using indirect techniques, such as S-parameter measurements with vector network analysers¹. Measured S-parameters are compared with simulated values, and if they match, the device is assumed to be working as designed. Disagreement can be difficult to debug, however, and indirect measurements are not suitable for identifying many internal

¹S-parameters measure the transmission and reflection of signals through each port on a device, generally as a function of frequency.

features. These include standing waves that may form between device components, or near field leakage between microwave components that have been placed too close together [58, 59]. Thus, there is a need for a practical direct measurement technique, which would allow for faster debugging, and the ability to increase the circuitry density [56, 60]. One solution is to use mechanical probes, placing hundreds of needle probes in contact around a device to directly measure the microwave currents, however this is bulky, intrusive, and impractical for complicated circuits [61]. The ideal characterisation technique is contactless, measuring the microwave near field above the device in order to impose minimal perturbations [62]. An ideal technique should also: minimally perturb the microwave device or its near fields; give high spatial and temporal resolution; provide vector-resolved information on the microwave amplitude and relative phase; be easily calibrated; be broadband, i.e. applicable at a range of microwave frequencies; give a wide field of view; and be simple and cheap to operate. The required parameters vary between microwave devices. The required spatial resolution is determined by feature sizes, which can vary from the centimeter to nanometer scale. Operating frequencies are typically in the GHz to 10s of GHz range.

Although far field electric and magnetic components of an electromagnetic wave can be easily related using Maxwell's equations, for practical purposes, the sub-wavelength features of a near field mean that the relationship between the components is no longer straightforward. Measurement techniques are therefore required for both the electric (E_{mw}) and magnetic (B_{mw}) microwave components.

Current Techniques

A number of methods have been investigated for imaging microwave near fields, mostly focusing on imaging E_{mw} . A comparison and summary of techniques is provided in Refs. [56, 62]. Many techniques directly measure the near field amplitude or intensity, such as scanning antennas [63, 64], SQUID probes [65], and NV centres [66, 67]. Another class of techniques relies on sufficiently high temporal resolution to directly detect the oscillating surface potentials induced by the microwave [61, 62]. The detection bandwidth is then determined by the timing resolution, typically on the order of picoseconds or 10s of picoseconds, corresponding to frequencies of a few GHz. This allows for the monitoring of active components, such as logic gates. Techniques include electron beam testing [68, 69], electric force microscopy [70], and electro-optic sampling [71].

Scanned antenna are a relatively simple and broadband probe [63, 72, 73], with the antenna often in the form of a modified coaxial cable [59, 60, 64]. Straight antennas are used to detect $|E_{mw}|^2$, and loop antennas are used to detect $|B_{mw}|^2$, with detection frequencies typically in the 1-20 GHz range [60, 74]. Antenna sizes are typically in the millimeter range, but can be as small as $100 \mu\text{m}$ [63]. The spatial resolution is on the order of 10s to 100s of μm [63, 64], and scans are typically performed a distance $10 \mu\text{m}$ to a few mm above a device. Drawbacks of antenna based measurements include the need for different antenna orientations to detect

each vector component of the field [72], and the field perturbations induced by the metallic probe [64].

Scanning SQUID probes provide the microwave magnetic field [65]. SQUIDS can provide very high sensitivity, on the order of $\text{fT Hz}^{-1/2}$ near dc, but this deteriorates with microwave frequency. SQUIDS capable of sensing microwave frequencies up to 200 GHz have been reported [75], but there are significant problems with signal non-linearity for operation modes above 200 MHz [76]. Spatial resolution is on the μm to 10s of μm level. SQUIDS require cryogenic cooling to operate, which is expensive, and also requires the device under test to be cooled, e.g. to 77 K.

Very recently, NV centres have also be used to detect [66] and image [67] the microwave magnetic field, with a demonstrated sensitivity of $\delta B_{mw} = 150 \text{ nT Hz}^{-1/2}$ for ~ 3 GHz microwaves, and a surface feature spatial resolution of 25 nm. NV center based imaging systems provide nanoscale resolution and typically work in scanning mode. They are thus complementary to our widefield imaging technique which is well adapted to image features on the micrometer scale with temporal resolution.

As an example of the second class of microwave sensing techniques, electron beam testing (EBT) uses a similar principle to a scanning electron microscope [62, 68, 69]. A primary beam of electrons is fired at a device, releasing secondary electrons where they hit the device surface. The secondary electrons reveal the local surface voltage, a function of the local E_{mw} . EBT measures the microwave oscillations directly, and the detection bandwidth is determined by the timing resolution, typically on the order of picoseconds or 10s of picoseconds, corresponding to frequencies up to 24 GHz [62]. The spatial resolution is given by the electron beam spot size, e.g. $0.1 \mu\text{m}$ [68, 69]. EBT is only able to measure surface E_{mw} currents (rather than near fields), and only in the top layer of a device. Measurements must also be performed under vacuum, a significant drawback of the technique.

Electric force microscopy (EFM) can also be used to measure the surface voltage on a device, and thus map the surface E_{mw} currents. The surface voltage is detected using a sharp conducting probe on the end of a cantilever, which is scanned over the device. The spatial resolution can be below 100 nm, and with appropriate sampling schemes, surface currents for microwave frequencies up to 40 GHz can be detected [70]. EFM is susceptible to cross-talk from neighbouring signal lines, and is again limited to measuring surface currents in the top layer of a device.

Electro-optic sampling (EOS) is based on the Pockels effect, where an electric field changes the refractive index of a medium. In the most generally applicable version, EOS is performed using a scanning probe. Pulsed laser light travels down the probe to an electro-optic crystal at the probe tip, and the change in polarisation of the light reflected from the device gives the local E_{mw} field. The EOS bandwidth can be extremely high, even above 1 THz [62], and the spatial resolution is typically on the order of a few μm , given by diffraction limits and the size of the probe crystal [71].

A common feature to all of the above techniques (with the exception of NV centres) is that their calibration and SI traceability present significant issues [60, 77]. Much of the literature provides only relative values of field strength or microwave

current across an image. In addition, the techniques are all scanning techniques, measuring at only a single point at a time. Parallel techniques, where data for all of the image is taken simultaneously, are preferable for imaging speed and temporal resolution over an image. There is also a trade-off in scanning techniques between spatial resolution and field of view. For example, μm or nm spatial resolution is generally unattainable over mm to cm fields of view for any reasonable measurement time.

Atoms as Sensors

Atom based sensors can present a clear SI traceability, and are a natural consideration for microwave sensing. The Rabi frequency, for example, is proportional to the microwave amplitude, and related only by well-known fundamental constants.

Early work to map microwave magnetic fields in a vapor cell using adiabatic rapid passage and a single, scanned probe laser beam was performed by Frueholz and Camparo [78]. Microwave magnetic field measurements have also been made in vapor cells using the atomic candle technique, which measures the Rabi frequency in a frequency domain technique [79, 80]. For imaging B_{mw} , our group has developed a time domain Rabi imaging technique [50, 51, 54]. Atoms in Rydberg states can be used to detect E_{mw} [47–49], and this appears to be the most promising technique for a new microwave power standard [81, 82] to replace calorimeters, which are slow, expensive, and difficult to evaluate [83]. A power standard based on measurements of the microwave magnetic component with ground state atoms has also received interest [80, 83].

Our imaging technique involves bringing a thin vapor cell above a microwave device to measure 2D slices of the microwave magnetic near field. As shown in Figure 1.1, we are able to build up a 3D image of the field by scanning the position of the cell. The imaging technique is minimally perturbing, as it is non-contacting and does not bring metallic devices near the device. By tuning the microwave to different atomic transitions, we are able to obtain images of each of the polarisation components of B_{mw} , and of the relative phase between them. The reliance on time domain measurements of the Rabi frequency makes us relatively insensitive to noise in the signal amplitude, and we avoid calibration issues through the intrinsic SI traceability of the Rabi frequency, which is related to the microwave amplitude through well-known fundamental constants. We have high spatial resolution, demonstrating sub-100 μm resolution. The technique is simple, requiring a relatively minimal investment in lasers and optics, and is parallel, measuring data for the entire image simultaneously on a CCD camera. In principle, this allows for fast measurements and high temporal resolution, with real-time monitoring of the field above a device. We are currently limited by our camera and data processing speeds, however.

Our microwave detection technique is not limited to ^{87}Rb , and can be applied to any system comprised of two states coupled by a microwave transition with optical read-out of the states. Examples of suitable systems are the other alkali atoms, and

solid state ‘atom-like’ systems, such as NV centres [66, 67].

This Thesis

An early result of this thesis was the development of new techniques for spatially resolved vapor cell characterisation. These provide images of the T_1 and T_2 relaxation times, and of the optical pumping efficiency, and are a convenient lab tool for quickly characterising setups, which I used extensively throughout this thesis. The imaging can also be used as a new window into vapor cell physics, which we used to provide spatially resolved information on Rb interactions with the cell walls, and to estimate the Rb relaxation probability in a collision with the cell wall.

The state of the microwave imaging project at the start of my PhD was a proof-of-principle experiment in a basic (and already broken) vapor cell setup, with very little understanding of vapor cell physics in the group. I built a new high resolution imaging setup from scratch, including redoing much of the experiment control. The new setup improved our spatial resolution and distance of approach for imaging by an order of magnitude: from $350 \times 350 \times 3000 \mu\text{m}^3$, imaging up to 1.5 mm above devices; to $50 \times 50 \times 140 \mu\text{m}^3$, imaging as close as $150 \mu\text{m}$ above devices. I improved the data taking speed by close to two orders of magnitude, and made the first characterisation of our imaging sensitivity, $\delta B_{mw} \approx 1 \mu\text{T Hz}^{-1/2}$. The current spatial resolution, distance of approach, and sensitivity of the high resolution setup are already sufficient for characterising 6.8 GHz microwave near fields above a range of real world devices. Orders of magnitude improvement in sensitivity are still possible, however, and I have identified the major limitations in our current setup and made suggestions on how to overcome them. In addition, I showed that our microwave magnetic field imaging techniques can be easily modified to image dc magnetic fields, and demonstrated dc magnetic field imaging using two separate methods.

As a first application of the imaging techniques developed in this thesis, I helped characterise a state-of-the-art Rb vapor cell atomic clock, obtaining images of the dc and microwave magnetic fields and relaxation times. Correction of the field inhomogeneities revealed by this characterisation will allow for real improvements in clock performance.

Finally, I showed that our B_{mw} imaging technique can be extended to image microwaves of any frequency, by using a dc magnetic field to Zeeman shift the hyperfine ground state transitions to the desired frequency. The lower frequency limit is given by the optical resolution of hyperfine states ($\sim\text{GHz}$), and the upper limit is given by the available dc magnetic field ($\sim 30 \text{ GHz}$ for a 1 T dc field, $\sim 1 \text{ THz}$ for a 35 T field). I prepared the theoretical groundwork, detected microwaves from 2.3 GHz to 26.4 GHz, and imaged an 18 GHz microwave field in a proof-of-principle demonstration. This demonstration of frequency tunability was an essential step in realising wider industrial application of our microwave imaging technique.

Thesis Outline

I begin in Chapter 2 by describing the various atomic physics processes that occur in vapor cells. In Chapter 3, I give the theory behind our microwave imaging, and describe the common features to the experiments presented in the later chapters: experiment sequences, spatial resolution, sensitivity, and equipment. Chapter 4 presents a new technique for imaging relaxation and wall interactions in vapor cells, and discusses diffusion. In Chapter 5, I present the characterisation of a vapor cell atomic clock, representing a first application of the imaging techniques we have developed. The development and characterisation of a high resolution setup for use with real world devices is presented in Chapter 6, and its use in imaging dc and microwave magnetic fields is demonstrated in Chapter 7. In Chapter 8, I describe a proof of principle setup for imaging microwaves at any frequency. Finally, future directions are discussed in Chapter 9.

Publications, Talks and Prizes Related to this Thesis

Journal Publications

- A. Horsley, G.-X. Du, Matthieu Pellaton, Christoph Affolderbach, and P. Treutlein. *Imaging of relaxation times and microwave field strength in a microfabricated vapor cell*. Phys. Rev. A 88, 063407 (2013).
- Christoph Affolderbach, G.-X. Du, T. Bandi, A. Horsley, P. Treutlein, and G. Mileti. *Imaging Microwave and DC Magnetic Fields in a Vapor-Cell Rb Atomic Clock*. IEEE Transactions on Instrumentation and Measurement, June 2015.
- A. Horsley, G.-X. Du, and P. Treutlein. *Widefield Microwave Imaging in Alkali Vapor Cells with sub-100 μm Resolution*. Accepted, New Journal of Physics (Fast Track Communications), 2015.

Conference Proceedings

- A. Horsley, G.-X. Du, Matthieu Pellaton, Christoph Affolderbach, and P. Treutlein. *Spatially Resolved Measurement of Relaxation Times in a Microfabricated Vapor Cell*. In Proceedings of the 2013 Joint IEEE-UFFC, EFTF and PFM Symposium, Prague 2013, pages 575-578.
- A. Ivanov, T. Bandi, G.-X. Du, A. Horsley, C. Affolderbach, P. Treutlein, G. Mileti, and A. K. A. Skrivervik. *Experimental and numerical study of the microwave field distribution in a compact magnetron-type microwave cavity*. In Proceedings of the 28th European Frequency and Time Forum, Neuchâtel 2014, pages 208-211.

- Christoph Affolderbach, G.-X. Du, T. Bandi, A. Horsley, P. Treutlein, and G. Mileti. *Imaging the Static Magnetic Field Distribution in a Vapor Cell Atomic Clock*. In Proceedings of the 2015 Joint Conference of the IEEE International Frequency Control Symposium and European Frequency and Time Forum, Denver 2015, pages 21-24.

Invited Talks

- Australian Institute of Physics Congress, 2014, Canberra
- Department Seminar, University of Oxford, May 2015. Invited by group of Ian Walmsley

Prizes

- European Frequency and Time Forum, 2014, Neuchâtel, Switzerland: Winner, Student Award 2014. Finalist 2013-2015.
- Australian Institute of Physics Congress, 2014, Canberra: Winner, student poster prize.

Chapter 2

Atomic Physics in Vapor Cells

In this chapter I run through some of the important processes occurring in vapor cells. I start with a description of the important features of the atomic structure of ^{87}Rb . I then discuss the Rb atomic density and its resulting optical density (OD), which was the principle measured quantity in this thesis. I discuss optical pumping in Section 2.4, and the various collisional interactions in Section 2.7.

The cell walls are a strong relaxation mechanism, and to address this, we fill the cells with an inert buffer gas. This acts to localise the Rb atoms, reducing the wall collision rate, and also improving our spatial resolution for imaging. The buffer gas introduces perturbations of its own, however, which are discussed in Section 2.7.3.

There are a number of references available which provide extremely useful, in depth coverage of vapor cell physics. A selection are in Refs. [4, 6, 84-87].

I use both cyclic (ν) and angular (ω) frequency units. The two are related by $\omega = 2\pi\nu$. In general, frequencies expressed without an explicit factor of 2π are in units of cyclic frequency. The notation also sometimes uses Γ for linewidths, which is in angular frequency units.

2.1 Rb Atomic Structure

There are two naturally occurring isotopes of Rb, ^{85}Rb and ^{87}Rb , with natural abundances of 0.7217 and 0.2783, respectively [88, 89]. We work with the ^{87}Rb , but vapor cells almost always have some mixture of both isotopes, which for the reason of cost is often given by the natural abundances. The influence of the ^{85}Rb can often be ignored during operation, but for our purposes it does have some negative effect on parameters such as the optical density and relaxation rates, as discussed at the end of this chapter.

We work on the ^{87}Rb D₂ line, $5\text{S}_{1/2} \rightarrow 5\text{P}_{3/2}$, shown schematically in Figure 2.1. The choice of the D₂ line was due to considerations of laser compatibility with other experiments in our lab. The line consists of two hyperfine ground state levels, $F = 1, 2$, split by ~ 6.8 GHz, and four hyperfine excited state levels, $F' = 0, 1, 2, 3$, split by 70 – 270 MHz. The hyperfine levels are each comprised of $2F + 1$ (or $2F' + 1$)

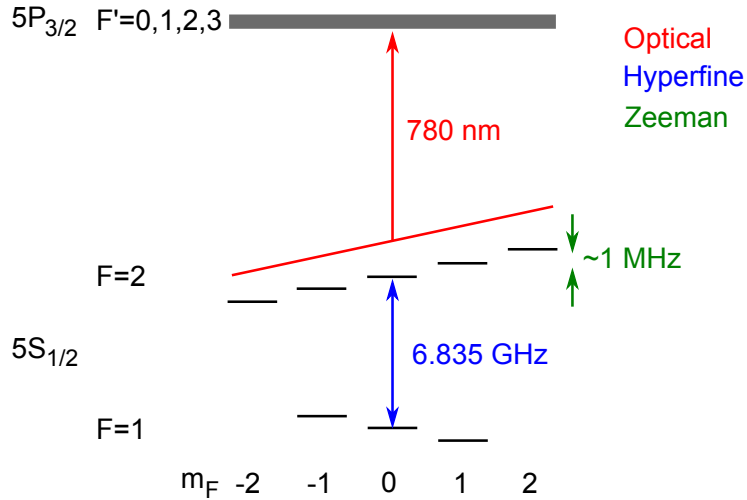


Figure 2.1: The ^{87}Rb D_2 line, including Zeeman splitting of the hyperfine m_F levels in a weak (~ 1 G) dc magnetic field. The optical, hyperfine, and Zeeman transitions are shown in red, blue, and green, respectively.

m_F sublevels.

The optical linewidth in a vapor cell is typically on the order of 0.5-2 GHz, due to a combination of Doppler broadening and collisional broadening from the buffer gas. The 6.8 GHz splitting of the hyperfine ground state levels is sufficient to resolve both states using our lasers (which themselves have negligible linewidths of below 1 MHz), but splitting of the F' levels is not resolved. Within the angular momentum selection rules, the laser therefore couples to all of the F' levels at once¹. This is illustrated in Figure 2.1 by depicting the F' states as a single, broad line.

We typically apply an external dc magnetic field on the order of 1 G, to Zeeman split the hyperfine ground state levels and provide a quantisation axis. The field splits adjacent m_F levels by 0.7 MHz/G (the Zeeman effect is discussed in more detail in Chapter 3). The m_F levels are then the projection of the total atomic angular momentum, F , onto the quantisation axis defined by the magnetic field.

In this thesis, I refer to transitions between the $5S_{1/2}$ and the $5P$ states as optical transitions. Transitions between the $F = 1$ and $F = 2$ ground states are referred to as hyperfine transitions, and transitions between m_F levels of the same F state as Zeeman transitions. These are illustrated in Figure 2.1. Unless explicitly noted otherwise, discussions of m_F states refer to the 8 m_F states of the ^{87}Rb $5S_{1/2}$ ground state.

For essentially all of the experiments in this thesis, I used lasers resonant with the $F = 2$ state atoms. The signal was changes in the absorption of a probe laser, driven by changes in the $F = 2$ state population.

¹The $F = 1$ state couples to $F' = 0, 1, 2$ and the $F = 2$ state couples to $F' = 1, 2, 3$. The coupling strength to each F' level is also frequency dependent

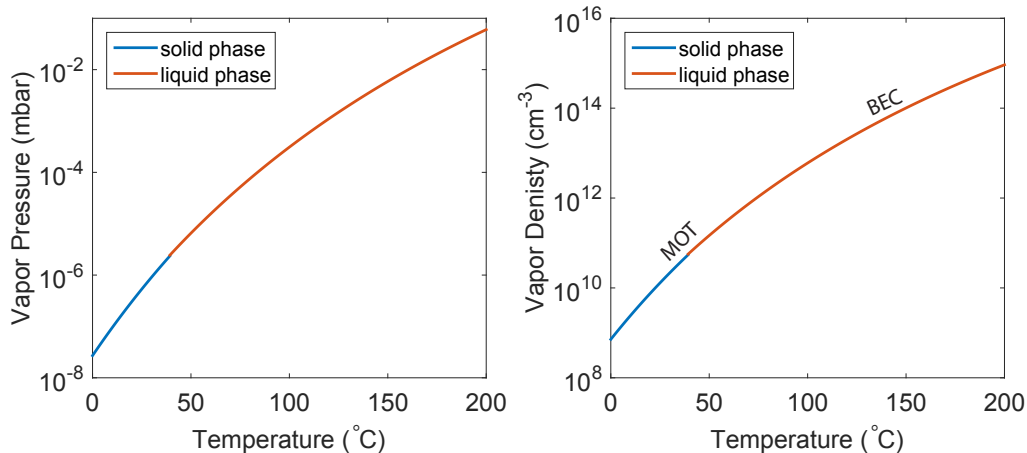


Figure 2.2: Total rubidium vapor pressure and density as a function of temperature. In a cell filled with natural Rb, the ^{87}Rb pressure and density is 28% of these values. For comparison, typical MOT and BEC densities are $10^{10} - 10^{12} \text{ cm}^{-3}$ and 10^{14} cm^{-3} , respectively.

2.2 Rb Vapor Pressure and Atomic Density

The Rb in a vapor cell comes from a macroscopic droplet of Rb metal on the cell wall, known as the Rb reservoir. The Rb droplet forms at the coldest point available to it. This can either be on the cell wall, or in a separate stem. The advantage of the stem is that it allows the reservoir temperature to be set independently of the rest of the cell. It is desirable to have the cell temperature slightly hotter (by a few degrees) than the reservoir, in order to prevent the buildup of Rb on the cell windows.

The vapor pressure of Rb, P_{Rb} , is given by [88]

$$\log_{10} P_{Rb}[\text{torr}] = 2.881 + 4.857 - \frac{4215}{T[\text{K}]} \quad (\text{solid phase, } < 39.3^\circ\text{C}) \quad (2.1)$$

$$\log_{10} P_{Rb}[\text{torr}] = 2.881 + 4.312 - \frac{4040}{T[\text{K}]} \quad (\text{liquid phase, } > 39.3^\circ\text{C}), \quad (2.2)$$

where P_{Rb} is in torr, and T in kelvin. The two different equations are for the solid and liquid phases of Rb, which has a melting point of 39.3°C . We can obtain the Rb density from the Ideal Gas Law,

$$n_{Rb} = \frac{P_{Rb}[\text{Pa}]}{k_B T[\text{K}]}, \quad (2.3)$$

where k_B is Boltzmann's constant. The above equations are valid for both ^{85}Rb and ^{87}Rb . When using an isotopically mixed vapor cell, the density of each isotope can be found by multiplying n_{Rb} by the relative abundance of the isotope. Note that

P_{Rb} must be in the SI unit of pascals when using Eq. (2.3), rather than the units of torr output by Eq. (2.1).

Figure 2.2 shows the rubidium vapor pressure and density as a function of temperature calculated using Eqs. (2.1) and (2.3). The Rb density is strongly dependent on temperature, rising almost exponentially with increasing temperature. We take advantage of this, by heating vapor cells to control the Rb density. Note, however, that even at 200°C, the Rb pressure is still several orders of magnitude below the typical 10s of mbar buffer gas pressures used in this work (discussed below). At room temperature, the Rb vapor pressure is a few 10^{-7} mbar. For comparison, typical Rb densities in a MOT and BEC are $10^{10} - 10^{12} \text{ cm}^{-3}$ and 10^{14} cm^{-3} , respectively. These correspond to vapor temperatures of 23 – 75°C and 150°C.

2.3 Optical Density and Absorption Profile

The absorptive properties of a medium are often described in terms of an optical density (OD). The OD is defined such that light passing through the medium will be attenuated according to

$$I = I_0 \exp(-OD), \quad (2.4)$$

where I_0 and I are the incident and exiting light intensities, respectively. The OD, proportional to the number of absorbing atoms, was the principle measurement parameter used in this thesis.

The Adams/Hughes group has developed a useful and accurate computer program for calculating the OD in alkali vapor cells, called ElecSus [90]. Their basic model is described in Ref [91], with expansions in Refs. [92–94]. I used this model extensively throughout this thesis (both in my own Matlab scripts and through ElecSus), and so summarise it briefly below.

The model provides the absorption coefficient, α , which is the OD per unit length. The calculation assumes a very weak laser beam which does not disturb the atomic populations [95], i.e. neither optical pumping nor saturation effects are considered. For an optical path of length L ,

$$OD = \alpha L. \quad (2.5)$$

The absorption coefficient for a particular optical hyperfine transition $F_g \rightarrow F_e$ is given as

$$\alpha_{F_g F_e}(\Delta) = k \cdot A \cdot B \cdot V, \quad (2.6)$$

$$= k \frac{C_F^2}{2(2I+1)} \frac{d^2 n}{\hbar \epsilon_0} \frac{s^I(y)}{ku}, \quad (2.7)$$

where k is the laser wavevector, $A = \frac{C_F^2}{2(2I+1)}$ is the transition strength including the m_F degeneracy, $B = \frac{d^2 n_{Rb}}{\hbar \epsilon_0}$ is a scaling factor for the optical line (eg D₂), and the Voigt profile $V = \frac{s^I(y)}{ku}$ describes the line shape. Δ is the laser detuning, n is

the relevant ^{87}Rb or ^{85}Rb number density, and I is the nuclear spin ($I = 3/2$ for ^{87}Rb). The dimensionless constant $C_F^2 = \sum c_{m_F}^2$ is the total transition strength of the optical transition $F_g \rightarrow F_e$, including all internal m_F states. Values of C_F^2 for linearly polarised light on the Rb D₂ line are given in Table 2.1. $u = \sqrt{\frac{2k_B T}{m_{\text{Rb}}}}$ is the $1/e$ velocity width of a Maxwell-Boltzmann distribution in 1D, and for the Rb D₂ line, the reduced matrix element d is $d = \langle L_g = 0 | e_{\underline{x}} | L_e = 1 \rangle = 5.177 e a_0$, where e is the elementary charge and a_0 is the Bohr radius. The dimensionless Voigt profile of the transition, $s^I(y)$ is given by²

$$s^I(y) = \sqrt{\pi} \Re \left[\exp[1/4(a - i2y)^2] \operatorname{erfc}[a/2 - iy] \right], \quad (2.8)$$

where $y \equiv \frac{\Delta}{ku}$, $a \equiv \frac{\Gamma}{ku}$, and Γ is the Lorentzian linewidth of the transition. In the absence of external broadening mechanisms, $\Gamma = \Gamma_{\text{nat}}$, the natural decay rate of the transition ($\Gamma_{\text{nat}} = 2\pi \times 6.066$ MHz for the Rb D₂ line). The complementary error function, erfc , is described in Appendix B. To obtain the total optical density, we need to sum α over all of the allowed transitions between the ground and excited hyperfine states, each with their respective detuning.

$$\alpha(\Delta) = \sum_{F_g, F_e} \alpha_{F_g F_e}(\Delta_{F_g F_e}). \quad (2.9)$$

The Lorentzian broadening due to buffer gas collisions [93] and Rb-Rb dipole-dipole interactions [92], can be included simply by adding the terms to Γ , giving a total Lorentzian linewidth of $\Gamma = \Gamma_{\text{nat}} + \Gamma_{\text{bg}} + \Gamma_{\text{dipole}}$. The total linewidth is then a Voigt convolution of the Gaussian Doppler broadening and the Lorentzian linewidth, included through the $s^I(y)/ku$ term in Eq. (2.6). The optical line shift is included by modifying the detuning: $\Delta' = \Delta + \delta\omega_{\text{shift}}$. The broadening and line shift mechanisms are discussed in Section 2.6.

Table 2.1: C_F^2 transition strengths on the Rb D₂ line for linearly polarised light [91].

^{85}Rb					^{87}Rb				
F_g	F_e				F_g	F_e			
	0	1	2	3		1	2	3	4
2	1/3	35/81	28/81	0	1	1/9	5/18	5/18	0
3	0	10/81	35/81	1	2	0	1/18	5/18	7/9

Figure 2.3 shows the OD as a function of cell temperature for 2 mm and 140 μm thick cells, representative of the cells used in this thesis. The laser was assumed to

²This definition is equivalent to that given in Ref. [91], which can be seen by noting that the two erfc terms in Ref. [91] are complex conjugates of one another.

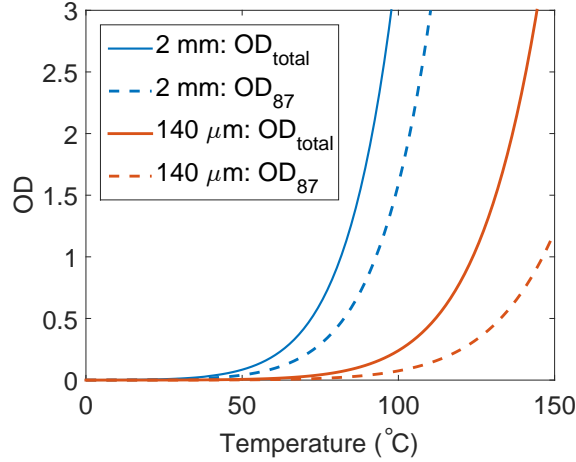


Figure 2.3: Calculated OD in 2 mm and 140 μm thick cells as a function of cell temperature, for a laser resonant with the (unshifted) ^{87}Rb $F = 2 \rightarrow F' = 2/3$ crossover peak (e.g. for a laser locked to a reference cell). The contribution of ^{87}Rb , OD_{87} , is shown in dashed lines. The cells are filled with natural Rb, with 63 mbar of N_2 buffer gas in the 2 mm cell, and a mixture of 75 mbar Kr and 25 mbar N_2 in the 140 μm cell.

be linearly polarised and locked to the $F = 2 \rightarrow F' = 2, 3$ crossover peak³. The optical depth increases rapidly with temperature, following the rapid increase in Rb vapor density with temperature. The cells were modelled for a natural Rb isotopic mixture. The 2 mm cell was modelled with 63 mbar of N_2 buffer gas (see Ch. 4), and the 140 μm thick cell was modelled with a mixture of 75 mbar of Kr and 25 mbar of N_2 buffer gas. The strong temperature dependence of the Rb density translates to a similarly strong temperature dependence in the OD. The necessity of heating the vapor cells is clear, given the negligible OD for both cells at room temperature.

Figure 2.4 shows the OD spectrum of a 140 μm thick cell, again filled with 75 mbar of Kr and 25 mbar of N_2 buffer gas, at a temperature of 140°C. The individual contributions of each isotope are also shown. Dotted lines show the OD without buffer gas, highlighting the shift and broadening of the optical lines induced by the buffer gas. In general, I did not compensate for the optical shift in experiments, and the laser was locked to ^{87}Rb $F = 2$ state atoms in a bufferless reference cell. This meant that the laser frequency was actually on the shoulder of the shifted ^{87}Rb $F = 2$ peak, and that the ^{85}Rb $F = 3$ transitions were shifted closer to the laser frequency.

³The crossover peaks are a feature of saturated absorption spectroscopy that occur at the midpoint of peaks corresponding to actual hyperfine levels [96]. The $F = 2 \rightarrow F' = 2, 3$ crossover is a convenient choice, as it gives the largest peak in the ^{87}Rb saturated absorption spectrum and therefore provides the strongest signal for laser locking.

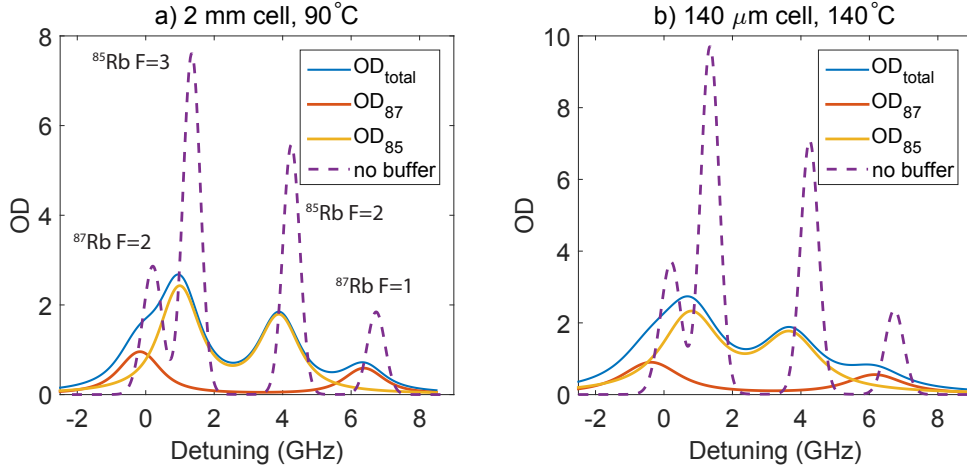


Figure 2.4: Calculated OD spectrum of the Rb D_2 line, as a function of detuning from the centre of the (unshifted) ^{87}Rb $F = 2 \rightarrow F' = 3$ transition for a) a 2 mm thick cell with 63 mbar of N_2 buffer gas; b) a $140\ \mu\text{m}$ thick cell filled with a 75 mbar Kr and 25 mbar N_2 buffer gas mixture. The cells are filled with natural Rb. Dashed lines show the OD in the same cells but without buffer gas, and so without the associated broadening and line shift. The four unbroadened peaks are labelled with their corresponding ground state levels.

2.4 Optical Pumping

Optical pumping is one of the core techniques in atomic physics, providing control over the atomic populations [4]. We use it to prepare the Rb atoms in a (reasonably) well defined initial state at the start of our time-domain experiments (see Section 3.2). These sequences first depopulate one of the hyperfine ground states through optical pumping, and then observe its repopulation. The repopulation can occur both passively, through relaxation processes, and actively, driven by microwave fields. The experiment signal is proportional to the optical pumping efficiency, and the lifetime of the optically pumped population imbalance is also of crucial importance.

I performed optical pumping in this thesis by depopulating the $F = 2$ ground state, a process known as hyperfine depopulation pumping [4]. The basic principle is simple, and is illustrated in Figure 2.5. Without optical pumping, atoms are equally distributed amongst the $8\ m_F$ states (three $F = 1$ states and five $F = 2$). A pumping laser is used to excite the $F = 2$ atoms to the excited $5P_{3/2}$ manifold, from which atoms can decay back to either of the ground F states. Atoms in the $F = 1$ state do not interact with the laser, and are said to be in a ‘dark’ state. Repeated excitation from the $F = 2$ state therefore depopulates it, and in the absence of relaxation, all of the atoms will be transferred to the $F = 1$ state.

With the use of polarised pumping light, it is also possible to take advantage

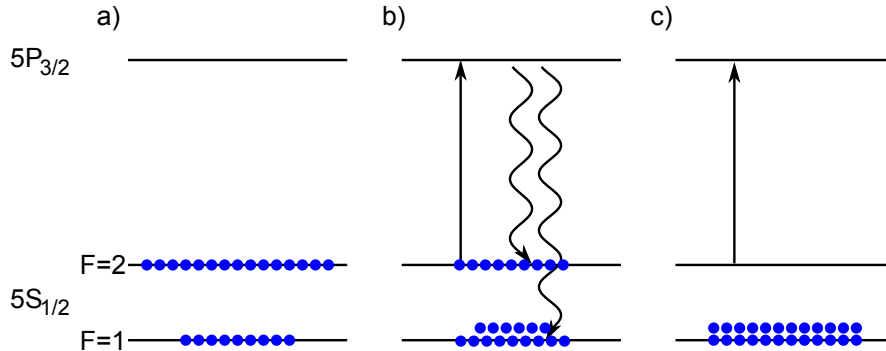


Figure 2.5: Schematic of optical pumping: a) unpumped atoms equally occupy each of the 8 ground m_F states; b) the pumping laser excites atoms from one of the ground states. Atoms can decay from the excited state back to either of the ground states; c) in the absence of relaxation, all of the population is pumped to the dark state.

of angular momentum selection rules to distribute atoms not just to a particular F state, but also a particular m_F state or set of m_F states. Good discussions are provided, for example, in Refs. [84, 87]. In this work, however, the presence of N_2 quenching gas in the cells meant that the decay from optical excitation was largely through collisions, rather than photon emission (see Section 2.4.2). Collisional relaxation can return the atom to any of the ground m_F states, with essentially equal probability. In such a case, the optical angular momentum selection rules no longer apply. As shown in Figure 3.2 in Chapter 3, the pumping polarisation had only minor effect on the optically pumped populations, particularly for the clock transition.

The literature often refers to the observables $\langle S_z \rangle$ and $\langle \mathbf{S} \cdot \mathbf{I} \rangle$. The observable measured in this thesis is $\langle \mathbf{S} \cdot \mathbf{I} \rangle$, which measures the polarisation of the F state populations. Polarisation of the m_F states, which is the orientation of the atomic spins along the magnetic quantisation axis, is measured by $\langle S_z \rangle$. This m_F optical pumping is the typical pumping used in vapor cell magnetometers.

2.4.1 Modelling Optical Pumping

We can use rate equations to model the effect of optical pumping on the OD and the hyperfine state populations. We describe optical pumping using two 3 level systems, each representing one of the two Rb isotopes. As shown in Figure 2.4, buffer gas collisional broadening of the optical lines leads to a significant overlap of the D_2 ^{87}Rb $F = 2$ and ^{87}Rb $F = 3$ absorption peaks. For the parameters used in Figure 2.4, approximately half of the OD at resonance with the ^{87}Rb $F = 2$ peak is due to ^{85}Rb atoms, and it is therefore necessary to consider both Rb isotopes in our modelling. The two modelled systems do not directly interact with one another, but both couple to the same light field.

The 3 level description for each isotope is justified by considering the typical 0.5-2 GHz optical linewidth in vapor cells. As mentioned in Section 2.1, this means that the Rb $5P_{3/2}$ states cannot be individually resolved. The hyperfine ground state splitting of several GHz is sufficiently large for optical resolution of the ^{87}Rb and ^{85}Rb ground states, but we cannot optically resolve the internal m_F states, which are typically split by \sim MHz.

A schematic of our model is shown in Figure 2.6. The three ^{87}Rb levels are the $5S_{1/2}$ $F = 1, 2$ states, levels $|1\rangle$ and $|2\rangle$, respectively, and the $5P_{3/2}$ excited state manifold, level $|3\rangle$. The three ^{85}Rb levels are the $5S_{1/2}$ $F = 2, 3$ states, levels $|4\rangle$ and $|5\rangle$, respectively, and the $5P_{3/2}$ excited state manifold, level $|6\rangle$. The internal states of these levels are included in the model through the coupling rates and branching ratios.

We begin by describing the model in the context of the ^{87}Rb atoms, however the discussion can be equally applied to the ^{85}Rb atoms by substituting the coupling rates given in Figure 2.6.b. The model closely follows that described, for example, in Ref. [8].

The laser couples states $|1\rangle$ and $|2\rangle$ to the excited state, $|3\rangle$, with optical excitation rates R_{P1} and R_{P2} , respectively. The decay rate of the excited state is given by $\Gamma^* = \Gamma_{nat} + \Gamma_Q$, where $\Gamma_{nat} = 2\pi \times 6.066$ MHz is the Rb D_2 natural linewidth, and Γ_Q is the collisional quenching rate of the excited state (see Section 2.4.2). We assume that the excited state is able to decay with equal probability to each of the 8 m_F ground states, which is true if the primary relaxation mechanism is through collisions rather than spontaneous emission ($\Gamma_Q \gg \Gamma_{nat}$). The branching ratio to states $|1\rangle$ and $|2\rangle$ is then $\frac{3}{8}$ and $\frac{5}{8}$, respectively. The ground states are also coupled through collisional exchange processes, with non-equilibrium population distributions decaying at a rate γ . The coupling rate for each state is equal to the fraction of m_F ground states in the opposing F state. $|1\rangle$ thus decays to $|2\rangle$ at a rate $\frac{5}{8}\gamma$, and $|2\rangle$ decays to $|1\rangle$ at a rate $\frac{3}{8}\gamma$.

The rate equations for the three populations are

$$\dot{N}_1 = -R_{P1} N_1 - \frac{5}{8}\gamma N_1 + \frac{3}{8}\gamma N_2 + \frac{3}{8}\Gamma^* N_3, \quad (2.10)$$

$$\dot{N}_2 = -R_{P2} N_2 + \frac{5}{8}\gamma N_1 - \frac{3}{8}\gamma N_2 + \frac{5}{8}\Gamma^* N_3, \quad (2.11)$$

$$\dot{N}_3 = R_{P2} N_2 + R_{P1} N_1 - \Gamma^* N_3, \quad (2.12)$$

Where $N_{1,2,3}$ are the populations of states $|1\rangle$, $|2\rangle$ and $|3\rangle$, respectively. Assuming that the excited population is in the steady state, ie $\dot{N}_3 = 0$, we find

$$N_3 = \frac{R_{P2} N_2 + R_{P1} N_1}{\Gamma^*}. \quad (2.13)$$

The rate equation model is valid in the limit of a weak pumping laser,

$$R_P \ll |\Omega_R| \ll \Gamma^*, \quad (2.14)$$

where $|\Omega_R|$ is the optical Rabi frequency. That is, the relaxation from the excited state should occur on a timescale much faster the optical pumping rate, and the

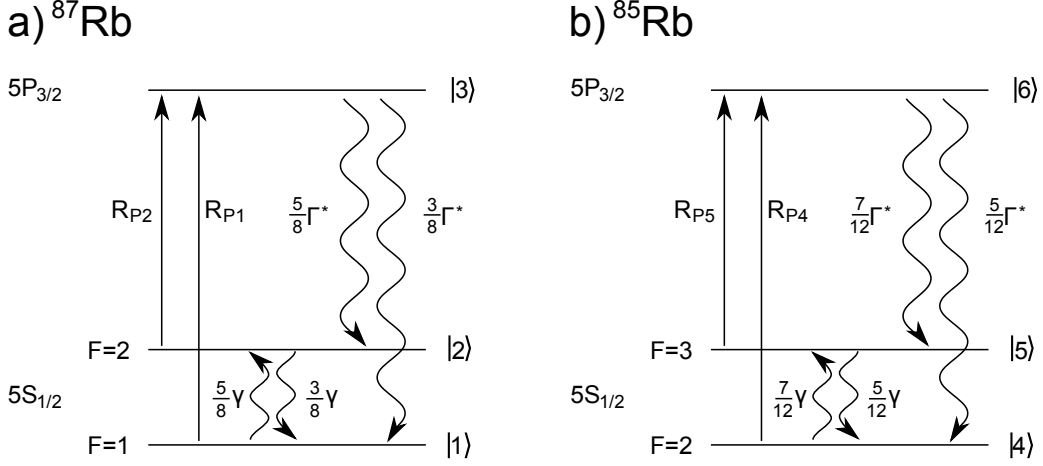


Figure 2.6: 3 level model of optical pumping in Rb. The mixture of ^{87}Rb and ^{85}Rb in our cells is modelled as two separate 3 level systems, with the light field coupling to both.

pumping rate should be sufficiently weak that the laser does not drive Rabi oscillations. In such a case, Eq. (2.12) tells us $N_3 \ll N_1, N_2$, and therefore $N_1 + N_2 \approx N$, where N is the total ^{87}Rb atom number. Even for $\Gamma^* = \Gamma_{nat}$, the typical pumping rate of $R_{P2} = 10^6 \text{ s}^{-1}$ results in an N_3 population less than 3% of the total.

Optical pumping was generally performed in this thesis by depopulating the $F = 2$ state. It is then convenient to define the change in population induced by optical pumping as

$$\Delta n \equiv \frac{N_1 - \frac{3}{5}N_2}{N} = 1 - \frac{N_2}{\frac{5}{8}N}. \quad (2.15)$$

For depopulation pumping and probing of the $F = 2$ state, Δn represents the ^{87}Rb optical pumping efficiency. In equilibrium without optical pumping, $N_2 = \frac{5}{8}$ and $\Delta n = 0$, whilst for complete depopulation of the $F = 2$ state, $N_2 = 0$ and $\Delta n = 1$. Using this definition, we can then rearrange Eqs. (2.10), (2.11) and (2.13) to give

$$\Delta \dot{n} = \frac{3}{8}(R_{P1} - R_{P2}) - \left(\frac{5}{8}R_{P1} + \frac{3}{8}R_{P2} + \gamma\right) \Delta n. \quad (2.16)$$

This gives a steady state population change of

$$\Delta n_{ss} = \frac{\frac{3}{8}(R_{P1} - R_{P2})}{\frac{5}{8}R_{P1} + \frac{3}{8}R_{P2} + \gamma}. \quad (2.17)$$

Assuming $\Delta n(t=0) = 0$, the full solution is

$$\Delta n(t) = \Delta n_{ss} \left(1 - \exp\left[-\Gamma_{P87} t\right]\right), \quad (2.18)$$

where

$$\Gamma_{P87} = \frac{5}{8}R_{P1} + \frac{3}{8}R_{P2} + \gamma \quad (2.19)$$

is the optical pumping rate.

We can carry through a similar derivation for the ^{85}Rb atoms. The population change induced by optical pumping is now

$$\Delta m \equiv \frac{N_4 - \frac{5}{7}N_5}{M} = 1 - \frac{N_5}{\frac{7}{12}M}, \quad (2.20)$$

where M is the number of ^{85}Rb atoms. This gives a steady state population change of

$$\Delta m_{ss} = \frac{\frac{5}{12}(R_{P4} - R_{P5})}{\frac{7}{12}R_{P4} + \frac{5}{12}R_{P5} + \gamma}, \quad (2.21)$$

and a full solution in time of

$$\Delta m(t) = \Delta m_{ss} \left(1 - \exp \left[-\Gamma_{P85} t \right] \right), \quad (2.22)$$

where the optical pumping rate is

$$\Gamma_{P85} = \frac{7}{12}R_{P4} + \frac{5}{12}R_{P5} + \gamma. \quad (2.23)$$

Assuming $R_P \ll |\Omega_R|$, the optical excitation rates for both Rb isotopes can be calculated using perturbation theory. For $\alpha = 1, 2, 4, 5$, we have [8, 96]

$$R_{P\alpha} = \frac{|\Omega_{R\alpha}/2|^2 \Gamma_{opt}}{(\Gamma_{opt}/2)^2 + \delta_\alpha^2}. \quad (2.24)$$

where $\Omega_{R\alpha}$ is the Rabi frequency, Γ_{opt} is the Doppler and collisionally broadened optical line, and δ_α is the optical detuning from resonance. For unpolarised pumping light, one can apply angular momentum selection rules [97] to show that

$$|\Omega_{R\alpha}|^2 = \frac{2}{3}|\Omega_R|^2, \quad (2.25)$$

where $|\Omega_R|^2 = \frac{\Gamma_{nat}^2 I_{pump}}{2 I_{sat}}$ is the familiar Rabi frequency derived for a two-level atom [96], and $I_{sat} \approx 1.7 \text{ mW/cm}^2$ is the two-level atom saturation intensity (and also the saturation intensity of the ^{85}Rb and ^{87}Rb cycling transitions). For $\Gamma_{opt} = 2\pi \times 2 \text{ GHz}$, $I_{pump} = 200 \text{ mW/cm}^2$, and $\delta_2 = 0$, we find $R_{P2} = 5.1 \times 10^6 \text{ s}^{-1} \ll |\Omega_{R2}| = 2.4 \times 10^8 \text{ s}^{-1}$, satisfying the condition given in Eq. (2.14).

Our optical pumping model is valid for pumping light of any frequency. The response of the cell, however, is dependent on the probe frequency. We can calculate the OD in the absence of optical pumping using the model described in Section 2.3, along with the contributions due to ^{87}Rb and ^{85}Rb , OD_{87} and OD_{85} . The optical pumping efficiency of the cell, u , is

$$u[\omega_{probe}] \equiv \frac{\Delta OD[\omega_{probe}]}{OD[\omega_{probe}]}, \quad (2.26)$$

where

$$\Delta OD[\omega_{probe}] = \Delta OD_{87}[\omega_{probe}] + \Delta OD_{85}[\omega_{probe}] \quad (2.27)$$

is the total change in OD due to optical pumping, and is a function of the probe frequency, ω_{probe} . For the typical $\Gamma_{opt} = 2\pi \times 2$ GHz used in this thesis, the hyperfine splitting of the Rb isotopes is sufficient that when probing ^{87}Rb , absorption is essentially only due to a single hyperfine state per Rb isotope: either the ^{87}Rb $F = 2$ and ^{85}Rb $F = 3$ states, or the ^{87}Rb $F = 1$ and ^{85}Rb $F = 2$ states. For a probe frequency near the ^{87}Rb $F = 2$ line, we have

$$\Delta OD_{87} = \frac{\Delta N_2}{\frac{5}{8}N} OD_{87} = \left(\frac{N_2}{\frac{5}{8}N} - 1 \right) OD_{87} = -\Delta n_{ss} OD_{87} \quad (2.28)$$

and

$$\Delta OD_{85} = \frac{\Delta N_5}{\frac{7}{12}M} OD_{85} = \left(\frac{N_5}{\frac{7}{12}M} - 1 \right) OD_{85} = -\Delta m_{ss} OD_{85}. \quad (2.29)$$

For a probe frequency near the ^{87}Rb $F = 1$ line, we have

$$\Delta OD_{87} = \frac{\Delta N_1}{\frac{3}{8}N} OD_{87} = \left(\frac{N_1}{\frac{3}{8}N} - 1 \right) OD_{87} \quad (2.30)$$

and

$$\Delta OD_{85} = \frac{\Delta N_4}{\frac{5}{12}M} OD_{85} = \left(\frac{N_4}{\frac{5}{12}M} - 1 \right) OD_{85}. \quad (2.31)$$

The optical pumping rate for the entire cell is in general governed by two time constants, Γ_{P87} and Γ_{P85} , with pumping following a double-exponential of the form

$$\Delta OD[t] = A \exp(-\Gamma_{P87}t) + B \exp(-\Gamma_{P85}t). \quad (2.32)$$

Figure 2.7 shows optical pumping rates and efficiencies calculated using the above model for typical experiment parameters in the $140 \mu\text{m}$ ultrathin cell described in Chapter 6: $\gamma = 10^5 \text{ s}^{-1}$, $\Gamma_{opt} = 2\pi \times 2$ GHz, laser tuned to the $F = 2 \rightarrow F' = 2, 3$ crossover, and $OD_{87} = OD_{85} = 0.5 OD$. Curves are shown for each of the Rb isotopes individually, and also for the net response of a cell filled with natural Rb. The ^{87}Rb and ^{85}Rb optical pumping rates can be seen to be primarily due to excitation of the upper hyperfine ground states, with the laser coupling only minimally to the lower hyperfine states. Scaled to $\frac{3}{8}R_{P2} = 1$, the optical excitation rates are $\frac{5}{8}R_{P1} = 0.03$, $\frac{7}{12}R_{P4} = 0.07$, and $\frac{5}{12}R_{P5} = 0.37$. The ^{85}Rb pumping rate and efficiency are much lower than for ^{87}Rb , due to the detuning of the laser from the ^{85}Rb resonance. For a natural Rb cell, this results in a lower net optical pumping efficiency, shown in yellow. The optical pumping efficiency flattens out above $I_{pump} = 75 \text{ mW/cm}^2$. Although the ^{87}Rb pumping efficiency approaches 90% for high laser intensities, the net pumping efficiency of the cell only reaches 80%. The reason $\Gamma_P \neq 0$ at $I_{pump} = 0$ is that Γ_P is also a function of the relaxation rate, γ .

Radiation trapping (see Section 2.4.2) was assumed to be negligible for the modelling in Figure 2.7. As shown in Chapter 6 however, radiation trapping can result in significant inhibition of optical pumping, by producing secondary light resonant with the level $|1\rangle$, $|4\rangle$, and $|5\rangle$ atoms.

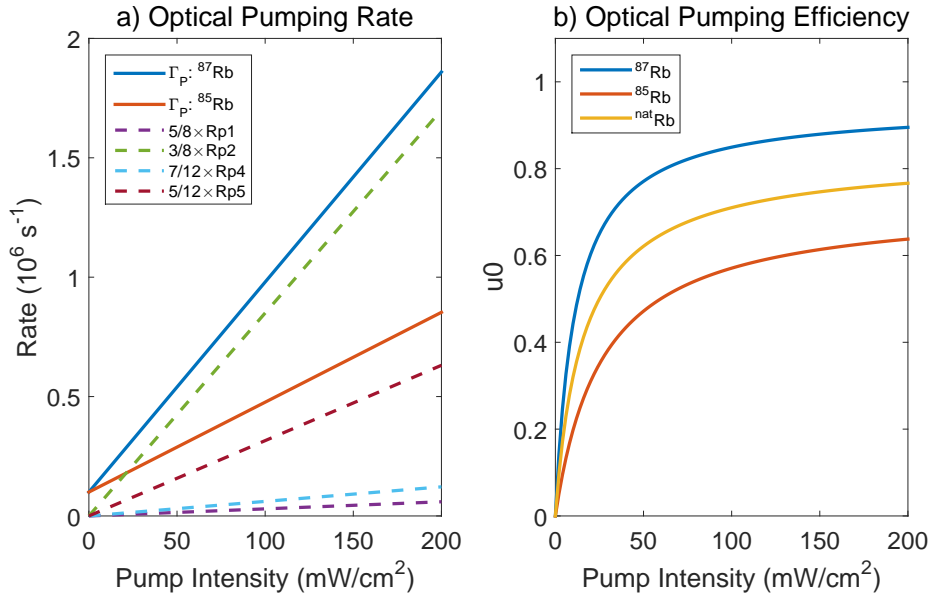


Figure 2.7: a) Optical pumping rate, and b) optical pumping efficiency as a function of pump laser intensity, calculated using the 3 level model described in Section 2.4.1, using parameters typical of the ultrathin cell described in Chapter 6. Curves are shown for pure ^{87}Rb (blue) and ^{85}Rb (red) systems, as well as a natural mixture of the isotopes (yellow). The contributions of the optical excitation rates to the pumping rates are also shown in dotted lines. In this figure, the laser frequency is resonant with the *collisionally shifted* ^{87}Rb $F = 2 \rightarrow F' = 2/3$ crossover peak.

2.4.2 Radiation Trapping and Quenching

Radiation trapping occurs in atomic samples of high OD [98, 99]. As an optically excited atom decays to the ground state, it emits a photon resonant with the transition from the ground F state it decayed to. In low OD systems, the most likely outcome is that this emitted photon simply flies out of the vapor cell. In high OD systems however, the photon is likely to be reabsorbed by the surrounding atoms, which in the case of decay to the $F = 1$ state, results in a pumping-back process. Depending on the OD, a single photon can undergo many such rescattering events (10s to 100s [98]), severely limiting the optical pumping efficiency. As the effect is proportional to the intensity of the pump laser, it cannot be overcome simply by increasing the laser power.

We address radiation trapping by introducing a quenching gas to the vapor cell. The most popular choice of quenching gas is N_2 , which presents a number of internal rovibrational states that are near-resonant with alkali optical absorption frequencies, and also has good properties as a buffer gas (see Tables 2.3-2.6). Excited Rb atoms colliding with the N_2 are therefore able to decay to the ground state by exciting

internal molecular states, suppressing spontaneous emission. The N₂ excitation leads to a heating of the gas, which for optical pumping powers of many watts can be 10s or 100s of degrees [100]. Such heating was assumed to be negligible for the ~ 10 mW pumping powers used in this thesis though.

The quenching rate is

$$R_Q = n_Q \sigma_Q \bar{v}_{rel}, \quad (2.33)$$

where n_Q is the number density of the quenching gas, σ_Q is the quenching collisional cross section, and \bar{v}_{rel} is the mean relative velocity between a Rb atom and the quenching gas. Values of σ_Q for N₂ and the Rb D₁ and D₂ lines are given in Table 2.2. The probability, Q , that a Rb atom will decay from an optically excited state via photon emission is

$$Q = \frac{1}{1 + R_Q/\Gamma_{nat}}, \quad (2.34)$$

where Γ_{nat} is the natural linewidth (and thus the spontaneous decay rate). It is convenient to rewrite this in terms of a characteristic pressure, P'_Q , such that $P_Q = P'_Q$ corresponds to a 50% suppression of spontaneous emission from the excited state [101],

$$Q = \frac{1}{1 + P_Q/P'_Q}. \quad (2.35)$$

P'_Q is (weakly) a function of temperature, through the \bar{v}_{rel} dependence of R_Q ⁴. Table 2.2 gives P'_Q values for two operating temperatures commonly used in this thesis. Quenching rates for representative conditions are given in Table 2.7. The quenching cross sections for Rb collisions with the noble gases are negligible, on the order of $10^{-20} - 10^{-24}$ cm² [102].

Figure 2.8 shows Q as a function of N₂ pressure. The calculation is performed on the Rb D₂ line, for a cell temperature of 140°C. Relaxation of the excited state via spontaneous photon emission is reduced by more than 80% for N₂ pressures above ~ 20 mbar. This broadly agrees with the experiments in Ref. [98], which showed that in their cell geometry, N₂ pressures of 1-10 torr were sufficient to suppress radiation trapping in low-medium Rb densities ($10^{12} - 10^{13}$ cm³). Radiation trapping is compared with our own experiment results in section 6.4.2, through inclusion in the 3 level optical pumping model.

2.5 Hyperfine Relaxation

Optical pumping produces a non-equilibrium population distribution in the hyperfine ground states. The lifetime of this population imbalance is $T_1 = 1/\gamma_1$, and the lifetime of coherence between pairs of m_F states is $T_2 = 1/\gamma_2$. In analogy with NMR, these can also be referred to as the longitudinal and transverse relaxation lifetimes,

⁴This neglects the temperature dependence of σ_Q , for which I could not find any data. The temperature dependence of collisions is discussed in more detail in Section 2.7.3.

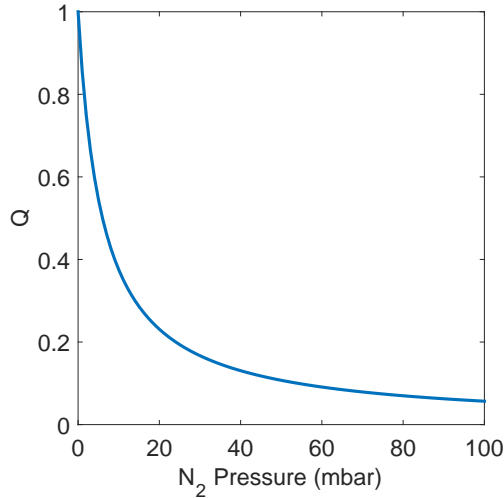


Figure 2.8: Quenching factor, Q , on the Rb D₂ line as a function of N₂ pressure, at a cell temperature of 140°C.

respectively. Relaxation back to equilibrium occurs through a variety of collisions, as described in Section 2.7. The relaxation rates for each of these mechanisms sum to give [6, 104]

$$\gamma_{1(2)} = \gamma_{1(2)SE} + \gamma_{1(2)bg} + \gamma_{walls}, \quad (2.36)$$

where the subscript 1(2) denotes T₁(T₂) relaxation, $\gamma_{1(2)SE}$ are the Rb-Rb spin exchange rates, given by Eqs. (2.48) and (2.49), $\gamma_{1(2)bg}$ are relaxation due to Rb collisions with the buffer gas atoms, given by Eq. (2.57), and γ_{walls} is relaxation due to Rb diffusion to the cell walls, given by Eqs. (2.71)-(2.73). γ_{walls} has been measured to be the same for both T₁ and T₂ relaxation [5].

It is worth noting explicitly that in our definition, T₁ refers to $\langle \mathbf{S} \cdot \mathbf{I} \rangle$ population relaxation of the F states, and so is an aggregate over the m_F sublevels, whilst T₂ is for a particular hyperfine transition between two m_F states. In this framework, Zeeman transitions between m_F states of the same F level contribute to T₂ relaxation, but not T₁. In the absence of perturbations due to external fields, I assume that T₂ is the same for all of the hyperfine transitions. I also assume that the T₁ relaxation rate is the same for both isotopes of Rb. This is important when considering population relaxation in isotopically mixed cells (all of the cells used in this thesis), where the experimental observable (the OD) is due to both Rb isotopes.

In addition to events that cause both T₁ and T₂ relaxation, there are a number of additional pure T₂ dephasing mechanisms, primarily through interactions with the buffer gas [5]. As discussed in Section 2.7.2, when Rb-Rb spin exchange is the dominant relaxation mechanism, it is nevertheless possible to have $T_2 > T_1$. For a two level system, T₂ is bounded by 2T₁. The bound is slightly lower in multi-level systems, and is determined by the nuclear spin.

Typical relaxation rates and times for the cells and conditions used in this thesis are given in Table 2.7.

2.6 Broadening and Line Shifts

Thermal motion and collisions in a vapor cell result in a frequency broadening and shift of the Rb optical and hyperfine transitions. The thermal motion of atoms results in Doppler broadening, discussed below. The collisional interactions in a cell are complex, and are discussed in detail in Section 2.7. Briefly, collisions involving a Rb atom distort the Rb electron cloud, inducing phase shifts and also state changes. The accumulation of phase shifts gives an average frequency shift of a resonance, and the random scattering in sign and amplitude of the phase shifts leads to a broadening of the resonance. The state changes also produce broadening.

Accurate knowledge of line shifts and broadening is important for modelling systems during the design phase, and can also be used to characterise systems, for example to measure the buffer gas pressure or cell temperature. Typical line shifts and broadening values for the cells and conditions used in this thesis are given in Table 2.7.

As mentioned at the start of this chapter, frequencies are discussed in both cyclic (ν) and angular (ω) units, which are related by $\omega = 2\pi\nu$. The cyclic frequency can be directly compared with the relevant collision rates and is convenient for ease of discussion, but it should be converted to units of angular frequency for calculating the OD. Shifts and broadening are denoted as $\delta\omega(\delta\nu)$ and $\Delta\omega(\Delta\nu)$, respectively. Linewidths are given as the full-width-half-maximum (FWHM).

2.6.1 Doppler Broadening

The thermal motion of atoms in a vapor cell results in Doppler broadening of the optical absorption line, given by the Gaussian FWHM of

$$\Delta\omega = \frac{\omega_0}{c} \sqrt{\frac{8k_B T \ln 2}{m_{87}}}, \quad (2.37)$$

where ω_0 is the optical absorption frequency, T is the cell temperature, c is the speed of light, k_B is Boltzmann's constant, and m_{87} is the ^{87}Rb mass.

Doppler broadening is often thought of as an inhomogeneous broadening mechanism, but for atoms in a buffer gas cell, the broadening functions more as a homogeneous mechanism. This is because each Rb atom undergoes velocity changing collisions with the buffer gas at a rapid rate, on the order of 10^9 s^{-1} (see Table 2.7), and thus samples a large fraction of velocity space during an interaction period, e.g. $T_1 = 10 \mu\text{s}$ or a $0.3 \mu\text{s}$ probe laser pulse.

2.6.2 Dicke Narrowing

The rapid velocity changing collisions in a buffer gas cell also lead to the effect of Dicke narrowing [84, 105]. When the Rb mean free path, L , is much shorter than the wavelength of a transition, λ , there is a motional averaging that cancels out the Doppler broadening. For the 6.8 GHz ^{87}Rb hyperfine ground state transitions, $\lambda \approx 4$ cm, and this condition is easily met with a few mbar of buffer gas. The Dicke narrowed linewidth is

$$\Delta\omega = 4\pi \frac{D}{\lambda^2}, \quad (2.38)$$

where D is the diffusion constant, given by Eq. (2.75), and λ is the wavelength of the transition. The resulting narrowed linewidths can be as small as a few Hz, dramatically smaller than the ~ 10 kHz Doppler broadening that would otherwise be present.

Dicke narrowing is not significant on the optical absorption lines in buffer gas cells⁵. Although it is possible to meet the $L \ll \lambda$ condition given by Eq. (2.38) with buffer gas pressures of several 10s of mbar (see Table 2.7), the resulting narrowing is only on the order of 10%. In addition, any narrowing is offset by buffer gas induced broadening, which is on the order of 10 – 20 MHz/mbar for the optical lines (see Table 2.5).

2.6.3 Optical Broadening and Line Shift

The optical line shift is primarily determined by buffer gas collisions, and is given by Eq. (2.55), below. The optical linewidth is given by a Voigt profile convolution of Gaussian Doppler broadening, given by Eq. (2.37) (Section 2.6.1), and the Lorentzian natural and collisionally broadened linewidths,

$$\Gamma_{Lor} = \Gamma_{nat} + \Gamma_{dipole} + \Gamma_{bg}, \quad (2.39)$$

where Γ_{nat} is the Rb D₂ natural linewidth, Γ_{dipole} is the Rb-Rb self broadening, given by Eq. (2.50) (Section 2.7.2), and $\Gamma_{bg} = \Delta\omega_{bg}$ is the buffer gas induced broadening, given by Eq. (2.56) (Section 2.7.3). The units should be in angular frequency. The convolution is included in the model summarised in Section 2.3.

2.6.4 Hyperfine Broadening and Line Shift

The microwave line shift is determined by the buffer gas species and density, and is given in Eq. (2.52). The hyperfine line width is limited by the Lorentzian broadening associated with the finite coherence time of the levels [6],

$$\Delta\omega = 2\gamma_2, \quad (2.40)$$

where γ_2 is the T₂ relaxation rate (see Sections 2.5 and 2.7). Externally applied electromagnetic fields, in particular the dc and microwave magnetic fields, induce

⁵It can, however, be seen in bufferless nano-cells [106].

further broadening. For the conditions in this thesis, the field-induced broadening was often the dominant broadening mechanism, typically resulting in linewidths on the order of kHz to 10s of kHz, but in extreme cases (inhomogeneities in the Tesla-order magnetic fields used in Chapter 8) giving 100 MHz broadening or more. The field-induced broadening is discussed further in Chapter 3.

2.7 Collisional Processes

Collisions affect relaxation, and give rise to line shifts and broadening on both optical and hyperfine transitions. The important collisions are Rb collisions with other Rb atoms, the buffer gas, and the cell walls. In this section, I give an overview of the various collision processes. I try to give both a qualitative understanding of the processes, as the quantitative modelling that follows is heavily based on experimentally obtained parameters, and can be somewhat phenomenological. The discussion is written in terms of the effects on the $^{87}\text{Rb } 5S_{1/2}$ valence electron.

2.7.1 Collision Rates

The collision interactions modelled in the following sections are functions of the collision rate for that interaction. For a particular interaction, the collision rate between Rb and some species, S_2 , is given by

$$\gamma = n_{S_2} \sigma \bar{v}_{Rb S_2}, \quad (2.41)$$

where n_{S_2} is the number density of the second species, and σ is the collision cross section for the interaction. Cross sections for various interactions are given in Table 2.3. The mean relative velocity of the Rb and S_2 particles, $\bar{v}_{Rb S_2}$, is given by

$$\bar{v}_{Rb, S_2} = \sqrt{\frac{8k_B T}{\pi M}}, \quad (2.42)$$

where k_B is Boltzmann's constant, and T is the temperature. M is the reduced mass of the colliding system, given by

$$M = \frac{m_{Rb} m_{S_2}}{m_{Rb} + m_2}, \quad (2.43)$$

where m_{Rb} and m_{S_2} are the atomic masses of the Rb and the second species. The mean free path between collisions is

$$L = \left(n_{S_2} \sigma \sqrt{m_{Rb}/M} \right)^{-1}. \quad (2.44)$$

In principle, the values of σ_{total} listed in Table 2.3, which were measured in atomic beam experiments, could be used for calculating the net mean free path for collisions of all types with the buffer gas. However, this yields a value that is incompatible with the measured diffusion rates. As discussed in section 2.7.4, general agreement

is reached by scaling the σ_{total} values by a factor of $\frac{1}{20}$. For calculating the net mean free path between buffer gas collisions, I used

$$L = \frac{3D}{\bar{v}_{Rb,S_2}}, \quad (2.45)$$

where D is the diffusion coefficient, given in Table 2.6. The net mean free path for collisions with multiple species is given by the inverse sum of the values for each species⁶,

$$\frac{1}{L} = \frac{1}{L_1} + \frac{1}{L_2} + \dots. \quad (2.46)$$

If the collision cross section, σ , is independent of temperature, γ scales with temperature as $T^{1/2}$, through the \bar{v}_{Rb,S_2} term in Eq. (2.41). The temperature dependence of σ is dependent on the exact form of the interaction potential between the colliding atoms or molecules however. The potential is typically modelled as $V(R) = \sum C_p/R^p$, where C_p are the interaction coefficients and R is the separation distance of colliding partners. Such potentials lead to a power-law temperature dependence [107],

$$\gamma(T) = \gamma_0 \left(\frac{T}{T_0} \right)^\kappa, \quad (2.47)$$

where T is the cell temperature, γ_0 is the collision rate at a reference temperature, T_0 , and κ is the temperature scaling coefficient. If the interaction potential is dominated by a single term, $\kappa \approx (p-3)/(2p-2)$ [107]. For a predominantly van der Waals type C_6/R^6 potential, as given by the larger noble gases, then the scaling coefficient is $\kappa \approx 0.3$ [107, 108]. In the following sections, the temperature scaling is treated separately for each collision and interaction type. For some cases, there is little discussion of the temperature dependence of σ in the literature. I then assume σ is temperature independent, and use $\kappa = 1/2$.

2.7.2 Rb - Rb Collisions

As the Rb-Rb collision rates are proportional to the Rb vapor density, they are strongly dependent on temperature (see Figure 2.2). Rb-Rb spin exchange thus tends to become the dominant relaxation mechanism at high temperatures.

Spin Exchange

Spin exchange (SE) collisions involve a swapping of the spins of the colliding partners [4, 84, 101]. The exact mechanisms are not completely understood. There is some contribution from binary collisions between two Rb atoms, however experiments at high (kG) dc magnetic fields indicate that 1/2 to 2/3 of Rb-Rb SE is field-dependent, and so must be due to other mechanisms [114]. These appear to be collisions with Rb₂ molecules, which are present in a vapor cell with a density of

⁶This is determined by the buffer gas collisions. The contribution of the Rb-Rb mean free path is in practice negligible, as seen in Table 2.7.

Table 2.2: Properties of N₂ as a quenching gas on the Rb D1 and D2 lines [86, 101, 103]. The reference temperature for the cross sections is $T_0 = 57^\circ\text{C}$.

Optical Line	σ_Q (cm ²)	P'_Q ($T = 90^\circ\text{C}$) (mbar)	P'_Q ($T = 140^\circ\text{C}$) (mbar)
D ₁ (5P _{1/2})	5.8×10^{-15}	4.1	4.4
D ₂ (5P _{3/2})	4.3×10^{-15}	5.6	6.0

Table 2.3: Cross sections for Rb collisions with various species. The cross-section for a collision of any kind to take place is σ_{total} . The cross sections for $\langle \mathbf{S} \cdot \mathbf{I} \rangle$ T₁ and T₂ relaxation are listed as σ_1 and σ_2 , respectively. The σ_2 values were measured in ⁸⁵Rb, and I assume they are the same for ⁸⁷Rb. This may result in an overestimation of γ_{2bg} . I could not find published values for σ_{total} or σ_2 for Rb-Kr collisions, so in this case I assumed $\sigma_{total} = 10^{-13}$ cm², and $\sigma_2 = 10 \times \sigma_1$. The measurement temperature, T_0 , is listed below the cross section. For the σ_{total} values, which were measured in atomic beam experiments, I used $T_0 = 0^\circ\text{C}$. The phenomenological factor of $\frac{1}{20}$ is required for agreement with measurements of the diffusion coefficient.

Species	σ_{total} (cm ²)	σ_{SE} (cm ²)	σ_{SD} (cm ²)
Rb	1.397×10^{-13} [109] (0°C)	1.9×10^{-14} [110] 78 – 277°C	9×10^{-18} [111, 112]
Species	σ_{total} (cm ²)	σ_1 (cm ²)	σ_2 (cm ²)
He	$(\frac{1}{20} \times) 1.52 \times 10^{-14}$ [109] (0°C)	8.7×10^{-24} [86] 150°C	2.94×10^{-21} [5] 27°C
Ne	$(\frac{1}{20} \times) 2.68 \times 10^{-14}$ [109] (0°C)	1.9×10^{-23} [6] 30°C	5.55×10^{-21} [5] 27°C
N ₂	$(\frac{1}{20} \times) 7.85 \times 10^{-14}$ [109] (0°C)	1×10^{-22} [86] 70°C	7.43×10^{-21} [5] 27°C
Ar	$(\frac{1}{20} \times) 5.72 \times 10^{-14}$ [109] (0°C)	6.1×10^{-22} [86] 27°C	3.71×10^{-21} [5] 27°C
Kr	$(\frac{1}{20} \times 10^{-13})$ (0°C)	2.7×10^{-21} [86] 27°C	(2.7×10^{-20}) (27°C)
Xe		2.2×10^{-19} [86] 150°C	1.1×10^{-18} [113] 21°C

approximately $10^{-6} \times n_{Rb}$. There is a nuclear-quadrupole interaction through collisions with Rb_2 molecules in the singlet state, and a spin-axis interaction through collisions with Rb_2 molecules in the triplet state [115, 116]. SE collisions conserve the total angular momentum, i.e. the total m_F value, but not necessarily the F value. The effect for Rb-Rb collisions is to scramble the collision partners' states amongst the 8 ground m_F states.

The Rb-Rb SE rate of the hyperfine populations, γ_{1SE} , is given by

$$\gamma_{1SE} = n_{Rb} \sigma_{SE} \bar{v}_{RbRb}, \quad (2.48)$$

where n_{Rb} is the Rb atom number density, which can be obtained from Eqs. (2.1), σ_{SE} is the Rb-Rb spin exchange cross section, given in Table 2.3, and \bar{v}_{RbRb} is the mean relative velocity of two Rb atoms, given by Eq. (2.42). Note that the SE rate is proportional to the total Rb density, including ^{85}Rb [3].

From a multilevel density matrix analysis (i.e. treating each m_F ground state individually) [6, 117], it can be seen that SE relaxation of coherence is slowed by a factor given by the nuclear spin. In general, the multilevel relaxation is determined by the populations of the transition and neighbouring m_F states⁷, and is not described by a single time constant. The general case is discussed, for example, in Refs. [6, 117]. For the special case of complete depopulation of one of the F states (i.e. optical pumping with 100% efficiency), and equal population of the m_F states in the other hyperfine level, the coherence decay of the clock transition, $|F-1, m_F=0\rangle \rightarrow |F, m_F=0\rangle$, is approximately exponential, with

$$\gamma_{2SE} = \frac{6I+1}{8I+4} \gamma_{1SE}, \quad (2.49)$$

where I is the nuclear spin. This relationship has been experimentally verified for both ^{87}Rb and ^{85}Rb [5, 6, 117]. For ^{87}Rb , where $I = 3/2$, we have $\gamma_{2SE} = \frac{5}{8} \gamma_{1SE}$. For modelling, I assumed that SE relaxation of coherence was the same for all hyperfine transitions.

The SE cross section, σ_{SE} , appears to be essentially independent of temperature, with measurements from 78°C to 277°C all giving the same $\sigma_{SE} = 1.9 \times 10^{-14} \text{ cm}^2$ [110, 118, 119]. SE becomes the dominant relaxation mechanism at high temperatures. The critical temperature depends mostly on the wall relaxation rate (Section 2.7.4), and is approximately 75°C for the microfabricated cells used in Chapters 4 and 8, and 160°C for the ultrathin cells used in Chapters 6 and 7. It is worth then quickly reviewing the available options to limit SE.

The conservation of total m_F in SE collisions means that the stretched m_F states, $|2, 2\rangle$ and $|2, -2\rangle$, are somewhat protected from SE relaxation. If two $|2, 2\rangle$ ($|2, -2\rangle$) atoms collide, spin exchange is not possible, as m_F conservation means that the only allowed output state is again two $|2, 2\rangle$ ($|2, -2\rangle$) atoms. $\langle \mathbf{S} \cdot \mathbf{I} \rangle$ SE relaxation can therefore be suppressed by optically pumping the atoms to one of

⁷The neighbouring states to a transition are those with $m_{F2} = m_{F1} \pm 1$, where m_{F1} is either of the two transition states.

these stretched states [13]. There will always be some population in the other m_F states however, particularly when driving oscillations between m_F states, and SE cannot be completely eliminated in this way. The conservation of total m_F also means that T_1 relaxation of $\langle S_z \rangle$ does not occur in collisions between identical atoms [3].

SE is suppressed at high dc magnetic fields [114, 115], through suppression of the Rb-Rb₂ interactions. A suppression factor of 1/3 was measured at a field of 6000 G [114].

It is also possible to suppress SE through the application of 2π microwave pulses repeated at the Larmor precession frequency [120], though it is unclear how well the technique could be applied in our relatively small cells, with short T_1 and T_2 times.

The complete suppression of SE relaxation is possible in a combination of low dc magnetic field and high Rb density. This is known as the SERF (spin exchange relaxation free) regime, and is exploited to great effect in some vapor cell magnetometers [101, 111]. The relaxation rate is then determined by Rb-Rb spin destruction collisions, and Rb collisions with the buffer gas.

SE can also be taken advantage of to polarise samples that would be otherwise difficult to polarise, such as noble gases and solids [121–123]. This is known as spin exchange optical pumping.

Spin exchange is normally considered an incoherent process, but recently coherent transfer of spin between alkali atoms has been observed, mediated through SE collisions [124]. Relatively favourable Rb properties, such as the T_1 and T_2 relaxation rates, were transferred to K. The coherent coupling was only observed in low dc magnetic fields (< 1 mG) though, and it is unclear at this point how it could be applied to our field imaging.

Spin Destruction Collisions

It is also possible for Rb-Rb collisions to randomise the Rb states, without conserving m_F . These collisions are known as spin destruction collisions. They are an important mechanism when SE has been reduced or eliminated, such as in SERF magnetometers. The spin destruction rate is several order of magnitude below the SE rate for the conditions in this thesis however, as seen by the spin destruction cross section (σ_{SD}) in Table 2.3, and I did not include it in my modelling.

Dipole-Dipole Interactions

Dipole-dipole interactions during Rb collisions with other Rb atoms lead to a broadening of the optical lines proportional to the Rb vapor density [92, 94]. This becomes important for Rb densities corresponding to temperatures above 125°C. For the Rb D₂ line, the dipole-dipole broadening is

$$\Gamma_{dipole} = \beta_2 n_{Rb}, \quad (2.50)$$

where $\beta_2 = 2\pi \times 1.10 \times 10^{-7} \text{ Hz cm}^3$ is the self-broadening coefficient [125], and n_{Rb} is the Rb vapor density. For the conditions in this thesis, this was a minor correction to the buffer gas induced broadening, as seen in Table 2.7.

2.7.3 Rb - Buffer Gas Collisions

The two important interactions with the buffer gas are the hyperfine shift interaction, caused by a change in spatial overlap of the electron and nuclear wavefunctions, and the spin rotation interaction, caused by coupling of the Rb electron spin to the angular momentum of the colliding pair⁸. The Hamiltonian for interaction between Rb and the buffer gas can be written as

$$\hat{H}_{bg} = \delta A(r) \mathbf{I} \cdot \mathbf{S} + \gamma(r) \mathbf{S} \cdot \mathbf{N}, \quad (2.51)$$

where \mathbf{I} and \mathbf{S} are the Rb nuclear and electron spins, respectively, \mathbf{N} is the angular momentum of the colliding pair, $\delta A(r)$ is the change in the hyperfine coefficient, and $\gamma(r)$ is the spin-orbit coupling coefficient. Both coefficients are functions of the internuclear separation, r . The hyperfine shift interaction results in shifts and broadening of the hyperfine transitions, while the spin-rotation interaction primarily results in shifts and broadening of the optical transitions, and T_1 relaxation of the hyperfine states.

Modelling of the coefficients $\delta A(r)$ and $\gamma(r)$ is extremely difficult for buffer gases more complex than H (i.e. all of them). Modelling tends to give only rough quantitative agreement with experiment, but does yield useful physical insights [6, 126, 127]. For quantitative modelling, we turn to more phenomenological models, using experimentally derived parameters.

I could not find values for the T_2 relaxation cross section, σ_{2bg} , measured for ^{87}Rb . The σ_{2bg} values given in Table 2.3 are for ^{85}Rb , and are likely to be an overestimation for ^{87}Rb . This is because of the smaller ^{85}Rb hyperfine splitting (3 GHz instead of 6.8 GHz), and the larger nuclear spin ($I_{85} = 5/2$ compared to $I_{87} = 3/2$).

The Hyperfine Shift Interaction: Hyperfine Transition Shift

In the hyperfine shift interaction, distortion of the Rb electron wavefunction during a collision changes the overlap of the electron with the nucleus, giving a shift in the hyperfine coupling coefficient, $\delta A(r)$. This results in a shift and broadening of the hyperfine transition frequencies. The interaction cannot induce T_1 relaxation however [6, 86], except at high magnetic fields [110]. The dominant mechanism for the hyperfine shift is binary Rb-buffer collisions, known as the Carver mechanism [110, 126], which is linear with buffer gas density. A secondary mechanism, scaling quadratically with buffer gas density, is the Bouchiat mechanism, in which

⁸The spin-rotation interaction with the Rb nuclear spin is typically neglected, as the differing gyromagnetic ratio ensures that the nuclear interaction is at least 3 orders of magnitude smaller than the electron interaction.

‘sticking’ 3 body collisions result in the formation of short-lived van der Waals (vdW) molecules [126, 128].

In a binary collision, the electron wavefunction distortion occurs in two stages. At large separation distances, so at the beginning and end of a collision process, attractive van der Waals forces pull the electron wavefunction outwards. This reduces the electron overlap with the Rb nucleus, and so reduces the hyperfine coupling, giving a negative frequency shift. At small separation distances, the electron clouds of the colliding partners overlap, giving a strong repulsive Pauli exclusion force. This pushes the electron wavefunction back into the nucleus, increasing the hyperfine coupling and giving a positive frequency shift. The random scatter of collision trajectories (e.g. head-on or grazing) will result in different distances of closest approach, and thus a random scatter in the $\delta A(r)$ shift magnitude and sign for each collision.

The perturbations in $\delta A(r)$ can be thought of as a phase shift of the electron spin. The accumulated phase shifts across many collisions result in a frequency shift of the hyperfine resonance. The dispersion (scattering in sign and amplitude) of the phase shifts results in broadening of the resonance. The balance between the short and long ranged binary collision interactions, which depends on the buffer gas species, determines the sign of the collisional shift. Larger buffer gas species, with strong vdW interactions (Ar, Kr, Xe), give a negative shift, whilst smaller species (He, Ne, N₂) give a positive shift (see Table 2.4). By using a mixture of buffer gas species (typically N₂ and Ar), it is possible to take advantage of this to reduce the hyperfine shift, and to cancel its first order temperature dependence. This is often used in vapor cell atomic clocks, and could be applied for our imaging when high stability of the microwave transition is required for imaging microwave and dc magnetic fields with high accuracy.

VdW molecules form in 3 body collisions with Rb and heavy buffer gas atoms (Ar, Kr, and Xe) [129], and are destroyed in a subsequent buffer gas collision. VdW molecule formation is neither expected nor observed for lighter buffer gas atoms (He, Ne, N₂) [129, 130]. VdW molecules are present at intermediate buffer pressures (10s of mbar), where the buffer gas pressure is high enough for vdW molecule formation, and low enough that molecules are not immediately broken up in a subsequent collision. The formation of vdW molecules, and the resulting shifts in both $\delta A(r)$ and $\gamma(r)$, result in a non-linear shift of the hyperfine frequencies. As the magnitude is less than 1% of the linear shift (10s to 100s of Hz in hyperfine frequency shift) [129, 130], we can safely neglect the non linear contributions for the calculations for this thesis.

The temperature dependence of the hyperfine shift for a given buffer gas density is modelled in a power-law expansion. Over large temperature ranges (-125°C to 800°C), 4th and 5th order polynomials have been used [131, 132], however for typical experiment parameters, the temperature dependence is usually modelled with a quadratic relationship [6, 133]. The hyperfine line shift is given by

$$\delta\nu_{bg}(T) = P \left(\beta + \delta(T - T_0) + \gamma(T - T_0)^2 \right) + \Delta^2\nu + b(T)P^2, \quad (2.52)$$

where T is the cell temperature, T_0 is the reference temperature the shift was measured at, and P is the buffer gas pressure scaled to the reference temperature T_0 . The experimentally determined coefficients β , δ , and γ , which represent the binary Carver mechanism, are given in Table 2.4. The nonlinear terms $\Delta^2\nu$, the vdW shift [129, 130], and $b(T)P^2$, a shift quadratic with buffer density and linear in temperature [133, 134], are included for completeness, but they are small and not included in calculations for this thesis. In the case of multiple buffer gas species, the line shifts due to each species can be summed linearly [6]⁹,

$$\delta\nu_{bg} = \delta\nu_{bg1} + \delta\nu_{bg2} + \dots \quad (2.53)$$

We do not explicitly calculate the broadening of the hyperfine transition induced by the hyperfine interaction, but rather the net broadening induced by buffer gas collisions of all types. This is because of the experimental difficulty in isolating the various contributions. Following the discussion in Section 2.6.4, the buffer gas broadening is given by $\Delta\omega = 2\pi(\gamma_{2bg}/\pi)$, where the buffer gas coherence relaxation rate, γ_{2bg} , is given by Eq. (2.56) in Section 2.6. Values of the Carver rate are given, for example, in Refs. [86] and [135].

Table 2.4: Hyperfine line shift coefficients, β , δ and γ , for the ^{87}Rb ground state in the presence of various buffer gases. Line shift coefficients from Refs. [6, 136] are for $T_0 = 333$ K and $T_{fill} = 300$ K.

Buffer Gas	β (Hz/torr)	δ (Hz/torr/°C)	γ (Hz/torr/°C ²)
Ne	+392 [4]		
N ₂	+546.9 [6, 136]	0.55 [6, 136]	1.5×10^{-3} [6, 136]
Ar	-59.7 [6, 136]	-0.32 [6, 136]	-3.5×10^{-4} [6, 136]
Kr	-593.5 [6, 136]	-0.57 [6, 136]	
Xe			

The Spin-Rotation Interaction: Optical Transition Shifts and Broadening

The spin-rotation interaction, $\gamma(r)\mathbf{S} \cdot \mathbf{N}$, acts as a perturbation to the fine structure splitting, $\mathbf{L} \cdot \mathbf{S}$, of the Rb 5S and 5P states. Like for the hyperfine transitions, this leads to collisional broadening and shifts of the optical transitions. The accumulation of phase shifts over many collisions gives an average frequency shift, and the dispersion of the phase shifts leads to broadening. Success has been shown modelling the $V(R) = \sum C_p/R^6$ type interaction potential using [108]

$$V(R) = -\frac{C_6}{R^6} - \frac{C_8}{R^8} + \frac{C_{10}}{R^{10}}. \quad (2.54)$$

⁹Though Vanier gives the summation rule in a different form, a bit of algebra shows that the two forms are equivalent.

For large buffer gases, the repulsive C_6 van der Waals term dominates. The higher order terms become more important for smaller buffer gases, where the van der Waals force is less strong and the Rb is able to penetrate further into the core of the buffer gas electron cloud. The C_{10} term is only dominant in He however, which is the only buffer gas giving a positive optical line shift.

The shifts and broadening are typically modelled as scaling linearly with buffer gas density. The temperature dependence has been less clear however. The optical line shift is described by,

$$\delta\nu_s = \alpha_s P \left(\frac{T_0}{T} \right)^{\kappa_s}, \quad (2.55)$$

where P is the buffer gas pressure at the reference temperature T_0 , α_s is the line shift coefficient, T is the cell temperature, and κ_s is the temperature scaling coefficient. Similarly, the optical broadening is given by

$$\Delta\nu_b = \alpha_b P \left(\frac{T_0}{T} \right)^{\kappa_b}, \quad (2.56)$$

where α_b is the broadening coefficient and κ_b is the temperature scaling coefficient. There has been significant variation in the few reported values of κ in the experimental literature, and large departures from theory [133, 137, 139–141]. Recent experiments using the newly discovered isoclinic point however, indicate that the spread in experimental values was due to difficult to account for systematic errors, and that the theoretical values are in fact sound [107]. Ref. [107] measured κ_s for Rb in Kr buffer gas, and found $\kappa_s = 0.36 \pm 0.06$, in good agreement with the calculated value of $\kappa_s = 0.31$ [108]. I have therefore used the theoretical scaling coefficients given in Ref. [108]. Experimentally obtained values of α and theoretically obtained values of κ are given for common buffer gases in Table 2.5.

For the systems presented in this thesis, the collisional broadening of the optical lines gives the upper limit on buffer gas pressure. This limit is imposed by the reduction in on-resonance OD as the buffer gas density is increased. The exact limit of the buffer gas density is a parameter of the cell thickness, operating temperature, and the OD required for operation.

The Spin-Rotation Interaction: Hyperfine Relaxation

The spin-rotation interaction is also the primary mechanism for buffer gas induced relaxation of the hyperfine states [110, 142], with the transfer of angular momentum between the electron spin and the rotational momentum of the colliding atoms or molecules randomising the electron spin. The relaxation is known variously as spin-damping (S-damping), spin-rotation, or simply as buffer gas relaxation. The spin-orbit coupling coefficient, $\gamma(r)$ in Eq. (2.51), is extremely difficult to model, and the relaxation rate due to collisions with buffer gas atoms, γ_{bg} , is modelled in terms of an experimentally obtained collision cross section [6, 104],

$$\gamma_{1(2)bg} = n_{bg} \sigma_{1(2)bg} \bar{v}_{Rb-bg}, \quad (2.57)$$

where the subscript 1(2) denotes $T_{1(2)}$ relaxation, n_{bg} is given by Eq. (2.61), $\sigma_{1(2)bg}$ is the spin relaxation cross section given in Table 2.3, and \bar{v}_{Rb-bg} is the mean relative Rb-buffer velocity, given by Eq. (2.42). For heavier buffer gases (Ar, Xe), σ_2 is approximately 10 times σ_1 . This ratio increases with lighter buffer gas species, and for He, $\sigma_2/\sigma_1 \approx 10^3$. We see that γ_{bg} scales linearly with buffer gas density. I have not found discussions of the temperature scaling of γ_{bg} in the literature, but it seems reasonable to assume that the scaling is similar to that of the optical line shift and broadening. I used the scaling

$$\gamma_{bg}(T) = \gamma_{bg}(T_0) \left(\frac{T}{T_0} \right)^{\kappa_b}, \quad (2.58)$$

where $\gamma_{bg}(T)$ is the relaxation rate at temperature T , $\gamma_{bg}(T_0)$ is the relaxation rate at the reference temperature, T_0 , and κ_b is the temperature scaling coefficient given in Table 2.5. The exact temperature scaling is in any case non-critical, as for the cell conditions in this thesis, γ_{bg} was only a minor contribution to the total relaxation rate, as shown in Table 2.7. If multiple buffer gas species are used, γ_{bg} is simply the linear sum of the individual rates,

$$\gamma_{bg} = \gamma_{bg1} + \gamma_{bg2} + \dots \quad (2.59)$$

From Table 2.3, it can be seen that σ_{bg} is 7 to 9 orders of magnitude smaller than σ_{total} , the cross section for Rb-buffer collisions of any type. This means that a Rb atom undergoes on the order of 10^7 to 10^9 collisions with buffer gas atoms before its state is depolarised, and up to 10^8 collisions before losing coherence.

Buffer Pressure, or Density?

Collisional interactions with the buffer gas are a function of the buffer gas density. However, the buffer gas interactions are commonly referred to as inducing ‘pressure’ shifts and ‘pressure’ broadening. This is for historical reasons, where the experimentally measured quantity is generally the buffer gas pressure, and the line shift and broadening coefficients are published in terms of frequency shift per unit pressure. The discrepancy can cause significant confusion when it comes to the scaling of these effects with temperature, and in the correct buffer gas pressure to input into various phenomenological models.

In a sealed vapor cell, the cell volume, V , and the number of buffer gas atoms, N , are constant. The Ideal Gas Law,

$$PV = N k_B T, \quad (2.60)$$

tells us that although the buffer gas density, $n = N/V$, is constant, the buffer pressure, P , is proportional to the temperature, T . The buffer gas is thus defined by the buffer pressure, P_{fill} , and temperature, T_{fill} , at the time of filling (and sealing) the cell. For the ultrathin cells used in Chapters 6 and 7, I used the lab temperature of $T_{fill} = 22^\circ\text{C}$. For the microfabricated cells used in Chapters 4 and 8, which were

produced by the Mileti group in Neuchatel, I used the temperature at which the buffer gas pressure was measured at: 80°C for the M1 cell used in Chapters 4 and 8, and 70°C for the M2 cell used in Chapter 8¹⁰. The buffer gas density is given by

$$n_{bg} = \frac{P_{fill}}{k_B T_{fill}}. \quad (2.61)$$

For this reason, the buffer gas shifts and broadening are sometimes given in the literature in units of amagats. 1 amg is the number density of an ideal gas at 0°C, and the units are thus independent of temperature. At 0°C, we have the conversion

$$1 \text{ GHz/amg} = \frac{1000}{760} \text{ MHz/torr}. \quad (2.62)$$

It is nevertheless common for various interactions to be modelled in terms of the buffer gas pressure. In such cases, the filling pressure, P_{fill} , should be scaled to the reference temperature, T_0 , at which the interaction coefficients were measured,

$$P = P_{fill} \frac{T_0}{T_{fill}}. \quad (2.63)$$

An interesting illustration of the importance in clearly distinguishing the roles of buffer pressure and density can be seen in the case of a cell with a temperature gradient [128, 135]. The buffer gas atoms or molecules, under isobaric conditions, will move to equalise the pressure across the cell.¹¹ This results in a density gradient of the buffer gas across the cell, which produces a corresponding gradient in line shifts and broadening. The effect can be a significant and difficult to account for systematic error in the determination of buffer gas collision coefficients.

2.7.4 Diffusion and Rb - Wall Collisions

When a Rb atom collides with the cell walls, it is generally assumed that the collision completely randomises the Rb state, i.e. that the wall collision results in complete T_1 and T_2 relaxation. After hitting the wall, the Rb atom is adsorbed for some time. Whilst on the wall, the atom is subject to strong fluctuating fields from the wall atoms, which act to mix the Rb states.

There is relatively little literature on Rb interactions with bare glass walls [143]. There have been extensive studies of Rb interactions with coated cell walls, however, and we can base our understanding off such work [3, 144, 145]. Coatings are typically hydrocarbon chains, eg of the form $(\text{CH}_2)_n$, which act to shield the Rb from the strongly depolarising glass. A key property of the coatings is their low magnetic

¹⁰For the filling station setup, where the cell was sealed by closing a valve, T_{fill} is easy to determine. Obtaining T_{fill} can be difficult for cells sealed using high temperatures though, such as in anodic bonding or when using a glassblowing flame. In practice, the buffer gas density in such cells is measured through the line shifts after sealing.

¹¹Temperature gradients will also produce a Rb density gradient, but I assume the effect to be negligible in this thesis.

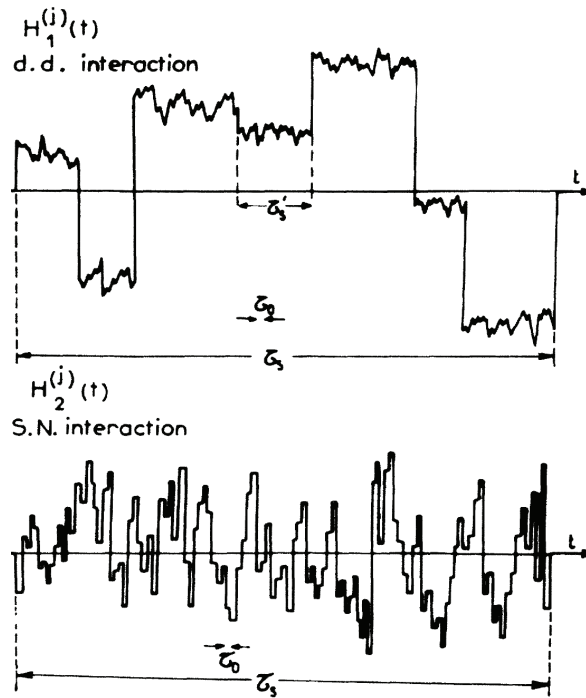


Figure 2.9: Schematic of Rb relaxation processes on an antirelaxation coating, showing fast spin-orbit fluctuations due to vibrational motion of the Rb atom within a given surface site, and slower, larger fluctuations due to site-hopping on the coating surface. Figure is taken from Ref. [3].

moment, and the H atoms act as a weakly-perturbing blanket to shield the Rb from the glass wall.

Measurements of Rb dwell times on coatings have given values on the order of 10^{-9} s and 10^{-6} s, depending on the measurement technique [145]. The two different timescales have been respectively proposed to be due to Rb atoms interacting with the coating surface and with the coating bulk. There is also some amount of Rb that becomes near-permanently trapped inside the coating. During physisorption, a Rb atom has two key interactions with the coating: 1) dipole-dipole coupling of the Rb spin to the nuclear spin of the H atoms; and 2) a spin-orbit interaction between the Rb and the C atoms [3]. A Rb atom is not stationary during its time adsorbed on a surface, undergoing thermal vibrations within a given surface site, and hopping between sites. The time constants for thermal vibrations and hopping are on the order of 10^{-12} s and 10^{-10} s, respectively. As illustrated in Figure 2.9, the interaction with the H nuclei produces relaxation due to the fluctuations induced as the Rb atom hops between surface sites, and the spin-orbit interaction produces smaller and faster fluctuations due to thermal vibration of Rb in a given site. Both interactions can be modelled as the electron spin coupling to a fluctuating magnetic field, with the weaker spin-orbit interaction described by a 50 G field. The dipole-dipole coupling

can be significantly reduced by replacing the H atoms with D (deuterium), which has a much smaller magnetic moment. The magnetic moments of atoms and molecules present on a bare glass surface are far larger, and therefore highly depolarising [146, 147].

It is also entirely possible that the Rb atoms do not interact with the glass, even in cells without antirelaxation coating. Rb has been observed to coat the cell wall with several monolayers, with 6-7 monolayers observed at 94°C [148]. It is unclear how thick the Rb coating is at elevated temperatures, and it is plausible that very little remains at the 140 – 150°C cell temperatures used with the ultrathin cells in Chapters 6 and 7, for example. In collisions with a macroscopic amount of Rb however, such as the Rb reservoir, relaxation is complete, as the incoming and outgoing atoms are not even necessarily the same atom.

The assumption that Rb collisions with the walls result in complete depolarisation is widely used, and justified, for example, by experiments showing that the population and coherence relaxation rates, γ_1 and γ_2 , are essentially equal for Rb colliding with uncoated walls [5]. These measurements were made on atoms in the cell bulk, however, and experiments measuring the Rb polarisation on or near the walls suggest the relaxation is not entirely complete [143, 149]. This is discussed further in Chapter 4, where we also observe incomplete relaxation at the walls [51].

Diffusion

In the absence of a buffer gas, Rb atoms travel ballistically through the cell, bouncing at ~ 300 m/s from wall to wall, with minimal collisions in between. In millimeter and sub-millimeter scale cells, this gives transit times, and thus lifetimes, on the order of μ s to sub- μ s. The spatial resolution for imaging also suffers. In order to reduce the wall collision rate and better confine the atoms, buffer gas is added to the cell. This transforms the ballistic motion of the Rb atoms to a diffusive one, with the Rb atoms bouncing like a pinball between buffer gas atoms or molecules. The motion is considered diffusive when

$$L \ll l = V/A, \quad (2.64)$$

where L the Rb mean free path, given by Eq. (2.44), and l is the characteristic length of the cell, given by the ratio of the cell volume, V , to the cell wall area, A . The diffusion speed is characterised by a diffusion constant, D . For a simple estimate of diffusion in 2 dimensions, we use

$$\Delta x = \sqrt{2Dt}, \quad (2.65)$$

where Δx is the distance diffused during a time t . Note that the diffusion distance scales with $t^{1/2}$. For a more in-depth treatment, we use the diffusion equation

$$\dot{u} = D \nabla^2 u - \gamma_{col} u, \quad (2.66)$$

where u , defined in Eq. (4.3), is the optically pumped hyperfine population imbalance, D is the diffusion constant, and γ_{col} represents relaxation due to Rb collisions

with other Rb atoms and the buffer gas, as described in the previous sections. The (Dirichlet) boundary condition is that $u = 0$ at the cell walls, representing the assumption that every Rb collision with the cell walls will randomise the Rb state. I discuss the case of a Robin boundary condition, where the walls are only partially depolarising, in Chapter 4.

The solution is determined by the cell geometry. For a cylindrical cell, we assume azimuthal symmetry, and write the boundary condition $u(R, z, t) = u(r, 0, t) = u(r, d, t) = 0$, where R and d are the radius and length of the cell, respectively. We take the initial condition as complete and uniform optical pumping, $u(r, z, 0) = 1$. Defining

$$\begin{aligned}\alpha_i(r) &= \frac{J_0(\mu_i r)}{J_1(\mu_i R)} \\ \beta_j(z) &= \sqrt{\frac{2}{d}} \sin(\nu_j z),\end{aligned}$$

where $\nu_j = j\pi/d$, J_0 and J_1 are Bessel functions of the first kind, and μ_i is defined by $J_0(\mu_i R) = 0$, the solution of Eq. (2.66) with the above boundary and initial conditions is

$$u(r, z, t) = \sum_{i=1}^{\infty} \sum_{j=1,3,5\dots}^{\infty} \frac{2\sqrt{\pi}}{\mu_i} \frac{2\sqrt{2}}{\nu_j \sqrt{d}} \alpha_i(r) \beta_j(z) \exp \left[- \left((\mu_i^2 + \nu_j^2) D + \gamma_{col} \right) t \right]. \quad (2.67)$$

We cannot measure the z dependence of $u(r, z, t)$ however, as our probe laser averages over the entire cell length as it passes through the cell. To model this, we integrate out the z dependence, giving

$$u(r, t) = \sum_{i=1}^{\infty} \sum_{j=1,3,5\dots}^{\infty} \frac{2\sqrt{\pi}}{\mu_i} \frac{8}{\nu_j^2 d} \alpha_i(r) \exp \left[- \left((\mu_i^2 + \nu_j^2) D + \gamma_{col} \right) t \right]. \quad (2.68)$$

For a rectangular cell geometry, the solution to Eq. (2.66) with the boundary conditions $u|_{walls} = 0$ is

$$\begin{aligned}u(x, y, z, t) &= \sum_{lmn} A_{lmn} \sin \left(\frac{l\pi}{a} x \right) \sin \left(\frac{m\pi}{b} y \right) \sin \left(\frac{n\pi}{c} z \right) \times \\ &\quad \exp \left(- \left[\left(\frac{l\pi}{a} \right)^2 + \left(\frac{m\pi}{b} \right)^2 + \left(\frac{n\pi}{c} \right)^2 \right] D + \gamma_{col} \right) t, \quad (2.69)\end{aligned}$$

where a , b , and c are the cell length, width, and height, and A_{lmn} is given by the initial condition.

From the above solutions, we can see that the time-evolution of the hyperfine population difference is not governed by a single decaying exponential with a single time constant, but rather by an infinite sum of decaying exponentials. In a region of uniform optical pumping however, e.g. away from the immediate vicinity of the cell walls, the lowest-order ($i = j = 1$) diffusion mode dominates, and relaxation is

well-approximated by a single exponential [1, 2, 6]. Eqs. (2.68) and (2.69) then yield a relaxation rate

$$\gamma = \gamma_{col} + \gamma_{walls}, \quad (2.70)$$

where

$$\gamma_{walls} = k^2 D, \quad (2.71)$$

and k is determined by the cell geometry. For a cylindrical cell,

$$k^2 = \nu_1^2 + \mu_1^2, \quad (2.72)$$

where $\nu_1 = \pi/d$, and $\mu_1 = 2.405/R$. For a rectangular cell,

$$k^2 = \pi^2 \left(\frac{1}{a^2} + \frac{1}{b^2} + \frac{1}{c^2} \right). \quad (2.73)$$

In Chapter 4, I present a detailed 2D model of diffusion in a cylindrical cell, which includes the optical pumping, multi-order diffusion, and the possibility of non-depolarising wall collisions.

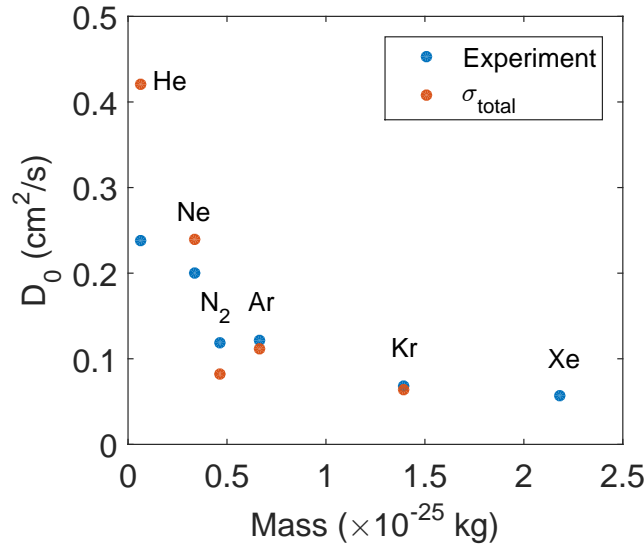


Figure 2.10: The diffusion constant, D_0 , plotted as a function of buffer gas mass. All values have been normalised to $T_0 = 0^\circ\text{C}$. The experimentally obtained D_0 values listed in Table 2.6 are shown in blue. In red are values of D_0 calculated using the σ_{total} values listed in Table 2.3 and Eq. (2.74). To match these values with the experimentally obtained D_0 , I modified σ_{total} by a factor of $\frac{1}{20}$.

We can estimate the diffusion constant using

$$D = \frac{1}{3} L \bar{v}_{Rb-bg} = \frac{1}{n_{bg} \sigma_{total}} \sqrt{\frac{8k_B T}{9\pi m_{Rb}}}, \quad (2.74)$$

Table 2.5: Optical pressure broadening, α_b , and line shift, α_s , coefficients, and their respective temperature coefficients, κ_b and κ_s , for the Rb D₂ line in the presence of various buffer gases. The reference temperature is $T_0 = 273.15$ K for the Ref. [137] values, and $T_0 = 394$ K for the Ref. [138] values. In the absence of available published temperature coefficients for N₂, I used $\kappa_b = \kappa_s = 0.3$.

Buffer Gas	α_b (MHz/torr)	κ_b	α_s (MHz/torr)	κ_s
He	23.8 [137]	0.42 [108]	0.61 [137]	1.20 [108]
Ne	9.47 [138]	0.27 [108]	-2.44 [138]	0 [108]
N ₂	18.3 [138]	(0.3)	-5.79 [138]	(0.3)
Ar	17.7 [138]	0.32 [108]	-5.76 [138]	0.31 [108]
Kr	17.2 [138]	0.32 [108]	-5.50 [138]	0.31 [108]
Xe	17.8 [138]	0.32 [108]	-6.19 [138]	0.31 [108]

Table 2.6: Diffusion coefficients for Rb in various buffer gases, with the reference temperature T_0 .

Buffer Gas	D_0 (cm ² /s)	T_0 (°C)
He	0.35 [150]	80
Ne	0.20 [151]	0
N ₂	0.159 [152]	60
Ar	0.14 [5]	27
Kr	0.068 [151]	0
Xe	0.057 [151]	0

where L is the mean free path of Rb atoms in the buffer gas, given by Eq. (2.44), \bar{v}_{Rb-bg} is the mean relative Rb-buffer gas velocity, given by Eq. (2.42), the buffer gas density, n_{bg} , is given by Eq. (2.61), σ_{total} is the total cross section for Rb-buffer gas collisions of any type, given in Table 2.3, and m_{Rb} is the Rb mass. We can see that D is inversely proportional to the buffer gas density, and that the temperature scaling is influenced by $T^{1/2}$ from \bar{v}_{Rb-bg} , and some unknown contribution from σ_{total} .

The estimation of the diffusion constant is useful for a qualitative understanding, but in practice we use a value derived from experiment. The published value is given as D_0 , the diffusion constant at a reference temperature T_0 and reference pressure $P_0 = 1$ atm. The reference temperature is often $T_0 = 0^\circ\text{C}$, but it can also be the measurement temperature. Values of D_0 for Rb in various buffer gases are listed in Table 2.6. The diffusion constant at general temperature T and buffer pressure P is [151]

$$D = D_0 \frac{P_0}{P} \left(\frac{T}{T_0} \right)^\kappa, \quad (2.75)$$

where P is given by Eq. (2.63), and $\kappa = 3/2$ [6, 152, 153]. If multiple buffer gas species are used, the diffusion constant is given by

$$\frac{1}{D} = \frac{1}{D_1} + \frac{1}{D_2} + \dots. \quad (2.76)$$

Figure 2.10 compares calculated and measured diffusion coefficients as a function of buffer gas atomic or molecular mass. The calculated values, obtained using Eq. (2.74) and the σ_{total} values listed in Table 2.3, do not match with the measured D_0 . This appears to be due to the σ_{total} values, which were obtained in atomic beam experiments, and appear to be a factor of 20 larger than that implied by the measured D_0 values. I have therefore plotted the calculated D_0 in Figure 2.10 using $\frac{1}{20}\sigma_{total}$. The agreement between the data sets for the variation in D_0 for the different buffer gases is then reasonably good, with He the only significant discrepancy. As one might expect, D_0 decreases with buffer gas mass. N_2 stands out with a smaller D_0 than the heavier Ar, most likely due to its molecular nature.

2.8 Antirelaxation Coatings

Antirelaxation (a.k.a. wall) coatings are the alternative technique to using buffer gases for minimising wall induced relaxation. The idea is to coat the inside of the cell wall with a more ‘friendly’ substance, with which the Rb can collide without changing its spin state. Coatings are typically made of some long hydrocarbon chain, with the H atoms acting as a weakly-perturbing blanket to shield the Rb from the wall. Paraffin, which allows Rb to bounce off the order of 10^4 times before depolarisation, was an early and particular favourite. The most effective coatings can allow as many as 10^6 bounces [154].

There are a number of disadvantages of wall coatings however, and barriers to their use. Wall coatings are notoriously difficult to apply, and for some coatings,

perhaps only a single group or person worldwide has mastered their application. The majority of coatings also fail at quite low temperatures. Paraffin wax, for example, is limited to 60 – 80°C [145]. Finally, the buffer gas in our cells is also important for confining the Rb atoms in order to provide high spatial resolution in imaging, and we would want to fill our cells with some buffer gas regardless ¹².

A coating that is compatible with the high operating temperatures required in the ultrathin cells presented in Chapters 6 and 7 is OTS (octadecyltrichlorosilane) [155], which is capable of operating at temperatures up to 160°C without permanent damage, and allows 100s to 1000s of bounces. Despite the OTS temperature tolerance being well below the 300 – 500°C required for anodic bonding, microfabricated cells with an OTS coating have been produced through a combination of anodic bonding and an indium seal [156]. Although I did not use OTS in this thesis, its use in future ultrathin imaging cells is worth investigation.

2.9 Conclusions

Table 2.7 shows typical parameter values in the three main vapor cells used in this thesis, using the theory presented in this chapter.

The presence of ⁸⁵Rb in a vapor cell has a number of negative influences on the optical and microwave responses of the cell. The ⁸⁷Rb density is reduced for a given temperature, as the temperature determines the total Rb density, regardless of the isotopic mixture. This results in faster SE relaxation for a given ⁸⁷Rb density, as the SE relaxation rate is given by the total Rb density. For a given temperature, the reduced ⁸⁷Rb density results in a reduction in OD₈₇ and therefore signal strength. Absorption from ⁸⁵Rb contributes significantly to the signal background, and for a laser tuned to the ⁸⁷Rb $F = 2 \rightarrow F'$ transition, OD₈₅ accounts for approximately 1/2 to 2/3 of the total cell OD, as seen in Figure 2.4 and Table 2.7. The overlap of the ⁸⁷Rb and ⁸⁵Rb optical absorption lines means that the ⁸⁷Rb $F = 2 \rightarrow F'$ transition generally does not correspond to a peak in the total OD spectrum of the cell, but is rather a bump on the shoulder of the ⁸⁵Rb $F = 4 \rightarrow F'$ transition. Measurements on the ⁸⁷Rb $F = 2 \rightarrow F'$ transition are thus particularly sensitive to frequency drifts, as frequency noise is almost linearly converted to amplitude noise.

It is likely then that for probing the atoms, the optimal transition is the ⁸⁷Rb $F = 1 \rightarrow F'$ transition, due to its reduced overlap with the ⁸⁵Rb absorption lines. Optical pumping is best performed on the $F = 2 \rightarrow F'$ transition however, as this results in the largest population per m_F state, with complete optical pumping giving 1/3 of the atoms in each of the $F = 1$ m_F states. The ⁸⁵Rb absorption has less influence for the optical pumping, and can be compensated for simply by increasing the pump laser intensity.

It is not immediately clear whether pumping or probing on the D₁ transition would be beneficial, and further analysis is worthwhile. The 0.8 GHz splitting of the

¹²The need for buffer gas to provide spatial confinement would be eliminated, however, if we used a cell comprised of an array of $\sim 10 - 20 \mu\text{m}$ sized antirelaxation coated microcells.

Table 2.7: Typical properties for the three main vapor cells used in this thesis. The laser is locked to the (unperturbed) $F = 2 \rightarrow F' = 2, 3$ crossover peak. Shifts are given in units of cyclic frequency (ν).

		M1 cell Chapters 4, 8	M2 cell Chapter 8	U1 cell Chapters 6, 7
Cell	Thickness (mm)	2	2	0.14
	Transverse T ($^{\circ}\text{C}$)	$R = 5$ mm 90	$R = 5$ mm 90	6×6 mm ² 140
Rb	⁸⁷ Rb abundance	0.2783	0.75	0.2783
	n_{Rb} (cm ⁻³)	3.1×10^{12}	3.1×10^{12}	6.1×10^{13}
	n_{Rb87} (cm ⁻³)	8.7×10^{11}	2.3×10^{12}	1.7×10^{13}
	P_{Rb87} (mbar)	4.3×10^{-5}	1.2×10^{-4}	9.6×10^{-4}
Buffer	T_{fill} ($^{\circ}\text{C}$)	80	70	22
	P_{N_2} (mbar)	63	15.3	25
	P_{Kr} (mbar)	0	0	75
	P_{Ar} (mbar)	0	18.7	0
OD	OD _{total}	1.79	4.21	2.40
	OD ₈₇	0.97	4.06	0.73
	OD ₈₅	0.82	0.15	1.67
Shifts and Broadening (FWHM)	$\Delta\nu_{opt}$ Lorentzian (GHz)	0.94	0.51	1.8
	$\Delta\nu_{opt}$ Doppler (GHz)	0.56	0.56	0.60
	$\delta\nu_{opt}$ shift (MHz)	-298	-165	-566
	$\Delta\nu_{mw}$ broadening (kHz)	1.1	1.3	38
	$\delta\nu_{mw}$ shift (kHz)	25.2	5.3	-27.4
Diffusion	D (cm ² /s)	3.1	6.0	1.5
	$\Delta x(t = T_1)$ (μm)	420	513	48.5
Mean Free Path	L_{Rb-Rb} (mm)	16	16	0.83
	L_{Rb-bg} (μm)	1.7	3.5	0.64
Collision Rates (s^{-1})	Rb-Rb (total)	1.8×10^4	1.8×10^4	3.8×10^5
	Rb-Rb (γ_{1SE})	2.5×10^3	2.5×10^3	5.2×10^4
	Rb-Rb (γ_{2SE})	1.9×10^3	1.9×10^3	4.0×10^4
	Rb-buffer (total)	3.5×10^8	1.6×10^8	7.0×10^8
	Rb-buffer (γ_{1bg})	7.9	16	253
	Rb-buffer (γ_{2bg})	612	236	2.8×10^4
	Rb-wall (γ_{walls})	1.1×10^3	2.0×10^3	7.5×10^4
Quenching (R_Q)	3.3×10^8	8.4×10^7	1.7×10^8	
Relaxation	γ_1 (s^{-1})	3.5×10^3	4.5×10^3	1.3×10^5
	γ_2 (s^{-1})	3.6×10^3	4.2×10^3	1.2×10^5
	T_1 (μs)	282	221	7.8
	T_2 (μs)	280	240	8.5

two ^{87}Rb $5P_{1/2}$ F states could be beneficial for some optical pumping, as might the presence of dark states on the D_1 line. The optical broadening and line shifts are almost identical on the two lines [138] however, and N_2 quenching is only slightly better on the D_1 line [101, 103]. Relaxation between the ground states would also remain unchanged.

The choice of buffer gas type and pressure depends on the geometry of the cell and the intended use. Thinner cells will require higher buffer pressures to reduce wall relaxation. The upper limit on the buffer gas pressure is given by the desired OD for a given operating temperature and cell thickness. The optical broadening should also be less than the 6.8 GHz hyperfine splitting. Cells with a large transverse OD, such as the ultrathin cells used in Chapters 6 and 7 are particularly prone to radiation trapping, necessitating the use of a quenching gas. The microfabricated cells used in Chapters 4 and 8 were produced by our collaborators in Neuchâtel. The cells are optimised for use in clocks, and thus have lower buffer gas pressures than would be optimal for our imaging purposes.

Chapter 3

Imaging Techniques using Atoms

In this chapter, I describe the features that are common to all of the experiments in this thesis. These include the theory for microwave field reconstruction (for fixed frequencies); the experiment sequences for double resonance, Franzen, Ramsey, and Rabi measurements; absorption imaging; field sensitivity; spatial and temporal resolution; and common pieces of equipment.

3.1 Microwave Field Reconstruction

The major drive of this thesis was developing techniques to image microwave magnetic fields. Our technique for microwave imaging using atoms was originally developed by Pascal Böhi *et al.* with ultracold atoms [54, 157], who then demonstrated microwave imaging with vapor cell atoms in a proof-of-principle setup in Ref. [50]. At the time however, many of the processes affecting the performance of this technique in a vapor cell were not yet carefully analysed.

We detect microwaves by driving Rabi oscillations on atomic hyperfine transitions and observing the resulting oscillations in OD. Rabi oscillations are coherent oscillations between two energy levels, driven by a near-resonant electromagnetic field [96, 158]. For a resonantly driven two level atom starting initially in state $|1\rangle$, the normalised population of state $|2\rangle$ in the absence of damping mechanisms is

$$p_2 = \sin^2\left(\frac{1}{2}\Omega_R t\right), \quad (3.1)$$

As shown below, the Rabi frequency, Ω_R , is proportional to the microwave field amplitude, with different hyperfine transitions driven by different polarisation components of the field. By measuring Rabi oscillations on several transitions, we are able to fully reconstruct the microwave magnetic field up to a relative overall phase: we can obtain each of the polarisation components and the relative phase between the polarisation components.

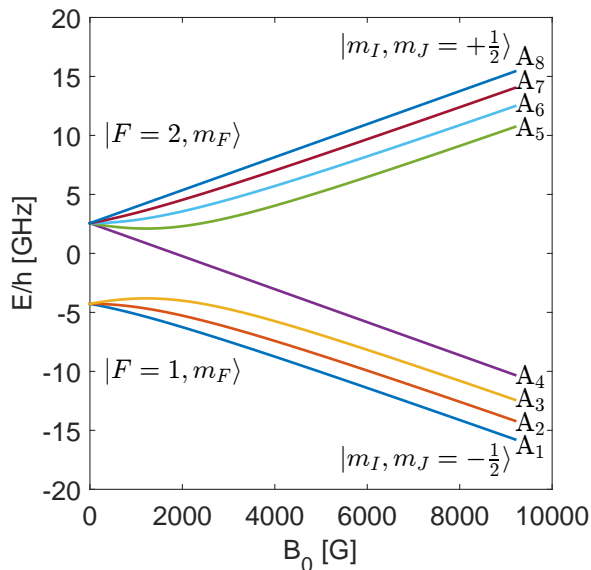


Figure 3.1: Energy splitting of the ^{87}Rb hyperfine ground state levels as a function of applied static magnetic field, B_0 . The labels $A_1\dots A_8$ are introduced and used in Chapter 8.

The following sections detail microwave reconstruction at fixed microwave frequencies, in the presence of a weak static magnetic field. Reconstruction of microwaves of arbitrary frequency, in the presence of intermediate to strong dc magnetic fields, is discussed in detail in Chapter 8. Values of various relevant constants are provided in Appendix A.

3.1.1 ^{87}Rb Hamiltonian in a DC Magnetic Field

In an unperturbed atom, the m_F levels of each F state are degenerate. We apply a static magnetic field to Zeeman shift the m_F levels and lift this degeneracy, allowing the ground state hyperfine transitions to be individually addressed by tuning the microwave frequency. Due to power broadening from the microwave, it is important that the splitting, ω_Z , is larger than the Rabi frequency, Ω_R . The Hamiltonian for the hyperfine splitting of an atom in an external static magnetic field $\mathbf{B}_0 = B_z \hat{\mathbf{z}}$ is

$$H = H_{hfs} + H_Z = A_{hfs} \mathbf{I} \cdot \mathbf{J} + \mu_B (g_I I_z + g_J J_z) B_z, \quad (3.2)$$

where H_{hfs} is the hyperfine coupling Hamiltonian, H_Z is the Zeeman Hamiltonian, \mathbf{I} and \mathbf{J} are the atomic nuclear and electronic spin, respectively, g_I and g_J are the corresponding g -factors, and A_{hfs} is the hyperfine coupling constant.

The hyperfine splitting at zero field is $E_{hfs} = A_{hfs}(I+1/2) \approx h \cdot 6.8 \text{ GHz}$ [88, 159]. For a weak magnetic field, we can obtain approximate analytic eigenvalues and eigenvectors for H by treating the Zeeman term, H_Z , as a perturbation to H_{hfs} . To

first order, the energies of the $^{87}\text{Rb } 5^2S_{1/2}$ hyperfine eigenstates, $|F, m_F\rangle$, are then given by

$$E = E_{hfs} + E_Z, \quad (3.3)$$

where the Zeeman shift for each $^{87}\text{Rb } 5^2S_{1/2}$ m_F level is

$$E_Z = g_F \mu_B m_F B_z. \quad (3.4)$$

The hyperfine g -factor g_F is

$$g_F = g_J \frac{F(F+1) - I(I+1) + J(J+1)}{2F(F+1)} + g_I \frac{F(F+1) + I(I+1) - J(J+1)}{2F(F+1)}, \quad (3.5)$$

which gives $g_F \approx -(+)1/2$ for $F = 1(2)$, respectively. For the $i = 4$ transition (see section 3.1.2), the first order Zeeman shift is zero, and the second order shift is given by [88]

$$E_Z(i = 4) = \frac{(g_J - g_I)^2 \mu_B^2}{2E_{hf}} B_z^2 = 575.15 \text{ Hz/G}^2. \quad (3.6)$$

The low-field Zeeman shift for each hyperfine transition is listed in Table 3.1.

For large magnetic fields, H_{hfs} becomes a perturbation to the Zeeman Hamiltonian, H_z . In this case, the ‘good’ quantum numbers are no longer F and m_F , but instead I , m_I , J and m_J . Within the $5^2S_{1/2}$ level, we always have $I = 3/2$, $J = 1/2$, and it is convenient to compress the state notation to $|m_I, m_J\rangle$. To first order, the energies of the $|m_I, m_J\rangle$ states are

$$E = g_I \mu_B B_z m_I + g_J \mu_B B_z m_J + A_{hfs} m_I m_J. \quad (3.7)$$

As g_I is 3 orders of magnitude smaller than g_J , we can usually neglect the first term.

For intermediate field strengths, where the magnitudes of H_{hfs} and H_z are of the same order, we can no longer take a perturbative approach. In general, one would have to resort to numerical modeling, but the D lines of the alkali atoms are a particularly fortunate case. As $J = 1/2$, we can use the Breit-Rabi formula, a simple analytical expression that gives the hyperfine energy splitting for all field strengths [88]. We have

$$E(F, m_F) = -\frac{E_{hfs}}{2(2I+1)} + g_I \mu_B m_F B_z \pm \frac{E_{hfs}}{2} \left(1 + \frac{4m_F x}{2I+1} + x^2\right)^{1/2}, \quad (3.8)$$

where $x = \frac{(g_J - g_I) \mu_B}{E_{hfs}} B_z$ and the \pm sign is determined by the sign of m_J . Figure 3.1 shows the resulting energies of the hyperfine states as a function of applied dc magnetic field. In the low field regime, the states are grouped according to the $|F, m_F\rangle$ basis, with three states in the lower $F = 1$ group and five in the $F = 2$ group. In the high field regime, the states are grouped according to $|m_I, m_J\rangle$, with four in the lower $m_J = -1/2$ group and four in the $m_J = +1/2$ group.

3.1.2 Hyperfine (Microwave) Transitions

In the low-field regime, there are nine possible hyperfine transitions between the ^{87}Rb ground states, three from each m_F level of $F = 1$. As the Zeeman shift is proportional to the m_F number, two pairs of transitions are degenerate: $|1, -1\rangle \rightarrow |2, 0\rangle$ and $|1, 0\rangle \rightarrow |2, -1\rangle$; and $|1, 0\rangle \rightarrow |2, 1\rangle$ and $|1, 1\rangle \rightarrow |2, 0\rangle$ ¹. This leaves us with seven resonances, which we label $i = 1 \dots 7$, in order of increasing frequency. Table 3.1 lists the transitions, along with the polarisation of the transition and the hyperfine states involved. $i = 4$ represents the ‘clock transition’, exploited in atomic clocks [6, 7]. Figure 3.2 shows example spectra of the 7 transitions, as a microwave applied to vapor cell atoms is swept across the resonances.

For imaging microwave magnetic fields, the $i = 1, 4, 7$ transitions are the most useful. The dc-field-insensitive $i = 4$ transition is the most robust for detecting the π microwave component, and the $i = 1, 7$ transitions are the only non-degenerate transitions sensitive to the σ components of the field. For imaging dc magnetic fields, the $i = 4$ transition is no longer useful. The dc field can then be measured using any of the $i = 1, 2, 6, 7$ transitions. Transitions $i = 2$ and $i = 6$ are useful in cancelling out common-mode shifts in dc field imaging, as they are both driven by the same (π) component of the microwave field.

Table 3.1: List of the hyperfine transitions between the ^{87}Rb ground states, in a weak static magnetic field. α_i , describing the relationship between Rabi frequency and the driving microwave field components, is defined in Eq. (3.16). Note that this definition of α_i depends on the choice of definition of the field components and Rabi frequencies given in Section 3.1.3. For the $i = 4$ transition, the first order Zeeman shift is zero, and the second order shift is given in brackets.

i	$ F, m_F\rangle$	Polarisation	α_i	Zeeman Shift (MHz/G)
1	$ 1, -1\rangle \rightarrow 2, -2\rangle$	σ_-	$-\sqrt{1/3}$	-2.1
2	$ 1, -1\rangle \rightarrow 2, -1\rangle$	π	$-\sqrt{4/3}$	-1.4
3	$ 1, -1\rangle \rightarrow 2, 0\rangle$	σ_+	$\sqrt{2}$	-0.7
	$ 1, 0\rangle \rightarrow 2, -1\rangle$	σ_-	$-\sqrt{2/3}$	
4	$ 1, 0\rangle \rightarrow 2, 0\rangle$	π	-1	0 (575.15 Hz/G ²)
5	$ 1, 0\rangle \rightarrow 2, 1\rangle$	σ_+	$\sqrt{2/3}$	+0.7
	$ 1, 1\rangle \rightarrow 2, 0\rangle$	σ_-	$-\sqrt{2}$	
6	$ 1, 1\rangle \rightarrow 2, 1\rangle$	π	$-\sqrt{4/3}$	+1.4
7	$ 1, 1\rangle \rightarrow 2, 2\rangle$	σ_+	$\sqrt{1/3}$	+2.1

¹Note that while this is accurate to first order for weak magnetic fields, the degeneracy breaks for strong fields, such as those addressed in Chapter 8

3.1.3 Rabi Frequencies

The microwave magnetic field reconstruction is based on experimentally determined absolute values of Rabi frequencies. This section follows Ref. [157] and the supplementary notes to Ref. [54]. We begin by defining the microwave magnetic field vector, $\mathcal{B}(\mathbf{r}, t) = \frac{1}{2}[\mathbf{B}(\mathbf{r})e^{-i\omega t} + \mathbf{B}^*(\mathbf{r})e^{i\omega t}]$, where $\mathbf{r} = (x, y, z)$ is the position in the fixed cartesian lab-frame coordinate system. The complex phasor of the microwave field is

$$\mathbf{B}(\mathbf{r}) \equiv \begin{pmatrix} B_x(\mathbf{r})e^{-i\phi_x(\mathbf{r})} \\ B_y(\mathbf{r})e^{-i\phi_y(\mathbf{r})} \\ B_z(\mathbf{r})e^{-i\phi_z(\mathbf{r})} \end{pmatrix}.$$

With $B_{x,y,z}(\mathbf{r}), \phi_{x,y,z}(\mathbf{r}) \in \Re_{\geq 0}$. It is these six real values, $B_{x,y,z}(\mathbf{r}), \phi_{x,y,z}(\mathbf{r})$, that we need to obtain in order to reconstruct the microwave magnetic field.

We take measurements with an applied static magnetic field, \mathbf{B}_0 , pointing along several axes. \mathbf{B}_0 defines the quantisation axis of the system, and the π and σ components of the microwave field, which drive the atomic transitions, are defined relative to \mathbf{B}_0 . We therefore introduce a new cartesian coordinate system, (x', y', z') , with the z' -axis pointing along the direction of \mathbf{B}_0 . Suppressing the dependence of $\mathbf{B}(\mathbf{r})$ on \mathbf{r} in order to simplify notation, the microwave magnetic field phasor in the new coordinate system is then

$$\mathbf{B} \equiv \begin{pmatrix} B_{x'}e^{-i\phi_{x'}} \\ B_{y'}e^{-i\phi_{y'}} \\ B_{z'}e^{-i\phi_{z'}} \end{pmatrix}.$$

We define the π and σ components of the microwave field in this new frame as

$$B_-e^{-i\phi_-} \equiv \frac{1}{2}[B_{x'}e^{-i\phi_{x'}} + iB_{y'}e^{-i\phi_{y'}}], \quad (3.9)$$

$$B_\pi e^{-i\phi_\pi} \equiv B_{z'}e^{-i\phi_{z'}}, \quad (3.10)$$

$$B_+e^{-i\phi_+} \equiv \frac{1}{2}[B_{x'}e^{-i\phi_{x'}} - iB_{y'}e^{-i\phi_{y'}}], \quad (3.11)$$

with $B_{-, \pi, +}, \phi_{-, \pi, +} \in \Re_{\geq 0}$. For transitions from an initial state $|1\rangle$ to a final state $|2\rangle$, the Rabi frequencies are

$$\Omega_- \equiv \frac{2\mu_B}{\hbar} \langle 2 | J_- | 1 \rangle B_- e^{-i\phi_-}, \quad (3.12)$$

$$\Omega_\pi \equiv \frac{2\mu_B}{\hbar} \langle 2 | J_z | 1 \rangle B_\pi e^{-i\phi_\pi}, \quad (3.13)$$

$$\Omega_+ \equiv \frac{2\mu_B}{\hbar} \langle 2 | J_+ | 1 \rangle B_+ e^{-i\phi_+}, \quad (3.14)$$

Where $J_z, J_+ = J_x + iJ_y$, and $J_- = J_x - iJ_y$ are the spin z , raising, and lowering operators, respectively.

Note that in the definitions of B_- and B_+ , a factor of $1/\sqrt{2}$ instead of $1/2$ can also be found in some of the literature (e.g. in Ref. [6]). This goes along with a change in the definitions of J_+ and J_- , which then read $J_{\pm} = \frac{1}{\sqrt{2}}(J_x \pm iJ_y)$. If this alternative definition is used, the coefficients α_+ and α_- in Eqs. (3.15-3.16) are larger by a factor of $\sqrt{2}$.

3.1.4 Microwave Amplitude

The magnitudes of the π and σ microwave components are given by a simple rearrangement of Eqs. (3.12)-(3.14),

$$B_{\gamma} = |\alpha_i| \frac{\hbar}{\mu_B} |\Omega_{\gamma}|. \quad (3.15)$$

Here, i labels the hyperfine transition, $\gamma = -, \pi, +$ is the polarisation of the transition, and

$$\alpha_i \equiv \frac{1}{2 \langle 2 | J_{\gamma} | 1 \rangle}. \quad (3.16)$$

Transition polarisations and α values are listed in Table 3.1.

The magnitudes of the microwave components in the lab frame, B_x , B_y , and B_z , are easily obtained by noting that $B_{\pi} = B_{z'}$, and by performing measurements of B_{π} with \mathbf{B}_0 pointing along each of the lab-frame x , y , and z axes.

3.1.5 Microwave Phase

The relative phases between the microwave polarisation components can be obtained from measurements of the microwave π and σ transitions taken with the static field pointing along each of the x , y , and z lab frame axes [157]. We have

$$\sin(\phi_y - \phi_x) = \frac{1}{\hbar B_x B_y} \left((B_-^z)^2 - (B_+^z)^2 \right), \quad (3.17)$$

$$\sin(\phi_x - \phi_z) = \frac{1}{\hbar B_x B_z} \left((B_-^y)^2 - (B_+^y)^2 \right), \quad (3.18)$$

$$\sin(\phi_z - \phi_y) = \frac{1}{\hbar B_y B_z} \left((B_-^x)^2 - (B_+^x)^2 \right), \quad (3.19)$$

where the superscript $B_{\gamma}^{x,y,z}$ denotes the orientation of the static field in the lab frame.

3.1.6 Power Broadening and Off-Resonant Microwaves

For a non-zero microwave detuning, the oscillations are

$$p_2 = \frac{\Omega_R^2}{\Omega_R^2 + \delta^2} \sin^2 \left(\frac{1}{2} \sqrt{\Omega_R^2 + \delta^2} t \right). \quad (3.20)$$

The atom oscillates at a new, faster frequency, $\Omega = \sqrt{\Omega_R^2 + \delta^2}$, where δ is the microwave detuning, and Ω_R is the Rabi frequency of the transition, as defined above. The oscillation amplitude is also reduced compared to the resonant case. The frequency dependence of the oscillation amplitude, $\Omega_R^2/(\Omega_R^2 + \delta^2)$, leads to a power broadening of the hyperfine transition. The FWHM of the power broadened line is $2\Omega_R$.

For measurements performed in an inhomogeneous static field, a microwave detuning of zero will not be achieved across the entire vapor cell. A detuned microwave is also difficult to avoid if the buffer gas shift is not constant (see Section 6.5.1). For weak microwave fields and large detunings, this can lead to a large overestimation of the microwave amplitude. In practice, the overestimation in this thesis was on the percent level or below. In Chapter 7, the microwave detuning was approximately 0 – 10 kHz. For a 30 μ T microwave driving 420 kHz Rabi oscillations, a 10 kHz detuning leads to a fractional overestimation of 2.8×10^{-4} . For a weaker 5 μ T microwave driving 56 kHz Rabi oscillations, the 10 kHz detuning leads to a fractional overestimation of 1.6×10^{-2} .

3.2 Experiment Sequences

I used four key experiment sequences in this work. In the frequency-domain, I took double-resonance (DR) spectra [7], and in the time-domain I used Franzen [1], Ramsey [160], and Rabi [158] sequences.

DR spectra are a versatile and quick experiment tool, providing the frequency-space locations and widths of the hyperfine transitions. Franzen, or relaxation-in-the-dark, sequences are all-optical, and are used to obtain T_1 times. Ramsey sequences provide both T_1 and T_2 times, and the microwave frequency detuning from resonance, which can be used to image dc magnetic fields. As noted in Section 2.5, the T_1 times refer to population relaxation between all $F = 1$ and $F = 2$ sublevels, whilst the T_2 times are specific for the particular hyperfine m_F transition probed. Rabi sequences are used to image applied microwave magnetic fields.

In a typical time-domain sequence, we first apply an optical pumping pulse to the vapor that depopulates the $F = 2$ state. This is followed by an evolution period, which may include microwave pulses that coherently manipulate the atomic hyperfine state. We then measure the OD in the $F = 2$ state with a probe laser pulse of the same frequency, but much shorter duration than the optical pumping pulse, in order to minimise optical pumping during the probe pulse. The sequence is then repeated, scanning the evolution time.

The example data provided in the following sections is from the setup described in Chapter 4 and Ref. [51]. The setup consisted of a 2 mm thick vapor cell, with natural Rb and 63 mbar of N₂ buffer gas, placed inside a microwave cavity. The transmission of the probe laser pulse was measured with a photodiode 10 μ s after its start, in order to accommodate the photodiode response time. A laser intensity of ≈ 5 mW/cm² was used, with the beam partially covering the cell. Scanning the

laser intensity from 0.1 mW/cm^2 to 10 mW/cm^2 produced no apparent variation in relaxation times. This indicates that the small, constant amount of optical pumping induced by the first $10 \text{ }\mu\text{s}$ of the probe pulse does not greatly affect the measured time constants. Uncertainties are taken from the 68% confidence bounds of fitting to the data.

3.2.1 Double-Resonance Spectra

I generally used DR spectra [7] as a convenient lab tool: for finding hyperfine resonances shifted by buffer gases or static magnetic fields; checking that the vapor cell atoms could ‘see’ a microwave field when aligning a setup; and checking that the hyperfine transitions were sufficiently separated for a given dc magnetic field and microwave power broadening. In Chapter 8, I also used DR sequences to image dc magnetic fields, by measuring the Zeeman shift of a transition. As discussed in Appendix G, it was often easier and faster to see the effect of microwaves on atoms using DR spectra than Rabi or Ramsey sequences. DR spectra can also be used as a precision experiment tool, with the DR spectrum of the $i = 4$ ‘clock’ transition used as the signal in cw atomic clocks, for example.

A DR spectrum is produced by scanning the frequency of an applied microwave as the laser illuminates the cell. For this measurement, both the microwave and laser are continuously on. Whenever the microwave comes onto resonance with a hyperfine transition, the optically pumped $F = 2$ state is repopulated. This results in a dip in the transmission of the laser, which is recorded by a photodiode. The area of the DR peak is proportional to the field strength, and this can be used to compare the relative strengths of the microwave polarisation components.

Figure 3.2 shows example DR spectra in the Chapter 4 setup, for different laser polarisations. The π -transitions, $i = 2, 4, 6$, are the strongest, as the microwave cavity is designed to operate in a mode where the π -component dominates. The $\sim 0.5 \text{ MHz}$ splitting of the transitions corresponds to a dc field of 0.7 G . By varying the laser polarisation, optical pumping is able to build up excess population in the positive or negative m_F states, and thus modulate the DR peak strengths. The strength of the $i = 4$ transition is relatively unaffected for the pumping parameters used here. Although I generally used a linearly polarised laser in this thesis, Figure 3.2 shows that the signal strength of the $i \neq 4$ transitions can be enhanced by tuning the pump laser polarisation.

3.2.2 Franzen Sequence

The Franzen sequence is shown schematically in Figure 3.3.a. We begin the sequence by optical hyperfine pumping of the atoms for $\sim 1 \text{ ms}$, depopulating the $F = 2$ ground state and reducing the OD of the cell [4]. The laser beam is then switched off with an AOM², and the pumped population difference begins relaxing at a rate

²acousto-optical modulator

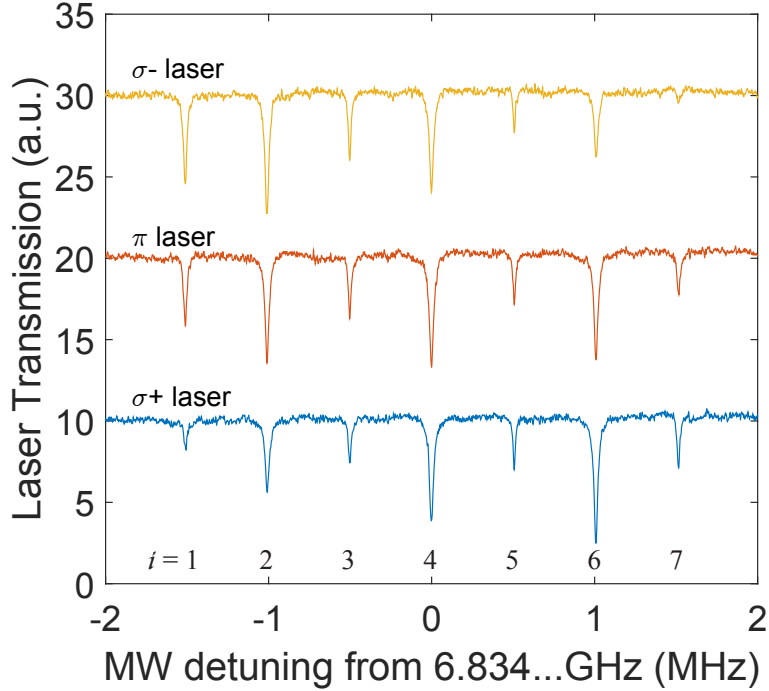


Figure 3.2: Double resonance signals in the Chapter 4 setup, for a σ_- , π , and σ_+ polarised laser. The transitions are labelled $i = 1 \dots 7$, according to the definition in Section 3.1.2. $\sigma_{-(+)}$ polarisations shift the optically pumped populations to the negative (positive) m_F levels, giving a corresponding increase in the DR peak areas from these levels. The three measurements are vertically offset for visibility.

$1/T_1$. After a time dt_{dark} , we measure the OD with a probe pulse. Scanning dt_{dark} allows us to observe the hyperfine population relaxation and to determine T_1 .

Figure 3.3.a shows data from an example Franzen sequence. As discussed in Section 2.7.4, atomic diffusion is generally dominated by the lowest order mode, and the T_1 time is well-described by a single exponential. We fit the following equation to the data:

$$OD = A - B \exp(-dt_{dark}/T_1), \quad (3.21)$$

where A , B , and T_1 are fitting parameters. For the data shown in Figure 3.3.a, this yields $T_1 = (244 \pm 6) \mu s$. Close to the cell walls, diffusion is no longer single-mode, and relaxation cannot be described by a single exponential. In this case, we can define the T_1 time as the time taken for the optical pumping to decay to $1/e$ of its

original value,

$$u(T_1) = \frac{1}{e}u(0), \quad (3.22)$$

where u is the degree of optical pumping (see Chapter 2). In the limit where the temporal decay of u can be described by a single exponential, this definition is identical to the exponential fit in Eq. (3.21). As seen in Chapter 4, the two T_1 definitions are in close agreement in most of the cell.

The simple nature of the Franzen data and the fitting equations result in fast fitting and robust T_1 values.

3.2.3 Ramsey Sequence

In Ramsey sequences [160], we introduce two microwave pulses between the pump and probe laser pulses of the Franzen sequence, as shown schematically in Figure 3.3.b, and slightly detune the microwave frequency from resonance. The first pulse creates a coherent superposition of the two hyperfine m_F states that are coupled by the microwave. During the subsequent free evolution of duration dt_R , the detuning of the microwave frequency from the atomic resonance results in the atomic superposition state accumulating a phase relative to the microwave local oscillator. The second microwave pulse converts this phase into a population difference between the hyperfine states. By scanning dt_R , oscillations of the atomic population are recorded. Each microwave pulse is nominally a $\pi/2$ pulse, however variation in the microwave field across the cell can result in atoms experiencing a range of pulse areas. For a given microwave power setting, the nominal $\pi/2$ pulse length is obtained by performing a Rabi sequence using a broad laser beam that illuminates the entire cell (or area of interest), and measuring the Rabi oscillation period on a photodiode. The $\pi/2$ length is then taken as 1/4 of this period. Ramsey sequences are robust to laser and microwave field induced decoherence, as the majority of the atomic evolution occurs in the dark, with the microwave and optical fields off. As such, they provide a good measure of the T_2 time of the cell.

Figure 3.3.b shows an example Ramsey sequence. The microwave power at the input to the cavity was 29.8 dBm. To record Ramsey oscillations in time, the microwave was slightly detuned by δ from the $i = 4$ transition. Although the data is only shown up to 500 μs , Ramsey oscillations are still clearly visible at evolution times past 1.2 ms. The data is fit with the equation

$$\begin{aligned} OD = & A - B \exp(-dt_R/T_1) \\ & + C \exp(-dt_R/T_2) \sin(\delta dt_R + \phi) \end{aligned} \quad (3.23)$$

Where A , B , C , ϕ , T_1 , T_2 , and δ are fitting parameters. The fit gives the two relaxation times as $T_1 = (245 \pm 0.5) \mu\text{s}$ and $T_2 = (322 \pm 4) \mu\text{s}$. The T_1 time is in excellent agreement with that obtained from the Franzen measurement. The exact detuning of the microwave from resonance is given by the Ramsey oscillation frequency, $\delta = 2\pi \times (135.764 \pm 0.006) \text{ kHz}$. This knowledge can be used to tune the

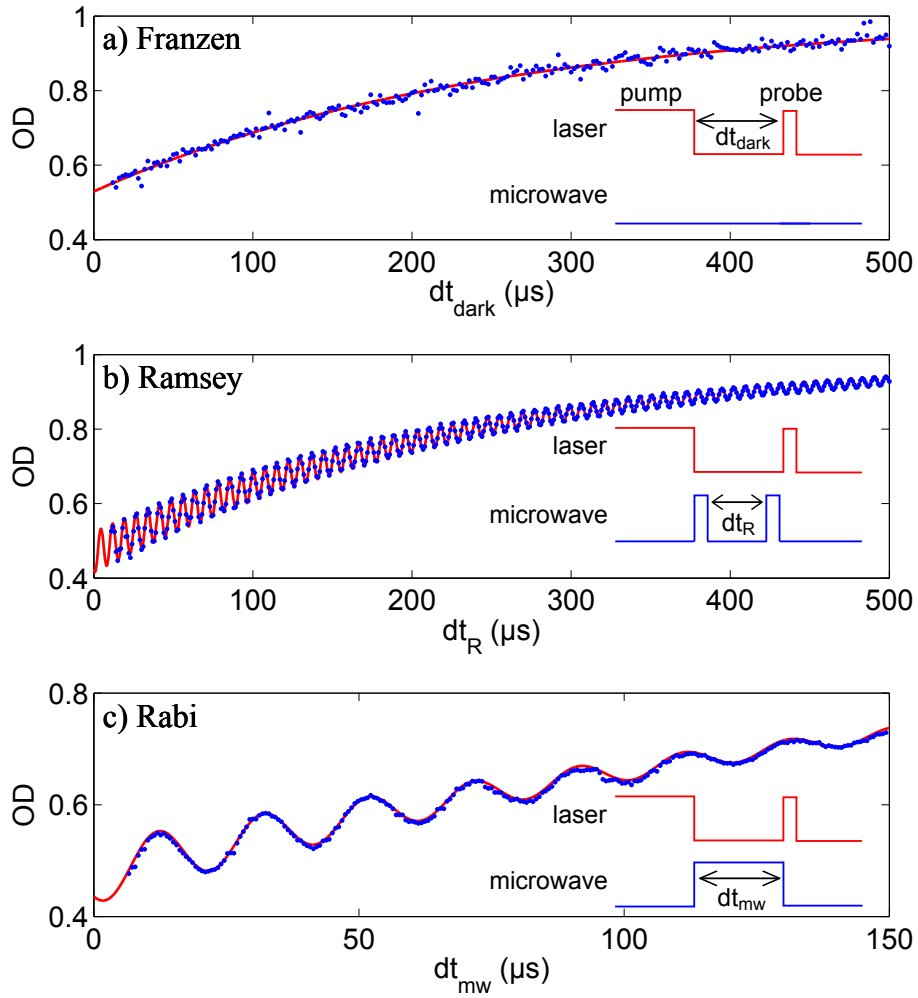


Figure 3.3: Cell OD response to a) Franzen, b) Ramsey, and c) Rabi sequences, recorded using a photodiode. Data is shown as blue dots, while the fitting curves (described in the text) are in red. Note the different scale in (c). The insets show the laser and microwave sequences used. The OD increases with laser dark time, as the hyperfine population difference relaxes. Figure adopted from Ref. [51].

microwave (almost) exactly on to resonance for a Rabi sequence, though at least two Ramsey measurements are generally needed, in order to know the sign of the detuning. The level shifts imposed by the microwave are different in Ramsey and Rabi sequences, however, as the microwave is off for most of the Ramsey sequence. Although in practice the microwave level shift is often small, the Ramsey detuning cannot account for this difference in level shifts.

The measured T_2 is specific to the clock transition. Tuning the microwave to field-sensitive transitions ($i \neq 4$), we see T_2 drop by a factor of two to three, primarily due to dephasing introduced by inhomogeneities in the static magnetic field.

Given that we have good knowledge of our generated microwave frequency, the microwave detuning (obtained by either a Ramsey or DR sequence) gives a measurement of the atomic resonance frequency. This can be used to image the dc magnetic field, by providing the Zeeman shift seen by the atoms, which we can fit to the Breit-Rabi formula, Eq. (3.8). We can eliminate common-mode frequency shifts, such as the buffer gas shift, by combining images obtained on different transitions. The common-mode rejection is also a convenient method for measuring the buffer gas shift.

3.2.4 Rabi Sequence

A Rabi sequence, shown schematically in Figure 3.3.c, consists of a single microwave pulse applied during the dark time between the laser pumping and probe pulses [158]. As discussed in section 3.1, the microwave pulse drives Rabi oscillations between the two resonantly coupled m_F sublevels of $F = 1$ and $F = 2$, at a frequency proportional to the microwave magnetic field strength. This allows us to use Rabi sequences to image the microwave magnetic field.

An example Rabi sequence is shown in Figure 3.3c. The microwave power at the input to the cavity was 27.8 dBm, and the microwave frequency was tuned exactly to the $i = 4$ transition, having been calibrated using a Ramsey sequence. Defining τ_1 , the population difference lifetime, and τ_2 , the Rabi coherence lifetime, the data is fit with the equation

$$OD = A - B \exp(-dt_{mw}/\tau_1) + C \exp(-dt_{mw}/\tau_2) \sin(\Omega dt_{mw} + \phi), \quad (3.24)$$

where A , B , C , ϕ , τ_1 , τ_2 , and Ω are fitting parameters. We obtain $\tau_1 = (231 \pm 9) \mu\text{s}$ and $\tau_2 = (94 \pm 3) \mu\text{s}$. The Rabi coherence lifetime is significantly shorter than the T_2 time obtained from the Ramsey measurement, principally due to the sensitivity of the Rabi oscillations to inhomogeneous dephasing induced by a spatially non-uniform microwave field. On the $i = 4$ transition, we are sensitive to the π component of the microwave magnetic field, and so $\Omega_4 = 2\pi \times 50.39 \pm 0.05$ kHz corresponds to $B_\pi = 3.600 \pm 0.003 \mu\text{T}$.

The sequence can be optimised for the detection of weak microwave fields by introducing a $\pi/2$ pulse from a uniform microwave source (eg an external microwave

horn) immediately after optical pumping. Rabi oscillations driven by the microwave field of interest then start their oscillations halfway up the sine curve, maximising the atomic response.

3.2.5 Fitting in Chapters 7 and 8

In Chapters 7 and 8, I used a modified absorption imaging sequence (see Section 3.3) for the Ramsey and Rabi sequences, where the only difference between the actual and reference images was the presence of the microwave. The resulting images were then of OD_{mw} , the change in OD induced by the microwave. For Ramsey sequences, I fit the data with

$$OD_{mw} = A + B \exp(-dt_R/T_2) \sin^2(\delta dt_R + \phi), \quad (3.25)$$

where A , B , T_2 , δ and ϕ were fitting parameters. For Rabi sequences, I used

$$OD_{mw} = A + B \exp(-dt_{mw}/\tau_2) \sin^2(\frac{1}{2}\Omega dt_{mw} + \phi), \quad (3.26)$$

where A , B , τ_2 , Ω and ϕ were fitting parameters. The isolation of the microwave contribution improved the sensitivity to weak signals. With less fit parameters, fitting was also significantly faster.

3.2.6 Alternative Techniques

The atomic candle technique is a frequency domain measurement of the Rabi frequency [79]. Interest has been shown in using the technique to develop a new microwave power standard, to replace the calorimeters currently used, which are slow, expensive, and difficult to evaluate [83]. Both cold atoms [161, 162] and vapor cells [80] have been used, with the atoms placed inside a microwave waveguide. In a setup similar to a DR sequence (Section 3.2.1) the microwave frequency is locked to a resonance, and the microwave phase is modulated. For a modulation frequency ω_m , there is a peak in OD when

$$2\omega_m = \Omega_{Rabi}. \quad (3.27)$$

The atomic candle may be more sensitive to weak microwaves than our time domain Rabi sequence, as DR spectra are obtainable at weaker fields than Rabi oscillations. This is not certain however, as Eq. (3.27) is derived assuming $\omega_m T_1 T_2 \gg 1$, and there is little discussion of the case $\omega_m T_1 T_2 \approx 1$ in the literature. The technique is nonetheless worth further consideration.

3.3 Absorption Imaging

Absorption imaging is a powerful technique that was perfected in experiments with ultracold atoms to obtain accurate images of atomic density distributions in a given

hyperfine state [163]. It has been used to provide single-atom sensitivity [164], and micrometer spatial resolution [165], however its use with room-temperature atoms has been a relatively unexplored area. In absorption imaging, a set of reference and dark images is usually taken in addition to the image where the atoms are present. This allows one to calibrate out spatial variation of the probe laser intensity and stray light [163]. An important difference between absorption imaging of cold atoms and a hot vapor is that the presence of the atoms cannot be easily controlled in the vapor cell, i.e. the vapor is always present in the laser beam path, even for the dark and reference images. However, we can modify the experimental sequence between the different images in order to be able to extract the relevant information from the observed variation in optical density, ΔOD .

We record four images to create an image of ΔOD . As described in Figure 3.4, these are the actual image (I_{image}), taken after the entire sequence of optical pumping, microwave pulses (for Rabi and Ramsey sequences), and probe pulse; a reference image (I_{ref}), taken 10 ms after every actual image, with a probe pulse, but without optical pumping or microwave pulse; a dark image for the actual image (I_{dark1}), taken with a pump pulse, but no probe or microwave pulse; and a dark image for the reference image (I_{dark2}), taken without any pump, probe, or microwave pulse. For a given setup, the two dark images are taken approximately once per day. In Chapters 7 and 8, the reference image (and its corresponding dark image) also included an optical pumping pulse. The ΔOD image is obtained by calculating

$$\Delta OD = -\ln \left[\frac{I_{\text{image}} - I_{\text{dark1}}}{I_{\text{ref}} - I_{\text{dark2}}} \right]. \quad (3.28)$$

The absolute OD can then be determined by normalising to the OD in the steady state without optical pumping. The use of reference and dark images significantly reduces our sensitivity to short and long term drifts in the imaging system and to spatial variations of the probe laser intensity.

The number of photons scattered per atom during the probe pulse can be estimated with

$$N_{\text{photons/atom}} = \frac{I_0 (1 - e^{-OD}) dt_{\text{probe}}}{\hbar \omega_L L n}, \quad (3.29)$$

where I_0 is the incident laser intensity, dt_{probe} is the probe pulse duration, ω_L is the laser frequency, L is the cell length, and n is the Rb number density. An upper limit is obtained by using the unpumped OD, calculated using the model presented in Section 2.3. In addition, a more accurate estimation can be obtained by treating the ^{87}Rb and ^{85}Rb isotopes separately.

In this thesis, I make a distinction between experiment *shots* and *runs*. Each experiment shot contains an actual image and a reference image, as shown schematically in Figure 3.4.b, which provide a single ΔOD image. A run is comprised of multiple shots of the experiment (typically 150), and I scan the experiment parameters (e.g. the dt evolution time) between the shots. I often performed multiple identical runs, and averaged the ΔOD images for each timestep. Figure 3.4.c shows an example of ΔOD images obtained from a set of 5 averaged Ramsey sequence

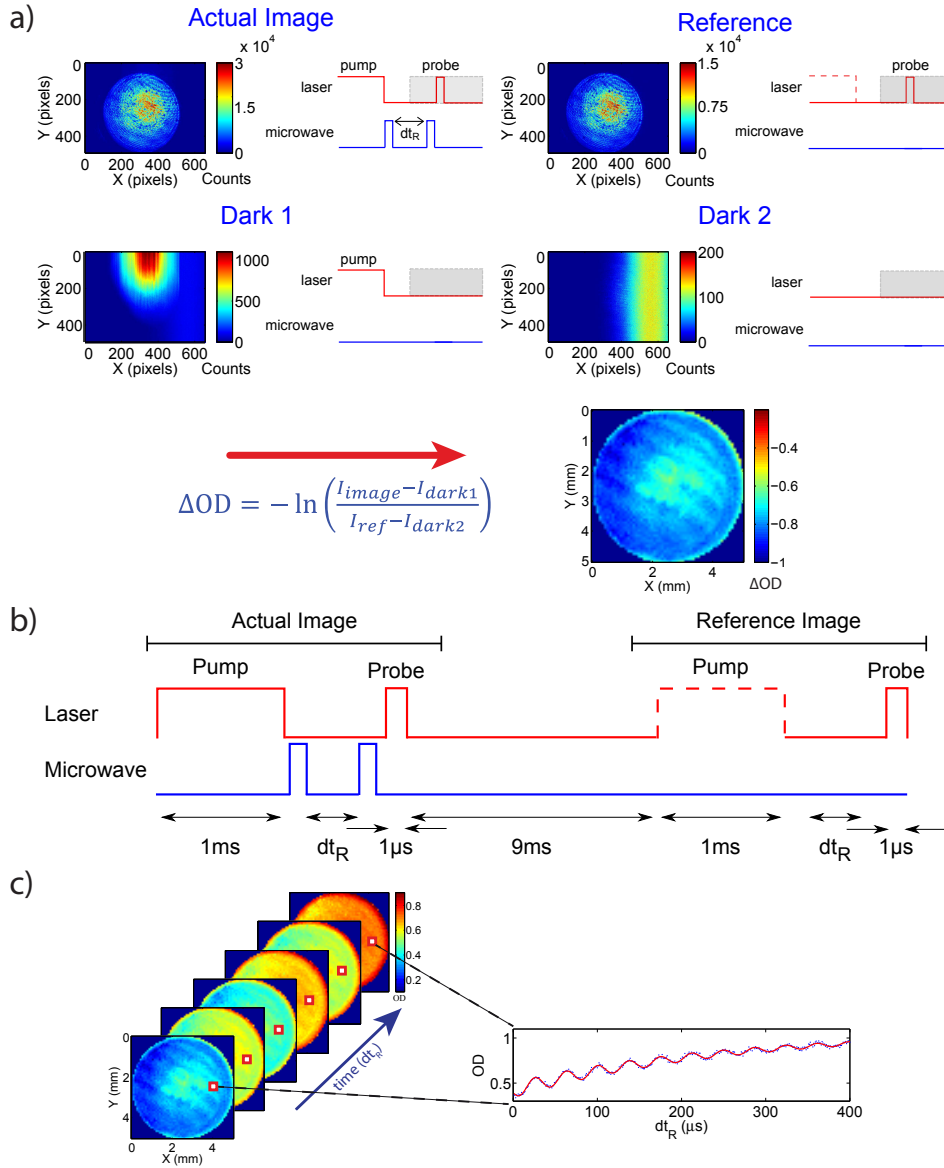


Figure 3.4: Absorption imaging, shown for an example Ramsey sequence in the setup presented in Chapter 4. a) Pulse sequences and example images of the actual, reference and two dark images. Grey boxes indicate when the camera electronic shutter is open. These four images are used to create an image of ΔOD ; b) Schematic of the sequence of an individual experiment shot, taking both an actual and reference image. The dotted line for the reference pump pulse reflects the fact that the reference images in Chapters 4 and 5 were taken without a pumping pulse; c) Each experiment shot results in an image of ΔOD . Here we see ΔOD images at $dt_R = 5, 25, \dots, 105 \mu s$. Examining a single pixel, we see oscillations in the OD in time, which for this Ramsey data, we can fit to obtain T_1 and T_2 at that location. Figure adopted from Ref. [166].

runs. The Ramsey evolution time was scanned between shots, and each image is the average of the 5 runs for that timestep. Examining a single pixel over the averaged runs, we see a time-varying signal (equivalent to the photodiode measurements in Figure 3.3), which we fit with Eqs. (3.21-3.24), for Franzen, Ramsey, and Rabi sequences, respectively. For a set of runs, I only fit the data once, after the runs are averaged together.

3.3.1 Pixel Binning

After taking each image, we often bin the CCD pixels into $N \times N$ blocks. This binning acts to reduce noise on the pixels and to reduce the computational intensity of the fitting process. There is considerable opportunity for confusion in the resulting nomenclature. In this thesis, I refer to the unbinned pixels as ‘CCD pixels’, and to the $N \times N$ binned blocks of CCD pixels as ‘image pixels’. I also use the unqualified term ‘pixel’ to refer to the image pixels.

We used a fairly basic CCD camera, and binning was performed on the PC during post-processing. A common feature on more expensive CCDs is the option to perform the binning on the CCD chip itself. This reduces readout noise and improves the readout speed and camera frame rate, as the binned electrons are processed in a single readout.

3.3.2 Measurements of the Absolute OD

To directly obtain the cell OD, I generally used a powermeter³ placed before and after the cell. When making many OD measurements, such as when measuring OD as a function of temperature, I instead used beam-samplers to send a portion of the laser beam to photodiodes before and after the cell. The photodiode signal was calibrated using the powermeter.

If a probe laser with a large mode-hop free tuning range is available, another good measurement of the OD is to measure an absorption spectrum of the Rb, sweeping the laser frequency from well-below the optical lines to well-above. The relative change in OD during the sweep is given by

$$\Delta OD = -\ln(PD), \quad (3.30)$$

where PD is the transmission signal of the probe laser beam on a photodiode. The absolute OD can be obtained by noting that the far-detuned signal corresponds to $OD = 0$.

3.3.3 Vibrations

Mechanical vibrations proved to be a significant experimental challenge in achieving reliable imaging. We were required to undertake steps in order to minimise them, such as rigidising mounting components.

³Newport, 1918-C, with 818-ST probe

3.4 Field Sensitivity and Spatial and Temporal Resolution

A vapor cell can be thought of as an array of sensors, with the sensor length given by the cell thickness, and sensor transverse dimensions given by the distance diffused by atoms over the course of a measurement. The spatial resolution is determined by the sensor size, and can be improved by using thinner vapor cells, higher buffer gas pressures, or shorter measurement sequences. A price is paid in sensitivity however. Smaller sensors contain less atoms and in general are interrogated by less photons, which increases both the atomic projection noise and photon shot noise limits. Shorter measurement times are also detrimental to sensitivity.

The following discussion is carried out in the context of microwave detection using Rabi sequences. The equations are equally valid for the detection of dc magnetic fields using Ramsey sequences though.

3.4.1 Atomic Projection Noise

The ultimate sensitivity of an atom-based sensor is given by the projection noise of measurements of the atomic state [13]. In a system under near-continuous measurement (or very short dead time between optimised pulsed measurements), the microwave magnetic field sensitivity on the $i = 4$ transition is given by

$$\delta B_{atom} = \frac{\hbar}{\mu_B} \frac{1}{\sqrt{N_{at} \tau_2 T_{meas}}}, \quad (3.31)$$

where τ_2 is the atomic coherence time, T_{meas} is the length of time over which measurements are made, and N_{at} is the number of atoms interacting with the field. τ_2 is the same as that used in Eq. (3.24)⁴, and δB_{atom} is expressed in units of $\text{T Hz}^{-1/2}$. As the number of atoms is proportional to the sensor volume, V , the sensitivity scales with $V^{-1/2}$.

3.4.2 Photon Shot Noise

Very few atomic sensors reach the atomic projection noise limit, and often a more realistic sensitivity limit is imposed by the finite number of photons reaching the detector. The photon shot noise is calculated from the shot noise in the number of electrons generated on the camera for each sensor,

$$N_{elec} = \frac{Q (I_0 e^{-OD}) A dt_{probe}}{\hbar \omega_L}, \quad (3.32)$$

where Q is the quantum efficiency of the camera, I_0 is the incident laser intensity, OD is the (unpumped) optical density, A is the sensor cross-sectional area in the cell plane, dt_{probe} is the length of the probe laser pulse, and ω_L is the laser frequency.

⁴The equivalent for dc field imaging with a Ramsey sequence is the T_2 time.

The number of camera counts for each pixel is given by $N_{counts} = G N_{elec}$, where G is the camera gain. The shot noise in camera counts is determined by N_{elec} ,

$$\Delta N_{counts} = G \sqrt{N_{elec}}. \quad (3.33)$$

The change in OD induced by the microwave is given by $OD_{mw} = -\ln(N_{act}/N_{ref})$, where N_{act} and N_{ref} are the number of counts for the actual and reference images, respectively. The smallest detectable change in OD, OD_{min} , is given by the OD shot noise,

$$OD_{min} = \sqrt{\left(\frac{\delta OD}{\delta N_{act}} \Delta N_{act}\right)^2 + \left(\frac{\delta OD}{\delta N_{ref}} \Delta N_{ref}\right)^2}. \quad (3.34)$$

The condition for the smallest detectable microwave amplitude is that, during the measurement time, the microwave must drive a Rabi oscillation fast enough to change the OD by OD_{min} . For an optimised experiment sequence (see Sec. 3.2.4), the change in OD induced by the microwave, OD_{mw} , is given by

$$OD_{mw} = OD_{mw}^{max} \exp(-dt_{mw}/\tau_2) \left(\sin^2\left(\frac{1}{2}[\Omega_R dt_{mw} + \frac{\pi}{2}]\right) - \frac{1}{2} \right), \quad (3.35)$$

where OD_{mw}^{max} is the maximum amplitude of the OD_{mw} oscillations, Ω_R is the Rabi frequency, dt_{mw} is the duration of the microwave pulse, τ_2 is the coherence lifetime (see Eq. (3.24)), and we have assumed the microwave detuning is zero. We can estimate OD_{mw}^{max} from the OD contribution of the ^{87}Rb atoms, OD_{87} , and optical pumping considerations. For pure ^{87}Rb , assuming 100% optical pumping efficiency and equal decay into the three $F = 1$ m_F states, we begin a sequence with atoms equally distributed among the $F = 1$ m_F states. The microwave couples to 1/3 of the atomic population, and $OD_{mw}^{max} = \frac{1}{3} OD_{87}$.

For weak fields, $\Omega_R dt_{mw} \ll \pi$, and we can expand Eq. 3.35 in Ω_R , to first order giving

$$\Omega_R = \frac{2}{dt_{mw}} \frac{OD_{min}}{OD_{mw}^{max}} \exp(dt_{mw}/\tau_2). \quad (3.36)$$

This shows that the sensitivity is maximised (i.e. Ω_R is smallest) for $dt_{mw} = \tau_2$. Assuming we are working on the $i = 4$ transition, with $\alpha_4 = -1$, the smallest detectable change in microwave amplitude for a single shot of the experiment is

$$\Delta B = \frac{\hbar}{\mu_B} \Omega_R = \frac{\hbar}{\mu_B} \frac{2}{\tau_2} \frac{OD_{min}}{OD_{mw}^{max}} \exp(1), \quad (3.37)$$

where ΔB is in units of T. For a run of N_{shots} taking a time dt_{run} , the photon shot noise sensitivity limit is

$$\delta B_{photon} = \sqrt{\frac{dt_{run}}{N_{shots}}} \delta B = \sqrt{\frac{dt_{run}}{N_{shots}}} \frac{\hbar}{\mu_B} \frac{2}{\tau_2} \frac{OD_{min}}{OD_{mw}^{max}} \exp(1), \quad (3.38)$$

with δB_{photon} expressed in units of $\text{T Hz}^{-1/2}$.

3.4.3 Spatial Resolution and Sensor Size

The spatial resolution and sensor size is given by the distance atoms move during a measurement. The longitudinal spatial resolution is given by the cell thickness. We can estimate the transverse spatial resolution from the distance an atom diffuses during the measurement time,

$$\Delta x = \sqrt{2D dt}, \quad (3.39)$$

where D is the diffusion constant given in section 2.7.4, and dt is the measurement time. Typically, we estimate using $dt = T_1$, because our T_1 estimates are more accurate than our coherence lifetime estimates.

3.4.4 Parallel Measurements (Imaging vs. Scanning)

Because our measurement technique is an *imaging* technique, we record data for all of the sensors in our array simultaneously. The ultrathin cells presented in Chapters 6 and 7 are comprised of $N_{sens} \approx 100 \times 100$ sensors. Compared to creating an image by scanning a single sensor, this improves our data taking speed by a factor of at least N_{sens} , so four orders of magnitude, and our effective sensitivity considered over the entire image by a factor of $\sqrt{N_{sens}}$. Parallel imaging is therefore more suitable than scanning for applications requiring a high temporal resolution.

3.4.5 Temporal Resolution

The best possible timing resolution is obtained by operating in single-shot mode (1 shot = 1 actual + 1 reference image), where B_{mw} is determined from counting the fringes on an OD_{mw} image (see Section 7.2 for example images). With a perfect camera and data saving system, the shot rate limit when running at maximum sensitivity is given by twice the evolution time, once for each of the actual and reference images. For an evolution time of $50 \mu\text{s}$ this gives a 10 kHz shot rate, and a temporal resolution of $100 \mu\text{s}$. Finer temporal resolution could be attained by taking fewer reference images.

Experiment Control Timing Limitations

The current imaging system takes shots with a rate of approximately 10 Hz, giving a timing resolution of 100 ms. This is 1000 times slower than optimal, and severely limits our sensitivity. The lab PC limits the number of shots to 150 in a single run, which takes a total time of 30 s including saving the data. The interaction time with the atoms during this 30 s is minuscule: for imaging with the ultrathin cells in Chapter 7, the microwave is interacting with the atoms for $150 \times 10 \mu\text{s} = 1.5 \text{ ms}$, and the detection laser is interacting with the atoms for only $150 \times 0.3 \mu\text{s} = 45 \mu\text{s}$. This ensures that the photon shot noise is several orders of magnitude larger than the atomic projection noise in the current setup.

Solutions include a faster camera, possibly with integrated data averaging capabilities to minimise the time taken transferring data to the computer, and a faster data saving algorithm, most likely compiled and perhaps running outside of the Matlab environment. For example, the 2500 fps imaging techniques demonstrated in Ref. [167] would be applicable to our setup. Another possible option for improvement of the photon shot noise limit would be to move to a different detection scheme altogether, of continuous weak measurement using Faraday rotation [167]. Such a scheme may require an array of photodiodes for sufficiently fast detection.

3.4.6 OD Image Streaming

A typical experiment sequence involves quickly taking the image data, and processing the data at some later point. However, we can also immediately process the raw data to provide images of the cell OD in real time. A stream of Rabi OD images, for example, provides images of OD_{mw} , and thus of the contour lines of the microwave magnetic field (see Figure 7.1, Chapter 7). The technique provided a particularly helpful experimental tool during alignment and parameter optimisation. The frame rate is considerably slower than in a conventional imaging sequence, with the frame rate determined primarily by the image processing speed on the PC. In order to streamline the data processing, we do not save the streamed data, and the current image processing provides an OD image streaming rate of 0.3 Hz. This is already useful, but significant improvement should be possible, even with the current hardware.

3.5 Equipment

A number of equipment items were common to all experiments, and these are described below. Equipment specific to particular experiments is described in the relevant chapter.

3.5.1 Experiment Control

We use a single PC for experiment control, data taking, and analysis. The experiment control software is based around *goodTime*, developed initially by Jakob Reichel, and contributed to by various people including Pascal Böhi [157] and Caspar Ockeloen [168]. We use *goodTime* to send programming commands to the various instruments via GPIB, and to send a ‘start’ signal. The software also controls looping of the experiment sequence, and communicates in a basic way with our data taking code, *Matcam lite*. The ‘start’ signal is sent as a TTL pulse via a digital I/O board⁵ to two pulse generators. The 8-channel pulse generators (also known as delay generators)⁶ then control the pump and probe laser pulses, the camera, and

⁵National Instruments, PCI DIO 32HS

⁶Stanford Research Systems DG645, both with Option 3 (Combinatorial Outputs), one with Option 5 (Rb timbase)

the mw pulses. One pulse generator also has a Rb clock timebase, which we use to provide a 10 MHz synchronisation signal to all of our instruments.

Matcam lite is a Matlab based interface for the camera that I wrote to replace the *Matcam* programs developed in our group for use in ultracold atom experiments. Although *Matcam* is entirely appropriate for ultracold experiments, where the cooling process limits the experiment repetition rate to sub-Hz, it is far too slow for the kHz or MHz repetition rates compatible with vapor cell experiments. *Matcam lite* accumulates and collates image data from the multiple actual and reference image shots taken during an experiment run, and automatically saves it afterwards. The number of experiment shots during a run was limited by our computer memory to 150. The data saving process is quite long, and is responsible for approximately half of the 30 s run time. Nonetheless, with *Matcam lite* I was able to achieve a nearly 100-fold improvement in experiment speed.

Matcam lite is integrated with *goodTime* as follows⁷: Each ‘execution’ of a *goodTime* script corresponds to a set of identical experiment runs, with a single experiment run performed per loop of the script. At the beginning of each loop, *goodTime* calls a short Matlab script, *ArmMatcam*, which in turn initiates the *Matcam lite* script. The use of *ArmMatcam* is necessary, as it is a built-in *goodTime* function that ensures (in principle) that *goodTime* should wait for the *Matcam lite* script to finish before the next *goodTime* loop begins. After a *goodTime* loop has completed (i.e. after a single experiment run), *goodTime* calls the function *StopMatcam*, which tells *Matcam lite* to save the data from that experiment run, and allows *goodTime* to proceed to the next loop. It is also possible to directly send commands from *goodTime* to Matlab, and this is used to send information on the experiment parameters to *Matcam lite*, to be included in the saved data files.

3.5.2 Lasers

I used two home-built diode lasers in this thesis, one grating stabilised (GS-laser) [169], and one interference filter stabilised (IF-laser) [170]. The lasers were frequency locked to Rb using saturated absorption spectroscopy [96] and polarisation spectroscopy [171] for the grating and interference filter stabilised lasers, respectively, in general to the $F = 2 \rightarrow F' = 2, 3$ crossover peak of the ^{87}Rb D2 line ($5S_{1/2} \rightarrow 5P_{3/2}$). Figure 3.5 shows schematics of the two laser and spectroscopy setups. The laser frequency sent to the experiment was 80 MHz red-detuned from the locking frequency, due to the acousto-optical modulator (AOM) used for switching.

The grating stabilised laser had an output power of approximately 30 mW from the box, and was used as the probe laser in Chapters 4-7, and simultaneously as the pump beam in Chapters 4 and 5. The interference stabilised laser had an output power of approximately 50 mW, and was used as the pump laser in the filling station setup in Chapters 6 and 7.

I also used a commercial laser⁸ for the work presented in Chapter 8. The laser

⁷This paragraph is aimed mostly at other members of our research group.

⁸Newport, TLB-6712 Velocity Laser

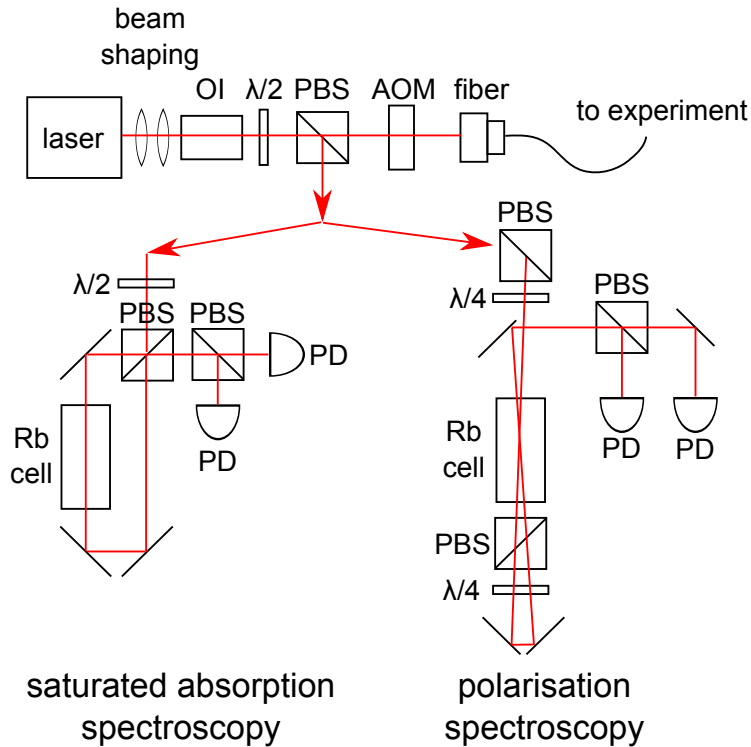


Figure 3.5: Schematic of the setup for the two home built lasers and their spectroscopies. The saturated absorption and polarisation spectroscopy were used with the GS-laser and IF-laser, respectively. OI = optical isolator; $\lambda/2$, $\lambda/4$ = waveplate; PBS = polarising beamsplitter; AOM = acousto-optical modulator; PD = photodiode.

was chosen for its large mode-hop free tunable range (ca. 80 GHz). The stated free-running linewidth of the commercial laser was < 200 kHz. Given the difficulty associated with locking the laser frequency over the extremely wide range of detunings required, I operated the laser without additional frequency stabilisation.

3.5.3 Microwave Generation

The microwave signal is provided by a 10 MHz to 26.5 GHz signal generator⁹, and is passed through a short microwave circuit, providing switching and amplification, before being sent to the experiment. In general, we use components capable of operating up to 26.5 GHz, with 26.5 GHz-compatible SMA connectors. The switch¹⁰ operates from dc to 40 GHz, and we use three separate amplifiers. The first amplifier¹¹ operates from 6 to 18 GHz, and provides 45 dB of gain, with a maximum

⁹HP8340B, from Hewlett Packard, now Keysight Technologies

¹⁰American Microwave Corporation, SWCH1K-DC40-SK

¹¹Miteq, AMF-2B-06001800-65-35P

output of 35 dBm. We use the other amplifiers in Chapter 8: a second amplifier¹² operating from 18 to 26.5 GHz, which provides 30 dB of gain with a maximum output of 29 dBm; and a third amplifier, kindly loaned from the Maletinsky group¹³, operating from 2 to 8 GHz, which provides 35 dB of gain with a maximum output of 33.5 dBm. Each amplifier is protected from back-reflections by a circulator¹⁴.

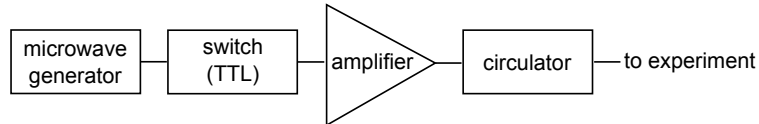


Figure 3.6: Schematic of the microwave circuit used in this thesis.

3.5.4 Detectors

We used both photodiodes¹⁵ and a CCD camera¹⁶ for detection. The response time of the photodiode signal was often improved using a 200 MHz current amplifier¹⁷, providing sub- μ s resolution. The camera CCD is comprised of 492×656 pixels, with a pixel size of $5.6 \times 5.6 \mu\text{m}^2$, and a quantum efficiency at 780 nm of $Q = 0.27$. The camera was chosen for its relatively fast frame rate, 127 fps. As discussed in Section 3.4.5, the experiment duty cycle is still severely limited by this frame rate.

¹²Miteq, AMF-8F-19002650-95-29P-TC

¹³Mini-Circuits, ZVE-3W-83+

¹⁴Ditom, DMC6018 and D3C1826; and Pasternack PE8432

¹⁵Thorlabs, DET10A/M

¹⁶Guppy Pro F031B

¹⁷Femto, DHPA-100

Chapter 4

Relaxation Imaging

There has been great interest in miniaturised vapor cells in recent years, with such cells showing particular success in miniaturised atomic clocks [9, 10] and low-frequency (dc to rf) electromagnetic field sensing [15–19]. A thorough knowledge of the properties of a cell is prerequisite to precision measurements, with the spatial dependence of relaxation times and excitation fields of particular importance for microfabricated cells and imaging applications. Despite this, there remain many unanswered questions regarding atomic interactions with the cell walls, and vapor cell production can at times resemble as much an art as a science.

In this chapter, I describe a new technique for obtaining spatially resolved information on the T_1 and T_2 lifetimes in a cell, as well as collisional properties of Rb with vapor cell walls. These properties have previously been studied without spatial resolution by looking at their effect on the bulk properties of the cell, or with some spatial resolution by scanning a narrow probe beam across the vapor cell or using evanescent-wave techniques [172–176]. Probe beam scanning is cumbersome and time-consuming, however, and characterisation with evanescent waves is not appropriate for arbitrary cell geometries or for many cell materials, such as the opaque Si walls investigated here.

I present the techniques through the characterisation of a microfabricated vapor cell [10, 177] in a microwave cavity designed for compact vapor cell atomic clocks [178]. The material presented in this chapter was published in Ref. [51].

4.1 Experiment Setup

We use the microfabricated cell shown in Figure 4.1.a, which we label cell M1. The cell has a $5\text{ mm} \times 2\text{ mm}$ internal diameter and thickness, and contains natural abundance Rb and $63 \pm 2\text{ mbar}$ of N_2 buffer gas [10]. The windows of the cell are glass, and the side-walls are Si. The buffer gas pressure was measured at 80°C from the line-shift induced on the ^{87}Rb clock transition [10], using the coefficients provided in [136]. The cell is inserted into a microwave cavity [178], which is tuned to have its resonance frequency at the 6.835 GHz ground-state hyperfine splitting of ^{87}Rb .

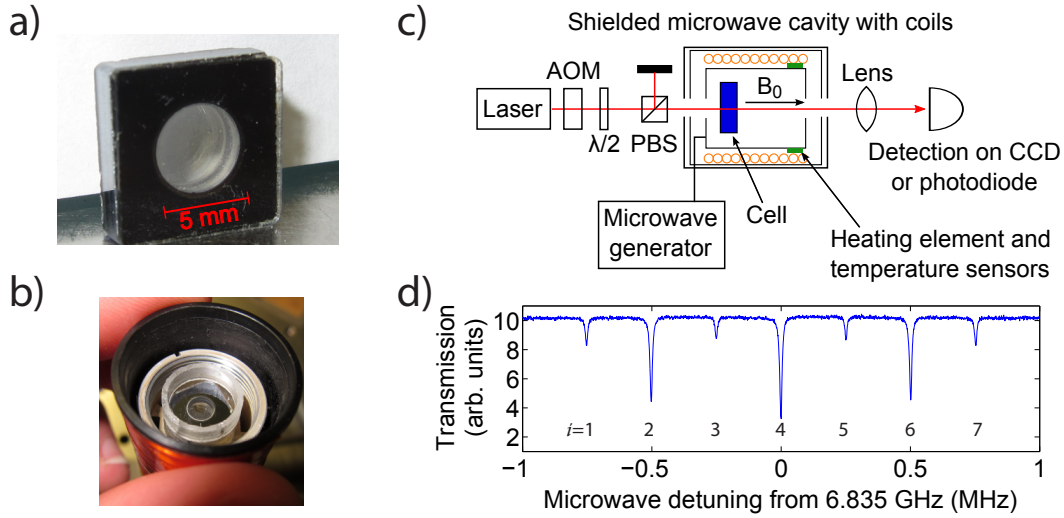


Figure 4.1: a) The microfabricated vapor cell used in this chapter, with glass windows and a black silicon frame; b) The vapor cell placed inside the microwave cavity (end-cap removed for photo) and the solenoid coils; c) The experimental setup; d) A double resonance spectrum of the cell inside the microwave cavity, showing the clearly resolved hyperfine transitions. The π transitions ($i = 2, 4, 6$) are strongest, as the microwave cavity is designed to operate in a mode where the π -component dominates. Figure adopted from Ref. [51].

The cavity is surrounded by a solenoid coil that provides a static magnetic field of $35 \mu\text{T}$, parallel to the direction of laser propagation (see Figure 4.1.c). The resulting 0.25 MHz Zeeman splitting between transitions allows all seven ^{87}Rb hyperfine transitions to be individually addressed, as shown in the double-resonance spectrum of Figure 4.1.d. An outer double-layer of μ -metal provides magnetic shielding, and a temperature control system is used to heat the cell and actively stabilise its temperature to within a few parts in 10^4 . The absolute temperature may have an offset of several percent from the set temperature, however. This is because the microwave cavity and temperature control system were designed for a much larger cell, with the heating element and temperature sensors placed some distance from the M1 cell (see Figure 4.1.c). The temperature was set to 90°C for the imaging data presented in this chapter.

We used a single laser (the grating-stabilised laser described in section 3.5.2) for both optical pumping and probing. For imaging, a single lens was used to create a 1:2 demagnified image of the cell. An ND filter is placed between the vapor cell and camera to avoid saturation of the CCD. As the camera does not have a mechanical shutter, the optical pumping pulse hits the CCD as well. The electronic shutter of the camera opens with a delay of $12 \mu\text{s}$ after the end of the pumping pulse. While some residual charges accumulated during pumping are visible on the images, they can be compensated for by taking a dark image (see Section 3.3). For the data

presented in this section, the laser intensity averaged over the 5 mm cell diameter was set to 30 mW/cm^2 to obtain strong optical pumping, which ensures a large signal amplitude. During probing, on the other hand, optical pumping is undesired, and a short probe pulse duration of $2.2 \mu\text{s}$ was chosen. The strong collisional and Doppler broadening of the optical transition ensure that the transition is not strongly saturated and the number of absorbed probe photons per atom is of order unity. In later setups, I used separate laser beams to avoid compromises between optical pumping and probing performance.

In order to reduce the imaging noise and the computational intensity of the fitting process, we bin the CCD pixels after taking each image. We bin the simpler Franzen CCD pixels into 3×3 blocks, and the Ramsey data into 7×7 blocks (see Section 3.3.1). Taking the approximate 1:2 demagnification given by the imaging lens into account, each of these 3×3 (7×7) pixel blocks corresponds to $35 \mu\text{m} \times 35 \mu\text{m}$ ($82 \mu\text{m} \times 82 \mu\text{m}$) in the cell. The spatial resolution of our imaging system is then $35 \mu\text{m}$ for Franzen data, and $82 \mu\text{m}$ for Ramsey data. The expected size of the smallest features in the atomic vapor, on the other hand, is given by atomic diffusion through the buffer gas during the measurement sequence, typically a few hundred μm for this cell (see section 4.3, below).

4.2 Temperature Dependence

The properties of the cell, such as the OD and relaxation times, are strongly temperature dependent, primarily due to the changing Rb density with temperature.

Figure 4.2.a shows the OD of the vapor in the cell as a function of temperature. Transmission through the centre of the cell of a 2 mm diameter, relatively low intensity ($I_0 < 600 \mu\text{W/cm}^2$) laser beam was measured with a photodiode. In this case, no optical pumping or microwave pulses were applied, although optical pumping was unlikely to be completely negligible. Using the model described in Section 2.4 with $\text{OD}_{87} = \text{OD}_{85}$, $\Gamma^* = 2\pi \times 1.5 \text{ GHz}$, $T_1 = 265 \mu\text{s}$, and an optical shift of $\delta\nu_{opt} = -300 \text{ MHz}$, we find that a $600 \mu\text{W/cm}^2$ beam results in a pumping efficiency of $u = 0.45$. This neglects factors such as radiation trapping, and is most likely an overestimate of the pumping efficiency. A theory curve is also shown, calculated using the model described in Section 2.3 (which neglects optical pumping), with only temperature as a free parameter. As discussed in Section 4.1, there was some uncertainty in the absolute cell temperature. In order to match the data to the theory curve, I assumed the actual temperature was described by

$$T_{actual} = T_{room} + A \times (T_{set} - T_{room}) + B \times (T_{set} - T_{room})^2, \quad (4.1)$$

where $A = 0.8$ and $B = 1.6 \times 10^{-3}$ are fitted scaling parameters, T_{set} is the set temperature, and $T_{room} = 22^\circ\text{C}$ is the room temperature. For $T_{set} = 90^\circ\text{C}$, this gives $T_{actual} = 83.8^\circ\text{C}$.

Figure 4.2.b shows T_1 times for a range of cell temperatures, obtained using Franzen sequences measured with the photodiode. The temperature has been scaled

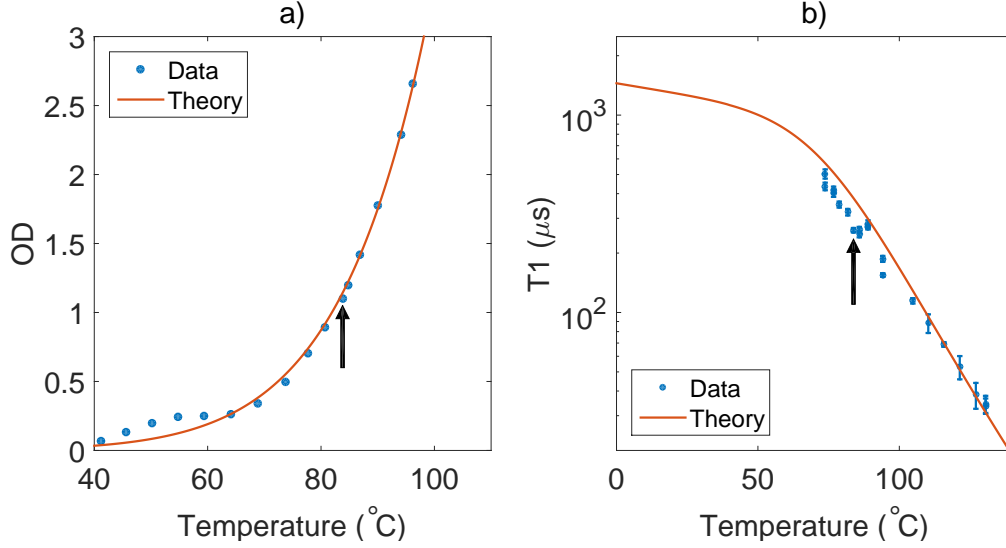


Figure 4.2: a) OD and b) T_1 in the cell as a function of temperature. The set temperature for the data has been scaled according to Eq. (4.1). The OD and T_1 theory curves have been produced using the models described in Chapter 2. The only free parameter is the temperature, which was scaled to match the data using Eq. (4.1). Arrows mark $T_{actual} = 83.8^\circ\text{C}$ ($T_{set} = 90^\circ\text{C}$), where the imaging data was taken. The T_1 error bars are 95% confidence bounds from the fitting. Figure adopted from Ref. [51].

using Eq. (4.1) and the same parameters as Figure 4.2.a. The data is compared with the model described in Chapter 2, which includes the effect of Rb-Rb spin exchange collisions, Rb-buffer gas collisions, atomic diffusion and atom-wall collisions. Considering only the lowest-order diffusion mode, the T_1 time is calculated as

$$T_1 = [(\mu_1^2 + \nu_1^2)D + \gamma]^{-1}, \quad (4.2)$$

where D is the diffusion coefficient. For a cell length d and radius R , $\nu_1 = \pi/d$, and μ_1 is defined by the first root of $J_0(\mu_1 R) = 0$, where J_0 is the Bessel function of the first kind. The relaxation rate $\gamma = \gamma_{SE} + \gamma_{bg}$ accounts for relaxation due to Rb-Rb spin exchange collisions at a rate γ_{SE} , and Rb-buffer gas collisions at a rate γ_{bg} . The parameters of the model are temperature-dependent; their values at 90°C are $\gamma_{SE} = 2500 \text{ s}^{-1}$, $\gamma_{bg} = 10 \text{ s}^{-1}$, and $D = 2.6 \text{ cm}^2/\text{s}$.

At low temperatures, relaxation is governed by Rb collisions with the cell walls, with a rate proportional to the diffusion coefficient D . As the temperature is increased, Rb-Rb spin-exchange collisions rapidly come to dominate, due to the Rb vapor density increasing almost exponentially with temperature [88]. There is good agreement between our data and the theory, particularly at spin-exchange dominated high temperatures.

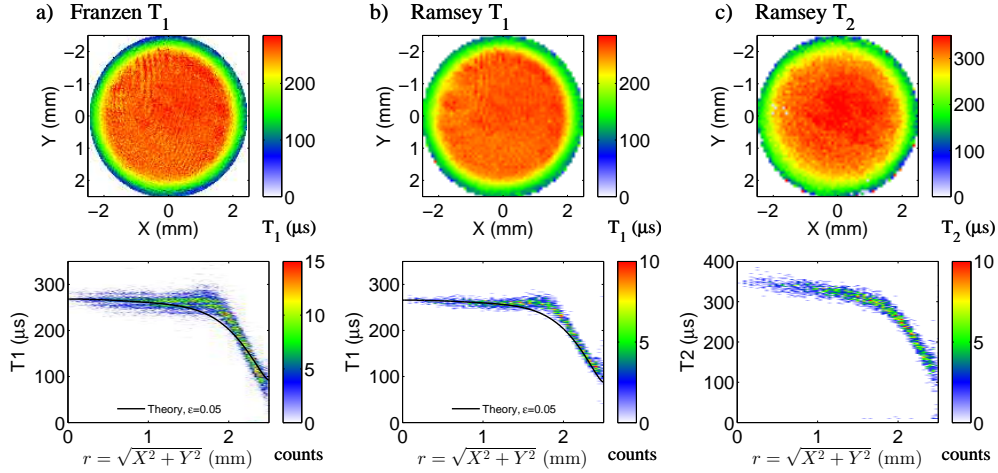


Figure 4.3: Measured T_1 and T_2 times across the cell. The top panels show a) T_1 times obtained from the $1/e$ decay time of a Franzen sequence (see text); b) T_1 times obtained from fitting a Ramsey sequence, fitting uncertainty $\pm 1\%$; and c) T_2 times obtained from the same Ramsey sequence, fitting uncertainty $\pm 4\%$. The bottom panels show radial profiles of each image in the form of a two-dimensional histogram. The radial distance from the cell center is binned into $27.5\ \mu\text{m}$ wide bins for the Franzen data, and $38.8\ \mu\text{m}$ wide bins for the Ramsey data. Franzen T_1 and Ramsey T_1 and T_2 times are binned into $0.99\ \mu\text{s}$, $1.4\ \mu\text{s}$, and $2.1\ \mu\text{s}$ wide bins, respectively. The T_1 profiles are compared to theory as described in section 4.4. Close to the walls, there is a significant decrease in T_1 and T_2 due to Rb-wall collisions. Figure adopted from Ref. [51].

4.3 Imaging Relaxation in the Cell

Figure 4.3 shows images of the T_1 and T_2 times across the cell, taken using both Franzen and Ramsey sequences. For the Ramsey sequence, the microwave input power to the cavity was 21.8 dBm, and the frequency was set slightly detuned from the $i = 4$ transition.

Two different methods have been employed to obtain T_1 times from the Franzen and Ramsey data. Each pixel of the Ramsey data was fit using Eq. (3.23), yielding T_1 and T_2 times with $\pm 1\%$ and $\pm 4\%$ fitting uncertainties, respectively. Fitting each pixel of the Franzen data in a similar way, using Eq. (3.21), yields essentially the same T_1 image as obtained from the Ramsey data. However, relaxation near the cell walls is not well-described by a single exponential. For the Franzen T_1 image, we therefore calculate T_1 as the $1/e$ decay time of the hyperfine population difference, as described by Eq. (3.22).

The bottom panels of Figure 4.3 show radial profiles of the T_1 and T_2 images. There is strong agreement between the structure of the Franzen and Ramsey T_1 images. The relaxation rate is uniform across the centre of the cell, with both Franzen

and Ramsey T_1 times around $265 \mu\text{s}$. Franzen and Ramsey T_1 times drop away to around $80 \mu\text{s}$ and $100 \mu\text{s}$, respectively, at the cell edge, due to the depolarisation of Rb atoms after collisions with the cell walls. The $0.34 \pm 0.05 \text{ mm}$ half-width of this ‘skin’ of reduced relaxation times is determined by the distance Δx an atom diffuses during the bulk relaxation time. A simple estimate yields $\Delta x = \sqrt{DT_1} = 0.31 \text{ mm}$, using the measured bulk $T_1 = 265 \mu\text{s}$. More detailed modelling is described in section 4.4 below. The shorter Franzen T_1 at the cell edge is due to the definition of the $1/e$ time that accounts for the multimode nature of the diffusional relaxation. The T_2 relaxation, shown in the right-hand panels of Figure 4.3, also exhibits an outer ‘skin’ of reduced relaxation times, with T_2 times around $130 \mu\text{s}$ at the cell edge. Unlike in the T_1 profiles however, the bulk T_2 times are not entirely flat, rising up to around $350 \mu\text{s}$ in the cell centre. This is significantly longer than the $284 \mu\text{s}$ calculated in Table 2.7. The most likely explanation is that the σ_{2bg} values in Table 2.3, which were measured for ^{85}Rb , are too large for ^{87}Rb . This is reasonable, given the larger ^{87}Rb hyperfine splitting, by a factor of two, and the different nuclear spin.

The relaxation times obtained in the centre of the cell are larger than the values obtained using the photodiode in section 4.2. Integrating over the images in Fig. 4.3a-c, we get average Franzen and Ramsey T_1 times of $176 \mu\text{s}$ and $221 \mu\text{s}$, respectively, and an average Ramsey T_2 time of $269 \mu\text{s}$. The Franzen T_1 time is more accurate, as it accounts for the multimode diffusional relaxation near the cell walls. The photodiode values lie between the central and average image values, indicating that the photodiode measurements averaged the relaxation time over some partial fraction of the cell.

In addition to the relaxation times, the absorption images also provide information about the optical pumping efficiency. We define the hyperfine population difference between the $F = 1$ and $F = 2$ states as

$$u \equiv 1 - \frac{n_2}{5/8}, \quad (4.3)$$

where n_2 is the fraction of atoms in $F = 2$. With this definition, $u = 0$ represents the unpumped equilibrium state where all m_F states are equally populated, and $u = 1$ corresponds to perfect optical pumping where the $F = 2$ state is empty. We neglect the contribution of ^{85}Rb , despite its often significant role, as discussed in particular in Chapters 2, 3 and 6. For the discussion in this chapter, we are only concerned with the overall polarisation and optical response of the cell, regardless of isotope. The B fitting parameter for Franzen data (see Eq. (3.21)) describes the amount the OD has changed through optical pumping. Normalising by the unpumped OD = 1.1 we obtain the hyperfine population difference in the optically pumped steady state, $u_0 = B/1.1$. Figure 4.4 shows the image and radial profile of u_0 obtained in this way. We observe a reduced pumping efficiency close to the cell edge because of atom-wall collisions. In addition, there is a broad dip in pumping efficiency in the centre of the cell. This is due to a deposit of Rb that had developed on the front cell wall, partially blocking the pumping light. We attribute the deposit to a small temperature gradient on the cell. The deposit was present when taking

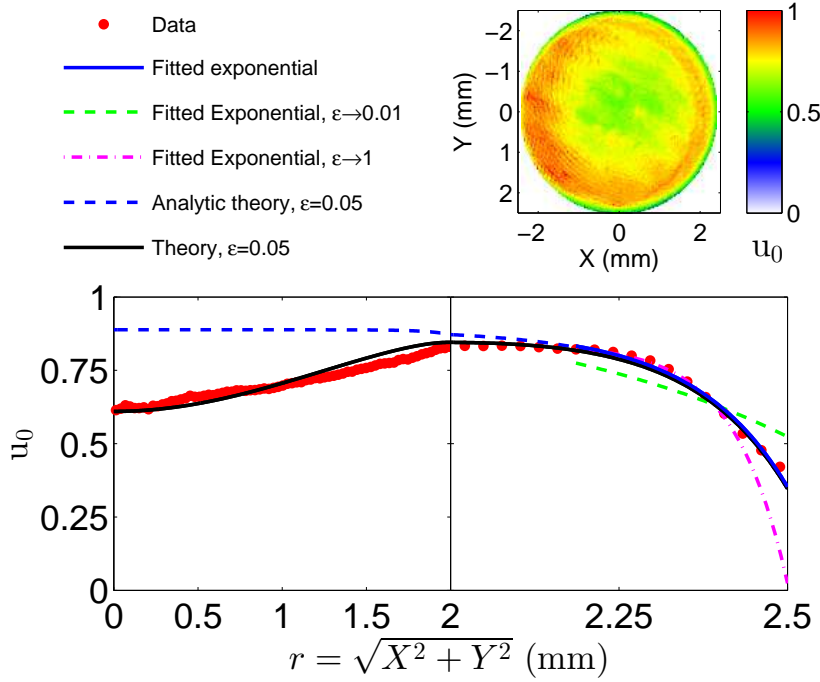


Figure 4.4: Image and radial profile of u_0 , the hyperfine population difference in the optically pumped steady state, obtained from Franzen data. The red data points in the lower panel show the mean u_0 for each radial position, binned in $27.5 \mu\text{m}$ bins. The error of the mean is smaller than the symbols. Note the change in scaling of the bottom axis at $r = 2$ mm to magnify the region near the cell wall. The data is compared to theory as described in section 4.4. The fit of Eq. (4.5) to the data near the cell wall is shown in solid blue. The ‘theory’ and ‘analytic theory’ curves respectively model u_0 with (Eq. (4.10)) and without (Eq. (4.9)) the inclusion of the central dip in optical pumping efficiency, which was caused by a Rb deposit on the front cell window. Figure adopted from Ref. [51].

all of the imaging data. The robustness of our T_1 , T_2 , and microwave magnetic field measurements is highlighted by the lack of correlation between the image of u_0 in Figure 4.4, and the images presented in Figure 4.3.

4.4 Modelling Relaxation in the Cell

We now describe a model for the hyperfine population relaxation in the cell and compare it with our imaging data. We begin by analyzing the optically pumped steady state in Fig. 4.4. Using a simple 1D model based on Ref. [143], we determine the probability that a Rb-wall collision destroys the hyperfine polarisation. We then use this probability in a 2D model valid throughout the entire cell to describe the

observed T_1 relaxation.

4.4.1 Depolarisation Probability of Rb-Wall Collisions

In Ref. [143], Grafström and Suter used evanescent-wave spectroscopy to study optical pumping of Na vapor near a glass wall. Using a simple model, they related the atomic $\langle m_F \rangle$ -polarisation at the wall to the depolarisation probability of atom-wall collisions. We adapt their model to our case of hyperfine population relaxation between states of different F in Rb collisions with Si walls.

Close to the cell walls, the evolution of the hyperfine population difference u can be described by a 1D diffusion equation

$$\frac{\partial}{\partial t} u(r, t) = D \frac{\partial^2 u}{\partial r^2} - (\Gamma + \Gamma_p) u(r, t) + \Gamma_p. \quad (4.4)$$

The first term on the right-hand-side describes diffusion of Rb atoms in the buffer gas. The second term describes relaxation at a rate $\Gamma + \Gamma_p$, where the bulk relaxation rate $\Gamma = \gamma_{SE} + \gamma_{\text{buffer}} + \gamma_z$ includes the effect of Rb-Rb spin exchange collisions (γ_{SE}) and Rb-buffer gas collisions (γ_{buffer}). Relaxation due to collisions with the front and back cell windows varies only slightly with r , and so we include it as a constant rate γ_z . The optical pumping rate Γ_p drives both relaxation in the second term of Eq. (4.4) and optical pumping in the third term. The steady-state solution to Eq. (4.4) is

$$u_0(r) = u_\infty - (u_\infty - u_R) \exp[\mu(r - R)], \quad (4.5)$$

where $u_\infty \equiv \frac{\Gamma_p}{\Gamma + \Gamma_p}$ is the population difference far from the walls, R is the cell radius, $u_R \equiv u_0(R)$ is the population difference at the wall, and $\mu \equiv \sqrt{\frac{\Gamma + \Gamma_p}{D}}$. Wall collisions produce a skin of reduced optical pumping near the cell edge, with the skin thickness given by μ^{-1} . The 1D model provides a good description of the behavior near the wall for $|r - R| \ll R$ and $\mu R \gg 1$, which is satisfied in our experiment.

From the behavior of $u_0(r)$ near the cell wall, it is possible to determine the probability ϵ that a Rb-wall collision destroys the atomic hyperfine polarisation [143]. Very close to the wall, on average half of the atoms have just collided with the wall, and half are arriving from a distance $L = \frac{2}{3}\lambda$ into the cell bulk, where $\lambda = 3.5 \mu\text{m}$ is the Rb mean free path in the buffer gas. Atoms from the bulk carry an average polarisation $u(R - L)$, which is reduced to $(1 - \epsilon)u(R - L)$ after the collision. Thus, $u(R) \simeq \frac{1}{2}(2 - \epsilon)u(R - L)$. Applying these considerations to Eq. (4.5) and noting that $\mu L \ll 1$, we obtain

$$\epsilon = \frac{2\mu L(u_\infty - u_R)}{u_R + \mu L(u_\infty - u_R)}. \quad (4.6)$$

Figure 4.4 shows a fit of Eq. (4.5) to the measured $u_0(r)$ profile of the Franzen data (blue solid line). We only fit to the data near the cell wall ($r \geq 2.15$ mm), where the 1D approximation is valid and the optical pumping rate is approximately

constant. The fit parameters are $\mu = (7 \pm 1) \times 10^3 \text{ m}^{-1}$, $u_R = 0.35 \pm 0.04$, and $u_\infty = 0.89 \pm 0.03$. Using these values in Eq. (4.6), we obtain a depolarisation probability of $\epsilon = 0.05 \pm 0.01$. When we analyse the initial state of the Ramsey data in a similar way (not shown), we obtain $\epsilon = 0.046 \pm 0.007$, consistent with the Franzen data. For comparison, Fig. 4.4 shows fits to the data where ϵ was constrained to $\epsilon = 1$ (purple) and $\epsilon = 0.01$ (green), respectively. Both values are inconsistent with our data.

The value of $\epsilon = 0.05$ obtained from our data is surprisingly small. It implies that the atomic hyperfine population can survive of order $\epsilon^{-1} \approx 20$ collisions with the Si wall. Previous experiments with Na and Cs atoms near glass walls have reported $\epsilon = 0.5$ [143, 149]. Our experiment differs not only in the measurement technique, the atomic species, and the wall material, but also in that we study relaxation between hyperfine states $F = 2$ and $F = 1$, while the previous experiment [143] studied the relaxation of $\langle m_F \rangle$ -polarisation within one hyperfine state. A systematic error in our measurement would arise if the images are clipped close to the cell wall, so that the actual location of the wall is at $r > 2.5$ mm. To make our data consistent with $\epsilon = 1$, the location of the wall would have to be shifted by $> 63 \mu\text{m}$ (more than two datapoints in Fig. 4.4), which is not very likely given the spatial resolution of our imaging system. Moreover, we point out that the surface properties of the interior cell walls are not precisely known. A layer of adsorbed Rb atoms or other residues on the Si walls could modify the collisional properties. A systematic study of these effects would require a dedicated setup and was beyond the scope of this thesis. However, our measurements show that absorption imaging is a powerful tool for the investigation of atom-wall collisions. The high spatial resolution opens up many intriguing possibilities such as laterally patterning the surface to modulate the collisional properties.

4.4.2 T_1 Relaxation: 2D Model

We now model T_1 relaxation in the Franzen sequence, considering the entire circular aperture of our cell. The diffusion equation for circular symmetry reads

$$\frac{\partial u}{\partial t} u(r, t) = D \frac{1}{r} \frac{\partial}{\partial r} \left(r \frac{\partial u(r, t)}{\partial r} \right) - (\Gamma + \Gamma_p) u(r, t) + \Gamma_p. \quad (4.7)$$

From the above considerations on diffusion and atom-wall collisions, we can derive the boundary condition

$$\left. \frac{\partial u}{\partial r} \right|_{r=R} + \frac{\epsilon/2}{(1 - \epsilon/2)L} u(R) = 0, \quad (4.8)$$

which reproduces Eq. (4.6) when applied to Eq. (4.5). The initial condition for modeling the Franzen sequence is given by the optically pumped steady state solution of Eq. (4.7) subject to the boundary condition Eq. (4.8),

$$u_0(r) = u_\infty \left(1 - \frac{I_0(\mu r)}{I_0(\mu R) + I_1(\mu R) (2/\epsilon - 1) \mu L} \right), \quad (4.9)$$

where I_0 and I_1 are modified Bessel functions of the first kind, and u_∞ and μ are defined as in the previous section. In the following, we take $\epsilon = 0.05$ as a fixed parameter determined as described above.

Figure 4.4 shows $u_0(r)$ given by Eq. (4.9) for the same parameters as in the previous section (blue dotted line). While the solution is indistinguishable from the 1D model close to the wall and matches the data well in this region, there is a discrepancy in the cell center ($r < 2$ mm). This is because we have so far assumed a spatially homogeneous optical pumping rate Γ_p , which was not the case in the experiment. To model T_1 relaxation, we can simply take the measured profile in Fig. 4.4 as the initial condition for the dynamics described by Eq. (4.7). It can be phenomenologically described by the function

$$u'_0(r) = u_0(r) - \frac{k_0}{2} \left[\cos\left(\pi \frac{r}{R}\right) + 1 \right]. \quad (4.10)$$

The additional term has been chosen such that it does not affect the boundary condition Eq. (4.8) and is thus consistent with the same value of ϵ as $u_0(r)$. The factor k_0 describes the reduced pumping efficiency in the cell center. Our data is well described by $u'(r)$ using $k_0 = 0.28$ (black solid line in Fig. 4.4).

We model relaxation in the dark by setting $\Gamma_p = 0$ at $t \geq 0$ and numerically solving Eq. (4.7) with the initial condition Eq. (4.10) and the boundary condition Eq. (4.8). At each radial position, we define T_1 as the time taken for u to decay to $1/e$ of its initial value. Recalling Eq. (3.22), we have

$$u(r, T_1) = \frac{1}{e} u(r, 0). \quad (4.11)$$

The simulated and measured T_1 profiles are compared in the bottom panels of Fig. 4.3.

We set $\Gamma = 3900 \text{ s}^{-1}$ in order to match the theory curves with the observed T_1 values in the centre of the cell. The central dip in optical pumping efficiency results in $T_1 > \Gamma^{-1}$ in the cell center due to the diffusive influx of atoms from neighbouring regions with higher optical pumping, partially offsetting relaxation. The agreement of our model with the data is reasonable. In particular, the width of the skin of reduced T_1 times at the cell edge is reproduced well. However, the transition from the cell bulk to the cell edge is sharper in the data than in the model.

4.5 Outlook

We have used time-domain spatially resolved optical and microwave measurements to image atomic relaxation in a microfabricated Rb vapor cell placed inside a microwave cavity. The relaxation times at the cell edge provide spatially resolved information on the interactions of Rb atoms with the Si cell walls. Our data suggest that Rb-Si collisions are not completely depolarising, agreeing with previous work on Na-glass collisions. It would be interesting to study these interactions in further detail on

a dedicated setup. This aspect of our technique could be particularly useful in the characterisation of wall coatings in coated cells. The temperature dependence of ϵ may also yield insights into Rb interactions with the bare glass walls. I used several other vapor cells in this thesis, for which ϵ was not measured. Except where explicitly noted, I used $\epsilon = 1$ for all other calculations in this thesis.

Our measurement technique is fast, simple, and produces high resolution images for vapor cell and microwave-device characterisation. It is of particular interest for characterising cells in miniaturised atomic clocks [179] and sensing applications [17, 21, 50], and I used it extensively as a characterisation tool throughout this thesis. It could be used to directly image diffusive transport of polarisation, following Ref. [180]. As shown in the next chapter, it is also of interest for characterising the cell and cavity properties in larger and high-performance vapor cell atomic clocks [52, 181–183].

Chapter 5

Clock Characterisation

The imaging techniques presented in this thesis are already being applied in characterising high-performance vapor cell atomic clocks. Applications of these miniaturised, low power clocks include telecommunications systems, and as the on-board clocks in GPS and Galileo satellites or deep-space probes. The state of the art is now aiming for stabilities better than 10^{-14} , which is better than the stability of a passive hydrogen maser, and at least an order of magnitude better than commercial lamp-based atomic clocks [181, 183, 184]. In this chapter, I present the characterisation of a state-of-the-art Rb clock, which has a stability of 1.4×10^{-13} after 1 s [185], and 4×10^{-14} after 10^4 s of integration [184]. The clock was produced by the Milet group at the Laboratoire Temps-Fréquence, Université de Neuchâtel, Switzerland, and the characterisation was published in Ref. [52]. The characterisation builds on the cavity characterisation techniques we developed in Ref. [51].

A Rb clock works by stabilising a quartz oscillator to the 6.8 GHz ^{87}Rb $i = 4$ ‘clock’ transition [6]¹. This π transition is chosen for its first order insensitivity to dc magnetic fields. The microwave field in the Neuchâtel clock is provided by a magnetron cavity [186], with the vapor cell placed inside, as shown in Figure 5.1. Magnetron cavities offer a $\sim 10\times$ stronger signal than similarly sized CPT clocks, due to the 2-photon nature of the CPT interaction, though CPT clocks can be miniaturised further [187]. The dimensions of the cavity, which has an external diameter of 40 mm and a length of 35 mm, are smaller than the 44 mm free-space wavelength of the 6.8 GHz microwave, resulting in a nonetheless very compact ‘physics package’. However, achieving a uniform microwave field in this cavity is a non-trivial task. Solenoid coils provide a dc magnetic ‘C-field’ of $40 \mu\text{T}$ (0.4 G), which provides a quantisation axis along the $-z$ direction, and allows the hyperfine transitions to be individually addressed, as seen in Figure 5.1.d.

The homogeneity of the applied dc and microwave magnetic fields is crucial for clock stability, and precise knowledge of the field distributions is a key requirement in clock characterisation and development. Homogeneity of the microwave field direction is important for driving the clock transition, which is driven by the mi-

¹The labelling of the hyperfine transitions is defined in section 3.1.2.

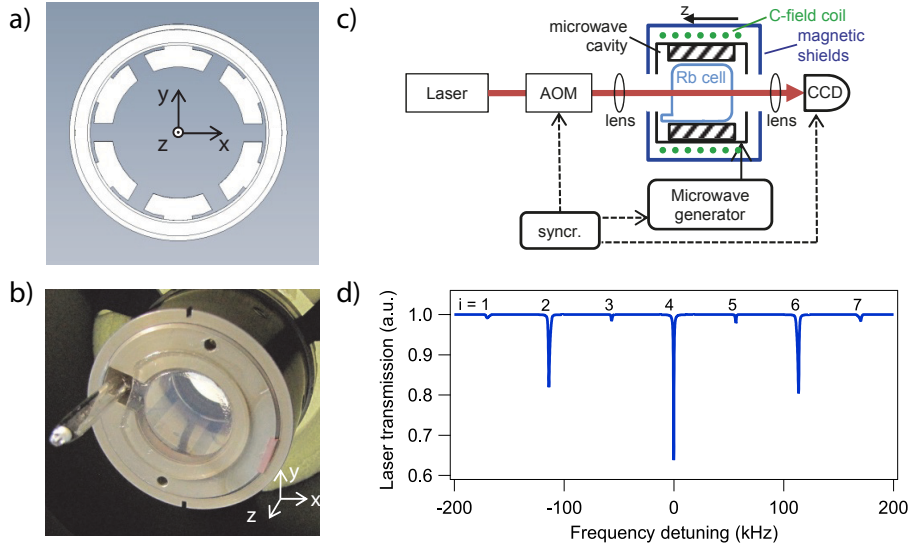


Figure 5.1: a) Cross section of the clock magnetron cavity; b) photo of the vapor cell inside the magnetron cavity; c) schematic of the measurement setup, where a single laser (the GS-laser) was used for both optical pumping and probing. Note that there was only optical access to the central 10 mm of the 25 mm cell diameter; d) DR spectrum of the clock, showing the strong π microwave component (transitions $i = 2, 4, 6$), weak σ components, and narrow resonance linewidths. Figure adopted from Ref. [52].

microwave component parallel to the quantisation axis. Homogeneity in the microwave amplitude is important for achieving a uniform microwave power shift of the clock frequency. For pulsed clocks, which operate using a frequency-domain Ramsey sequence, microwave homogeneity is also required in order to uniformly apply the $\pi/2$ Ramsey pulses. Despite the first-order insensitivity of the clock transition to Zeeman shifts, the C-field homogeneity is also important. Influences of dc field inhomogeneities include the second order Zeeman shift and T_2 dephasing, the dc field dependence of the microwave power shift [178, 188], and the need for homogeneity in the quantisation axis direction.

The field distributions depend on the assembly of the clock, with the microwave field particularly influenced by the presence and position of the vapor cell, which provides a dielectric filling to the cavity. This means that measurements using dc and microwave field probes inside the disassembled clock components, which anyway introduce field perturbations of their own, are of only minor benefit. Previous clock characterisations have therefore relied on computer simulations, and measurements of the fields have been based on the bulk properties, integrated over the vapor cell without (or with minimal) spatial resolution [183, 184, 186]. Our imaging techniques allow the clock atoms themselves to be used as sensors to map the clock fields. This allows a fast, in-situ characterisation of the fully assembled clock, in its operational

mode. Our techniques will therefore also allow the study of long term drifts in the clock, such as possible changes in the C-field due to magnetisation of the magnetic shielding.

The 25 mm length of the clock vapor cell is 1-2 orders of magnitude longer than the other cells used in this thesis. The imaging techniques were found to be nevertheless compatible with the longer cell, and we obtain images with sub-100 μm transverse spatial resolution, given by the diffusion length of atoms during a measurement.

To characterise the clock dc and microwave fields, we used Ramsey and Rabi imaging sequences, respectively, as described in Section 3.2. The imaging optics produced a 1:4 demagnification on the CCD camera. The CCD image was binned into image pixels of 3×3 CCD pixels, with an image pixel size of $72 \times 72 \mu\text{m}^2$ in the cell plane.

5.1 Clock C-Field

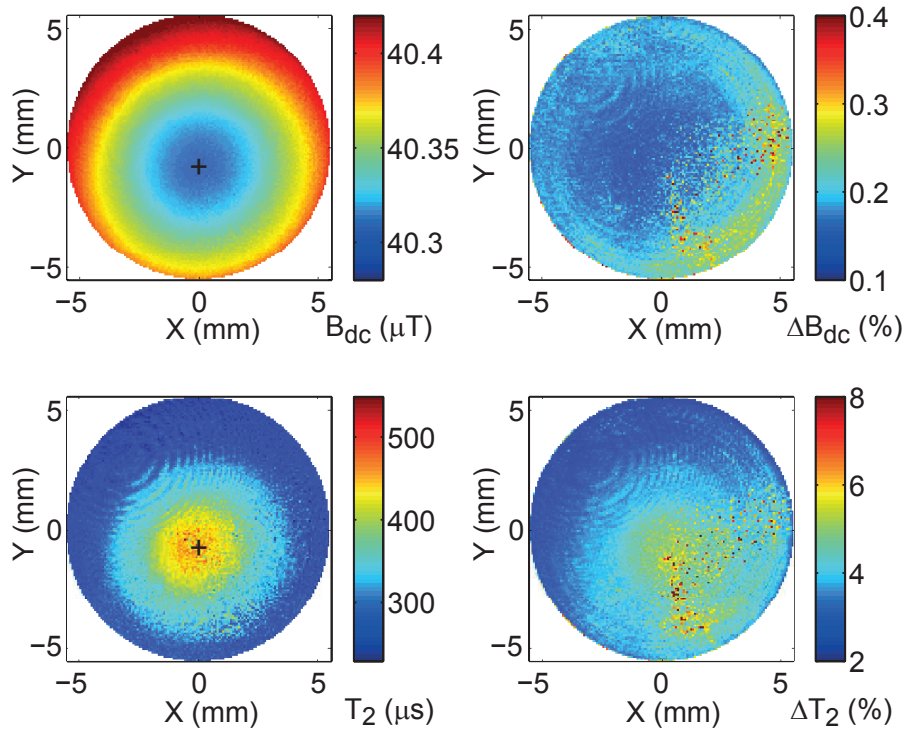


Figure 5.2: Images of the clock dc magnetic field, and the T_2 time of the $i = 2$ transition (left column), and the corresponding fitting uncertainties (right column). The cross in the left column images indicates the concentric centre of B_{dc} , and shows the alignment of the T_2 image with this centre. Figure adopted from Ref. [52].

Figure 5.2.a shows an image of the clock C-field, obtained with a Ramsey sequence detuned from the $i = 2$ transition, and with common-mode frequency shifts removed using a similar measurement on the $i = 6$ transition, whose Zeeman shift is of the same magnitude but opposite sign. The field is highly uniform, to within 0.3%, and is slightly offset from the cell centre. The corresponding T_2 time, shown in Figure 5.2.b, is inversely correlated with the C-field inhomogeneity, and is at a maximum where the C-field is most homogeneous. The fitting uncertainties on each pixel for B_{dc} and T_2 are $< 0.5\%$ and $< 8\%$, respectively. Despite the only 0.3% C-field inhomogeneity, T_2 on this field-sensitive transition drops by a factor of two towards the cell edges. The effect on the clock transition (not shown) is much less dramatic, with T_2 varying from $1.55 \mu\text{s}$ in the image centre, to $1.45 \mu\text{s}$ at the image edge.

As described in Ref. [52], we can model the dephasing influence of C-field gradients on T_2 from models developed for NMR spin echo experiments. The general agreement with the measurements indicates that the observed spatial variation in T_2 is indeed be caused by inhomogeneous dephasing due to magnetic field gradients.

5.2 Clock Microwave Magnetic Field

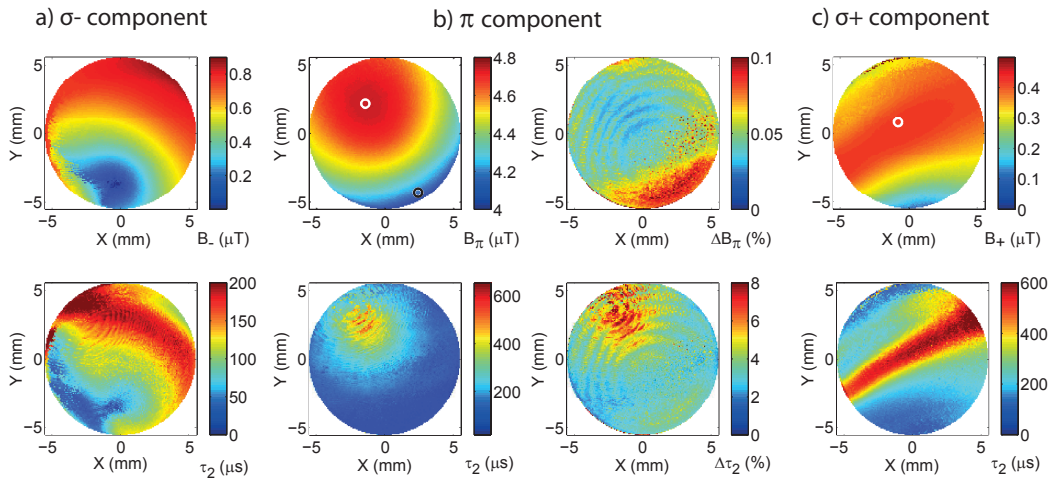


Figure 5.3: Images of the a) σ_- , b) π , and c) σ_+ components of the clock cavity microwave magnetic field, and the respective τ_2 Rabi oscillation lifetime. The fitting uncertainties of the π component images are also shown. White and black circles in (b) correspond to pixels (88,98) and (39,15), respectively, which are further analysed in Figure 5.4. Figure adopted from Ref. [52].

Figure 5.3 shows images of the σ_- , π , and σ_+ components of the clock cavity microwave magnetic field. The images were obtained in Rabi sequences driven on transitions $i = 1, 4, 7$, respectively. The π component is reasonably uniform, to

within 20%, which is sufficient for both cw and pulsed clock operation [11]. The field is again off-centre with respect to the vapor cell, however this is not correlated with the C-field spatial offset. Subsequent modelling revealed that the microwave offset is due to the vapor cell stem [57], and this can now be accounted for in the next generation cavity. The σ_- and σ_+ components of the microwave field are 10% and 20% of the π component amplitude, respectively. This matches with the cavity design, and the DR spectrum in Figure 5.1.d. Although the σ components do not interact with the atoms during clock operation, their images are important to the characterisation of the cavity. At the time of writing, the spatial variation of the σ components had not yet been explained.

Below the microwave field images in Figure 5.3 are images of τ_2 , the lifetime of Rabi oscillations driven by each field component. In a similar way to T_2 dephasing from C-field gradients, τ_2 is a measure of how the coherent Rabi oscillations are dephased by inhomogeneities in the microwave field, and is inversely correlated with the field inhomogeneity seen in the microwave images above.

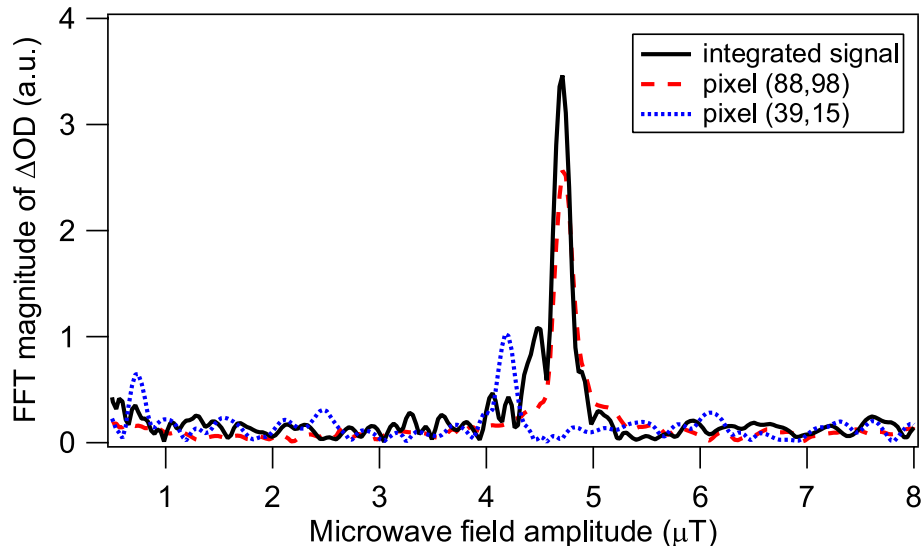


Figure 5.4: Fourier analysis of the π component of the microwave field. FFT traces are shown for pixels (88,98) and (39,15), respectively marked with white and black circles in Figure 5.3.b, and for the integrated signal across the entire image. The horizontal axis has been scaled to the corresponding microwave field amplitude. For better visibility, the FFT magnitudes of pixel (39,15) and for the integrated signal were multiplied by factors of 2 and 15, respectively, to compensate differences in FFT magnitudes caused by the different T_2 times of the time domain signals. Figure adopted from Ref. [52].

The images in Figures 5.2 and 5.3 are integrations of the fields along the z axis, over the laser path through the cell. The images therefore do not tell us about field gradients along the z axis. In such a thick (25 mm) cell however, field homogeneity

along the z axis is just as important as for the transverse axes. We are able to extract some information on the z axis variation by taking a Fourier transform of the Rabi or Ramsey oscillations. As an example, Figure 5.4 shows a Fourier analysis of the π component of the microwave magnetic field. Spectra are shown for pixels (88,98) and (39,15) of the π component image in Figure 5.3.b, as well as for the Fourier transform of the averaged signal of all the image pixels. The two example pixels are chosen as representative bounds of the microwave amplitude, corresponding to regions of high and low microwave amplitude, respectively. All three Fourier spectra show narrow peaks for the microwave field distribution, with a spread of 10% or less for the two individual pixels. For pixel (39,15), the small peak at $B_{mw} < 1 \mu\text{T}$ indicates the presence of some z -region with very low field amplitude. The integrated signal shows a structure composed of the distinct features of both example pixels, plus an intermediate feature at $4.5 \mu\text{T}$, as expected from the general field distribution in Figure 5.3.b. Small dips in the integrated signal are seen at 4.14, 4.3, and $4.55 \mu\text{T}$, making this signal appear to be comprised of several distinct peaks. Given the overall smooth field distribution of Figure 5.3.b, these dips might well be artifacts without statistical significance, arising from measurement noise or instabilities converted by the FFT routine employed. The contribution of the low field amplitudes, such as in pixel (39,15), to the integrated signal is small. This matches with the small image area in Figure 5.3.b showing such low amplitude values. The reasonably sharp peaks for all three spectra allow us to conclude that the variation of B_{mw} along the z -axis is small ($< 10\%$).

5.3 Conclusions

The imaging techniques presented in this thesis can be employed as an important tool in the characterisation and development of state-of-the-art clocks. The imaging techniques provide spatially resolved information on parameters that were previously typically measured without spatial resolution, and often through indirect means. For example, a common technique is to use DR spectra to characterise the dc and microwave magnetic fields. The relative areas of the σ and π peaks give the relative strengths of the microwave components, and the linewidths give an indication of the microwave and dc field homogeneity. However, it is very difficult, if not impossible, to extract from the DR spectra the rich information on the spatial variation within each of the σ and π microwave components that is provided by our imaging techniques. Correcting for these inhomogeneities can give real improvements in clock performance. The simplicity of our imaging techniques make their adoption feasible in most lab environments, and the wealth of information now available should significantly aid the development of these precision devices.

Chapter 6

Ultrathin Vapor Cells and the Cell Filling Station

Microwave imaging using vapor cells was demonstrated in a proof of principle experiment in Ref. [50]. The setup was far too bulky for practical use, however, and a central project of this thesis was to develop a high resolution setup appropriate for imaging real world devices. The new setup is based on ultrathin vapor cells, which are attached to a filling station to give us complete flexibility in the buffer gas pressures, species, and mixtures used in the cells. The new setup provides $50 \times 50 \times 140 \mu\text{m}^3$ spatial resolution in the cell bulk, and allows us to image fields as close as $150 \mu\text{m}$ above surfaces with a $6 \times 6 \text{mm}^2$ field of view. This represents an order of magnitude improvement in spatial resolution compared to previous vapor cell experiments, and allows us to enter the relevant regime for imaging fields of industrial microwave devices. A particularly promising feature of our system is that it can be configured to also image microwave electric fields (see Section 7.7) [49].

Sub-millimeter spatial resolution has been reported in the vapor cell bulk for a number of sensing techniques [32, 46–51, 175], but typical cell dimensions have limited useable spatial resolution to the millimeter-scale or larger. Feature sizes in near-fields are on the order of the distance from the field source, meaning that in order to resolve small structures on objects under investigation, it is crucial to measure fields at similarly small distances above the structures. There are many applications where higher spatial resolution is essential, such as integrated microwave circuit characterisation [189], corrosion monitoring [190–192], and in lab-on-a-chip environments for microfluidic analytical chemistry and bio-sensing [31, 32, 193, 194], and molecular imaging [24, 195, 196].

This chapter describes the setup and characterisation of the ultrathin cells and the filling station. In the next chapter, I present examples of field imaging results.

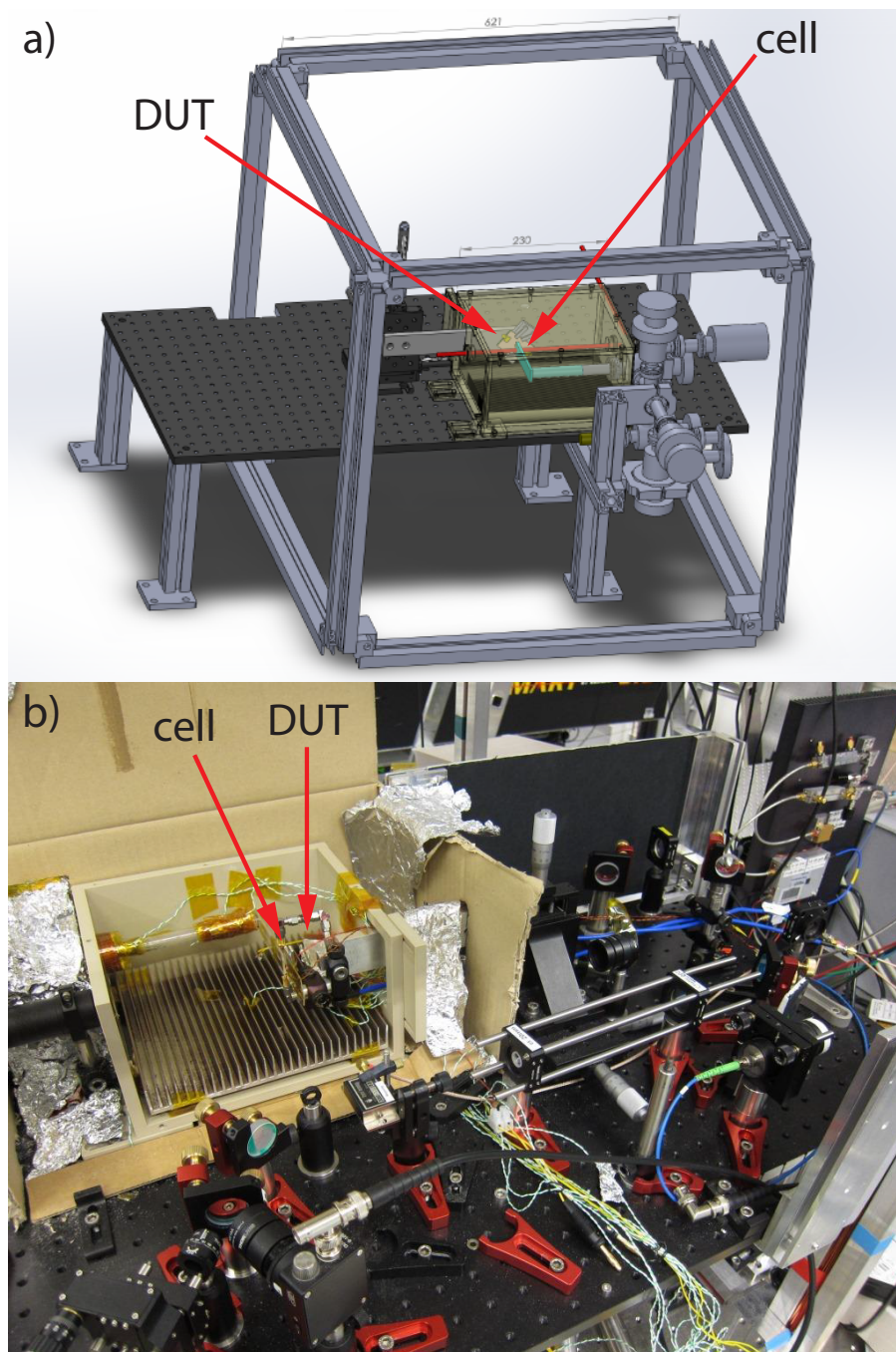


Figure 6.1: a) CAD schematic and b) photo of the filling station setup. The photo is taken with the SRR chip placed in front of the cell for imaging (see section 7.3.3).

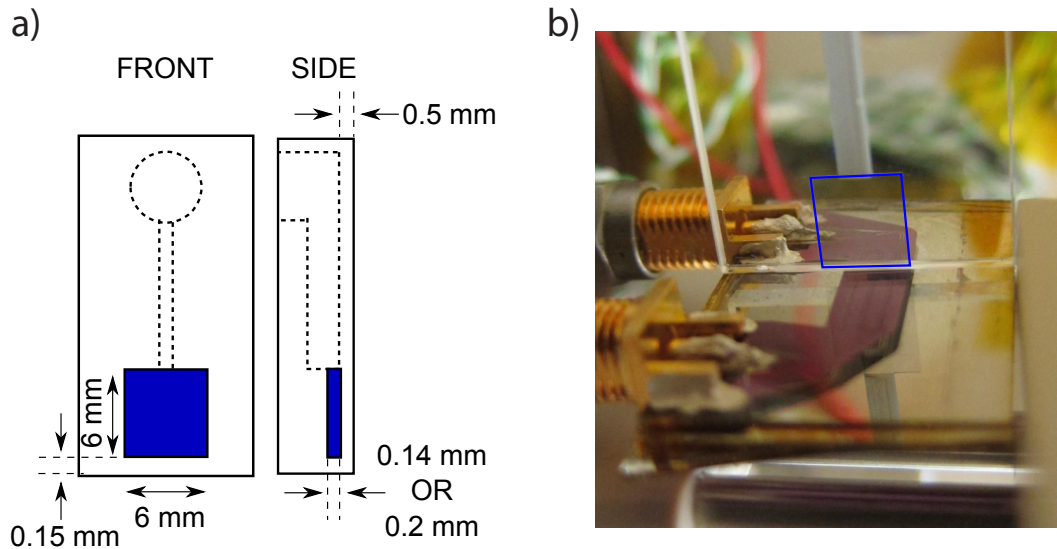


Figure 6.2: a) Schematic of the ultrathin vapor cells used in this thesis (not to scale). The cell chamber is shown in blue, and the etched channel and through-hole are indicated with dotted lines. The key features are the extremely thin external cell walls: $500\ \mu\text{m}$ on the side, and only $150\ \mu\text{m}$ at the end of the cell; b) Photo of cell U1 in operation with the Zigzag chip (see Sec. 7.3.2). The outline of the cell chamber is highlighted in blue.

6.1 Equipment and Setup

Figure 6.1 shows a CAD schematic and photo of the filling station setup. The vapor cell is attached to a vacuum system, and placed inside an oven. The oven, imaging optics, and DUT (device under test) mount are on a raised breadboard, and the setup is surrounded by a set of Helmholtz coils. The following section describes the key components. Further information is available in Appendix E.

6.1.1 Ultrathin Vapor Cells

The design of the ultrathin vapor cells was a critical component in our high resolution imaging. The commercially obtained cells¹ consist of two optically bonded $0.5\text{-}1.5 \times 20 \times 90\ \text{mm}$ pieces of Suprasil (quartz) glass. As shown schematically in Figure 6.2.a, a cell chamber is etched into one end of the 1.5 mm-thick piece. An etched channel connects the cell chamber to a through-hole, around which we attach a glass-to-metal transition with epoxy (see Appendix E.1). We had cells made with nominal cell chamber thicknesses of $100\ \mu\text{m}$ and $200\ \mu\text{m}$, which we refer to as cells U1 and U2, respectively.

The thickness of cell U1 was measured at two points using an optical profilome-

¹The custom cells were produced by Hellma Analytics.

ter² to be $136 \pm 3 \mu\text{m}$ and $146 \pm 7 \mu\text{m}$. I therefore took the thickness to be $140 \pm 10 \mu\text{m}$. This is within the $100 \pm 50 \mu\text{m}$ manufacturing tolerance.

The ultrathin thicknesses represent an order of magnitude increase in longitudinal spatial resolution compared to the 3 mm thick cell used in the proof-of-principle setup presented in Ref. [50]. However, the key advance of the cells are their thin external walls (see Figure 6.2.a), as thin as $150 \mu\text{m}$ ³, which allow us to image near fields as close as $150 \mu\text{m}$ above devices. The general rule for near fields is that the smallest feature size is on the order of the distance from the source. Near field imaging using cells with a more typical millimeter-scale wall thickness can therefore only detect millimeter-scale features. Our thin walls allow us to for the first time take practical advantage of the high spatial resolution available in vapor cells, and should serve as a model for future near field sensing cells.

We fill the cells with a 3:1 mixture of Kr and N₂ buffer gasses, with typical filling pressures between 90 mbar and 120 mbar. The heavy Kr acts to localise the Rb atoms, improving our spatial resolution and limiting depolarising Rb collisions with the cell walls. The cell geometry, with relatively large transverse dimensions and transverse OD, is particularly susceptible to radiation trapping (see section 2.4.2). The N₂ gas is therefore included for quenching.

6.1.2 Temperature Control

The cell and microwave device are placed inside an oven, with operating temperatures of 130°C to 150°C chosen to give $OD \approx 1$. The oven has two layers: an inner box made of 1 cm thick PEEK plastic, and an outer box made of cardboard. Heating is provided by several resistive heating pads⁴. The Rb vapor density is controlled by a cold finger wrapped around the end of the glass-to-metal transition (see Figure 6.3), with a macroscopic droplet of Rb, known as the Rb reservoir, forming under the cold finger. The cold finger is made from a strip of mesh wire, with one end wrapped around the glass tube, and the other attached to a heat sink outside the oven. The 5 – 10°C temperature gradient between the cold finger and the cell helps reduce the deposition rate of Rb and other contaminants on the cell windows. The temperature is characterised by T_{cell} , the temperature near the cell chamber, and T_{res} , the temperature under the cold finger. The thermal time constant is quite slow (Figure 6.7.a, for example, shows that the temperature takes several hours to stabilise after turn-on), and the steady-state temperature stability is better than 0.5°C, as measured on thermistors placed around the oven (see Figure E.2). The absolute temperature accuracy, however, is on the order of a few degrees Celsius. This is due to the placement of the temperature sensors relative to the Rb, and also due to the low accuracy of the temperature readout devices used (which included a changing response with battery power). An improved temperature measurement

²Keyence VK-X2000

³The manufacturing tolerances allow for external walls up to $50 \mu\text{m}$ thicker than the specified values.

⁴From Minco.

system would have more control over the sensor placement, and would not use battery powered devices. We could also use the optical absorption spectrum to obtain the temperature using the atoms as sensors, for example fitting the spectrum using ElecSus [90], or using the temperature shift of the isoclinic point [197].

6.1.3 Imaging Setup

I used two separate lasers for optical pumping and probing, allowing separate optimisation of the pump and probe intensities. In general, I used the GS-laser as the probe, and the IF-laser as the pump. As shown in Figure 6.3, the pump beam was sent in to the cell at a slight angle, ensuring that transmitted pump light did not hit the camera. Both lasers were locked to the ^{87}Rb $F = 2 \rightarrow F' = 2/3$ crossover peak. Note that better performance is expected if the probe laser is tuned to the $F = 1$ ground state (see discussion in section 2.9).

The device under test (eg a microwave chip) is mounted next to the cell on a long arm, which extends outside of the oven to a 3D translation stage. There are two possible imaging modes. In most cases, the microwave device is placed at the end of and perpendicular to the cell, as shown in Figure 6.3. For devices built on transparent or reflective substrates however, it is possible to image in a second imaging mode, with the device placed in front of or behind the cell. This is exploited in section 7.3.3 with the SRR chip.

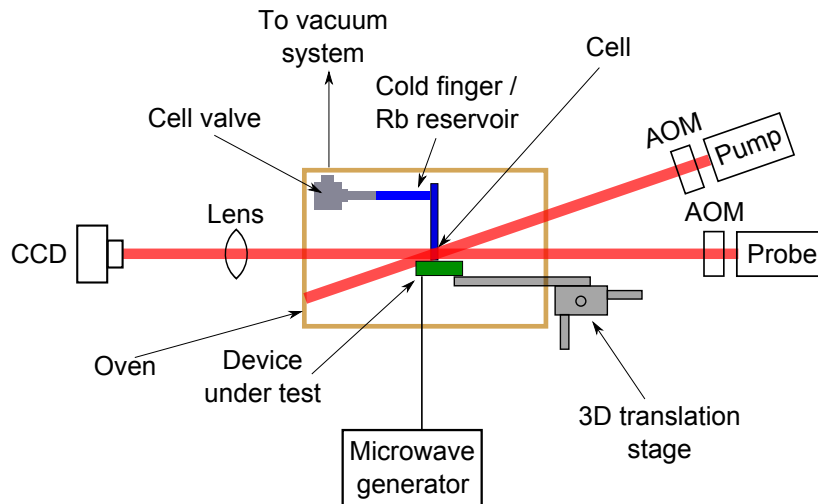


Figure 6.3: Schematic diagram showing the imaging setup used with the ultrathin cells. The laser beam radii are several mm. AOM = acousto-optical modulator.

6.1.4 Vacuum System

The cell is attached through a glass-to-metal transition to a vacuum system, shown schematically in Figure E.2. This differs from many vapor cell experiments (such as those in rest of this thesis), where a free-standing, permanently sealed-off vapor cell is used. The vacuum system allows us to evacuate the cell, transfer Rb, and fill the cell with arbitrary buffer gas mixtures and pressures, giving us flexibility at the expense of a compact setup. In addition, its construction does not require expertise in microfabrication or glass blowing. Schematics of the vacuum system, and a description of the Rb transfer and buffer gas filling procedures are provided in Appendix E.

6.1.5 Coils

The filing station is surrounded by a cage of Helmholtz coils, which cancel the Earth's magnetic field, and provide a static field of 1-2 G along the X , Y , or Z axes. This field serves as the quantisation axis, and the resulting \sim MHz Zeeman splitting of the ^{87}Rb hyperfine ground state transitions allows each transition to be individually addressed by the microwave magnetic field.

Figure 6.4 shows images of the dc magnetic field produced by each of the filling station coils. The data was taken using the 200 μm thick cell, which was in a slightly different location to the 100 μm thick cell (rotated upwards in the $Y-Z$ plane). The measurements were taken as part of the B_{dc} measurements presented in Section 7.4 (Figure 6.4 shows the C field measurements of Section 7.4). The microwave field used to drive the Ramsey oscillations was provided by the X component of the splitting resonator, described in section 7.3.3. The X measurement was taken on the $i = 6$ transition with a 316 μT (3.16 G) dc field, and shows a 0.4% variation in dc field strength across the field of view. The Y and Z measurements were taken on the $i = 7$ transition, with 134 μT and 141 μT dc fields, respectively. The dc field strength varies by 3% for both the Y and Z measurements. The inhomogeneities are likely to be due to imperfect centering of the cell with respect to the coil centres, and imperfect cancelling of the Earth's magnetic field.

6.2 Controlling the Rb Vapor Density, and Vapor Cell Curing

The Rb density in a vapor cell is at a basic level determined by the temperature of the Rb reservoir and the resulting Rb vapor around it. There are a number of additional complicating factors at work however, such as Rb transport, cell geometry, and interactions with the cell walls. The three main mechanisms present in our ultrathin cells are: 1) Diffusion of Rb to and from the Rb reservoir, which is separated from the cell by a narrow channel; 2) Desorption of Rb from the cell walls; and 3) Rb loss through interactions with the cell walls.

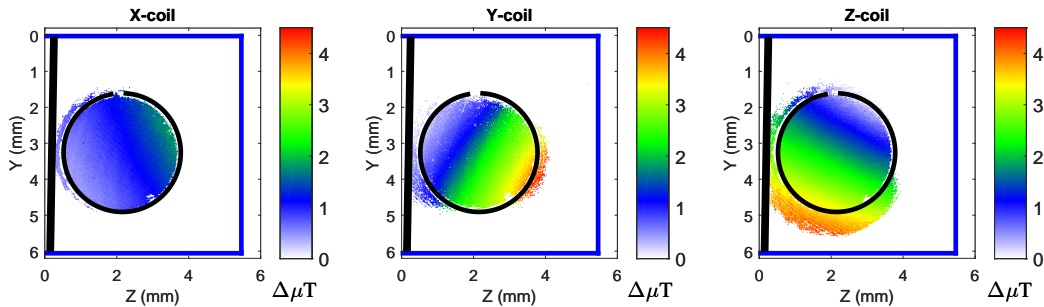


Figure 6.4: Experimentally obtained images of variations in the magnitude of the dc magnetic field produced by the filling station coils. The variations are on top of $316 \mu\text{T}$, $134 \mu\text{T}$ and $141 \mu\text{T}$ dc magnetic fields, for the X , Y , and Z coils, respectively, and are scalar measurements, insensitive to field orientation. The outlines of the cell and split-ring resonator (see section 7.3.3) are shown in blue and black, respectively. The field of view is defined by the microwave field of the split-ring resonator.

The experiment temperature is an important parameter, due to the strong dependence of the Rb density on temperature, but difficult to accurately obtain, due to the poor temperature sensor readout devices and uncertainty in sensor placement, as discussed in Section 6.1.2. We can estimate the temperature, however, by matching the experimental and theoretical temperature dependence of the OD. In the following sections, I scaled the measured temperatures to match the theory curves, giving

$$T_{\text{actual}} = T_{\text{room}} + A \times (T_{\text{meas}} - T_{\text{room}}), \quad (6.1)$$

where A is the scaling parameter, T_{meas} is the measured temperature, and $T_{\text{room}} = 22^\circ\text{C}$ is the room temperature. Variation of A between data sets is due to changes in the sensor positions, and the battery power of the readout device.

6.2.1 Rb Transport

The cell chamber in our ultrathin cells is separated from the Rb reservoir by a narrow channel, 76 mm long, with a $2 \times 1 \text{ mm}^2$ cross section, and a conductance of 0.01 L/s . In the absence of buffer gas, this low conductance is not a problem. Rb is able to travel through the channel sufficiently quickly that the Rb density in the cell volume follows the reservoir temperature, T_{res} . An example of this is shown in Figure 6.5. Introducing a buffer gas to the system significantly slows down Rb motion through the channel however, and the channel becomes a significant barrier between the cell chamber and Rb reservoir.

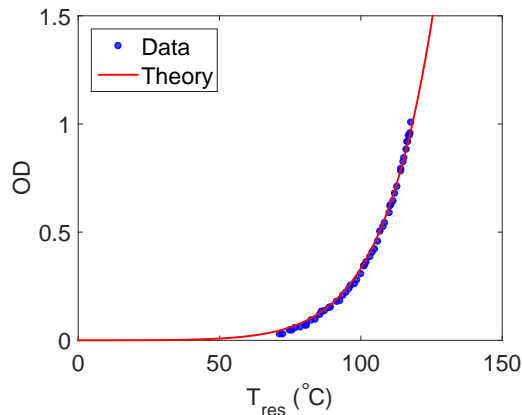


Figure 6.5: OD in cell U1 as a function of T_{res} , with no buffer gas present. The laser frequency is locked to the $F = 2 \rightarrow F' = 2/3$ crossover peak, and offset by -80 MHz by an AOM. The theory curve is calculated using the model presented in Section 2.3. To match the data and theory curves, I modified the measured T_{res} using Eq. (6.1) with $A = 0.92$.

6.2.2 Cell Walls as a Rb Source

In steady-state, the Rb density is controlled by the reservoir temperature, T_{res} . At the beginning of each run however, the Rb density is often actually controlled by the cell temperature, T_{cell} . During the cool-down period after each run, much of the Rb vapor will stick to the immediate cell walls, rather than return to the distant Rb reservoir. When subsequently reheating the cell, this wall-Rb can act as a Rb reservoir of its own. The effect is most apparent with high buffer gas pressures, which slow transport of Rb between the reservoir and cell chamber. This is illustrated in Figure 6.6, which tracks the OD during a single experiment run as the cell is heated up. The cell is filled with 70.1 mbar of Kr and 18 mbar of N_2 . The OD, and thus Rb density, evolves in three distinct stages: 1) The OD initially rises rapidly, with the OD plotted as a function of T_{cell} matching the theory curve, until $t = 125$ mins; 2) The OD then drops over the next 25 mins; 3) At $t = 150$ mins, the OD then begins rising again, with the theory curve now matched by OD plotted as a function of T_{res} .

The explanation is as follows. When heating the cell up, the Rb from the reservoir takes some time to diffuse through the channel to the cell, and the Rb in the cell is initially mainly due to desorption from the cell walls, with a density given by T_{cell} . As $T_{cell} > T_{res}$, during this period there will be an equilibrating flux of Rb atoms leaving the cell and heading towards the reservoir. The Rb density in the cell is kept close to that given by T_{cell} , as Rb atoms lost to the reservoir are quickly replaced by newly desorbed atoms from the cell walls. Eventually however, this extra Rb from the cell windows runs out. The Rb density in the cell then begins to decrease, as

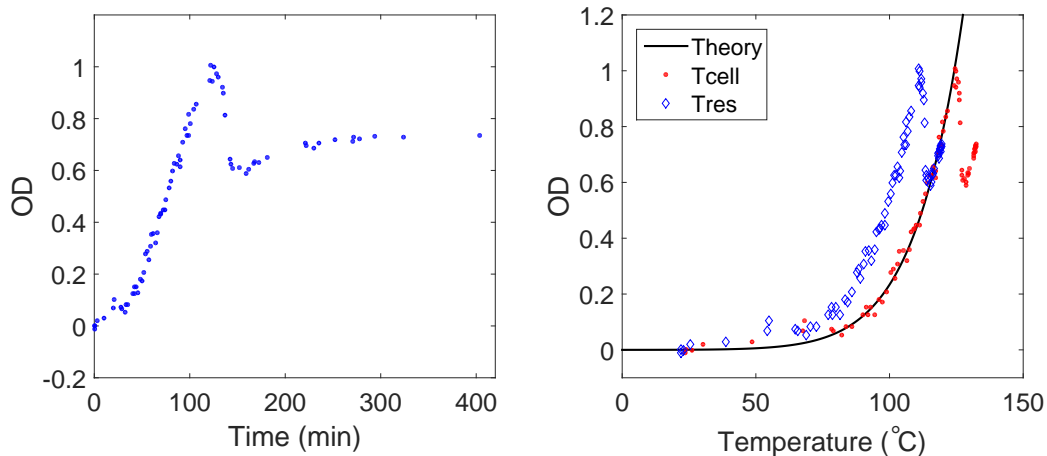


Figure 6.6: OD in cell U1 as a function of a) time; and b) temperature. The data is for a single experiment run, and is plotted twice in (b), as a function of both T_{res} (blue diamonds) and T_{cell} (red dots). A theoretical curve using the nominal buffer gas filling pressures of 70.1 mbar of Kr and 18 mbar of N_2 is also shown. The laser frequency is locked to the $F = 2 \rightarrow F' = 2/3$ crossover peak, and offset by -80 MHz by an AOM. To match the data and theory curves, I modified the measured temperatures using Eq. (6.1) with $A = 0.88$.

Rb atoms diffuse to the lower density region around the reservoir. For the buffer mixture in Figure 6.6, the timescale for the drop in Rb density is around 25 minutes. After reaching equilibrium, the Rb density is given by T_{res} (as long as T_{res} changes adiabatically relative to the 25 minute equilibration timescale, which in this case it does). Note that the data in Figure 6.6 was taken many months after the cell curing process (see next section), and so Rb loss into the cell walls was minimal. The run was performed immediately after a Rb transfer (see Appendix E.3), so the cell walls were also particularly well-primed with Rb.

The effect is greatly reduced when using lower buffer gas pressures. I didn't notice it when using 15 mbar of Kr, for example. The lower pressures mean faster diffusion between the cell and the reservoir, and so a shorter equilibration constant, inhibiting any build-up of a Rb density differential between the cell and reservoir. The effect is also a function of the history of the cell: If the previous run was performed with a high Rb density, then the cell walls will be a more effective reservoir at the start of the following run.

6.2.3 Cell Walls as a Rb Loss Mechanism

When Rb is introduced to a vapor cell, it begins modifying the cell walls, in a process known as 'curing'. The most extensive work on curing has been performed for antirelaxation coated cells, particularly by Bouchiat and Brossel [3]. The interac-

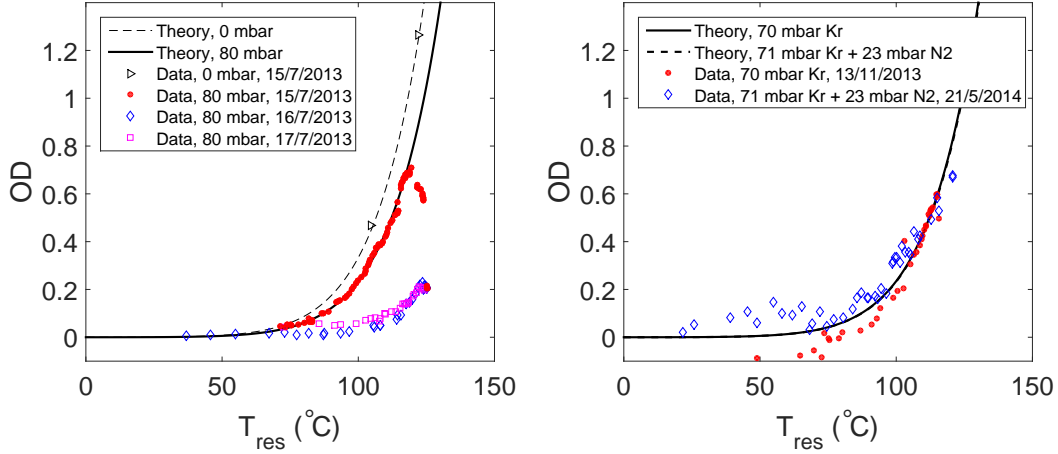


Figure 6.7: a) OD in cell U1 for experiment runs performed over several days, before cell curing. The first run was performed without buffer gas, while subsequent runs were performed with 80 mbar of Kr. The laser frequency is locked to the $F = 2 \rightarrow F' = 2/3$ crossover peak, and offset by -80 MHz by an AOM. To match the data and theory curves, I modified the measured T_{res} using Eq. (6.1) with $A = 0.97$. b) OD as a function of T_{res} , taken after the two weeks of cell curing. The measured T_{res} has been scaled using $A = 0.93$ and $A = 0.90$ for the 13/11/2013 and 21/5/2014 data, respectively.

tion with bare glass walls is less well understood, but there have been some recent studies [148, 198], and information is also available from studies of Rb discharge lamps [7, 199–201]. The main result for our ultrathin cells was that there was a very significant loss of Rb into the uncured cell walls. The exact mechanism is unclear, and several possibilities are discussed below.

Observations

Figure 6.7.a shows an example of the cell behaviour before curing. The OD is shown as a function of T_{res} for a sequence of experiment runs performed over several days. First, a run was performed without buffer gas, in order to calibrate the temperature sensor. After scaling the measured T_{res} using Eq. (6.1) with $A = 0.97$, the no-buffer run matches the theory curve well. On the same day, I then filled the cell with 80.2 mbar of Kr, and performed a second run. The OD at first followed the theory curve given by T_{res} , however after reaching $T_{res} = 120^{\circ}\text{C}$ at $t = 120$ mins, the OD began to drop. After several hours, the OD stabilised at $OD = 0.21$. Repeating the run the next day, the OD followed a new trajectory, and only rose to $OD = 0.21$. The following day, having emptied the cell and then refilled with fresh buffer gas to the same pressure, the OD followed this same new trajectory, with almost no detectable signal for temperatures below 110°C .

On the first day in Figure 6.7.a, the Rb density in the cell is determined by three mechanisms: the flux of Rb coming from the Rb reservoir in the glass stem; the desorption of Rb from the cell walls; and Rb loss through some mechanism presumably involving the cell walls. In the no-buffer run, the flux of Rb from the reservoir is much higher than the other mechanisms, and the Rb density follows T_{res} . On introducing 80 mbar of Kr to the cell, however, the Rb flux through the cell channel is drastically reduced. The Rb density initially follows T_{cell} , until the Rb left on the walls from the previous no-buffer run is exhausted. The Rb density then drops to a new equilibrium value, given by the competition between the (low) flux of Rb from the reservoir, and the loss of Rb into the cell walls. There is no significant replenishment of Rb on the walls between the subsequent runs, and so both runs follow a new trajectory given by this second equilibrium condition. The separation of the Rb reservoir and cell means that the reduced OD cannot be explained by contamination of the Rb reservoir.

In order to cure the cells, I evacuated the cells and heated them to $\sim 140^\circ\text{C}$ for two weeks (with the cell valve closed). This accelerated the interaction of Rb with the cell walls, allowing a relatively stable, saturated regime to be reached. The process exhausted the supply of transferred Rb (see Figure E.4), and after the curing process I had to perform a second Rb transfer. Figure 6.7.b shows the cell behaviour after curing. The steady-state OD now approaches the value predicted by theory and T_{res} , and the behaviour is consistent between runs performed more than 6 months apart.

Discussion of Mechanisms

The loss of Rb into cell walls has been observed in many experiments. An early study of cell curing in coated cells found the Rb density was reduced by a factor of 1.2 through loss into the coated walls [3], and Rb consumption is a limiting factor in the lifetime of Rb rf discharge lamps, which are often used as the light source in Rb vapor cell clocks [7, 199–201]. Possible mechanisms include: chemical reactions with the glass or contaminants; adsorption into the glass; and the formation of a thin layer on top of the glass. Rb is considered lost or consumed when it is no longer in its elemental form. Note that the data in Figure 6.7 was taken before problems developed with the cell valve (Section 6.5.1).

Rb is highly reactive, and there is an initial consumption of Rb when it is first introduced to a cell, as it quickly reacts with available contaminants [199]. Curing is seen to increase the effectiveness of antirelaxation coatings, possibly through Rb chemical reactions removing contaminants from the coating [3, 147, 202].

In equilibrium, the walls in a vapor cell are coated with a thin layer of Rb, measured to be 6-7 monolayers at 94°C [148]. Molten Rb is a good solvent, and it is possible that this layer will leach O_2 out of the glass, forming a layer of (brown) Rb_2O . Such a Rb_2O surface layer has been observed in Rb discharge lamps [199]. In the cell used in Chapter 4, a semitransparent brown area appeared on the cell window, presumably due to a relatively thick layer of RbO_2 . The Rb also penetrates

into the glass substrate, forming Rb_2SiO_3 (rubidium silicate). Measurements of the penetration depth with and without the use of the discharge lamp rf coils (which create a plasma) show Rb to $1/e$ depths of $5\ \mu\text{m}$ and $15\ \mu\text{m}$, respectively [199]. In a more recent vapor cell measurement, Rb penetration into in cured quartz glass was observed to result in Rb comprising $0.5 - 4\%$ of the glass within the first 10 nm below the surface [198].

For several types of glass, the Rb loss in discharge lamps has been shown to be primarily due to Rb diffusion into the glass walls, with the loss following [199, 200]

$$C(t) = A + B\sqrt{t}, \quad (6.2)$$

where A is the relatively small and almost instantaneous loss of Rb due to chemical reactions that occurs when a lamp is first turned on, and $B = 0.1 - 1\ \mu\text{g}\ \text{hr}^{-1/2}$ represents loss due to diffusion into the glass [201]. This corresponds to a diffusion rate on the order of $D = 10^{-14}\ \text{cm}^2/\text{s}$ for the Corning 1720⁵ and Schott 8436 aluminosilicate glass typically used in discharge lamps [199]. We would expect the loss rate to be higher in our ultrathin cells: quartz glass, used in our ultrathin cells, is relatively permeable and we might expect a faster diffusion rate [203]; Rb penetration seems to be inhibited by the plasma in a Rb discharge lamp [199]; and our $130 - 150^\circ\text{C}$ operating temperatures are also above typical $70 - 120^\circ\text{C}$ discharge lamp operating temperatures [199, 204], which would likely accelerate our loss rate into uncured glass.

These Rb loss mechanisms generally result in consumption of 10s or 100s of μg of Rb. From the relative sizes of the 1 g Rb ampule and the Rb reservoir in the cell, I would not expect the Rb transferred to the cell to amount to much more than a mg, and it may be significantly less. It is not obvious that our curing or occasional complete consumption of Rb is explained by the above mechanisms, however. For example, the diffusive loss of Rb should not saturate; rather, consumption should continue essentially forever [199].

Several features of our setup may have made us particularly susceptible to Rb consumption: the relatively large surface to volume ratio in our cells; the (likely) small amount of Rb transferred to the cells; and the used of porous glass. The resulting problems can be solved by transferring a large amount of Rb, and by curing the cell at high temperature for several weeks. In future generations of the ultrathin cells, it may be advantageous to use Schott 8436 aluminosilicate glass instead of quartz, and to modify the cell geometry to give better conduction between the Rb reservoir and the cell chamber.

6.3 Exploring the Parameter Space

The operation of the ultrathin cells is dependent on a number of tunable parameters, in particular the operating temperature and the buffer gas species and density.

⁵No longer in production.

In this section, I present an analysis of the response of the cell to tuning these parameters.

6.3.1 Relaxation

The relaxation rates are calculated using the theory presented in Chapter 2, and the spatial resolution is calculated using Eq. (3.39). Only single-species buffer gas filling is considered (no buffer gas mixtures).

Figure 6.8 shows T_1 and T_2 , relaxation rates, and the spatial resolution for different buffer gas pressures and species. As P_{fill} rises, γ_{bg} rises, and D and γ_{walls} fall, as shown in Figure 6.8.b. With the exception of Xe, the reduction in γ_{walls} dominates for all buffer gases over the range of plotted pressures. High buffer gas pressures can even reduce γ_{walls} below the Rb-Rb SE relaxation rate. The result is longer T_1 and T_2 times as P_{fill} is increased, shown in Figure 6.8.a. However, the limit on P_{fill} is generally given by the optical broadening. Figure 6.8.c, which plots T_1 and T_2 against optical broadening, is therefore a fairer comparison of buffer gases. The performance of Ne can then be seen to be equivalent with N_2 and Ar, due to the balance between the different broadening and diffusion coefficients. However, in both Figure 6.8.a and c, the best T_1 and T_2 times are clearly given by Kr.

Figure 6.8.d shows that the best spatial resolution is given by Xe, which has the lowest diffusion constant of the considered buffer gases. The use of Xe is precluded by its strong γ_{bg} relaxation though. Kr gives a similar spatial resolution, without the strong relaxation induced by Xe.

Figure 6.9 shows T_1 , T_2 , and relaxation rates as a function of cell temperature. There are two regimes, with γ_{walls} dominating at low temperatures, and γ_{SE} dominating at high temperatures. The strong temperature dependence of γ_{SE} is driven by the temperature dependence of the Rb vapor density, as seen in Figure 2.2. All of the relaxation rates increase with temperature, and so T_1 and T_2 decrease with temperature in both regimes. As SE comes to dominate, T_2 becomes longer than T_1 , as T_2 SE relaxation is approximately a factor of 5/8 slower than T_1 relaxation⁶.

Figure 6.10 shows T_1 , T_2 as a function of cell thickness. For very thin cells, γ_{walls} dominates, and T_1 and T_2 are equal. As the cell thickness is increased, γ_{walls} decreases, leaving γ_{SE} as the dominant relaxation mechanism. The T_1 and T_2 times then split up according to the slower T_2 SE relaxation. The exception is Xe, for which γ_{bg} relaxation dominates T_2 and contributes to T_1 . The figure also highlights the sensitivity to uncertainty in the cell thickness.

The best buffer gas under all conditions in the ultrathin cells is Kr, as seen in Figures 6.8-6.10. This is because of the strong need to suppress wall relaxation in such thin cells, and so the need for a low diffusion constant, and is despite the fact that Kr induces γ_{bg} relaxation 5 – 100 times more strongly than the lighter buffer gases commonly used in atomic clocks (Ne, N_2 , Ar). Although the diffusion constant of Xe is slightly lower than for Kr, its relaxation cross sections are two

⁶Strictly speaking, this is true for the ^{87}Rb clock transition with complete depopulation of one of the hyperfine ground states. See Section 2.7.2).

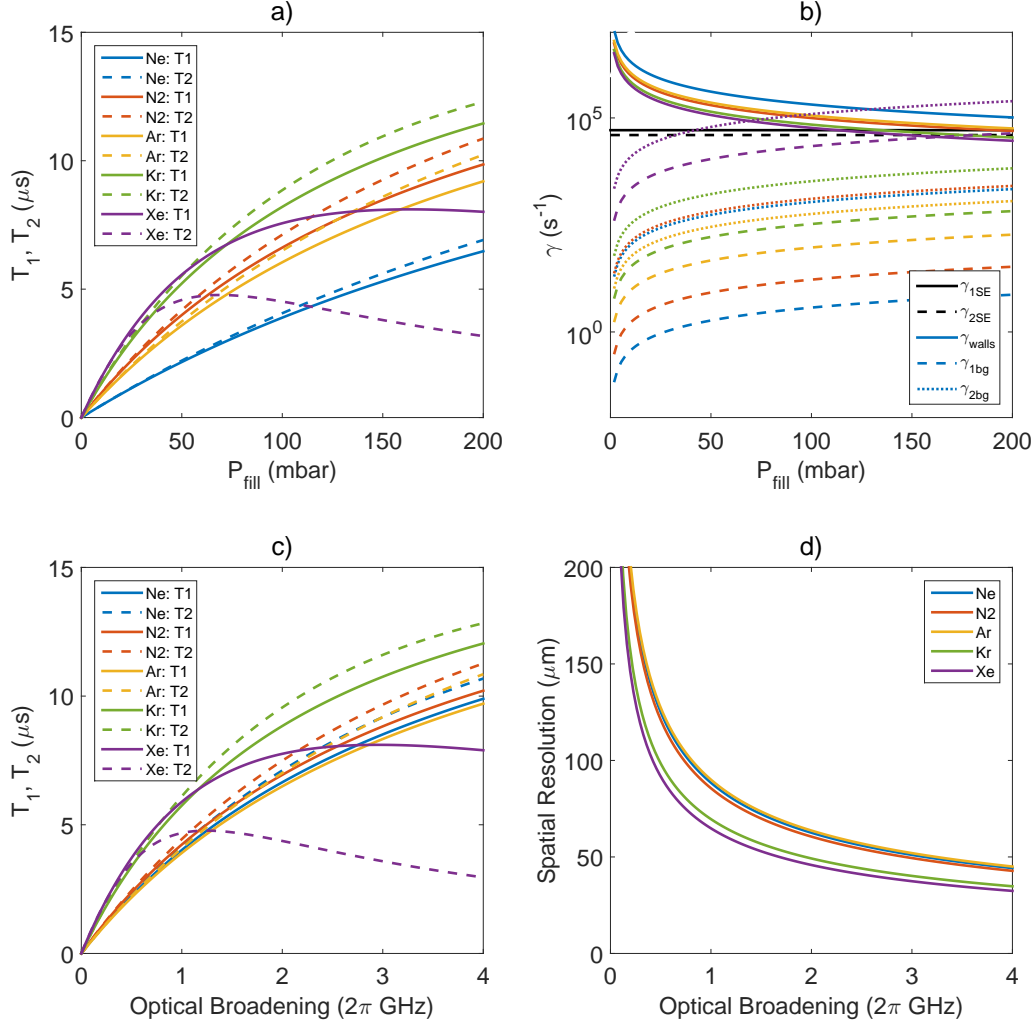


Figure 6.8: Cell parameters scanning the buffer gas filling pressure for a range of common buffer gases, in a $140 \mu\text{m}$ thick cell at $T = 140^\circ\text{C}$. a) T_1 and T_2 times and b) relaxation rates as a function of P_{fill} ; c) T_1 and T_2 times as a function of buffer gas induced optical broadening, which is the limiting factor for the buffer gas pressure; d) spatial resolution for an imaging time of $dt_{\text{image}} = 10 \mu\text{s}$, again as a function of optical broadening.

orders of magnitude higher, and disqualify Xe for our purposes. In order to limit radiation trapping, we also need some N₂ in the cell, and so the optimal cell filling is with a mixture of Kr and N₂.

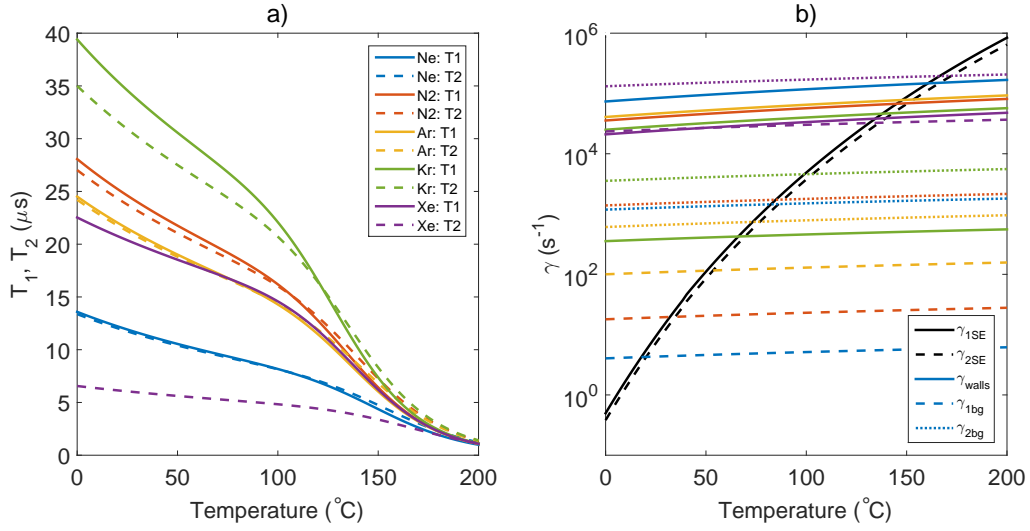


Figure 6.9: a) T_1 and T_2 times and b) relaxation rates as a function of cell temperature for a range of common buffer gases. The buffer gas pressure is $P_{\text{fill}} = 150$ mbar, and the cell thickness is $140 \mu\text{m}$.

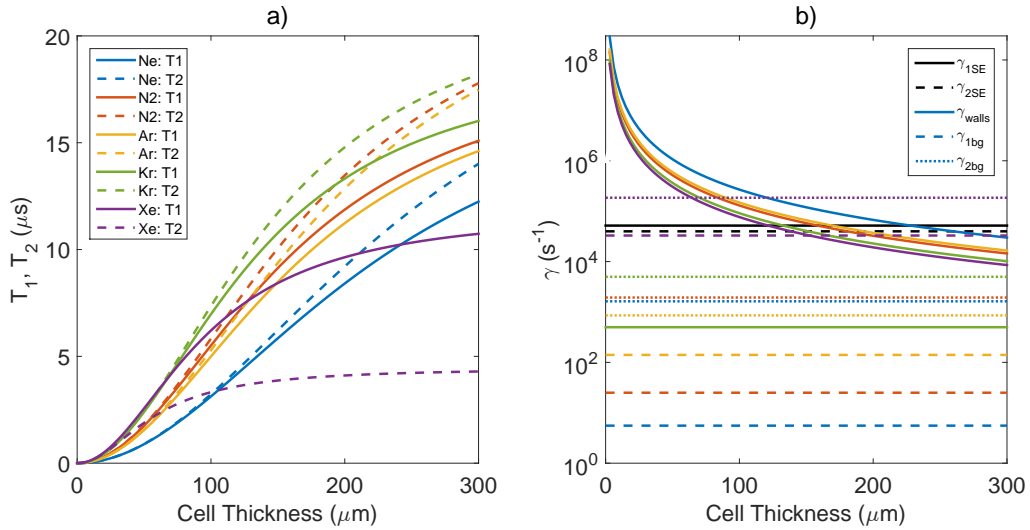


Figure 6.10: a) T_1 and T_2 times and b) relaxation rates as a function of cell thickness for a range of common buffer gases. The buffer gas pressure is $P_{\text{fill}} = 150$ mbar, and the cell temperature is 140°C .

6.3.2 Optical Response

Figure 6.11 shows calculated optical absorption spectra in cell U1 at $T = 140^{\circ}\text{C}$ for various Kr filling pressures. The Kr shifts and broadens the optical lines, obscuring the ^{87}Rb signal with ^{85}Rb absorption, and reducing the on-resonance OD. This

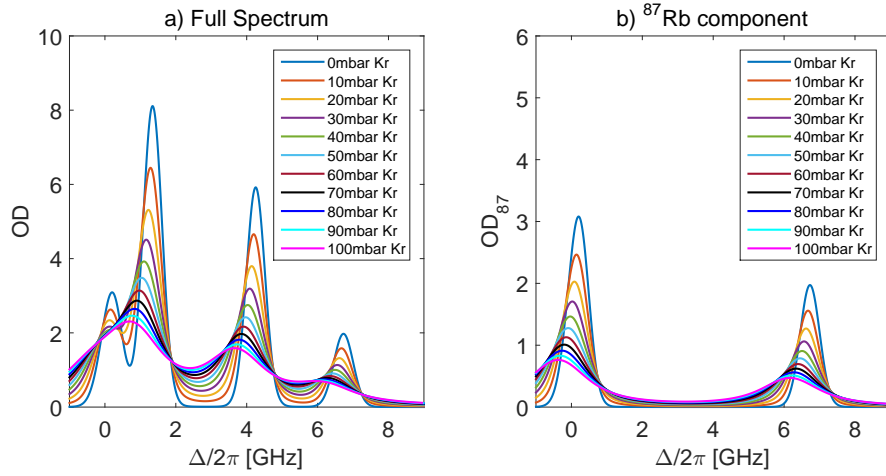


Figure 6.11: Absorption spectra for various Kr pressures, calculated for the $140\ \mu\text{m}$ thick cell at 140°C . a) The entire natural-Rb absorption spectrum. b) The ^{87}Rb component of the spectrum. As the buffer pressure increases, the line shifts and broadens, and the on-resonance OD decreases.

places an upper limit on the allowable buffer gas pressure in order to have a given absorption signal strength.

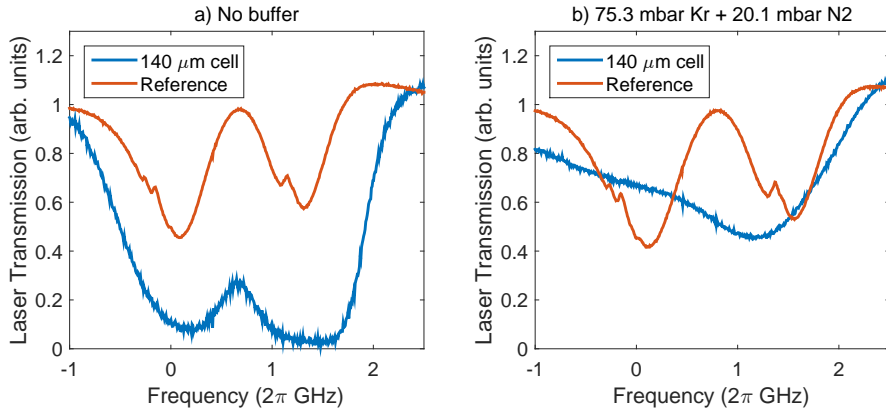


Figure 6.12: Example experimentally obtained absorption profiles using the U1 cell, with the following parameters: a) No buffer gas, $T_{res} = 144^\circ\text{C}$ and $T_{cell} = 158^\circ\text{C}$; b) Cell filled with 75.3 mbar Kr and 20.1 mbar N_2 , $T_{res} = 126.4^\circ\text{C}$ and $T_{cell} = 144^\circ\text{C}$.

Examples of measured absorption spectra are shown in Figure 6.12. The spectra are taken with no buffer gas, in Figure 6.12.a, and a mixture of 75.3 mbar Kr and 20.1 mbar N_2 in Figure 6.12.b. The spectra are compared with the saturated absorption spectroscopy of an enriched ^{87}Rb cell, at room temperature and without buffer gas.

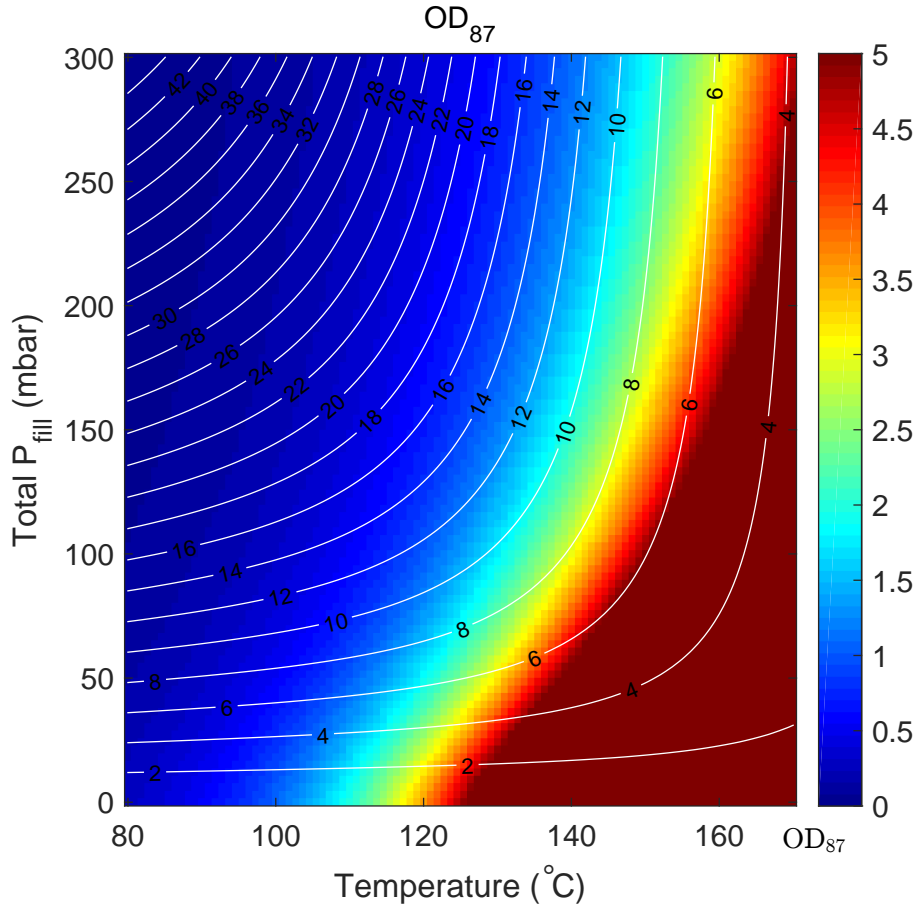


Figure 6.13: OD_{87} (colourmap) and T_1 (contour lines, units μs) as a function of temperature and buffer gas pressure in the $140 \mu m$ thick cell, for a laser resonant with the centre of the shifted ^{87}Rb $F = 2 \rightarrow F' = 2$ peak. The buffer gas pressure is plotted as the sum of Kr and N_2 pressures, assuming a 3 : 1 pressure ratio. For high temperatures, the T_1 rapidly decreases with temperature, as Rb-Rb spin exchange collisions come to dominate relaxation.

Figure 6.13 is a map of OD_{87} and T_1 as a function of temperature and buffer gas pressure. The calculations are performed for the U1 cell, filled with Kr and N_2 in a 3:1 mixture. The figure highlights the competition between signal strength, OD_{87} , and relaxation lifetime, T_1 . OD_{87} increases with temperature and decreases with buffer gas pressure, while T_1 decreases with temperature and increases with buffer gas pressure. For high temperatures, there is very little return in increasing the buffer gas pressure, as the relaxation rate is largely determined by Rb-Rb SE relaxation.

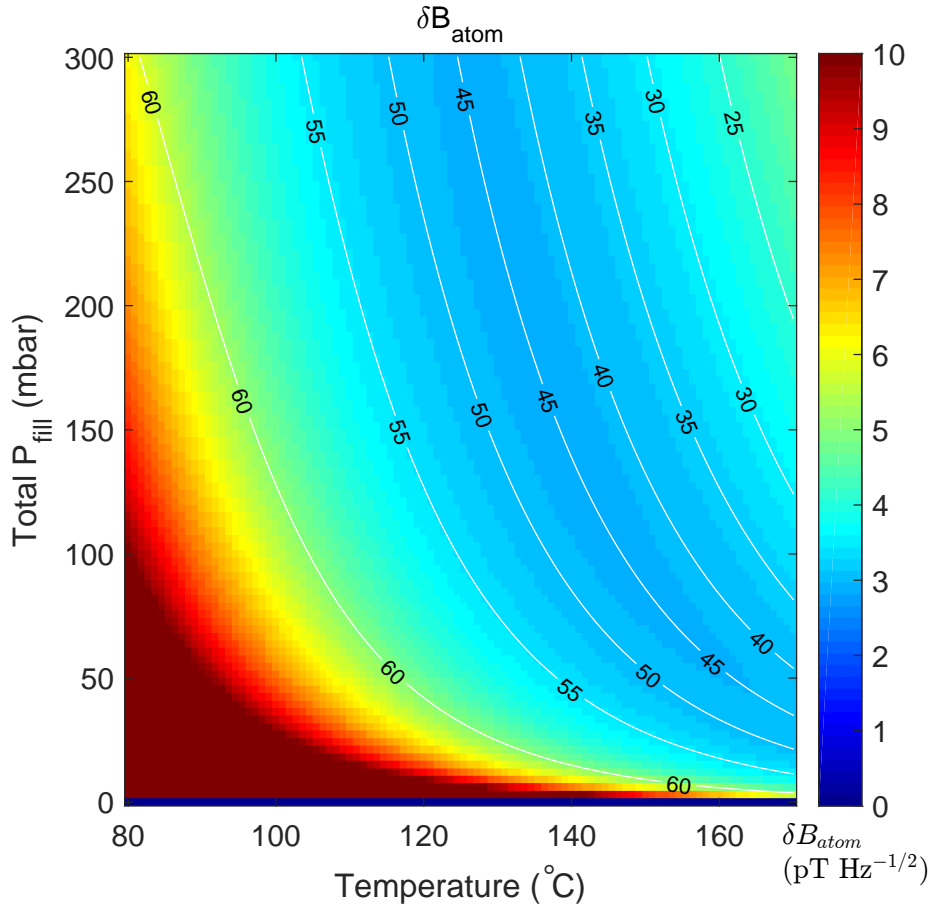


Figure 6.14: Atomic projection noise limited sensitivity (colourmap) and spatial resolution (contour lines, units μm) as a function of temperature and buffer gas pressure in the $140\ \mu\text{m}$ thick cell. The laser is resonant with the centre of the shifted ^{87}Rb $F = 2 \rightarrow F' = 2$ transition. The buffer gas pressure is plotted as the sum of Kr and N_2 pressures, assuming a 3 : 1 pressure ratio.

6.3.3 Sensitivity and Spatial Resolution

We can apply the models presented in Section 3.4, to estimate the sensitivity and spatial resolution for imaging microwave magnetic fields. Calculations are performed for imaging on the $i = 4$ transition, with optical pumping and probing on the ^{87}Rb $F = 2 \rightarrow F'$ D_2 line. We recall the atomic projection noise limited sensitivity,

$$\delta B_{atom} = \frac{\hbar}{\mu_B} \frac{1}{\sqrt{N_{at} \tau_2 T_{meas}}}, \quad (6.3)$$

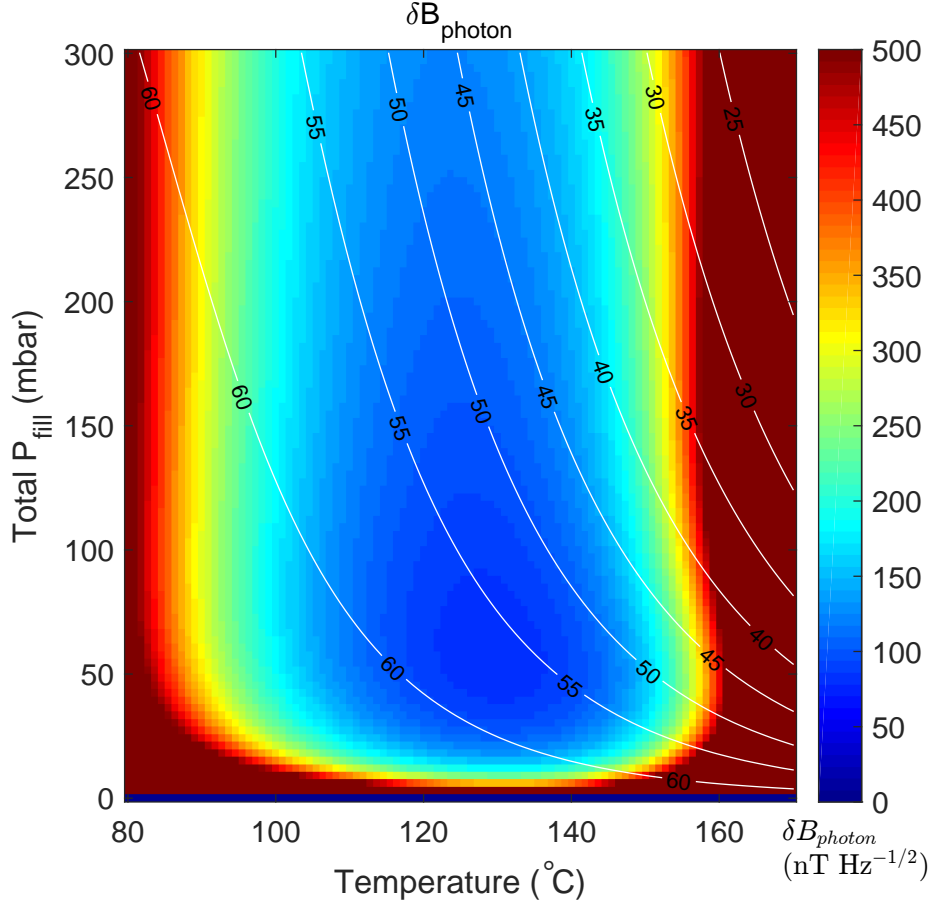


Figure 6.15: Photon shot noise limited sensitivity (colourmap) and spatial resolution (contour lines, units μm) as a function of temperature and buffer gas pressure in the $140\ \mu\text{m}$ thick cell. The laser is resonant with the centre of the shifted ^{87}Rb $F = 2 \rightarrow F' = 2$ transition. The buffer gas pressure is plotted as the sum of Kr and N_2 pressures, assuming a 3 : 1 pressure ratio.

and the photon shot noise limited sensitivity,

$$\delta B_{\text{photon}} = \sqrt{\frac{dt_{\text{run}}}{N_{\text{shots}}}} \frac{2}{dt_{\text{mw}}} \frac{\hbar}{\mu_B} \frac{OD_{\text{min}}}{OD_{\text{mw}}^{\text{max}}} \exp(dt_{\text{mw}}/\tau_2), \quad (6.4)$$

where $OD_{\text{mw}}^{\text{max}} = \frac{1}{3}OD_{87}$ and $OD_{\text{min}} = \sqrt{2}[Q I_{\text{probe}} e^{-OD} A dt_{\text{probe}}/(\hbar\omega_L)]^{-1/2}$. The spatial resolution is estimated by

$$\Delta x = \sqrt{2Ddt_{\text{mw}}}. \quad (6.5)$$

This definition of spatial resolution provides the resolution for the optimised sensitivity parameters, where $dt_{\text{mw}} = \tau_2$. One should keep in mind, however, that the

definition is not optimal for examining the change in spatial resolution with temperature and pressure. If τ_2 is reduced but not D , such as through the increase in SE relaxation with temperature, then the spatial resolution will appear to improve, even though there would be little change in Δx for a given fixed value of dt_{mw} .

Figure 6.14 shows spatial resolution and δB_{atom} in a 140 μm cell as a function of temperature and buffer gas pressure; Figure 6.15 shows the same for δB_{photon} . The model parameters are: $T_{meas} = 1$ s, $Q = 0.27$, $I_{probe} = 30$ mW/cm², $dt_{probe} = 0.3$ μs , $A = 2DT_1$, $N_{shots} = 150$, $dt_{run} = 30$ s, and $dt_{mw} = \tau_2$. I used $\tau_2 = T_1$, due to the relative simplicity and reliability of the T_1 calculation, and their approximately equal experimental values (at least for the conditions used in Chapter 7). The laser is resonant with the centre of the shifted ⁸⁷Rb $F = 2 \rightarrow F' = 2$ transition. The cell is filled with Kr and N₂ buffer gas, in a 3:1 ratio and with $T_{fill} = 22^\circ\text{C}$. Parameters such as N_{atom} , T_1 , and the OD are calculated using the models presented in Chapter 2. These parameters match with those used for Figure 6.13.

The optimisation of δB_{atom} is a balance between maximising N_{atom} and minimising relaxation. Figure 6.14 shows that for low temperatures, δB_{atom} improves with increasing temperature, as N_{atom} increases. At higher temperatures, δB_{atom} is degraded by the reduction of T_1 (and thus τ_2) due to SE relaxation. The change in relaxation with buffer gas pressure also plays a minor role. δB_{atom} is optimised over a broad line to give $\delta B_{atom}^{optimal} = 3$ pT Hz^{-1/2}, corresponding to a spatial resolution of $\Delta x = 45$ μm .

Figure 6.15 shows that δB_{photon} has a similar temperature response, with δB_{photon} improving with temperature at low temperatures, but degrading with temperature as SE relaxation comes to dominate. δB_{photon} is more strongly dependent on τ_2 than δB_{atom} , and for low buffer gas pressures, δB_{photon} improves with increasing pressure due to the suppression of wall relaxation. δB_{photon} degrades at higher buffer gas pressures, due to the reduction of OD with buffer gas broadening. An optimal value of $\delta B_{photon}^{optimal} = 80$ nT Hz^{-1/2} is reached for $T = 130^\circ\text{C}$ and $P_{fill} = 60$ mbar, corresponding to a spatial resolution of $\Delta x = 57$ μm , $OD_{87} = 0.7$, $OD = 1.2$, and $T_1 = 6.8$ μs .

We can perform similar analyses for cells filled with pure ⁸⁷Rb or for 200 μm thick cells. The results are presented in Table 6.1.

6.4 Optical Pumping and Relaxation

6.4.1 Modelling Optical Pumping and Relaxation with the Diffusion Equation

Following the theory used in Chapter 4, we can use the diffusion equation to model optical pumping and relaxation in the ultrathin cells, which are well-suited to a 1D treatment. The diffusion equation is essentially the 1D version of Eq. (4.4),

$$\frac{\partial}{\partial t}u(z, t) = D\frac{\partial^2 u}{\partial z^2} - (\gamma_1 + \Gamma_p)u(z, t) + \Gamma_p, \quad (6.6)$$

where Γ_P is the optical pumping rate, γ_1 is the T_1 relaxation rate, and z is the position between the cell walls (the front and back windows), which are at $z = 0$ and $z = d$. The steady state solution gives the distribution of optical pumping across the cell,

$$u_0(z) = A \exp(\mu z) + B \exp(-\mu z) + u_\infty, \quad (6.7)$$

where $u_\infty = \Gamma_P/(\Gamma_P + \gamma_1)$ and $\mu = \sqrt{(\Gamma_P + \gamma_1)/D}$, as in Chapter 4. The constants A and B are determined by the boundary conditions,

$$\begin{aligned} \frac{\partial u}{\partial z} \Big|_{z=0} - \frac{\epsilon/2}{(1 - \epsilon/2)L} u(0) &= 0, \\ \frac{\partial u}{\partial z} \Big|_{z=d} + \frac{\epsilon/2}{(1 - \epsilon/2)L} u(d) &= 0, \end{aligned} \quad (6.8)$$

where again $L = \frac{2}{3}\lambda$, where λ is the Rb mean free path. Applying the boundary conditions to Eq. (6.6) yields

$$\begin{aligned} A &= S u_\infty \frac{\mu + S + (\mu - S) \exp(-\mu d)}{(\mu + S)^2 - (\mu - S)^2 \exp(-\mu d)}, \\ B &= \frac{A(\mu - S) - S u_\infty}{\mu + S}, \end{aligned} \quad (6.9)$$

where

$$S \equiv \frac{\epsilon/2}{(1 - \epsilon/2)L}, \quad (6.10)$$

and ϵ is again the wall collision depolarisation probability. We can obtain the T_1 time in the cell by again setting $\Gamma_p = 0$ at $t \geq 0$ and numerically solving Eq. (6.6) with the initial condition Eq. (6.7) and the boundary conditions given in Eqs. (6.8). The T_1 time is again the $1/e$ decay rate given by Eq. (4.11).

Figure 6.16 shows the optical pumping efficiency and T_1 time along z , in cells of varying thickness. The modelling is performed for the conditions presented in Table 2.7. In addition, I have used $\Gamma_P = 10^6 \text{ s}^{-1}$ and $\epsilon = 1$. The modelling is presented for a range of cell thicknesses. This demonstrates the effect of the uncertainty in the cell thicknesses, and also the differences between the $100 \mu\text{m}$ and $200 \mu\text{m}$ thick cells.

The dashed lines in Figure 6.16 show the limits of optical pumping efficiency and T_1 imposed by SE and buffer gas relaxation. The lines are given by $u_\infty = \Gamma_P/(\Gamma_P + \gamma_{1SE} + \gamma_{1bg}) = 0.95$ and $T_1^\infty = (\gamma_{1SE} + \gamma_{1bg})^{-1} = 19.1 \mu\text{s}$, respectively, using the values of γ_{1SE} and γ_{1bg} listed in Table 2.7. The dotted lines include wall relaxation in a $140 \mu\text{m}$ cell, assuming it is described by the lowest order diffusion mode, as in Eq. (2.71). The dotted lines are given by $u_\infty^{avg} = \Gamma_P/(\Gamma_P + \gamma_1) = 0.89$ and $T_1^{avg} = \gamma_1^{-1} = 7.9 \mu\text{s}$, using the γ_1 listed in Table 2.7. Comparison with the $140 \mu\text{m}$ cell u_0 and T_1 multimode diffusion curves show that the dotted lines are approximate averages of the multimode curves.

The cell thickness and diffusion constant are only sufficient to form a cell-bulk region in the thicker cells, where the central atoms are sufficiently separated from

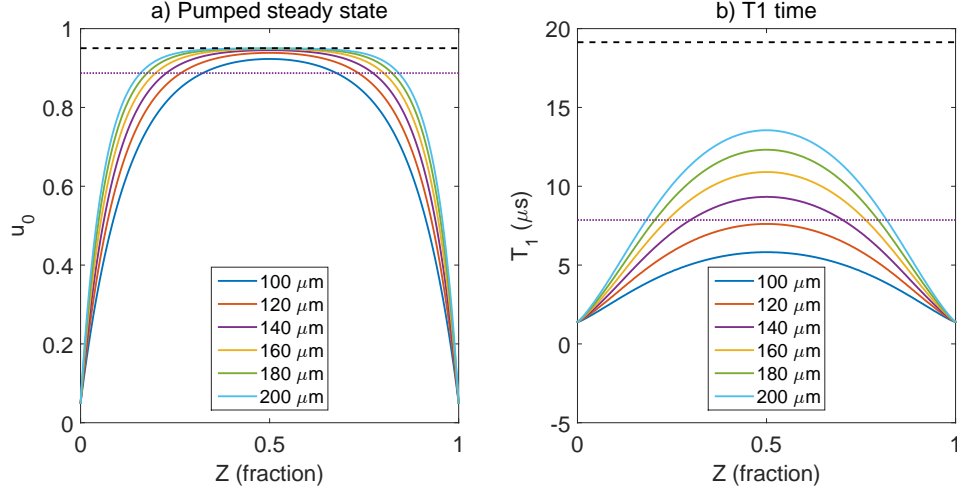


Figure 6.16: Calculated a) optical pumping efficiency and b) T_1 time in a 1D slice through cells of various thickness. $z = 0$ and $z = 1$ correspond to the front and back cell windows. The black dashed lines in (a) and (b) correspond to u_∞ and T_1 calculated considering only bulk relaxation mechanisms (ie SE and buffer gas relaxation). The dotted purple lines include the wall relaxation rate for a $140 \mu\text{m}$ cell, assuming only lowest-order diffusion.

the walls so that they do not interact with the walls. Despite using $\epsilon = 1$, $u_0 \neq 0$ at the walls, due to the flux of polarised atoms diffusing in from the cell bulk. This flux also results in a nonzero T_1 at the walls.

6.4.2 Characterisation of Optical Pumping

I performed a series of characterisation measurements on the optical pumping of the cured U1 cell, shortly after taking the data presented in Figure 6.7.b. I used two techniques for the characterisation measurements. In the first, I looked at the change in absorption of a probe beam immediately after an optical pumping beam is turned on, obtaining the change in OD induced by optical pumping, ΔOD_{pump} , and the optical pumping rate, Γ_P . I called this an OPR (optical pumping rate) sequence. In the second measurement, I used a Franzen sequence (see section 3.2.2) to measure ΔOD_{pump} and also the T_1 time. Franzen measurements are insensitive to optical pumping from the probe beam, and are thus the better way to measure ΔOD_{pump} . I found that for a sufficiently weak probe beam, both OPR and Franzen measurements did yield similar results.

Figure 6.17 shows example data from each of the OPR and Franzen characterisation sequences. The experiment parameters are runs 1 and 2 in Table 6.2. With similar pump beam intensities and a weak probe beam intensity of $I_{probe} = 0.56 \text{ mW/cm}^2$, the OPR and Franzen methods yield similar optical pumping values,

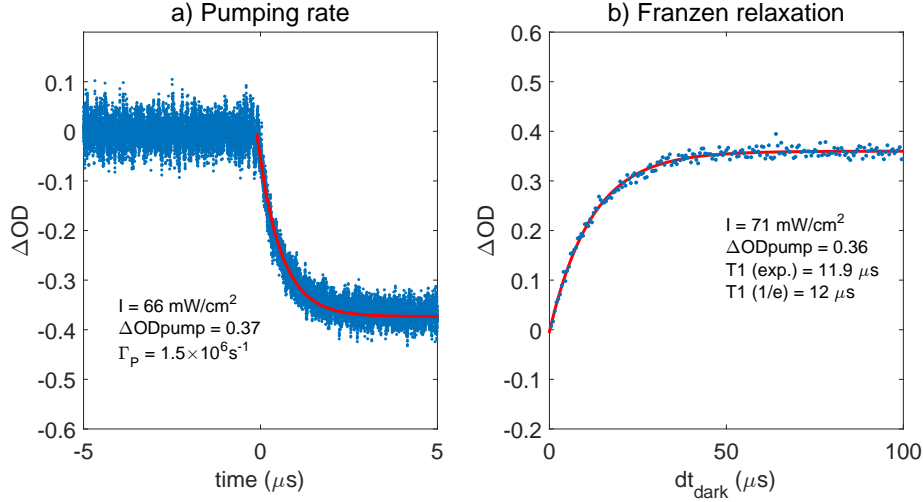


Figure 6.17: Example data for the two measurement types used to characterise optical pumping in the $100 \mu\text{m}$ cell. Data is shown in blue, and fitted curves in red. The text gives the optical pumping intensity, I_{pump} , as well as values extracted from the fitting.

of $\Delta OD_{\text{pump}} = 0.37$ and $\Delta OD_{\text{pump}} = 0.38$, respectively. I assumed $\Gamma_{P87} \approx \Gamma_{P85}$ (see Eq. (2.32)), and fit the OPR data with a single exponential,

$$\Delta OD = -\Delta OD_{\text{pump}}(1 - \exp[-\Gamma_P t]), \quad (6.11)$$

where ΔOD_{pump} and Γ_P are fit parameters. ΔOD_{pump} is the change in OD induced by optical pumping, Γ_P is the optical pumping rate, and A is a fit constant. Eq. (6.11) is equivalent to Eq. (2.18), which describes the response of the ground state populations to optical pumping, derived from a 3-level model. The Franzen data was fit with the equation

$$\Delta OD = A - \Delta OD_{\text{pump}} \exp[-t/T_1], \quad (6.12)$$

where ΔOD_{pump} , T_1 , and A are fit parameters. The data could also be fit using the $1/e$ fitting described in Section 4.4.

Low Optical Pumping Efficiency

Figure 6.18 shows Γ_P and the optical pumping efficiency, u_0 , as a function of pump laser intensity, I_{pump} . The experimental parameters are listed in Table 6.2. The optical pumping efficiency was calculated as $u_0 = \Delta OD_{\text{pump}}/OD$, equivalent to the definition used in section 2.4.1. The two striking features are the large variation between data sets, and the low optical pumping efficiency. The saturation of u_0 requires 10s of mW/cm^2 of pumping intensity, and gives u_0 values around 0.3, but with variation from 0.15 to 0.6. In the model presented in section 2.4.1, the total

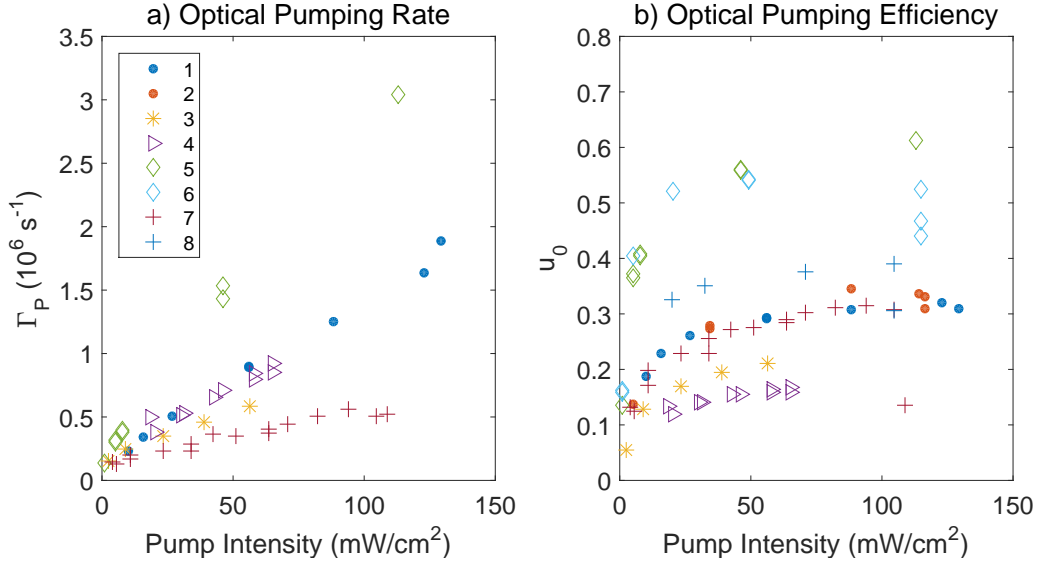


Figure 6.18: Optical pumping rate, Γ_P , and efficiency, u_0 , as a function of optical pumping power, for two different pumping lasers. The experimental parameters are listed in Table 6.2.

saturated pumping efficiency was $u_0 = 0.75$ and the ^{87}Rb efficiency was $u_0^{87} = 0.85$. The data sets were taken with a range of beam sizes, beam intensities, and temperatures. Runs 5 and 6 were performed using a loaned TA Pro laser for optical pumping⁷.

Much of the scatter in Figure 6.18 is likely to be due to the difficulty in accurately measuring I_{pump} and the OD. At the point of taking this data, there was a significant amount of residue built up on the cell windows (this is discussed further in Appendix F). This created large OD background in the cell which had to be accounted for when measuring the Rb OD, and partially blocked the optical pumping beam. The residue build-up was non-uniform across the cell, and increasing in time, resulting in a baseline OD ranging over $OD_{cell} = 0.2 - 0.6$. The data sets are internally consistent, in that if we plot u_0 against $u_\infty = \Gamma_P / (\Gamma_P + \gamma_1)$, we find that $u_0 \propto u_\infty$, with the proportionality constant different for each data set.

Γ_P is reasonably consistent between runs 1 – 4, and the variation in u_0 between the runs is likely to be due to the variations in I_{probe} . Runs 3 and 4 used probe intensities large enough to cause significant optical pumping on their own, which would then have reduced the observed ΔOD_{pump} and thus u_0 .

The large beams used in runs 5 and 6 may have been clipped on the powermeter, resulting in an underestimation of I_{pump} . Moreover, since $r_{probe} \ll r_{pump}$ in runs 5 and 6, we may have only probed the centre of the pumped region, where the Gaussian pump beam profile gave large Γ_P and u_0 . The changes in the pump and

⁷Toptica, 2 W TAPro tapered amplifier laser

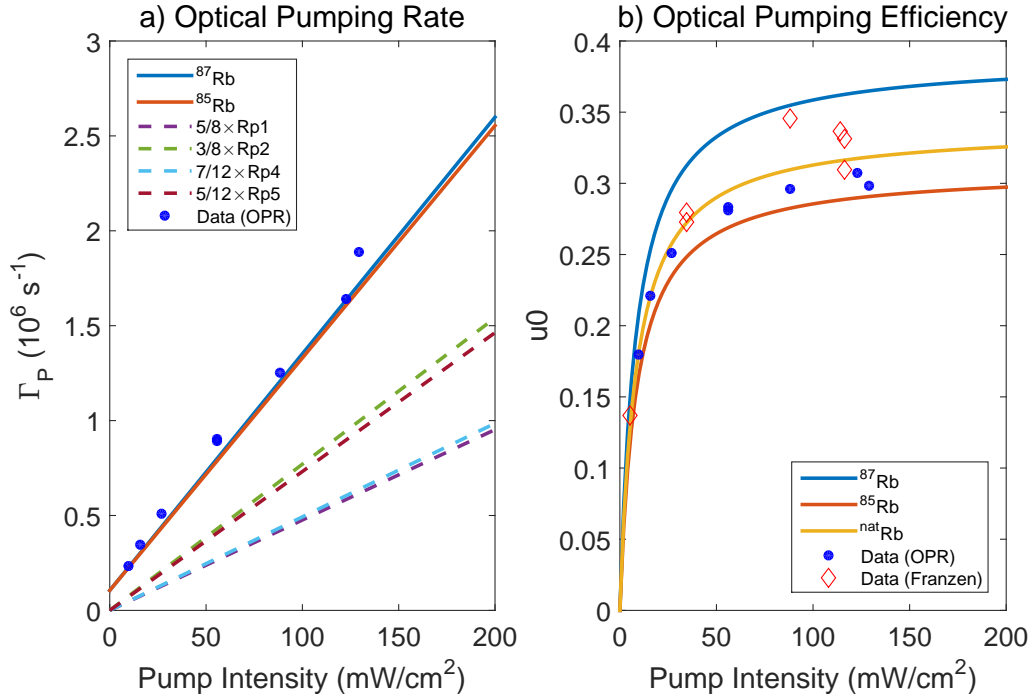


Figure 6.19: Comparison of data sets 1 and 2 (see Table 6.2) with the optical pumping model presented in section 2.4.1. The model has been fit (by hand) to the data by tuning a radiation trapping parameter (see text).

probe beam sizes seem to have minimal influence on optical pumping with the IF laser, however. The insensitivity to beam size on a millimeter scale matches with what we would expect from the diffusion speeds in the cell, where $D \approx 1.6 \text{ cm}^2/\text{s}$.

Both Γ_P and u_0 are substantially higher when using the TAPro laser. It is unclear exactly why this is. Some possible reasons have been discussed above, but a definitive answer is not possible without retaking the data under more controlled conditions. It is also possible that the difference is due to properties of the lasers themselves, rather than calibration errors or differences in experiment parameters. Despite the possibly superior nature of the TAPro laser, I kept using the IF-laser for optical pumping. Aside from the considerable cost and ordering time associated with ordering a new TAPro (I was borrowing the one used here), I found that the IF-laser was sufficient for use in imaging, as seen in Chapter 7. Figure 6.18 indicates that an investigation of alternative pumping lasers would be of interest when designing a next-generation, optimised setup though.

Comparison with the Optical Pumping Model

Figure 6.19 compares the data from runs 1 and 2 in Table 6.2 with the optical pumping model presented in section 2.4.1. Runs 1 and 2 were chosen because of

their self-consistency and weak probe beam. The model parameters were calculated using the theory presented in Chapter 2, for a 140 μm thick cell, filled with $P_{fill} = 80.4$ mbar of Kr, and operated at $T = 126^\circ\text{C}$. The laser, locked to the $F = 2 \rightarrow F' = 2/3$ crossover peak, was detuned by $\omega_{shift} = -2\pi \times 444$ MHz from the level $|2\rangle$ resonance. This gave $\gamma_1 = 1.05 \times 10^5 \text{ s}^{-1}$, $\Gamma^* = \Delta\omega_{broad} = 2\pi \times 2$ GHz, and unpumped ODs of $OD = 0.90$, $OD_{87} = 0.34$, and $OD_{85} = 0.56$. I included radiation trapping in the model by introducing light that was resonant with levels $|1\rangle$, $|4\rangle$, and $|5\rangle$. The intensities of the 3 new frequencies were fit by hand to the data, to give $I_{1,4,5} = 0.16 \times I_2$, where I_2 was the input laser intensity. The optical excitation rates were then given by the sum of the excitation driven by each of the four optical frequencies,

$$R_{P\alpha}^{total} = \sum_n R_{P\alpha}(\omega_n), \quad (6.13)$$

where ω_n is the angular optical frequency, $n = 1, 2, 4, 5$, and $R_{P\alpha}$ is the optical excitation rate due to a single optical frequency, given by Eq. (2.24). Figure 6.19 shows that the apparently low optical pumping efficiency can be explained by a combination of radiation trapping, the presence of ^{85}Rb , optical broadening, and the detuning of the laser from the collisionally shifted ^{87}Rb line.

6.4.3 Optical Pumping During Imaging Experiments

The data presented in Chapter 7 was taken with a broad range of buffer gas pressures, due to a leak in the cell valve that had developed by that time. The leak is discussed further in section 6.5.1. We can examine this inadvertent scan of buffer gas pressure to further characterise optical pumping in the ultrathin cells, as presented in Figure 6.20.

Each run gave experimentally measured values of ΔOD_{pump}^{exp} and T_1 . The T_1 time was obtained from the reference image, which was taken using a Franzen sequence. In some cases I also measured the OD (OD^{exp}), and could directly calculate the optical pumping efficiency, $u_0^{exp} = \Delta OD_{pump}^{exp} / OD^{exp}$. However, the time constraints imposed by buffer gas loss over the course of a day meant that I generally performed the B_{mw} imaging without measuring the OD, and I had to extract the OD from the measured temperature, T_{stem} , and T_1 times. The extraction involved first fitting the buffer gas pressure, P_{fill}^{calc} , to the observed T_1 and then using the extracted P_{fill}^{calc} to calculate OD^{calc} . I assumed that Kr and N_2 were present in a 3:1 ratio. I could then use the extracted OD^{calc} and measured ΔOD_{pump}^{exp} to give $u_0^{calc} = \Delta OD_{pump}^{exp} / OD^{calc}$. This is obviously a process subject to a degree of error, driven primarily by uncertainties in the temperature and cell thickness, and the u_0^{calc} values in Figure 6.20 can be seen to be lower than u_0^{exp} , due to an overestimation of OD^{calc} . The u_0^{calc} / u_0^{exp} ratio appears reasonably constant, however, and the u_0^{calc} values are useful because they are available for every run.

I could also model optical pumping, using the model presented in Chapter 2, modified to include radiation trapping as described in section 6.4.2. For each experimental data point, I used the extracted OD^{calc} and P_{fill}^{calc} as input parame-

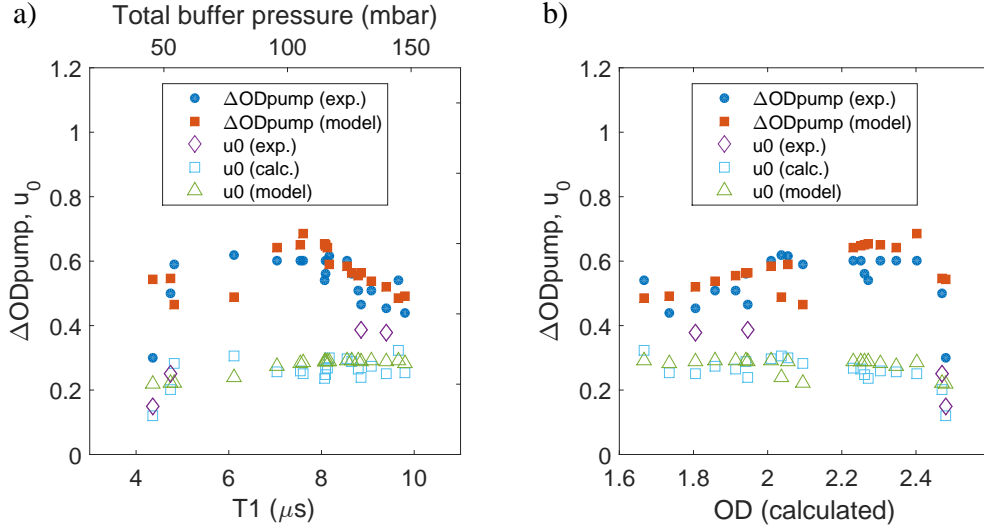


Figure 6.20: Optical pumping in the U1 cell as a function of a) measured T_1 and b) extracted OD^{calc} . The top axis of (a) gives an estimate of the total buffer pressure, based on the measured T_1 and assuming a 3:1 mixture of Kr and N_2 . See text for details.

ters to obtain values of u_0^{model} and ΔOD_{pump}^{model} . I used a representative value of $I_{pump} = 120 \text{ mW/cm}^2$ for the optical pumping intensity, which is well within the saturated pumping regime seen in Figure 6.18. I used the measured values for the hyperfine relaxation rate, $\gamma_1 = 1/T_1$, and the measured cell temperatures, which were in a range $T_{res} = (141.5 \pm 2)^\circ\text{C}$. For radiation trapping, I used $I_{1,4,5} = 0.2 \times I_2$. Despite the presence of N_2 , this is similar to the value of $0.16 \times I_2$ found for the pure Kr filling in Figure 6.20. This could be explained by the much higher cell temperature used for the Figure 6.20 data, $T_{res} = (141.5 \pm 2)^\circ\text{C}$ compared to $T_{res} = 124.5^\circ\text{C}$, giving a higher OD and stronger radiation trapping.

Figure 6.20.a plots ΔOD_{pump} and u_0 values against the measured T_1 , whilst Figure 6.20.b plots the same values against OD^{calc} . Due to variations in buffer gas pressure, the T_1 times vary from 4 μs to 10 μs . This corresponds to buffer gas pressures in a range of 50-100 mbar, as illustrated in the top axis of Figure 6.20.a. The measured optical pumping efficiency reaches $u_0^{exp} = 0.38$, slightly higher than the $u_0^{exp} \approx 0.3$ seen in Figure 6.19. There is a dip in u_0 for low T_1 times and high OD^{calc} (low T_1 corresponds to low P_{fill} , and thus low optical broadening and high OD). Although not reproduced by the model, this drop in u_0 is likely to be due to pumping being inhibited by stronger wall relaxation. The flat nature of u_0 outside of the low- T_1 region is reproduced in the model, and likely explained by the varying OD contributions from ^{87}Rb and ^{85}Rb with buffer gas pressure.

The agreement between measured, calculated and modelled values in Figure 6.20 demonstrates again that the low optical pumping efficiency can be explained by a

combination of radiation trapping, the presence of ^{85}Rb , optical broadening, and the detuning of the laser from the collisionally shifted ^{87}Rb line.

6.5 Discussion of Setup and Possible Improvements

6.5.1 Cell Valve Leak

After some months of operation, the U1 cell began developing a leak. This gradually worsened to the point that the cell was losing several mbar of buffer gas per hour. At the end of a day, the buffer gas pressure was unusably low, and the cell had to be refilled at the start of each day. This was a time-consuming process, as the buffer gas transfer needed to be performed at room temperature, and heating the oven up each morning took 2-3 hours.

The leak was due to the Viton O-ring used to seal the cell valve. Photos of the degraded o-ring and valve are shown in Appendix E.6. The O-ring was most likely attacked by the highly reactive Rb. Reactions with Rb are a bigger problem in vapor cells than cold atom experiments, as the high temperatures result in large Rb densities in all of the vacuum system, not just at the position of the trap. Materials that may be compatible with cold atom experiments are therefore not necessarily appropriate for vapor cells⁸. I was also operating close to (or possibly above) the 150°C recommended long-term operation limit for a Viton seal.

The Rb loss during this period was also extremely high, and I had to perform a new transfer of Rb from the ampule every two weeks. I was able to operate the cell for several months before the valve seal degraded and started leaking. If you know what you are doing, this is a lifetime sufficient for many tasks.

Valves are also available based on copper seals, instead of Viton O-rings. These are likely to be more resilient to the Rb, and can tolerate much higher temperatures. The downside is that copper seals have a limited number of open/shut cycles, as the seal is formed by compressing the copper. If the desired cell filling parameters are well known however, there may be little need for repeated opening of the valve. In this case, a copper seal could greatly extend the lifetime of the valves (though I suspect the valves would still fail at some point).

6.5.2 White Residue

A white residue appeared in the cell after a few weeks of operation. The residue was unlikely to be Rb_2O , which is brown, and was perhaps RbH. The first appearance was after the second transfer of Rb to the cell, indicating that the source was some contamination that had built up in the Rb ampule, which was housed at that point in a crushed copper tube, or from somewhere in the vacuum system. The amount of white residue grew in time however, so it is possible that there was also a source within the cell system, such as the cell valve O-ring.

⁸Though ultrahigh vacuum and bakeout requirements would also prevent a Viton seal from being used in cold atom experiments.

The residue was initially only present in the glass-metal transition and under the cold finger. The residue began building up on the cell windows however, due to a temperature gradient created by the presence of a microwave device at the end of the cell, which was slightly cooled through a rudimentary cold finger. The residue appears to stick strongly to the walls, and did not appear to migrate once it had struck the cell windows. The fan pattern formed as the residue came out of the cell channel can be seen in Figure F.2. The residue built up to the point that the OD of the cell (without Rb) approach unity, rendering the cell inoperable.

I was able to remove the residue from the cell windows by evacuating the cell, and heating the cell windows to reverse the temperature gradient. Details and photos of the process, which took several days, are provided in Appendix F.

6.5.3 Mechanical Noise

The filling station setup suffered from vibrational instabilities. These were introduced from the mounting of the vapor cell, and from the raised breadboard that held the oven, imaging optics, and DUT mount.

The cell chamber was mounted in a vibrationally insecure way, at the end of a long arm. The closest point secured to the table was at the cell valve. In addition, vibrations in the vacuum system may have been transferred to the cell. In an optimised setup, the cell would be secured much closer to the cell chamber.

The initial mounting of the raised breadboard was insufficient for its stiffness, causing large instabilities in the optical path. This was reduced to a manageable level by bolting to a rigid frame and taking care not to fix the breadboard under strain.

6.5.4 Oven and DUT Heating

There are a number of improvements that can be made to the existing oven.

The optical access is currently quite restricted, and would be greatly improved with enlarged windows. If covered with glass, the windows would likely have little impact on the insulation provided by the two-layer oven. The size of the oven was also sometime quite restrictive when mounting test devices and their cables.

The heating and cooling of the oven is currently a slow process, taking 2-3 hours to heat up and 1-2 hours to cool down. This means that debugging of the setup is a very inefficient process, if there is a problem inside the oven area.

A more fundamental issue is that the DUT (device under test) must be placed inside the oven along with the vapor cell. Although this may not be a problem for some devices, many are unlikely to be compatible with operation at such high temperatures. For near-field imaging, it is unlikely to be feasible to remove the DUT from the oven entirely, due to the required proximity of the cell and DUT. However, there are a number of options available to reduce the heating of the DUT.

Our first thought might be to actively cool the DUT. I have used this to reduce the DUT temperature to approximately 100°C from the oven temperature of

140°C. However, it is difficult to cool the DUT without also producing a temperature gradient in the cell, and thus quickly causing a build-up of residue on the cell windows.

One of the many benefits of using isotopically pure ^{87}Rb would be a reduction in the temperature required to reach a given ^{87}Rb density. At 140°C in a natural Rb cell, the ^{87}Rb density is $1.7 \times 10^{13} \text{ cm}^{-3}$ (see Table 2.7). An isotopically pure ^{87}Rb cell would achieve this density at 117°C. If Cs is used instead of Rb, the temperature can be reduced even further, with similar Cs density achieved at 102°C [205]. This is because Cs only has a single naturally occurring isotope, and has a higher vapor density than Rb for a given temperature.

There are also options for controlling the Rb density without heating the DUT. The technique of LIAD (light induced atomic desorption) uses pulses of blue or UV light to desorb atoms from the cell walls [198, 206]. This can be used to give a temporary boost in atomic density without heating the cell. It is not immediately clear how well this would work with the high buffer gas pressures used in our cells. The most promising option is to directly heat the cell using a laser, as performed with a $1.5 \mu\text{m}$ laser in Chapter 8. With a heating laser, it may be possible to locally heat the cell with minimal heating of the DUT.

6.5.5 Buffer Gas Filling

The cell valve leak led to the imaging presented in Chapter 7 being performed with a large range of buffer gas pressures. The modelling presented in Section 6.3.3 indicates that the optimum pressure for a 3 : 1 Kr:N₂ mixture is 60 mbar, however this remains to be experimentally verified.

The optimum ratio of Kr for Rb localisation and N₂ for quenching is unclear at this point. The low observed optical pumping efficiencies are likely to be in part due to radiation trapping, despite the presence of N₂ as a quenching gas, implying that more N₂ is needed. The optical pumping and radiation trapping model presented in Ref. [98] would be a good starting point for an analysis of the required quenching gas pressure.

6.5.6 Isotopically Pure ^{87}Rb

Isotopically pure or enriched ^{87}Rb is significantly more expensive than natural Rb, and we have so far avoided its use. As discussed throughout this thesis however, the presence of ^{85}Rb can be highly detrimental, and an optimised setup should use pure ^{87}Rb . Benefits would include: 1) There would be no background OD due to ^{85}Rb , giving increased stability and better signal to noise ratio; 2) For a given operating temperature, we would see a fourfold increase in ^{87}Rb density, and thus signal strength; 3) For a given ^{87}Rb density, SE relaxation would be reduced by a factor of 4. This would either allow us to operate at higher temperatures (giving a stronger signal) or give us longer relaxation times. This increase in the SE relaxation ‘ceiling’ would be essential to taking full advantage of a wall coated cell

(see Section 6.5.7); and 4) For a given ^{87}Rb density, we could significantly reduce the operating temperature (see Section 6.5.4).

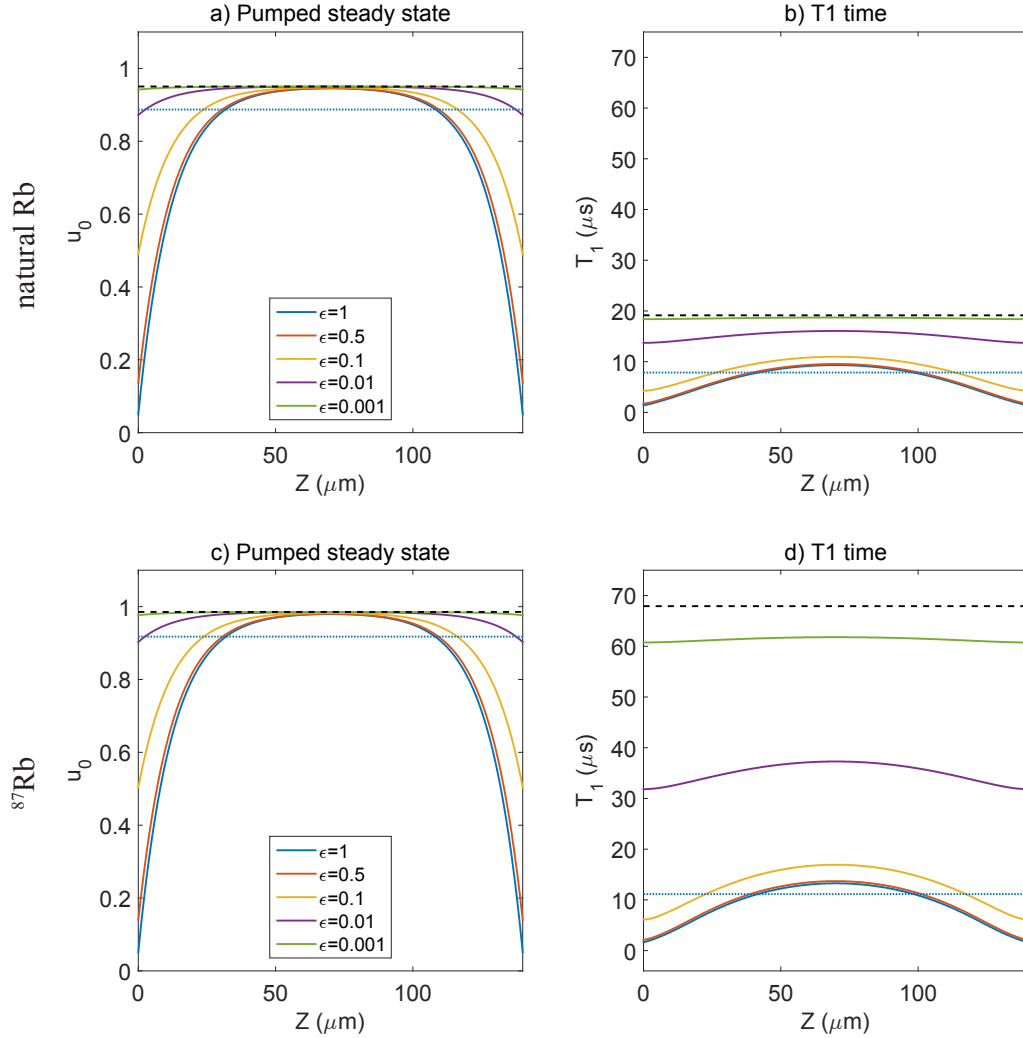


Figure 6.21: Calculated optical pumping efficiency and T_1 time through a $140\ \mu\text{m}$ antirelaxation coated cell, for various ϵ values. Following section 6.4.1, the black dashed lines correspond to u_∞ and T_1^∞ far away from the cell walls. The blue dotted lines include wall relaxation assuming $\epsilon = 1$, and lowest order diffusion. Modelling is shown for both a natural Rb cell (a+b) and a pure ^{87}Rb cell (c+d).

6.5.7 Antirelaxation Coated Cells

Antirelaxation coatings are a natural consideration in an environment dominated by wall collisions, such as in our ultrathin cells. As discussed in section 2.8, OTS is

a promising candidate for use in our cells. It gives 100s to 1000s of bounces, and is stable at long-term operation temperatures of up to 160°C [155]. Figure 6.21 shows modelling of the optical pumping efficiency and T_1 time in a 1D slice through an antirelaxation coated cell. The model is presented in section 6.4.1, and I have used natural Rb and the values in Table 2.7 as the input parameters. As the coating effectiveness increases (lower ϵ), the profiles approach the bulk limits, u_∞ and T_1^∞ , given by γ_{SE} and γ_{bg} . Panels (a+b) show modelling for a natural Rb cell, and panels (c+d) show modelling for cell filled with pure ^{87}Rb . The temperature of the enriched cell has been reduced to give the same ^{87}Rb density in both cells, and the resulting decrease in SE relaxation gives a dramatic improvement in pumping efficiency and T_1 time in the enriched cell.

It is interesting to note how close the curves for $\epsilon = 1$ and $\epsilon = 0.5$ are, and that the effect of a factor of 2 reduction in wall relaxation probability would be very difficult to experimentally detect.

6.5.8 Other Notes

I used the edges of the cell chamber to calibrate the pixel size in images. The cell and pixel sizes are of a very different order however, being 6 mm and $\sim 20\ \mu\text{m}$, respectively. An optimised setup would have $10\ \mu\text{m}$ -order calibration marks on the glass near the cell chamber.

I have not considered molecular buffer gases in this thesis, beyond N_2 . Ref. [146] lists several species, such as C_2H_4 , that have attractively low relaxation cross sections. There may be heavy buffer gases that give superior relaxation cross sections and diffusion coefficients to Kr. Hydrocarbons may make good candidates, for similar reasons to their suitability as wall coatings.

In magnetometry experiments, broadband lasers are used with linewidths from 10s of MHz to a few nm [207]. The observable in these experiments is $\langle m_F \rangle$, and so they are not required to optically resolve the $F = 1$ and $F = 2$ ground states. We may be able to operate with a slightly more broadband laser, say 10s of MHz instead of the current 1 MHz. Such a laser is likely to be cheaper and simpler to operate, which would be attractive for industrial applications.

Table 6.1: $\delta B_{\text{photon}}^{\text{optimal}}$ and optimised parameters for different ^{87}Rb purities and cell thicknesses. As illustrated in Figure 6.15, the optimal parameter space is quite large, with only a small change in δB_{photon} for a broad range of buffer pressures and temperatures.

^{87}Rb purity	Thickness (μm)	T ($^{\circ}\text{C}$)	P_{fill} (mbar)	Δx (μm)	OD	OD ₈₇	T ₁ (μs)	$\delta B_{\text{photon}}^{\text{optimal}}$ (nT Hz ^{-1/2})
0.2783	140	130	60	57	1.2	0.7	6.8	80
1	140	125.5	145.5	52	0.97	0.97	13.8	28
0.2783	200	121.8	54.6	79	1.2	0.76	12.2	30.1
1	200	115.5	121.2	74	0.94	0.94	24.4	11.3

Table 6.2: The experiment parameters for the data presented in Figure 6.18. For all data, the cell was filled with 80.4 mbar of Kr buffer gas, the GS-laser was used as the probe beam, and both pump and probe beams were locked to the ^{87}Rb $F = 2 \rightarrow F' = 2/3$ crossover peak. The OD for sets 3 and 4 (marked with *) was estimated from the cell temperature.

#	Pump Laser	r_{pump} (mm)	r_{probe} (mm)	I_{probe} (mW/cm ²)	T_{stem} ($^{\circ}\text{C}$)	T_{cell} ($^{\circ}\text{C}$)	OD	T ₁ (μs)	Method
1	IF	1.2	1.2	0.56	124.5	140.6	0.53		OPR
2	IF	1.2	1.2	0.56	124.5	140.6	0.53	13.6	Franzen
3	IF	2	2.5	9.8	124.5	140.6	0.53*		OPR
4	IF	2	1	8	126	141	0.56*		OPR
5	TAPro	2.6	0.7	1.2	129.7	146	0.68		OPR
6	TAPro	2.6	0.7	11	129.7	146	0.68	12.3	Franzen
7	IF	1.1	1.1	1.4	110	123	0.2		OPR
8	IF	1.1	1.1	1.4	110	123	0.2	15.6	Franzen

Chapter 7

Imaging Microwave and DC Magnetic Fields with $< 100\mu\text{m}$ Spatial Resolution

In this chapter, I demonstrate the capabilities of the high-resolution imaging system described in Chapter 6, through the imaging of microwave magnetic near-fields above a selection of microwave circuits. As an illustration of the flexibility of our vapor cell system, I also present vector-resolved images of the dc magnetic field above a wire loop. The material presented in this chapter was published in Ref. [53].

7.1 Experiment Parameters

Much of the experiment setup and operating parameters are described in Chapter 6. The microwave imaging was performed using the U1 cell ($140\mu\text{m}$ thickness), and the dc magnetic field imaging was performed using the U2 cell ($200\mu\text{m}$ nominal thickness). Rabi sequences were used for microwave imaging, and Ramsey sequences for dc field imaging. Typical operating parameters were: separate pump and probe lasers, both locked to the $F = 2 \rightarrow F' = 2, 3$ crossover peak of the ^{87}Rb D₂ line; pump laser intensity of $110 - 140\text{mW}/\text{cm}^2$; probe laser intensity of $30\text{mW}/\text{cm}^2$; probe pulse duration of $dt_{\text{probe}} = 0.3\mu\text{s}$; cell filled with Kr and N₂ buffer gas in a 3:1 ratio, with $T_{\text{fill}} = 22^\circ\text{C}$; measured temperatures of $T_{\text{res}} = 140^\circ\text{C}$ and $T_{\text{cell}} = 145^\circ\text{C}$. As discussed in Section 6.2, the measured temperatures may overestimate the actual temperatures. Equation (6.1), with $A = 0.9$, suggests that the actual reservoir temperature may have been closer to 128°C . For $P_{\text{fill}} = 100\text{mbar}$, $T = 140^\circ\text{C}$ gives a Rb diffusion distance during a measurement of $\delta x = \sqrt{2DT_1} = 48.5\mu\text{m}$, whilst $T = 128^\circ\text{C}$ gives $\delta x = \sqrt{2DT_1} = 53.7\mu\text{m}$. We thus take the area of each diffusion-limited sensor to be $50 \times 50\mu\text{m}^2$ (see Section 3.4).

The 1:3.6 demagnification given by the imaging lens meant that the CCD pixels corresponded to $21 \times 21\mu\text{m}^2$ in the imaging plane. I did not bin the CCD pixels for the images presented in this Chapter, and so the ‘image pixels’ and ‘CCD pixels’

are identical (see Section 3.3.1). However, the $21 \times 21 \mu\text{m}^2$ pixel area was a factor of 2.4^2 smaller than the $50 \times 50 \mu\text{m}^2$ diffusion limited sensor area. In Section 7.5, I therefore considered 2×2 binned CCD pixels with an area of $42 \times 42 \mu\text{m}^2$, in order to better estimate the experimental sensitivity. This binning is relevant for the analysis presented in Figures 7.7 to 7.9.

7.2 OD_{mw} Images

For Chapters 6-8, I used a slightly different absorption imaging sequence to the previous Chapters. As described in Section 3.3, the reference image sequence was changed to include an optical pumping pulse, making the presence of the microwave the only difference between the actual and reference images. This gives images of OD_{mw} , the change in OD induced by the microwave. The effects of the microwave are clearer, giving more robust and faster fitting. In addition, the reference image sequence, consisting of optical pumping, waiting, and probing, is a Franzen sequence, and can be used to obtain T_1 and OD_{pump} for each shot.

Figure 7.1.a shows OD_{mw} images for different Rabi pulse durations above the Zigzag chip (described in Section 7.3.2). The chip surface is at approximately $Z = 0$. The OD_{mw} images trace out contour lines of the microwave magnetic field. Peaks in OD_{mw} correspond to atoms at the top of a Rabi oscillation (and so a $(2n - 1)\pi$ local microwave pulse), and troughs correspond to atoms at the bottom of a Rabi oscillation. The outermost/rightmost $n = 1$ contour line corresponds to atoms at the peak of their first oscillation (π pulse). Moving inward/left, the n^{th} contour line corresponds to atoms at the top of their n^{th} oscillation. As discussed in Refs. [50, 54, 157], it is possible to reconstruct a component of the microwave field from only a single OD_{mw} image, from the n value of each contour line. Over time, we see the oscillations ‘propagating’ into the cell, and the signal washing out due to relaxation. As discussed in Chapter 6, the dominant relaxation mechanism in the ultrathin cells is collisions with the front and back cell walls.

Figure 7.1.b shows a zoomed-in section of the $dt_{mw} = 4.65 \mu\text{s}$ OD_{mw} frame. Peak-to-trough feature sizes as small as $70 \pm 10 \mu\text{m}$ can be seen in the highlighted section. This is approaching the estimated diffusion-limited spatial resolution, $\Delta x = \sqrt{2D dt} = 37 \mu\text{m}$, where I have used $D = 1.5 \text{ cm}^2/\text{s}$ and $dt = 4.65 \mu\text{s}$, corresponding to a buffer gas mixture of 75 mbar of Kr and 25 mbar of N_2 .

Figure 7.1.c shows signals in time for a pixel at $Z = 0.48 \text{ mm}$, $Y = 2.6 \text{ mm}$ in Figure 7.1.a. We fit the OD_{mw} oscillations using Eqs.(3.25) and (3.26), for Ramsey and Rabi sequences, respectively.

7.3 Imaging Microwave Fields Above Test Structures

In order to characterise and demonstrate our imaging system, we created three test structures. The structures, shown in Figures 7.2-7.4, respectively, are: a coplanar waveguide (CPW); a waveguide making several bends across its substrate, which we

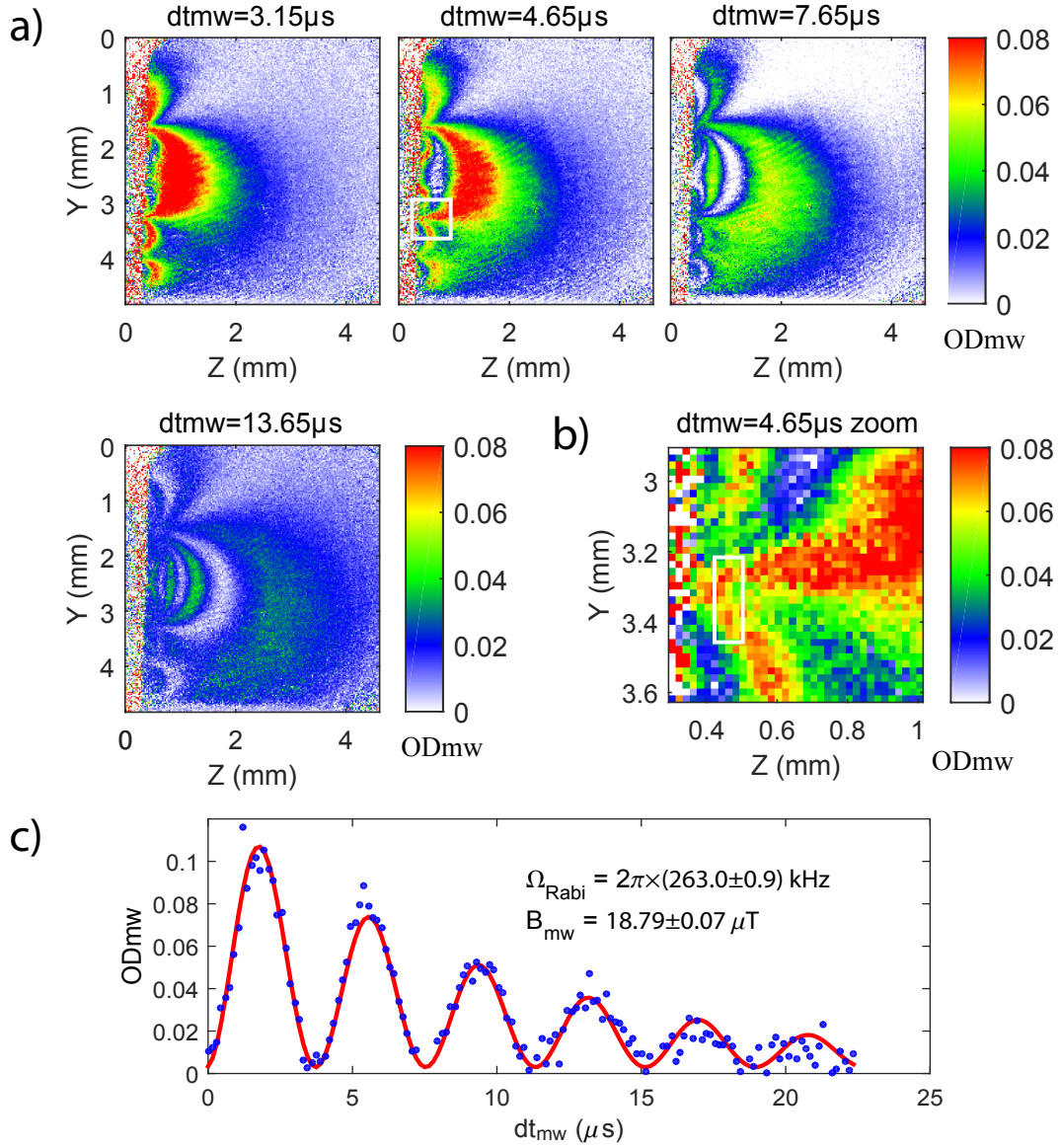


Figure 7.1: a) OD_{mw} images for various dt_{mw} durations. The surface of the Zigzag chip (see Section 7.3.2) is at $Z = 0$; b) zoomed in section of OD_{mw} for $dt_{mw} = 4.65 \mu\text{s}$. The zoomed-in section is indicated by the white box in (a). The smallest feature size, highlighted in the zoomed-in image, is only $70 \mu\text{m}$ peak-to-trough; c) OD_{mw} in time for the pixel at ($Z = 0.48 \text{ mm}$, $Y = 2.6 \text{ mm}$), showing Rabi oscillations as the microwave pulse length is scanned.

dubbed the ‘Zigzag’ chip; and a split-ring resonator (SRR). All of the microwave field measurements were made using the U1 cell. S-Parameter characterisations of the three structures are provided in Appendix H.

Simulations of the microwave fields were based on the microwave simulation program Sonnet. Sonnet outputs the microwave current in the devices, from which we used the Biot-Savart law to calculate the microwave near field. This approximation is valid in the near-field limit, i.e. for distances, r , above a device much smaller than the microwave wavelength, λ_{mw} . As $\lambda_{mw} = 4.4$ cm for 6.8 GHz microwaves, and we are probing the microwave field over a range $r = 0.15 - 6$ mm, the condition $r \ll \lambda_{mw}$ is easily satisfied. The only free parameters in comparisons with measurement were the amplitude of the input microwave signal and the exact position of the cell relative to the chip.

I assumed that the external wall at the end of the cells was given by its specified value, $150 \mu\text{m}$, however the manufacturing tolerances allowed for the wall to be up to $200 \mu\text{m}$ thick. The agreement between measured and simulated fields indicates that the external wall thickness was within the manufacturing tolerance, but it is difficult to draw much stronger conclusions without a direct measurement of the glass thickness.

7.3.1 CPW

CPWs are a ubiquitous building block of microwave circuits [189], and provide a simple structure which can be readily and robustly compared with simulations. The CPW used in this thesis, shown in Figure 7.2.a, has a $500 \mu\text{m}$ wide central signal strip, with $105 \mu\text{m}$ gaps to ground planes on either side. Figure 7.2.b shows images of the Z and Y components of the CPW microwave magnetic field (the very weak X component was not imaged). Simulations of the microwave field are shown as overlaid contour lines. The slight asymmetry is related to the bends in the wires. The strong agreement with the simulated field demonstrates the reliability of the imaging technique. Discrepancies may be due to imperfect coupling into the waveguide, and the use of a finite mesh size for modelling the microwave field through the bends. The images in Figure 7.2.b demonstrate the importance of thin external vapor cell walls: a vapor cell with standard millimeter-scale external walls would see none of the interesting features.

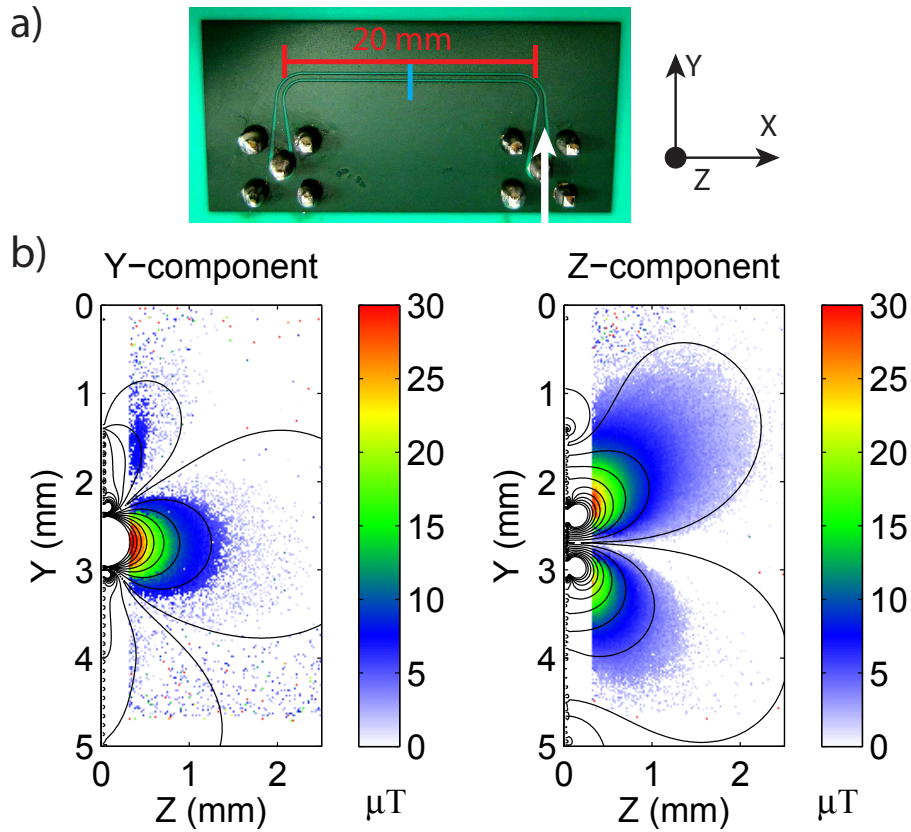


Figure 7.2: a) Photo of the CPW chip, with the orientation of the chip in relation to the coordinate system defined by the imaging cell shown on the right. The approximate position of the imaging plane is indicated by a blue line, and a white arrow indicates the microwave insertion port; b) Experimentally obtained images of the Y - and Z -components of the microwave magnetic field above the CPW. The waveguide surface is at approximately $Z = 0$. The simulated microwave field is shown in black contour lines, starting at $1 \mu\text{T}$ for the outermost line and increasing in $5 \mu\text{T}$ steps inwards.

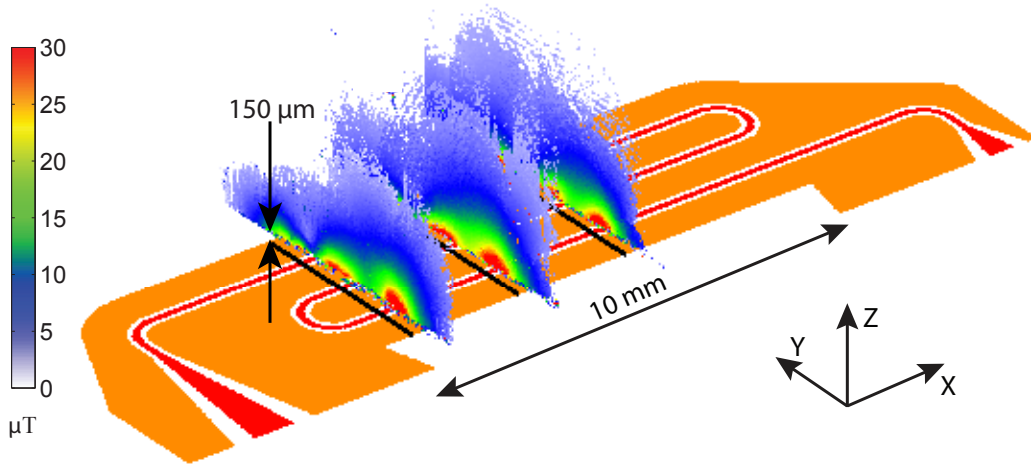


Figure 7.3: Experimentally obtained images of $|B_{mw}|$, the absolute microwave magnetic field amplitude, in several cross-sections $150\ \mu\text{m}$ above the Zigzag chip (see Sec. 7.3.2). The central signal line is shown in red, and the ground planes in orange. Black lines show the positions of the imaging planes on the chip. Differences in field shape at each position are due to differences in the relative phase of the microwave signal on the three loops of the signal line. The field at the middle imaging position is examined in more detail in Figure 7.4.

7.3.2 Zigzag Chip

The Zigzag chip, shown in Figure 7.4.b, has smaller and more complex features than the CPW, allowing us to highlight the spatial resolution of our setup. The Zigzag waveguide has a $200\ \mu\text{m}$ thick central signal strip, with $50\ \mu\text{m}$ gaps to ground planes either side. The waveguide goes through two bends, resulting in a cross-section in the imaging plane containing three waveguide sections, each separated by $900\ \mu\text{m}$. Figure 7.3 shows quasi-2D slices of the absolute microwave amplitude, $|B_{mw}|$, at three positions above the Zigzag chip. The variation in field shape between the positions is due to the standing wave produced in the waveguide. Figure 7.4.a then examines the middle imaging plane of Figure 7.3 (indicated by the blue line in Figure 7.4.b) in more detail, showing images of each of the polarisation components of the microwave field above the chip, which are compared with contour lines from simulation. Cross-sections of the field near the edge of the vapor cell are shown in Figure 7.4.c. The wide field of view in Figures 7.3 and 7.4 ($> 6\ \text{mm}$) was obtained by stitching two sets of images together.

There is general agreement between the measured and simulated fields in Figure 7.4, but not for all features. The amplitude of the simulated X component of the field is well below the experimental sensitivity, and the measured X component of the field is likely to be some projection of the Y and Z components, caused by imperfect orthogonality between the chip, cell, and coil axes. Additionally, as seen in the cross-sections in Figure 7.4.c, the measured microwave field is much broader

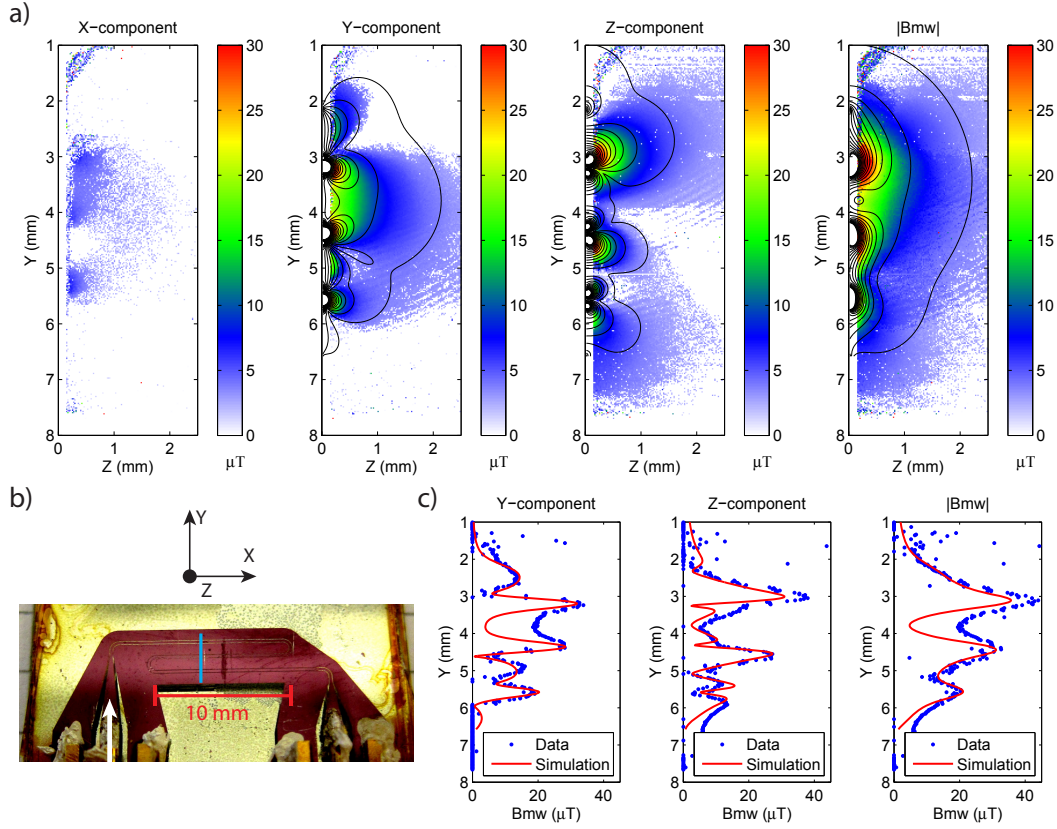


Figure 7.4: a) experimentally obtained images of the X , Y , and Z components of the microwave magnetic field above the Zigzag chip. The magnitude of the microwave field, $|B_{mw}| = \sqrt{B_X^2 + B_Y^2 + B_Z^2}$, is also shown on the far right. The waveguide surface is at approximately $Z = 0$. The simulated microwave field is shown in black contour lines, starting at $2 \mu\text{T}$ for the outermost line and increasing in $3 \mu\text{T}$ steps inwards; b) Photo of the Zigzag chip. The approximate position of the imaging plane for (a+c) is indicated by a blue line, and a white arrow indicates the microwave insertion port; c) Cross-sections of the experimentally obtained microwave field (blue dots) approximately $250 \mu\text{m}$ above the Zigzag chip surface, and comparison to simulation (red lines).

than the simulation around $Y = 3 \text{ mm}$ to $Y = 4.5 \text{ mm}$. Given the spatial resolution shown at $Y = 5.6 \text{ mm}$, it is reasonable to conclude that this broadening is a real feature of the microwave field. It is unlikely to be due to perturbations induced by the vapor cell, for which we were unable to measure any effect with the Zigzag or CPW chips. Such discrepancies highlight the difficulty of accurately manufacturing and simulating even relatively simple structures such as the Zigzag chip, and the need for direct measurements.

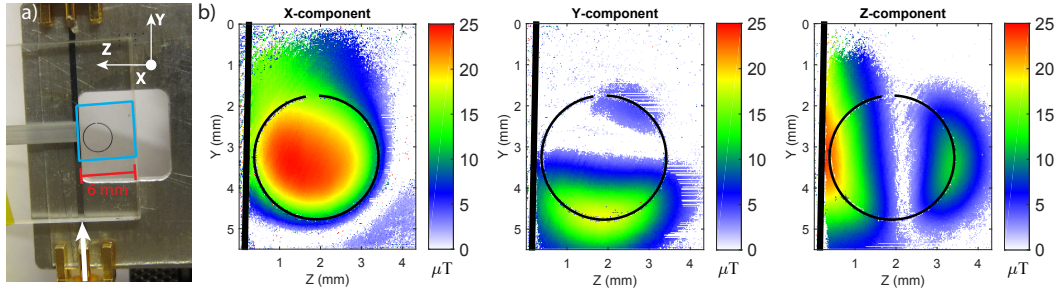


Figure 7.5: a) Photo of the SRR chip, demonstrating a second operation mode of the imaging setup, with the glass cell parallel to the transparent chip surface; b) Experimentally obtained images of the X , Y , and Z components of the microwave magnetic field above the split-ring resonator (SRR). The waveguide surface is parallel to, and a few millimeters in front of, the cell. Black outlines show the positions of the signal line and ring.

7.3.3 Split-Ring Resonator

The SRR chip, shown in Figure 7.5.a, consists of a signal line coupling inductively into a split ring. The split-ring is built on a transparent glass substrate, allowing us to operate in a second mode, with the SRR placed in front of and parallel to the vapor cell. The resonator linewidth was 160 ± 20 MHz, corresponding to a quality factor of 40 ± 5 .

The presence of the vapor cell significantly changed the properties of the SRR, by filling the space around the resonator with a glass dielectric. We used this to tune the resonance frequency to match the 6.835 GHz splitting of the ^{87}Rb ground states, adjusting the gap between the cell and the SRR until the resonance was in the desired position (see Appendix H). A shift of $1 \mu\text{m}$ corresponded to a shift in resonance of 5.7 MHz. Note that we were unable to detect any influence of the cell on the CPW or Zigzag chips.

The SRR field is shown in Figure 7.5.b. Like in a solenoid, the SRR field is strongest inside the split-ring, parallel to the split-ring axis in the X direction. The field then turns outward, seen in the Y and Z component images, before returning with a less-dense flux in the X direction outside the split-ring. The minima in the centres of the Y and Z components are because the field lines travel out from the field centre, and so cancel out along the central axes. The lopsided nature of the Y component is due to the presence of the split in the ring.

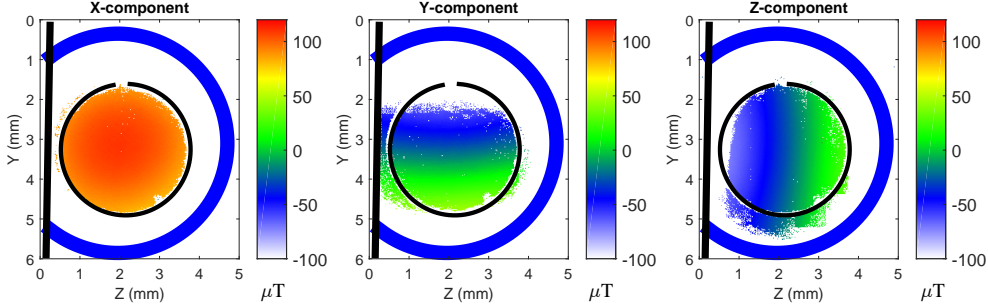


Figure 7.6: Experimentally obtained images of the X , Y , and Z components of a dc magnetic field 0.6 mm above a wire loop. Positive and negative field values represent opposite directions. The field of view corresponds to the X component of the SRR microwave magnetic field, which was used to drive the Ramsey oscillations used to image the dc field. Outlines show the positions of the current loop (blue) and SRR (black). The coordinate system is the same as shown in Figure 7.5.a.

7.4 Vector Imaging of a DC Magnetic Field

Similar to the clock characterisation presented in Chapter 5, we can also use a Ramsey sequence in our ultrathin cells to image dc magnetic fields. Driving Ramsey oscillations on the magnetic field sensitive $|F = 1, m_F = 1\rangle \rightarrow |F = 2, m_F = 1, 2\rangle$ transitions ($i = 6, 7$), the oscillation frequency of the Ramsey fringes is equal to the detuning of the microwave from resonance, allowing us to measure the Zeeman shift induced by the applied dc magnetic fields.

The Ramsey B_{dc} measurement technique is fundamentally scalar, as the Zeeman shift is determined by the absolute value of the dc magnetic field. There are standard tricks for using scalar magnetometers for vector imaging, however [13]. For an applied dc magnetic field, C , that is much larger than the field of interest, B , we are primarily sensitive to the component of B that is parallel to C . For C along the X axis, the measured field, B_{meas} , is

$$B_{meas} = \sqrt{(C + B_X)^2 + B_Y^2 + B_Z^2} \approx C + B_X. \quad (7.1)$$

We can obtain C in a separate reference measurement, and subtract this from B_{meas} to obtain B_X . The full vector magnetic field can be obtained by imaging with the C field applied along each of the X , Y , and Z axes. In our case, C is provided by the coil cage around our system (described in Section 6.1.5).

Figure 7.6 shows images of the DC field above a 2 mm diameter wire loop. The images were taken using the U2 cell (200 μm nominal thickness), after replacing the leaking valve and the U1 cell (see Section 6.5.1). The cell was filled with 70 mbar of Kr and 20 mbar of N_2 , and operated at $T_{res} = 130^\circ\text{C}$, $T_{cell} = 135^\circ\text{C}$. The Ramsey

oscillations were driven using the X component of the SRR field, which defines the field of view¹. We see a solenoid-like field, with a strong, uniform X component, and the field turning outwards in the Y and Z components.

7.5 Sensitivity

We estimate the imaging sensitivity from the fitting uncertainty to the Rabi oscillations. Figure 7.7.a shows images of the Z component of B_{mw} and the fitting uncertainty, δB_{mw} , above the Zigzag chip in the leftmost imaging plane shown in Figure 7.3.a. The highest sensitivity region is in the centre of the topmost lobe. The high sensitivity is most likely due to a combination of relatively homogenous field and low field amplitude. The best spatial resolution, on the other hand, is closer to the chip surface in the high-field region on the left, where atomic diffusion over a Rabi period is smallest. The distance from the end-wall of the cell (near $Z = 0$) is inconsequential, as the skin of reduced optical pumping efficiency near the walls (see Figure 4.3) in the ultrathin cells is on the order of 10s of μm only. The fitting error to our microwave Rabi data was as low as $\Delta B_{mw}^{exp} = 21 \text{ nT}$ per sensor². This gives a sensitivity of $\delta B_{mw}^{exp} = 1.4 \mu\text{T Hz}^{-1/2}$ per sensor over the 4440 s measurement time (148 averaged runs). Depending on the size of the microwave field gradients, integrating over a larger volume would give an increase in sensitivity at the expense of spatial resolution. We have a similar sensitivity for B_{dc} imaging, observing $\delta B_{dc}^{exp} = 1.6 \mu\text{T Hz}^{-1/2}$ for a $42 \times 42 \times 200 \mu\text{m}$ sensor.

We can estimate the photon shot noise limited sensitivity for our experiment parameters using the model presented in Section 3.4. We recall

$$\delta B_{photon} = \sqrt{\frac{dt_{run}}{N_{shots}}} \frac{2}{dt_{mw}} \frac{\hbar}{\mu_B} \frac{OD_{min}}{OD_{mw}^{max}} \exp(dt_{mw}/\tau_2), \quad (7.2)$$

where for an operating temperature of $T_{res} = 140^\circ\text{C}$, $OD_{mw}^{max} = \frac{1}{3}OD_{87} = 0.24$ and $OD_{min} = \sqrt{2}[Q I_{probe} e^{-OD} A dt_{probe}/(\hbar\omega_L)]^{-1/2} = 1.0 \times 10^{-2}$. I use the parameters $Q = 0.27$, $I_{probe} = 30 \text{ mW/cm}^2$, $dt_{probe} = 0.3 \mu\text{s}$, $A = 42 \times 42 \mu\text{m}^2$, $\tau_2 = T_1 = 7.8 \mu\text{s}$, $dt_{mw} = 22.5 \mu\text{s}$, $N_{shots} = 150$, and $dt_{run} = 30 \text{ s}$. The laser is red-shifted by an AOM 80 MHz from the ^{87}Rb $F = 2 \rightarrow F' = 2/3$ crossover peak. The cell is filled with Kr and N_2 buffer gas, in a 3:1 ratio, with $T_{fill} = 22^\circ\text{C}$, and $P_{fill} = 100 \text{ mbar}$. Parameters such as the OD are calculated using the models presented in Chapter 2. We obtain $\delta B_{photon} = 0.45 \mu\text{T Hz}^{-1/2}$. As discussed in Section 6.2, it is possible that the operating temperature was closer to $T_{res} = 130^\circ\text{C}$, which would give $\delta B_{photon} = 0.28 \mu\text{T Hz}^{-1/2}$. We therefore conclude that our measured $\delta B_{mw}^{exp} = 1.4 \mu\text{T Hz}^{-1/2}$ is 3 – 5 times the photon shot noise limit determined by our

¹The restricted field of view compared to the X -component image in Figure 7.5 is explained by the fact that we are using a different cell in Figure 7.6, with a different chip-cell distance and alignment.

²I.e., per 2×2 binned pixels, corresponding to $42 \times 42 \times 140 \mu\text{m}^3$.

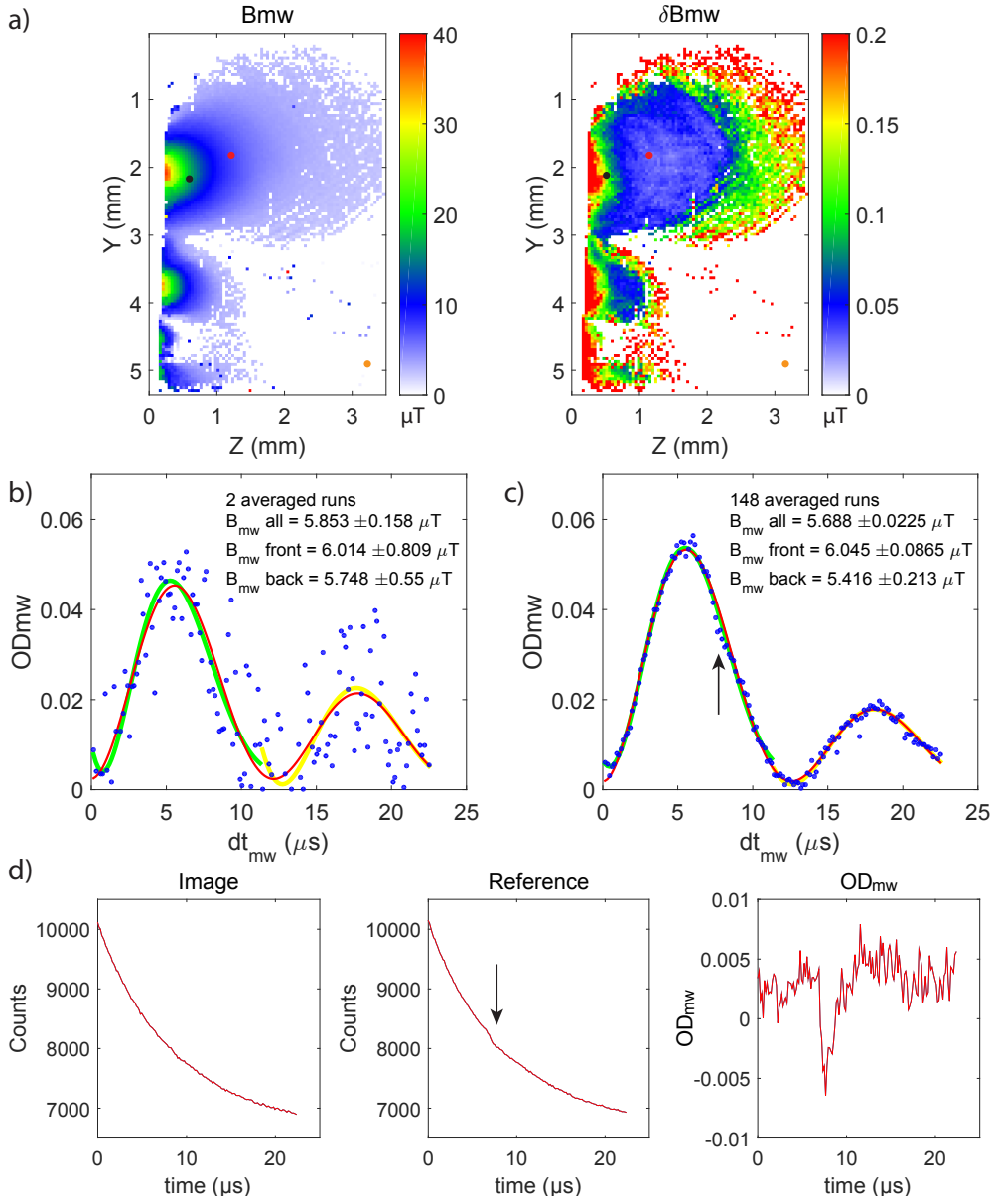


Figure 7.7: a) Images of B_{mw} and the fitting uncertainty δB_{mw} above the Zigzag chip; b+c) an example pixel corresponding to the red dot in (a), with data for 2 averaged runs (b) and 148 averaged runs (c). Fits are shown considering all of the data, and also just the first and second halves; d) Data for the pixel marked by an orange dot in (a), which is well away from the microwave chip (and field). The kink in the B_{mw} curve around $dt_{mw} = 7 \mu\text{s}$ is due to some unidentified problem in the reference image sequence.

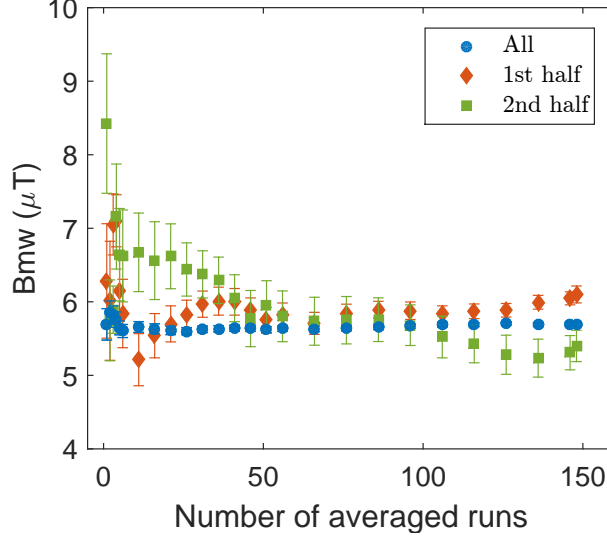


Figure 7.8: Extracted B_{mw} as a function of the number of averaged runs. Data is shown for the Figure 7.7.b pixel, with B_{mw} obtained from fits to all of the data, and just the first and second halves. The error bars are given by ΔB_{mw} , the fitting uncertainty.

(non-optimal) experiment parameters. Noting that the optimal photon shot noise limited sensitivity was determined in Section 6.3.3 to be $\delta B_{photon}^{optimal} = 0.08 \mu\text{T Hz}^{-1/2}$, we could expect a factor of 17.5 improvement in sensitivity by optimising the buffer gas pressure, temperature, and laser frequency, assuming that we reach the photon shot noise limit by reducing noise from the camera and other sources.

We can measure the imaging noise by performing a run without microwave field. The noise is given by the standard deviation in OD_{mw} between experiment shots. Excluding the kink in OD_{mw} , discussed below, this yields $\Delta OD = 1.8 \times 10^{-2}$ for a single shot, which is 1.6 (2.6) times the photon shot noise limit of $\Delta OD_{photon} = 1.1$ (0.68) $\times 10^{-2}$ for $T_{res} = 140$ (130)°C. Approximately half of the δB_{mw}^{exp} in excess of δB_{photon} is therefore caused by imaging noise, due to factors such as camera readout noise, and fluctuations in the intensities and frequencies of the lasers. We have not fully identified the sources for the second half of the excess noise, but they include fitting errors and problems with the experiment sequence, as discussed below.

Figures 7.7.b and c show data from an example pixel in the high sensitivity region of Figure 7.7.a (the approximate location is marked with a red dot). The data is shown for both 2 averaged runs and 148 averaged runs, and almost two Rabi oscillation periods can be seen. We were curious as to whether better results could be found by only taking data at select times, and if the first or second half of the data were more important to the fit. I therefore show fits to all of the data, and to the first and second halves. The conclusion is that fitting to all of the data gives far more precise, and likely more accurate results. In addition, the first half of the

data, where the signal is strongest, is the most important and reliable for obtaining B_{mw} . This is more easily seen in Figure 7.8, which plots B_{mw} for each of the three fits as a function of the number of averaged runs. After the first 5 runs, the fit to all of the data gives a very consistent B_{mw} value, with uncertainties smaller than the data points. The fits to the first and second halves of the data give considerable disagreement however, and much larger uncertainties. The drifts of B_{mw} extracted from the second half are particularly striking. In fitting the data, I left the phase as a free parameter. This may have been unfair to the second-half fits, which would probably have been significantly better constrained by fixing the (reasonably well known) initial phase.

In Figures 7.7.b and c, data taking stopped before the Rabi oscillations did. This is clearly non-optimal: more data was available for collection, with which we would probably have been able to achieve a better fit (see discussion above). The broad range of microwave amplitudes seen in a near field, which drops off exponentially with distance from the source, presents a problem for optimal spacing of a finite number of data points. In this thesis, the spacing was determined by the temporal resolution required to see the fastest Rabi oscillations ($\Omega > 1$ MHz). An optimised sequence would most likely have closely spaced data points at the start, to see the fast oscillations, and more widely spaced data points towards the end, to more completely observe the slower oscillations. It would be interesting to perform a similar analysis to Figure 7.8, comparing fitting using all of the data points in the first half of the run, and every second data point across the entire run. Any binning of CCD pixels could also be varied across an image in order to match the image pixel size with the local spatial resolution, as defined by the distance of atomic diffusion during a Rabi oscillation period.

In the averaged data in Figure 7.7.c, a kink (marked by an arrow) can be seen around $dt_{mw} = 7 \mu s$. In Figure 7.7.b, the kink is obscured by the statistical noise. This kink is not due to the microwave, but rather due to some unidentified problem in the reference image sequence. This can be seen in Figure 7.7.d, which compares the actual and reference images, and the corresponding OD_{mw} image, for a pixel well away from the microwave source, marked in Figure 7.7.a by an orange dot. The data is shown for 148 averaged runs. The kink appears in other data sets, and may be more a function of shot number than dt_{mw} . A reasonable conclusion is that the kink is due to some bug in the reference image sequence, resulting in a deterministic timing jitter. This kink would have made a significant contribution to the noise in δB_{mw}^{exp} in excess of that imposed by the imaging noise, ΔOD . There also appears to be some slight difference in the actual and reference image sequences, as indicated by the slight offset of the average OD from zero. If we exclude the dip and examine only the data from $dt_{mw} = 70 \mu s$, we have $OD_{mean} = (3.9 \pm 0.2) \times 10^{-3}$.

Figure 7.9 shows the reduction in ΔB_{mw} with measurement time. Data is plotted for 2×2 binned pixels located under the red and black dots in Figure 7.7.a, and is compared to δB_{photon} calculated for the experiment parameters, and the optimal $\delta B_{photon}^{optimal}$ and $\delta B_{atom}^{optimal}$, as calculated in Section 6.3.3. There is a 4 orders of mag-

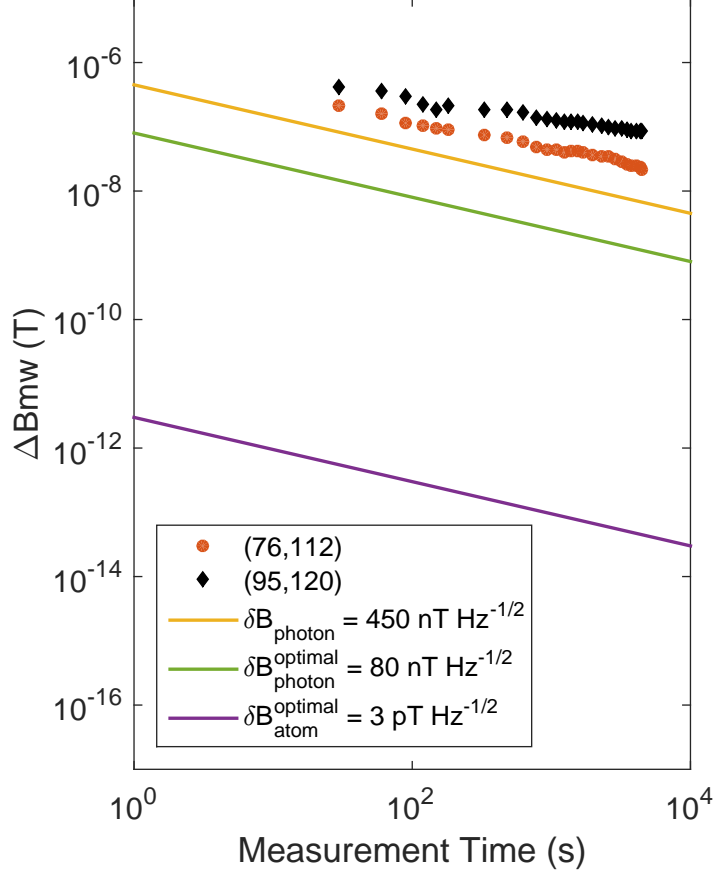


Figure 7.9: Uncertainty in the microwave amplitude, ΔB_{mw} , as a function of measurement time. Data is shown for the pixels under the red (76,112) and black (95,120) dots in Figure 7.7.a. The data is compared with the photon shot noise, calculated using both experimental and optimal parameters, and the optimised atomic projection noise.

nitude gap between $\delta B_{photon}^{optimal}$ and $\delta B_{atom}^{optimal}$, primarily due to our poor experiment duty cycle, as discussed in Chapter 3. We are limited by the camera readout speed and data saving time, which give a 30 s duty cycle for an experiment run comprised of 150 shots³, and result in the atoms sitting uninterrogated for the vast majority of the time.

Although we do not expect to reach the atomic projection noise in the near future, orders of magnitude improvement in the sensitivity seem achievable. The minimisation of dead-time will ultimately require moving to some quasi-continuous measurement scheme, possibly based on Faraday rotation [13, 111]. For sufficiently

³1 shot = 1 actual + 1 reference image. See Chapter 3.

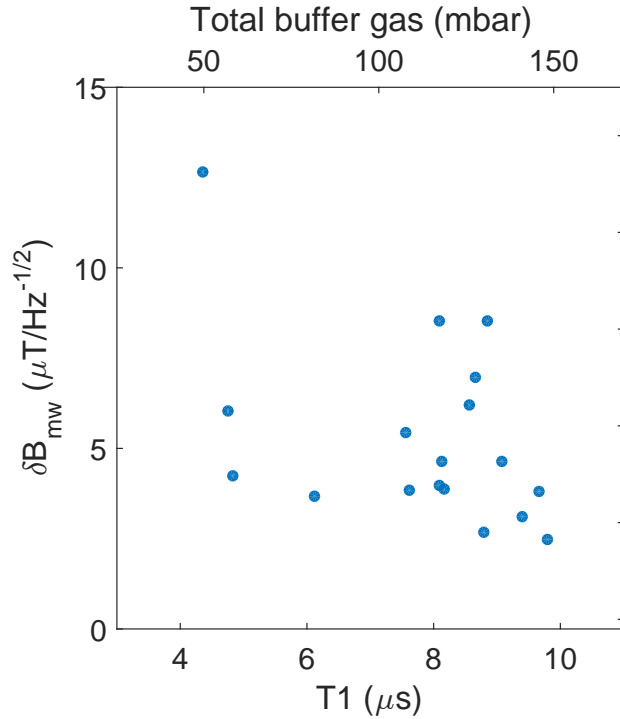


Figure 7.10: Measured microwave sensitivity as a function of measured T_1 , for single ($21 \times 21 \mu\text{m}^2$) pixels. The top axis shows the buffer gas pressure, estimated from T_1 and assuming a 3:1 Kr:N₂ ratio.

fast detection speeds (e.g. on the order of $10^5 - 10^6$ fps), weakly-perturbing Faraday measurements could even be used to observe Rabi oscillations in real-time. The camera frame rate could be dramatically sped up with a different camera and camera operation mode. 50×50 pixel imaging of ultracold atoms has been reported with a continuous⁴ frame rate of 2500 fps [167].

The cell valve had a leak during the microwave field measurements. As discussed in Section 6.5.1, the buffer gas pressure dropped over the course of a day, meaning that the buffer gas pressure for each measurement was unknown, and lower than optimal. In Section 6.4.3, I analysed optical pumping in this inadvertent scan of buffer gas pressure. Figure 7.10 considers the effect on sensitivity. The measured sensitivity for single ($21 \times 21 \mu\text{m}^2$) pixels is plotted as a function of measured T_1 . The top axis shows an estimate of the corresponding total buffer gas pressure. There is a large scatter in the data, but the best sensitivity is achieved with the longest T_1 , and thus highest buffer gas pressure.

⁴Continuous, as opposed to burst-imaging, where a small number of images are taken very quickly. In Ref. [167], a series of 2000 images were taken of the same cloud of ultracold atoms, using the technique of dark field Faraday imaging.

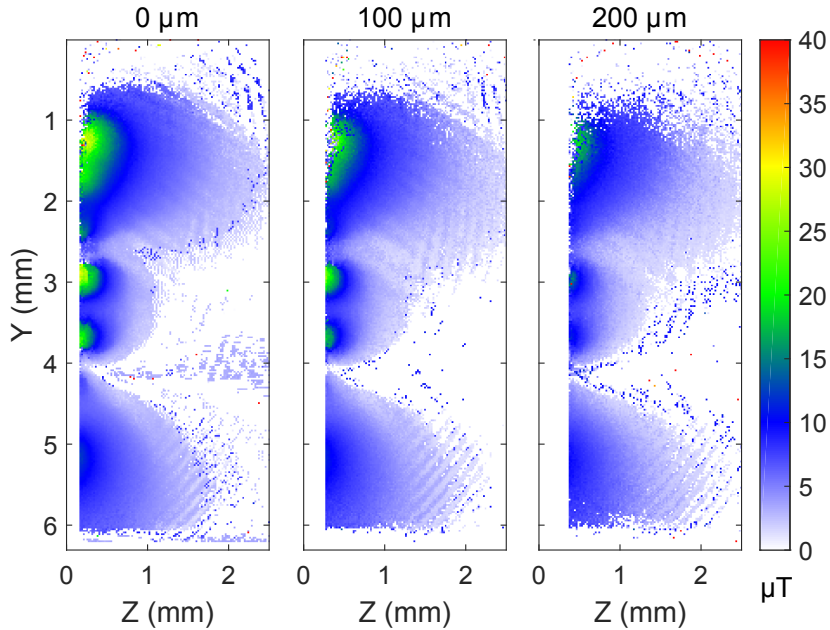


Figure 7.11: Microwave field images above the Zigzag chip, with the cell touching the chip, $100\ \mu\text{m}$ above, and $200\ \mu\text{m}$ above the chip. The microwave field patterns are extremely similar for all three images.

7.6 Effect of the Cell on the Microwave Field

From Maxwell’s equations, the presence of the dielectric glass walls of the vapor cell, and to a lesser extent the presence of the Rb atoms themselves, will necessarily have a perturbing effect on the fields we are imaging. The perturbation should generally be minimal compared to measuring the microwave field using a metallic antenna. As noted in Section 7.3.3 however, this can be quite significant for resonant devices.

The effect of the cell on non-resonant devices appears negligible. Figure 7.11 shows images of the Z component of B_{mw} above the Zigzag chip, in the rightmost imaging plane in Figure 7.3.a. B_{mw} is shown with the cell touching the chip, and then at separation distances of $100\ \mu\text{m}$ and $200\ \mu\text{m}$. Figure 7.12 then compares rows of pixels along Z for different Y values. The two figures show that any effect of the cell on the Zigzag chip microwave field is below our detection sensitivity. The field patterns in Figure 7.11 are extremely similar between the images, and the data points in Figure 7.12 are overlapping. The images also highlight the importance of thin cell walls in imaging close above microwave devices.

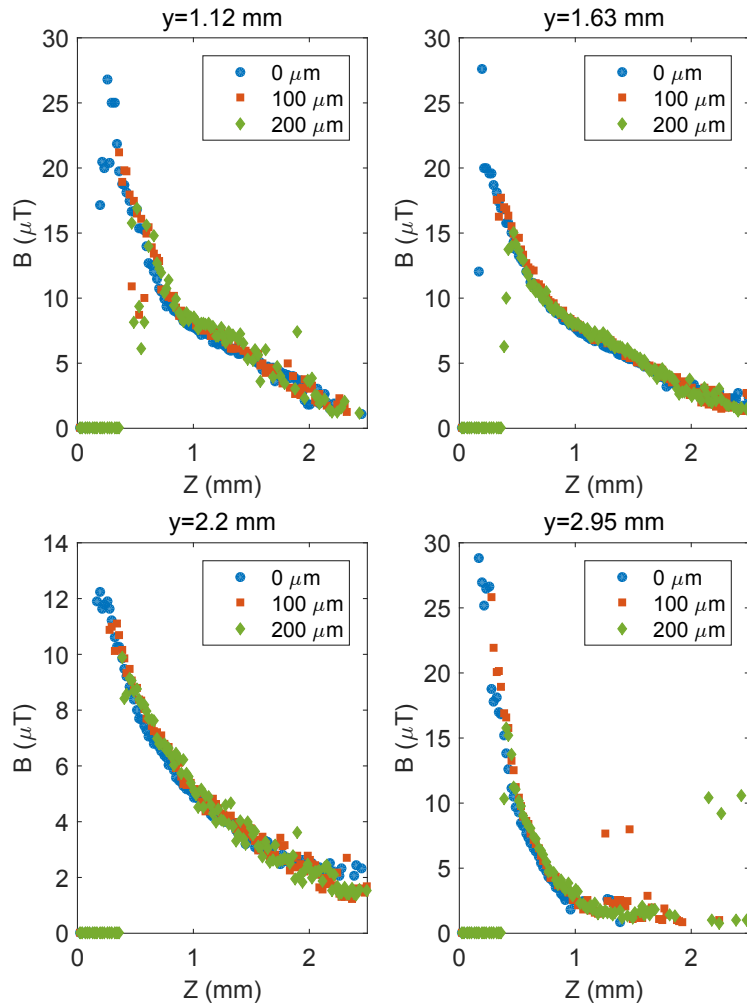


Figure 7.12: Comparisons of rows of pixels from Figure 7.11 at different Y values. The data points fall on the same lines, regardless of the distance between the chip and cell, indicating negligible perturbation of the field by the presence of the cell.

7.7 Imaging both B_{mw} and E_{mw}

For far field electromagnetic fields, there is a straightforward relationship between the electric and magnetic components, given by Maxwell's equations. In a near field however, the relationship is non-trivial, meaning that the electric and magnetic components must be independently obtained for a full characterisation of the microwave near field above a device. Vapor cell atoms in Rydberg states have been successfully used to detect [47, 48] and image [49] the electric component of microwave fields, E_{mw} . The electric dipole transitions between the closely spaced Rydberg states are at microwave frequencies, and are extremely sensitive to electric fields, with polarisabilities on the order of 1000 times stronger than for transitions from the ground state. Rydberg states are relatively fragile however, and are quickly destroyed in collisions with buffer gas atoms. E_{mw} imaging using Rydberg atoms is therefore incompatible with the high buffer gas pressures we use for B_{mw} imaging with ground state atoms. For sealed cells, such as the M1 and M2 cells used in Chapters 4 and 8, this means that B_{mw} and E_{mw} measurements must be performed using different vapor cells. This is clearly non-ideal, and for field characterisations requiring high spatial resolution, would bring significant experimental challenges in cell alignment. However, we have full control of the buffer gas pressure inside our ultrathin cells⁵, which are attached to a filling station. This makes our setup ideal for measurements of both field components. With the addition of a 480 nm laser to excite Rb Rydberg states, the filling station setup would allow us to perform an E_{mw} measurement without buffer gas, then fill the cell with buffer gas and image B_{mw} .

We could use our ultrathin cells to improve the spatial resolution and distance of approach for E_{mw} imaging by orders of magnitude. As seen in Table 7.1, to date, the proof-of-principle E_{mw} detection and imaging demonstrations have been performed in large and bulky cells. Similarly to our proof-of-principle experiment for B_{mw} imaging in vapor cells [50], E_{mw} imaging has been limited to distances more than 2.7 mm above a microwave device [49]. The longitudinal spatial resolution was at best 3 cm, given by the cell thickness. The 66 μm transverse resolution is somewhat more comparable to the transverse B_{mw} resolution seen in this Chapter, and is essentially given by the resolution of the imaging optics, rather than atomic motion. This is because the Rydberg E_{mw} measurements are performed in the frequency domain, and the response of atomic level splittings to local fields as atoms move through the cell can be considered effectively instantaneous.

E_{mw} imaging would also allow us to detect substantially weaker microwave fields than in our current setup. We can perform an approximate comparison of published sensitivities by using the relationship between E and B for monochromatic plane waves in a vacuum. Maxwell's equations yield

$$B = E/c, \tag{7.3}$$

where c is the speed of light. We can use this relationship to estimate the equivalent B_{mw} (E_{mw}) near field amplitude, given E_{mw} (B_{mw}), as shown in Table 7.1. Due to

⁵Now that we have replaced the leaking valve.

the strong electric polarisability of Rydberg transitions, E_{mw} measurements using Rydberg atoms can be seen to be orders of magnitude more sensitive than even B_{mw} sensing using ultracold atoms.

Table 7.1: Comparison of published B_{mw} and E_{mw} sensitivities, spatial resolutions, and distances of approach. For Rabi-imaging with hot atoms, I give the experimentally achieved sensitivity for a single sensor, and the equivalent sensitivity required by a single scanning sensor to match our parallel measurements on a 120×120 sensor array. I also give the optimised photon shot noise ($\delta B_{photon}^{optimal}$) and atomic projection noise ($\delta B_{atom}^{optimal}$) limits for a single sensor in a $140 \mu\text{m}$ cell (see Section 6.3.3). The Rydberg imaging is described in terms of minimum detectable field, rather than sensitivity.

Technique	δE_{mw} (μV $\text{cm}^{-1} \text{Hz}^{-1/2}$)	δB_{mw} ($\text{T Hz}^{-1/2}$)	Sensor Size (μm^3)	Approach (μm)
Ultracold B_{mw} Single [54]	6×10^4	2.0×10^{-8}	$8.2 \times 8.2 \times 100$	10
Vapor cell B_{mw} Single: δB_{mw}^{exp}	4.2×10^6	1.4×10^{-6}	$50 \times 50 \times 140$	150
Parallel: $\frac{1}{120} \delta B_{mw}^{exp}$	3.5×10^4	1.2×10^{-8}	$50 \times 50 \times 140$	150
$\delta B_{photon}^{optimal}$	2.4×10^5	8.0×10^{-8}	$50 \times 50 \times 140$	150
$\delta B_{atom}^{optimal}$	9	3.0×10^{-12}	$50 \times 50 \times 140$	150
Rydberg E_{mw} Photodiode [47]	30	1.0×10^{-11}	$100 \times 100 \times 10^5$	
Imaging [49]	$50 \mu\text{V}/\text{cm}$	$1.7 \times 10^{-11} \text{ T}$	$66 \times 66 \times 3000$	2700

Chapter 8

Frequency Tunable Imaging

In Chapters 6 and 7, I presented a setup capable of imaging microwave fields above real world devices at the fixed frequency of 6.8 GHz. Wider applications require a frequency tunable technique, with microwave frequencies above 18 GHz of particular interest. In this Chapter, I present a proof-of-principle setup, where a large solenoid is used to Zeeman shift the hyperfine ground state splitting, allowing us to detect microwaves with frequencies ranging from 2.3 GHz to 26.4 GHz.

In this Chapter, all frequencies are given in units of cyclic frequency, not angular frequency. This includes Rabi frequencies.

8.1 Hyperfine Transitions in an Arbitrary DC Magnetic Field

In order to find the ^{87}Rb microwave transition strengths and frequencies in an arbitrary dc magnetic field, we first need to find the hyperfine level energies and eigenvectors. From Chapter 3, we recall that the Hamiltonian for the hyperfine splitting of an atom in an external dc magnetic field $\mathbf{B}_0 = B_z \hat{\mathbf{z}}$ is

$$H = H_{hfs} + H_Z = A_{hfs} \mathbf{I} \cdot \mathbf{J} + \mu_B (g_I I_z + g_J J_z) B_z, \quad (8.1)$$

The angular momentum matrices I_z and J_z are given in Appendix C. The energies of each hyperfine level can be obtained numerically from the eigenvalues of H , or analytically by using the Breit-Rabi formula (Eq. (3.8)). The energy splitting of the hyperfine levels as a function of dc magnetic field is shown in Figure 8.1.a. The levels are labelled $A_1 \rightarrow A_8$, in order of increasing energy ($E_1 < E_2 \dots < E_8$). Figure 8.1.b plots the resulting hyperfine transition frequencies. Transitions between levels A_i and A_f are labelled T_{if} , with energies $E_{if} = E_f - E_i$. The σ_+ transitions are shown in red, π transitions in green, and σ_- transitions are shown in blue.

The H_Z term in Eq. (8.1) means that as the magnetic field is scanned, the eigenfunctions of the Hamiltonian must change. It is therefore best to describe the hyperfine levels in some field-independent basis, for which the $|m_I, m_J\rangle$ basis is a convenient choice. The composition of each of the hyperfine levels in this basis is

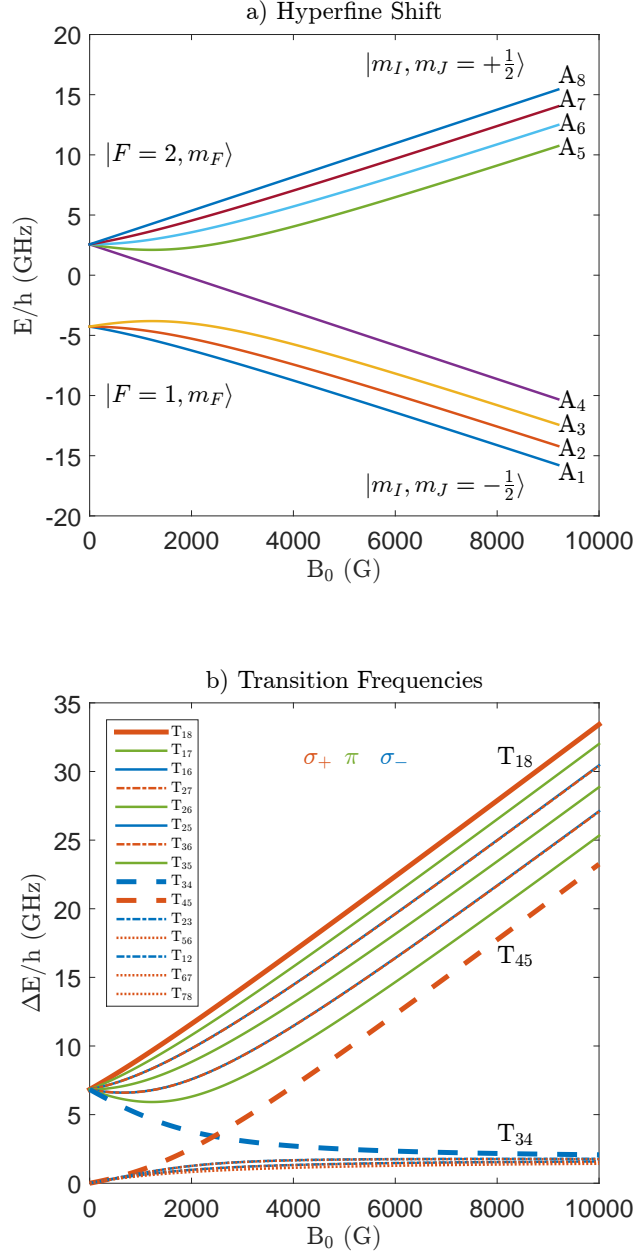


Figure 8.1: a) Energy splitting of the ^{87}Rb hyperfine ground state levels as a function of applied dc magnetic field; b) Hyperfine transition frequencies as a function of applied dc magnetic field. The legend lists the transitions in order of decreasing frequency. The σ_+ transitions are shown in red, π transitions in green, and σ_- transitions are shown in blue. Dashed lines are used for clarity.

Table 8.1: Notation used in this Chapter for the ^{87}Rb $5S_{1/2}$ hyperfine levels. The levels $A_1 \rightarrow A_8$ are in order of increasing energy.

	Weak Field ($ F, m_F\rangle$)	General ($ m_I, m_J\rangle$)	Strong Field ($ m_I, m_J\rangle$)
A ₁	$ 1, 1\rangle$	$a_1 3/2, -1/2\rangle + b_1 1/2, 1/2\rangle$	$ 3/2, -1/2\rangle$
A ₂	$ 1, 0\rangle$	$a_2 1/2, -1/2\rangle + b_2 -1/2, 1/2\rangle$	$ 1/2, -1/2\rangle$
A ₃	$ 1, -1\rangle$	$a_3 -1/2, -1/2\rangle + b_3 -3/2, 1/2\rangle$	$ -1/2, -1/2\rangle$
A ₄	$ 2, -2\rangle$	$ -3/2, -1/2\rangle$	$ -3/2, -1/2\rangle$
A ₅	$ 2, -1\rangle$	$a_5 -3/2, 1/2\rangle + b_5 -1/2, -1/2\rangle$	$ -3/2, 1/2\rangle$
A ₆	$ 2, 0\rangle$	$a_6 -1/2, 1/2\rangle + b_6 1/2, -1/2\rangle$	$ -1/2, 1/2\rangle$
A ₇	$ 2, 1\rangle$	$a_7 1/2, 1/2\rangle + b_7 3/2, -1/2\rangle$	$ 1/2, 1/2\rangle$
A ₈	$ 2, 2\rangle$	$ 3/2, 1/2\rangle$	$ 3/2, 1/2\rangle$

given Table 8.1. In general, each hyperfine level is a superposition of two $|m_I, m_J\rangle$ states, and the coefficients a and b can be determined by numerically diagonalising H^1 . The two stretched states, $|F = 2, m_F = \pm 2\rangle \leftrightarrow |m_I = \pm 3/2, m_J = \pm 1/2\rangle$, are comprised of only a single $|m_I, m_J\rangle$ for all fields. In the absence of dc magnetic field, a and b are given by the Clebsch-Gordon coefficients, listed in Table 8.2. As the dc field strength increases, $a \rightarrow 1$ and $b \rightarrow 0$.

Figure 8.2 plots the a and b coefficients for each level as a function of dc magnetic field, showing the changing composition of each hyperfine level in the $|m_I, m_J\rangle$ basis. The subplots are ordered according to the weak field $|F, m_F\rangle$ positions of the states, with the F=2 states on the top row, and the F=1 states on the bottom row. The superposition states are listed above each subplot, with the a coefficient state, which dominates at high dc magnetic fields, listed on top. Even at a field strength of 1 T, the b coefficient is still non-negligible, with an approximate value of $b = 0.1$.

Table 8.2: Coefficients a and b in the $|m_I, m_J\rangle$ basis for the ^{87}Rb $5S_{1/2}$ hyperfine levels in the absence of external static magnetic field. The coefficients are the relevant Clebsch-Gordon coefficients for each state [208].

	$ F, m_F\rangle$	a	b
A ₁	$ 1, 1\rangle$	$\sqrt{3}/2$	$-1/2$
A ₂	$ 1, 0\rangle$	$1/\sqrt{2}$	$-1/\sqrt{2}$
A ₃	$ 1, -1\rangle$	$1/2$	$-\sqrt{3}/2$
A ₄	$ 2, -2\rangle$		
A ₅	$ 2, -1\rangle$	$1/2$	$\sqrt{3}/2$
A ₆	$ 2, 0\rangle$	$1/\sqrt{2}$	$1/\sqrt{2}$
A ₇	$ 2, 1\rangle$	$\sqrt{3}/2$	$1/2$
A ₈	$ 2, 2\rangle$		

¹I.e. a and b are the coefficients of the eigenvectors for each hyperfine level.

The strengths of the hyperfine transitions also change with the dc magnetic field, and are proportional to the $\langle f | J_\gamma | i \rangle$ matrix element, where $\gamma = -, \pi, +$ is the transition polarisation. Figure 8.3 gives the strengths of σ_\pm and π transitions from each hyperfine level for varying static magnetic field, plotting the $\langle f | J_\gamma | i \rangle$ matrix elements as a function of dc magnetic field. The subplots are again ordered according to the weak field $|F, m_F\rangle$ positions of the states. Transitions within each of the two hyperfine groups (ie $F = 1, F = 2$ at weak fields and $m_J = +1/2, m_J = -1/2$ at strong fields) are shown in dashed lines. The key feature of Figure 8.3 is that as the magnetic field strength is increased, σ_+ transitions come to dominate, and σ_- and π transitions become weak. The σ_+ transition strengths within the hyperfine groups also go to zero at high dc fields. As a practical comparison, for $\langle f | J_\gamma | i \rangle = 1$, a $B_{mw} = 1 \mu\text{T}$ microwave field will drive $\Omega_R = 28 \text{ kHz}$ Rabi oscillations, whilst for the same microwave field, $\langle f | J_\gamma | i \rangle = 0.1$ results in $\Omega_R = 2.8 \text{ kHz}$ Rabi oscillations².

²Remember, all frequencies in this Chapter are given in units of cyclic frequency, and not angular frequency.

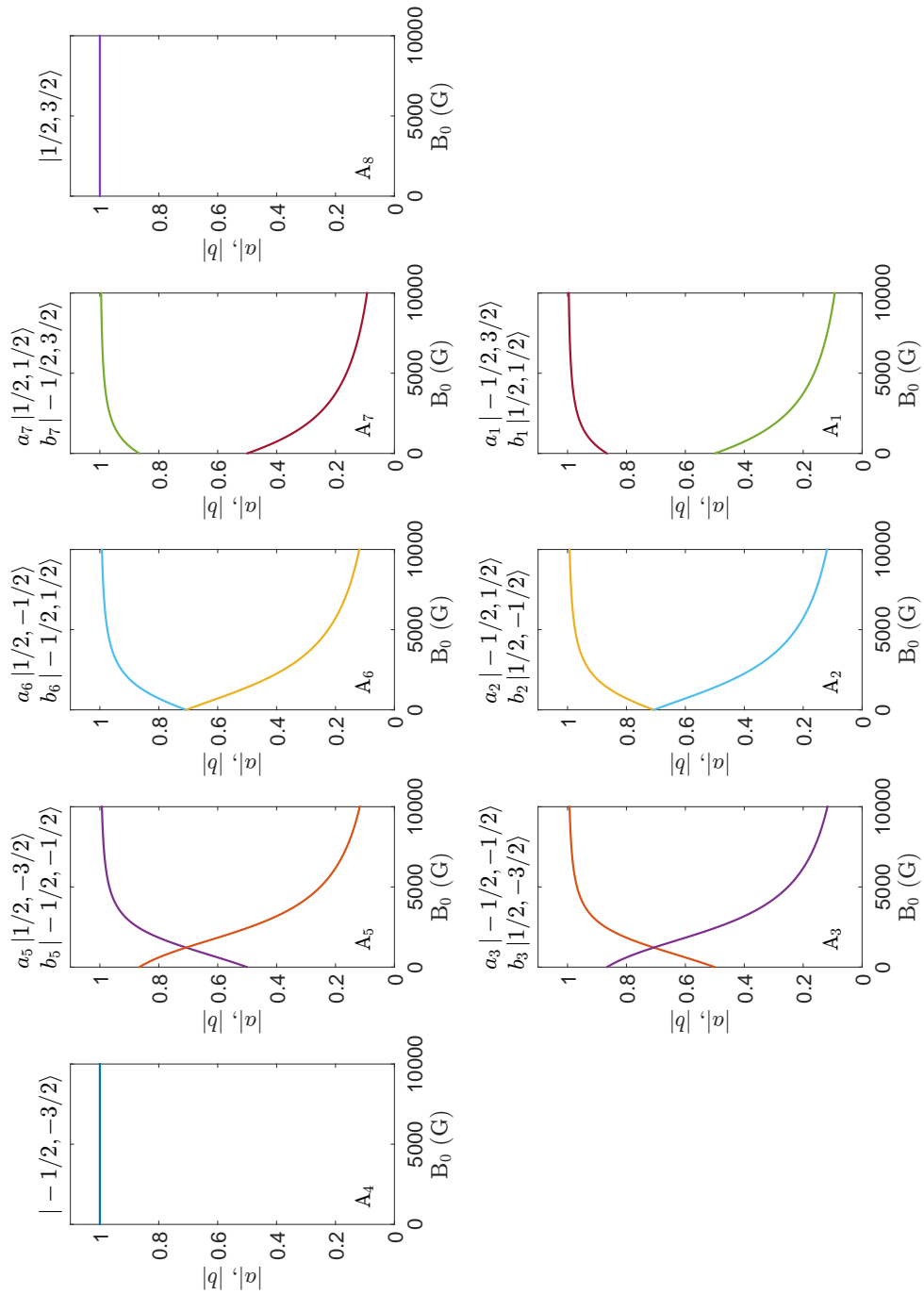


Figure 8.2: Composition of the $^{87}\text{Rb } 5^2S_{1/2}$ hyperfine levels in the $|m_I, m_J\rangle$ basis as a function of applied dc magnetic field. The $|m_I, m_J\rangle$ states for each hyperfine level are listed above each subplot, with the $|m_I, m_J\rangle$ state dominating at high magnetic fields listed on top.

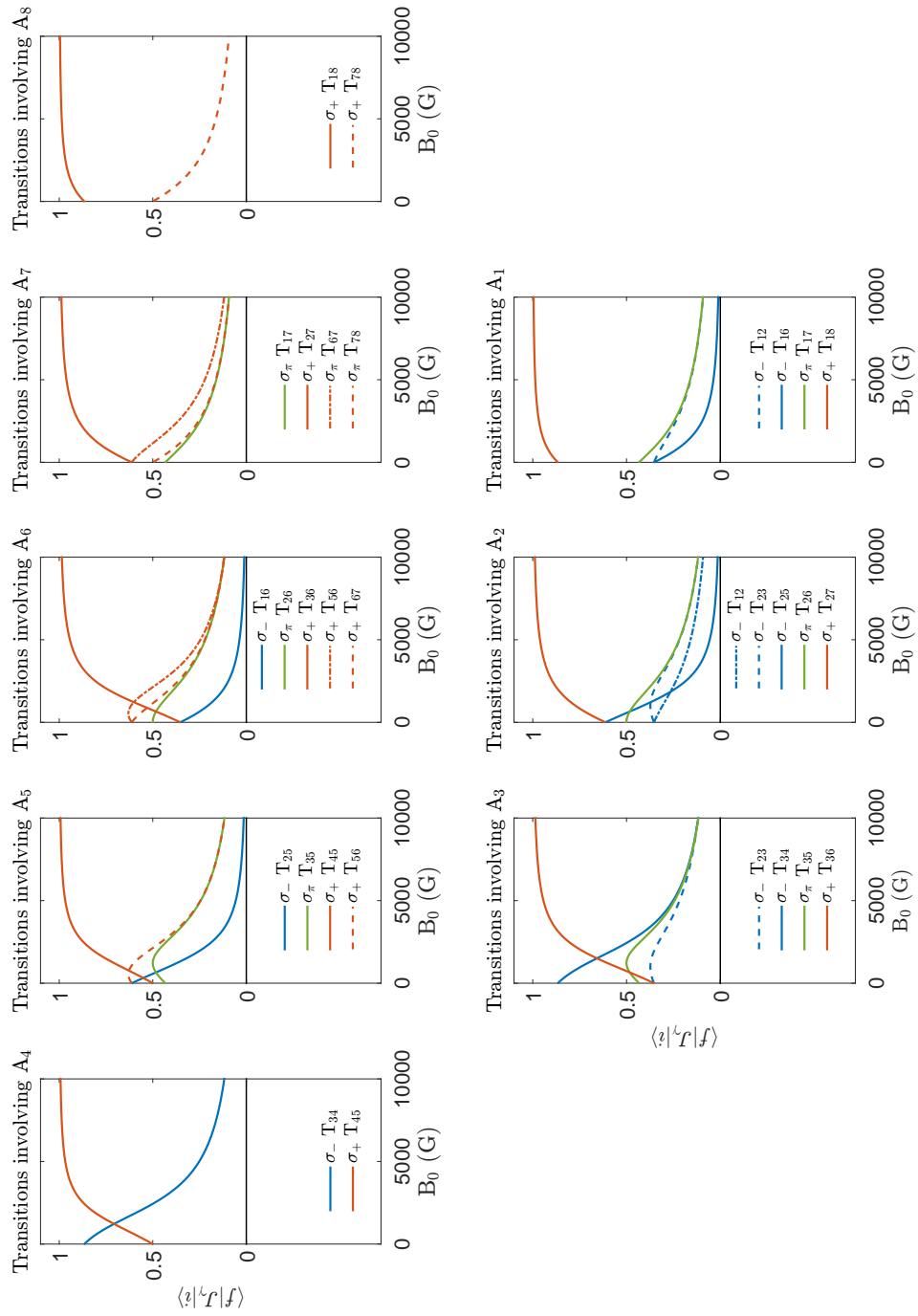


Figure 8.3: Strengths of the σ_+ , π , and σ_- hyperfine transitions within the ^{87}Rb $5^2S_{1/2}$ ground state, as a function of external dc magnetic field.

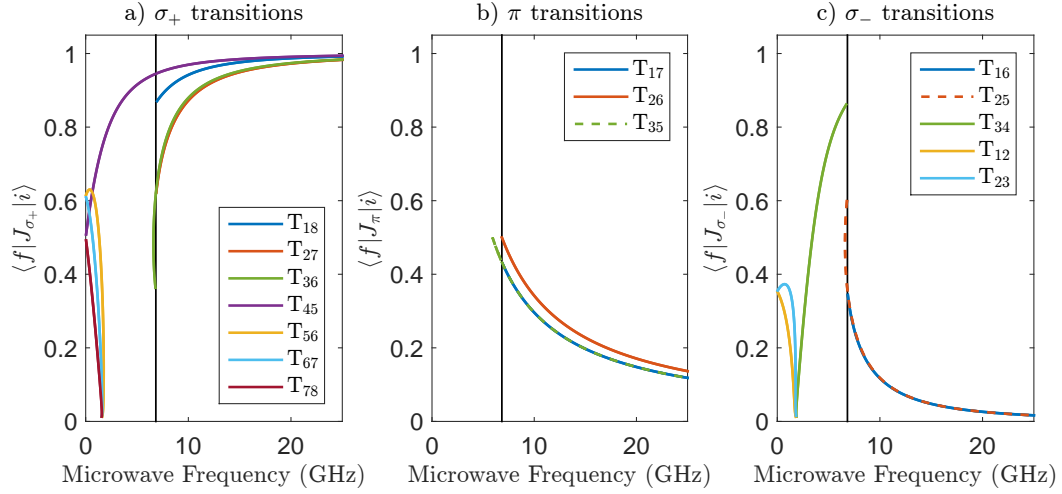


Figure 8.4: Strengths of the σ_+ , π , and σ_- hyperfine transitions within the ^{87}Rb $5^2S_{1/2}$ ground state, as a function of the microwave transition frequency. The black vertical line is at 6.835 GHz.

8.1.1 Hyperfine Transitions for Microwave Sensing

The important considerations when choosing a hyperfine transition for microwave sensing are: the microwave frequency of interest, the hyperfine transition strength, the optical resolution of the hyperfine transition states (i.e. the degree to which absorption due to each state can be distinguished), the microwave polarisation of interest, and the dc magnetic field required to tune a hyperfine transition to frequency of interest. Figure 8.4 provides a useful analysis tool, showing the σ_+ , π , and σ_- transition strengths as a function of microwave transition frequency.

T_{45} is the most versatile σ_+ transition, covering all microwave frequencies above dc. Above 0.6 GHz, it is also the strongest σ_+ transition for a given microwave frequency. As seen in Section 8.4, however, the optical resolution of the neighbouring A_4 and A_5 states can be poor, particularly at low B_{dc} (corresponding to low microwave frequencies). For microwave sensing of frequencies above 6.835 GHz, the best σ_+ transition is therefore generally T_{18} . The A_1 and A_8 levels are maximally spectrally resolved from one another, and optical transitions from these levels enjoy minimal background absorption due to ^{85}Rb . The T_{18} transition is almost as strong as T_{45} for a given microwave frequency, and requires much smaller B_{dc} to be tuned to a given frequency. For example, to achieve an 18 GHz microwave transition requires $B_{dc} = 0.44$ T on the T_{18} transition, but $B_{dc} = 0.81$ T on the T_{45} transition.

The selection of π microwave transition is less clear-cut. T_{26} is the strongest π transition, but the difference with T_{17} and T_{35} is not dramatic. T_{17} has the best optical resolution, due to the low ^{85}Rb absorption background for optical transitions from A_1 and the large spectral separation of the A_1 and A_7 levels. The T_{35} transition is first-order insensitive to dc magnetic fields around $B_{dc} = 0.12$ T, corresponding to

Table 8.3: Summary of the transitions available in various alkali species for sensing the σ_+ , π , and σ_- components of a microwave field. I is the nuclear spin. I took the maximum σ_+ frequency as the highest transition frequency available at our maximum solenoid field, $B_{dc} = 0.8$ T. Plots of the transitions strengths as a function of transition frequency are given in Appendix D.

Isotope	Abundance	I	E_{hfs}/h (GHz)		Min. (GHz)	Max. (GHz)
^{23}Na	1	3/2	1.772	σ_+	0	23.8
				π	1.53	5.90
				σ_-	0.56	2.35
^{39}K	0.9326	3/2	0.462	σ_+	0	22.8
				π	0.40	1.54
				σ_-	0.15	0.61
^{85}Rb	0.7217	5/2	3.036	σ_+	0	25.0
				π	2.26	10.1
				σ_-	0.74	4.15
^{87}Rb	0.2783	3/2	6.835	σ_+	0	27.9
				π	5.92	22.8
				σ_-	2.17	9.06
^{133}Cs	1	7/2	9.193	σ_+	0	30.8
				π	6.08	30.6
				σ_-	1.62	12.7

a microwave frequency of 5.92 GHz, and is thus the optimal transition around this point. Figure 8.4 indicates that the π transitions can be used for sensing microwaves even above 20 GHz, with the T_{26} transition strength dropping to $\langle 6 | J_\pi | 2 \rangle = 0.15$ at 22.8 GHz.

The σ_- transition strengths quickly drop away for microwave frequencies above 6.835 GHz, with the T_{16} and T_{25} transition strengths dropping to $\langle f | J_{\sigma_-} | i \rangle = 0.15$ at 9.06 GHz. However, the T_{34} transition can be used to detect microwaves below 6.835 GHz. The T_{34} transition strength drops to $1/e \langle 4 | J_{\sigma_-} | 3 \rangle = 0.15$ at 2.17 GHz.

We can perform a similar analysis for other alkali species. Plots of microwave transition strengths as a function of transition frequency for ^{23}Na , ^{39}K , ^{85}Rb , and ^{133}Cs are given in Appendix D. The ranges of detectable frequencies for σ_+ , π , and σ_- polarised microwaves are summarised in Table 8.3. The frequency range was defined as that for which there is a transition with a strength above $\langle f | J_\gamma | i \rangle = 0.15$, neglecting transitions between states with the same m_J value. Strong σ_+ polarised transitions are available at all microwave frequencies and dc magnetic field strengths, however, and order to compare the different alkali species, I took the maximum σ_+ frequency as the highest transition frequency available at our maximum solenoid field, $B_{dc} = 0.8$ T. Vapor cells filled with multiple species can be used to span larger frequency ranges. For example, a natural Rb cell provides π transitions over the range 2.26 – 22.8 GHz.

8.2 Reconstruction of Microwave Fields of Arbitrary Frequency

In this section, I provide a framework for reconstructing a microwave magnetic field using ^{87}Rb atoms in an applied static magnetic field (\mathbf{B}_0) of any strength. This builds on the framework given for the weak field regime in Chapter 3. The framework is not restricted to ^{87}Rb , and is valid for microwave transitions in a general system.

Recalling Chapter 3, the components of the microwave magnetic field are defined

$$B_- e^{-i\phi_-} \equiv \frac{1}{2} \left[B_{x'} e^{-i\phi_{x'}} + i B_{y'} e^{-i\phi_{y'}} \right], \quad (8.2)$$

$$B_\pi e^{-i\phi_\pi} \equiv B_{z'} e^{-i\phi_{z'}}, \quad (8.3)$$

$$B_+ e^{-i\phi_+} \equiv \frac{1}{2} \left[B_{x'} e^{-i\phi_{x'}} - i B_{y'} e^{-i\phi_{y'}} \right], \quad (8.4)$$

with the Rabi frequencies defined

$$\Omega_- \equiv \frac{2\mu_B}{\hbar} \langle f | J_- | i \rangle B_- e^{-i\phi_-}, \quad (8.5)$$

$$\Omega_\pi \equiv \frac{2\mu_B}{\hbar} \langle f | J_z | i \rangle B_\pi e^{-i\phi_\pi}, \quad (8.6)$$

$$\Omega_+ \equiv \frac{2\mu_B}{\hbar} \langle f | J_+ | i \rangle B_+ e^{-i\phi_+}. \quad (8.7)$$

The angular momentum matrices, J_γ , are given in Appendix C, where $\gamma = -, \pi, +$ is the polarisation of the transition. The microwave amplitude is then given by

$$B_\gamma = |\alpha_{if}| \frac{\hbar}{\mu_B} |\Omega_\gamma|, \quad (8.8)$$

where if labels the hyperfine transition, and

$$\alpha_{if} \equiv \frac{1}{2 \langle f | J_\gamma | i \rangle}. \quad (8.9)$$

8.2.1 Microwave Amplitude

From Eq. (8.6), it is straightforward to determine the amplitudes of the microwave magnetic field (B_x , B_y and B_z) when strong π transitions are present. The matrix element $\langle f | J_z | i \rangle$ can be calculated numerically for a any static magnetic field, and so we can obtain the amplitudes along each axis by measuring $|\Omega_\pi|$ with the quantisation axis along X , Y and Z respectively. The π (and σ_-) transitions become very weak in the strong field regime, however, and in the general case, we need to determine the microwave field amplitudes using only σ_+ transitions.

In the following discussion, the superscript index represents the quantisation axis in the lab frame, i.e. the direction of the applied static magnetic field. Thus for example, Ω_+^{+y} (B_+^{+y}) means Ω_+ (B_+) for \mathbf{B}_0 pointing along the Y axis in the

positive direction, whilst Ω_+^{-y} (B_+^{-y}) is for \mathbf{B}_0 pointing along the Y axis in the negative direction.

We begin by finding the sum of B_-^2 and B_+^2 . From Eq. (8.7) we see that for σ_+ transitions, we only obtain B_+ . However, for measurements along a given axis, B_+ measured antiparallel to that axis is equivalent to B_- measured parallel to the axis. That is, $B_+^- = B_-^+$. By measuring $|\Omega_+|$ with the static field both parallel and antiparallel to our axis of measurement, we can thus obtain both B_+ and B_- . This gives us

$$B_-^2 + B_+^2 = \frac{\hbar^2}{4\mu_B^2} \left[\frac{|\Omega_+^-|^2}{|\langle f | J_+ | i \rangle|^2} + \frac{|\Omega_+^+|^2}{|\langle f | J_+ | i \rangle|^2} \right]. \quad (8.10)$$

We can also find the $B_-^2 + B_+^2$ sum using Eqs. (8.2) and (8.4). Equating this with Eq. (8.10) gives

$$\frac{1}{2}(B_{x'}^2 + B_{y'}^2) = \frac{\hbar^2}{4\mu_B^2} \left[\frac{|\Omega_+^-|^2}{|\langle f | J_+ | i \rangle|^2} + \frac{|\Omega_+^+|^2}{|\langle f | J_+ | i \rangle|^2} \right]. \quad (8.11)$$

Defining

$$K_+ \equiv \frac{|\Omega_+^-|^2}{|\langle f | J_+ | i \rangle|^2} + \frac{|\Omega_+^+|^2}{|\langle f | J_+ | i \rangle|^2}, \quad (8.12)$$

we can write

$$B_{x'}^2 + B_{y'}^2 = \frac{\hbar^2}{2\mu_B^2} K_+. \quad (8.13)$$

Next, we apply this formula with the quantisation axis defined along each of the X , Y and Z axes. Starting with \mathbf{B}_0 along the X axis, and thus with z' along x , we transform from the primed coordinate system back into the unprimed lab frame, according to the following coordinate transformation:

$$x' = -z, \quad (8.14)$$

$$y' = y, \quad (8.15)$$

$$z' = x. \quad (8.16)$$

$$(8.17)$$

This transforms the microwave magnetic field phasor to

$$\mathbf{B} \equiv \begin{pmatrix} B_{x'} e^{-i\phi_{x'}} \\ B_{y'} e^{-i\phi_{y'}} \\ B_{z'} e^{-i\phi_{z'}} \end{pmatrix} = \begin{pmatrix} -B_z e^{-i\phi_z} \\ B_y e^{-i\phi_y} \\ B_x e^{-i\phi_x} \end{pmatrix},$$

with

$$\begin{aligned} B_{x'} &= B_z & \phi_{x'} &= \phi_z + \pi, \\ B_{y'} &= B_y & \phi_{y'} &= \phi_y, \\ B_{z'} &= B_x & \phi_{z'} &= \phi_x. \end{aligned} \quad (8.18)$$

Applying this coordinate transformation to Eq. (8.13) then gives us

$$B_z^2 + B_y^2 = \frac{\hbar^2}{4\mu_B^2} K_+^x, \quad (8.19)$$

with K_+^x defined in Eq. (8.25). We can follow a similar process for \mathbf{B}_0 along the Y and Z axes to get

$$B_z^2 + B_x^2 = \frac{\hbar^2}{4\mu_B^2} K_+^y, \quad (8.20)$$

$$B_x^2 + B_y^2 = \frac{\hbar^2}{4\mu_B^2} K_+^z. \quad (8.21)$$

Solving these equations simultaneously gives the magnitude of the magnetic field along the (lab frame) X , Y , and Z directions,

$$B_x^2 = \frac{\hbar^2}{8\mu_B^2} \left[-K_+^x + K_+^y + K_+^z \right], \quad (8.22)$$

$$B_y^2 = \frac{\hbar^2}{8\mu_B^2} \left[K_+^x - K_+^y + K_+^z \right], \quad (8.23)$$

$$B_z^2 = \frac{\hbar^2}{8\mu_B^2} \left[K_+^x + K_+^y - K_+^z \right], \quad (8.24)$$

where K_+^γ is defined as

$$K_+^\gamma \equiv \frac{|\Omega_+^{-\gamma}|^2}{|\langle f | J_+ | i \rangle|^2} + \frac{|\Omega_+^{+\gamma}|^2}{|\langle f | J_+ | i \rangle|^2}. \quad (8.25)$$

$|\Omega_+^{-\gamma}|$ and $|\Omega_+^{+\gamma}|$ are experimentally determined quantities. The matrix element $\langle f | J_+ | i \rangle$ can be calculated numerically for a general applied static magnetic field, \mathbf{B}_0 .

8.2.2 Microwave Phase

To reconstruct the field phases, ϕ_x , ϕ_y and ϕ_z , we begin with the difference of B_-^2 and B_+^2 . Again, this can be found using Eq. (8.7), measuring $|\Omega_+|$ with the static field both parallel and antiparallel to our axis of measurement, and also using Eqs. (8.2) and (8.4):

$$B_-^2 - B_+^2 = \frac{\hbar^2}{4\mu_B^2} \left[\frac{|\Omega_+^-|^2}{|\langle f | J_+ | i \rangle|^2} - \frac{|\Omega_+^+|^2}{|\langle f | J_+ | i \rangle|^2} \right] = B_{x'} B_{y'} \sin(\phi_{y'} - \phi_{x'}).$$

This time we define

$$K_- \equiv \frac{|\Omega_+^-|^2}{|\langle f | J_+ | i \rangle|^2} - \frac{|\Omega_+^+|^2}{|\langle f | J_+ | i \rangle|^2},$$

and so we have

$$\sin(\phi_{y'} - \phi_{x'}) = \frac{\hbar^2}{4\mu_B^2 B_{x'} B_{y'}} K_-. \quad (8.26)$$

We measure $|\Omega_+|^2$ parallel and antiparallel to the X , Y , and Z axes, and use equation 8.26 with the same coordinate transformations as in Section 8.2.1. Inserting the field magnitudes obtained with equations 8.22-8.24, we get

$$\sin(\phi_z - \phi_y) = 2 \left[(K_+^x - K_+^y + K_+^z)(K_+^x + K_+^y - K_+^z) \right]^{-1/2} K_-, \quad (8.27)$$

$$\sin(\phi_x - \phi_z) = 2 \left[(-K_+^x + K_+^y + K_+^z)(K_+^x + K_+^y - K_+^z) \right]^{-1/2} K_-, \quad (8.28)$$

$$\sin(\phi_y - \phi_x) = 2 \left[(-K_+^x + K_+^y + K_+^z)(K_+^x - K_+^y + K_+^z) \right]^{-1/2} K_-, \quad (8.29)$$

with K_+^γ as defined in equation 8.25 and K_-^γ defined as K_- for a static magnetic field along the direction γ :

$$K_-^\gamma \equiv \frac{|\Omega_+^{-\gamma}|^2}{|\langle f | J_+ | i \rangle|^2} - \frac{|\Omega_+^{+\gamma}|^2}{|\langle f | J_+ | i \rangle|^2}. \quad (8.30)$$

$|\Omega_+^{-\gamma}|$ and $|\Omega_+^{+\gamma}|$ are experimentally determined quantities. The matrix elements $\langle f | J_- | i \rangle$ and $\langle f | J_+ | i \rangle$ can be calculated numerically for a general applied static magnetic field, \mathbf{B}_0 .

8.3 Experiment Setup

I used two vapor cells in this Chapter, both produced using the same design by the Mileti group in Neuchâtel, Switzerland [10, 177]. I primarily used the M1 cell, filled with natural Rb and 63 mbar of N_2 buffer gas, which was also used in Chapter 4. The second cell, M2, was filled with Rb enriched to 75% ^{87}Rb and a buffer gas mixture of 15.3 mbar of N_2 and 18.7 mbar of Ar.

For simplicity, I used a single laser beam for optical pumping and probing. The commercial 780 nm laser³ was chosen for its large, 80 GHz mode-hop-free tuning range, which allowed us to measure the optical spectrum in a single sweep.

I experimented with a range of microwave devices, including antennas, microwave horns, and a coplanar waveguide. For the results presented in this Chapter, I simply used an SMA jack⁴, as seen in Figure 8.5.c. The SMA jack responded relatively well over the broad range of microwave frequencies used, and was small enough to easily fit within the tight geometry imposed by the solenoid.

³Newport, TLB-6712 Velocity Laser. This is a great laser when it works, but it is very time-consuming to get repaired in Europe, as all repairs are performed in the USA. Our brand new laser broke after less than an hour of use, and repairs took 2 months.

⁴Molex, 73251-2120

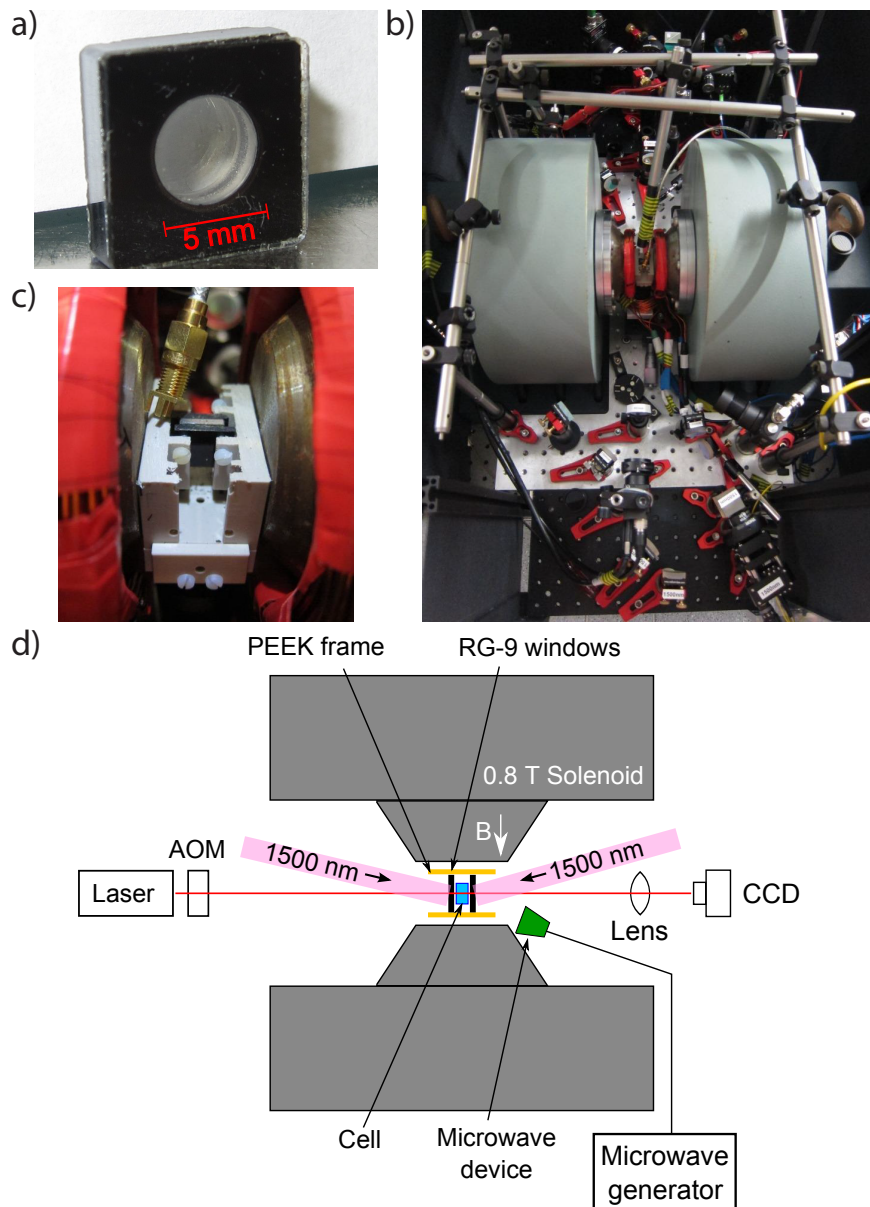


Figure 8.5: a) Photo of the M1 cell, which was predominantly used in this Chapter. The design of the M2 cell is identical; b) photo of the experiment setup, showing the solenoid in grey; c) the vapor cell sandwiched between two RG-9 glass pieces and mounted on the PEEK frame inside the solenoid. The gold microwave output coupler can be seen above the cell, near the optimised point for coupling 18 GHz microwaves in to the microwave cavity created by the solenoid cones; d) schematic of the experiment setup.

8.3.1 Solenoid

I used a 0.8 T solenoid⁵ to provide the dc magnetic field in this Chapter. As seen in Figures 8.5.b and 8.5.c, the solenoid is comprised of two sets of water-cooled wires, each wrapped around a metal (presumably iron) core. The cores extend as tapered cones towards the solenoid centre, and are separated by a gap of 26 mm.

The solenoid field is homogeneous to better than 10^{-3} in the region seen by the cell (as seen in Figure 8.11.a). However, as the dc magnetic fields were on the order of 1000 G, the inhomogeneities were nevertheless on the order of a few gauss. Atomic motion through this inhomogeneous B_{dc} field was the dominant dephasing mechanism, resulting in coherence times on the order of $\tau_2 \lesssim 20 \mu\text{s} \approx 0.1 T_1$, and presenting a significant experimental challenge.

To align the cell to the centre of the Y and Z components of the dc field, I used quasi-real-time streaming of OD images, as described Section 3.4.6. I illuminated the cell with a near-resonant microwave field, so that the OD image streaming provided images of OD_{mw} in the cell (like that in Figure 8.11.b), with a 0.3 Hz frame rate. To optimise the cell position along the X axis, I passed a narrow laser beam through the spatial centre of the dc magnetic field, and adjusted the cell position with a translation stage to minimise the FWHM DR peak.

In an attempt to flatten the inhomogeneous field in the centre of the solenoid, I installed three sets of coils, along each of the X , Y , and Z axes. The Z axis pair can be seen in red in Figure 8.5. The correction field needed to be on the order of 1-5 G to match the size of the solenoid field inhomogeneities. Application of the correction field then shifted the atomic transition frequency by a few MHz. This shift was too large to practically use the offset coils, as it would quickly shift the transition outside of a given microwave frequency scan range.

The solenoid magnetic field experiences drifts on the order of gauss on a 10s of minutes timescale. This prevents taking many runs to average together, and meant that I had to optimise the microwave frequency immediately before running each Rabi sequence. The optimisation was performed either using the DR signal in the centre of the dc magnetic field, detected on a photodiode, or by using streamed OD_{mw} images and manually scanning the microwave frequency.

The two solenoid cores imposed boundary conditions on the microwaves in the 26 mm space between them, and may have formed a crude microwave cavity. The strongest microwave signals in the cell were generally seen when the SMA jack was placed near one of the solenoid cores, rather than directly over the cell (see Figure 8.5.c), and the resulting microwave fields appeared reasonably uniform over the cell volume. Although the influence of the solenoid on microwave fields was not critical in the proof-of-principle microwave imaging presented in this Chapter, it is of course of major concern when attempting to image the near fields above microwave devices. We may find, however, that the solenoid influence becomes negligible in a high resolution setup, such as the ultrathin cells used in Chapters 6 and 7. The cell

⁵Brukner, B-E 10 solenoid with B-MN C4 power supply. Made in 1979 and found in the basement.

wall thickness of the M1 and M2 cells prevented imaging microwave fields closer than 2 mm from a microwave source. The ultrathin cells, on the other hand, allow imaging as close as $150\ \mu\text{m}$ from a source, at which distance the amplitude of microwaves reflected from the solenoid may be negligible compared with the near field produced by the device.

8.3.2 Temperature Control by Laser Heating

Due to the high dc magnetic fields and spatial constraints imposed by the solenoid, we avoided using resistive heaters in this setup. Instead, we heated the cell using a 1500 nm laser⁶. The cell was placed between two 2 mm thick pieces of RG9 glass, which is strongly absorptive at 1500 nm, but has better than 90% transmission at 780 nm⁷. The use of a 1500 nm laser with RG9 glass has seen great success in low-power, miniaturised vapor cell devices, such as chip-scale atomic clocks and magnetometers [209]. In Ref. [209], a $(1.5\ \text{mm})^3$ cell was heated to 150°C using only 140 mW of heating power. Our setup is somewhat less efficient, requiring approximately 2 W of laser output power to achieve cell temperatures of $90 - 120^\circ\text{C}$. This is due to a number of factors, in particular thermal isolation, and also the heating laser beam size and alignment. The best efficiencies are reached for vapor cells placed inside a second vacuum cell. Nonetheless, I found that using a laser to heat the cell was extremely effective. The temperature of the cell quickly responded to the heating laser, reaching equilibrium within minutes of heating (compared to hours for the filling station setup in Chapters 6 and 7). The direct heating of the cell windows ensures that there is no build-up of Rb on the windows, and the localised cell heating will be advantageous for future imaging of the microwave fields produced by temperature-sensitive devices.

The local nature of the heating made it difficult to measure the cell temperature with external sensors, and the only reliable measure was the atoms themselves. I could obtain the cell temperature by fitting the absorption spectra (taken at $B_{dc} = 0$) with the OD model described in Section 2.3.

One downside of the RG9 glass is that it is opaque over the visible spectrum. This complicates the alignment of the heating lasers with the cell windows, which cannot be seen. The temporal response of the cell temperature is reasonably fast, however, on the minute scale or faster, and a DR signal can be used for a coarse optimisation of the heating laser alignment.

In an optimised setup, the heating laser would only illuminate one side of the cell, and the front RG9 thickness would be 0.25 mm, chosen to absorb 50% of the heating light [209]. The back RG9 piece would remain thick, to ensure complete absorption of the remaining heating light. It may also be possible to directly heat the cell windows, without the use of RG9 glass. This would be less efficient, requiring more heating laser power, but it would eliminate the 780 nm light losses through

⁶Seminex, 15P-112, 4 W maximum output

⁷RG9 Schott glass, data sheet available, for example, at http://www.vpglass.com/filter_glass/schott_rg9_filter_glass.html

the RG9 glass. Although these losses are relatively small in the current setup, RG9 losses would become problematic in the multipass cells discussed in Chapter 9.

8.4 Optical Transitions in an Arbitrary Magnetic Field

The dc magnetic fields used to shift the hyperfine transitions also affect the optical transitions. Figure 8.6 shows calculated and measured optical spectra in the M1 and M2 cells for a selection of dc magnetic field strengths. The calculated spectra were obtained using the program ElecSus [90], with zero detuning corresponding to the centre of the ^{87}Rb D₂ line. The measured spectra were obtained from the transmission of a weak laser illuminating the entire cell, which was detected using a photodiode. The laser intensity was $I = 35 \mu\text{W}/\text{cm}^2$ for the M1 cell measurements, and $I = 400 \mu\text{W}/\text{cm}^2$ for the M2 cell measurements. The laser polarisation is controlled by a $\lambda/2$ plate placed after a polarising beam-splitter. With the laser propagation perpendicular to the quantisation axis provided by the solenoid, the laser polarisation can thus be tuned from π polarised, through an equal mixture of π , σ_- , and σ_+ polarisation (33% each), to an equal mixture of σ_- , and σ_+ polarisation (50% each). Measured spectra are shown for the 50/50 σ_-/σ_+ mixture and for π polarised light. ElecSus is currently only able to analyse σ transitions, and so only the 50/50 σ_-/σ_+ calculated spectrum is shown. The data represent a single frequency sweep of the laser, without averaging, and with a sweep rate of 1 Hz. Differences in the calculated and measured spectral shapes (e.g. for the $B_{dc} = 0.2\text{ T}$ M2 cell spectrum) can be attributed to small differences between the experimental dc magnetic field and that used for modelling. For the M2 cell, the flattened left-most peak measured in the zero-field spectra is due to the high OD, and corresponding loss of signal on the photodiode.

Figure 8.6 shows that the π , σ_- , and σ_+ optical transitions diverge in frequency as B_{dc} is increased, as is also seen in the hyperfine transitions. This implies that for a laser polarisation of 50/50 σ_-/σ_+ light, a single transition can absorb at most 50% of the laser light, limiting peak heights to $OD = 0.7$. Due to the large spectral separation of the transition frequencies for each polarisation, this is not affected by the 1-1.5 GHz optical linewidths in the two cells. However, the measured spectra for both cells in Figure 8.6 show $OD \gg 0.7$ for absorption due to σ_- or σ_+ transitions. This implies that the laser polarisation (as defined by the solenoid B_{dc} field) changes as the beam passes through the cell. It is not immediately clear how this occurs. One possibility is that the laser polarisation undergoes sufficient Faraday rotation through the cell such that incident σ_- polarised light can be significantly absorbed by σ_+ transitions. In order to match the theory and measured spectra, I calculated the spectra in Figure 8.6 separately for σ_{\pm} transitions, assuming 100% σ_{\pm} polarised incident laser light, and then summed the resulting absorption spectra. To roughly match the experimental and calculated OD amplitudes, I multiplied the calculated spectra by a factor $\alpha = 0.5$. Regardless, the experimental data shows larger absorption on the π peaks, and I therefore performed the microwave detection and imaging

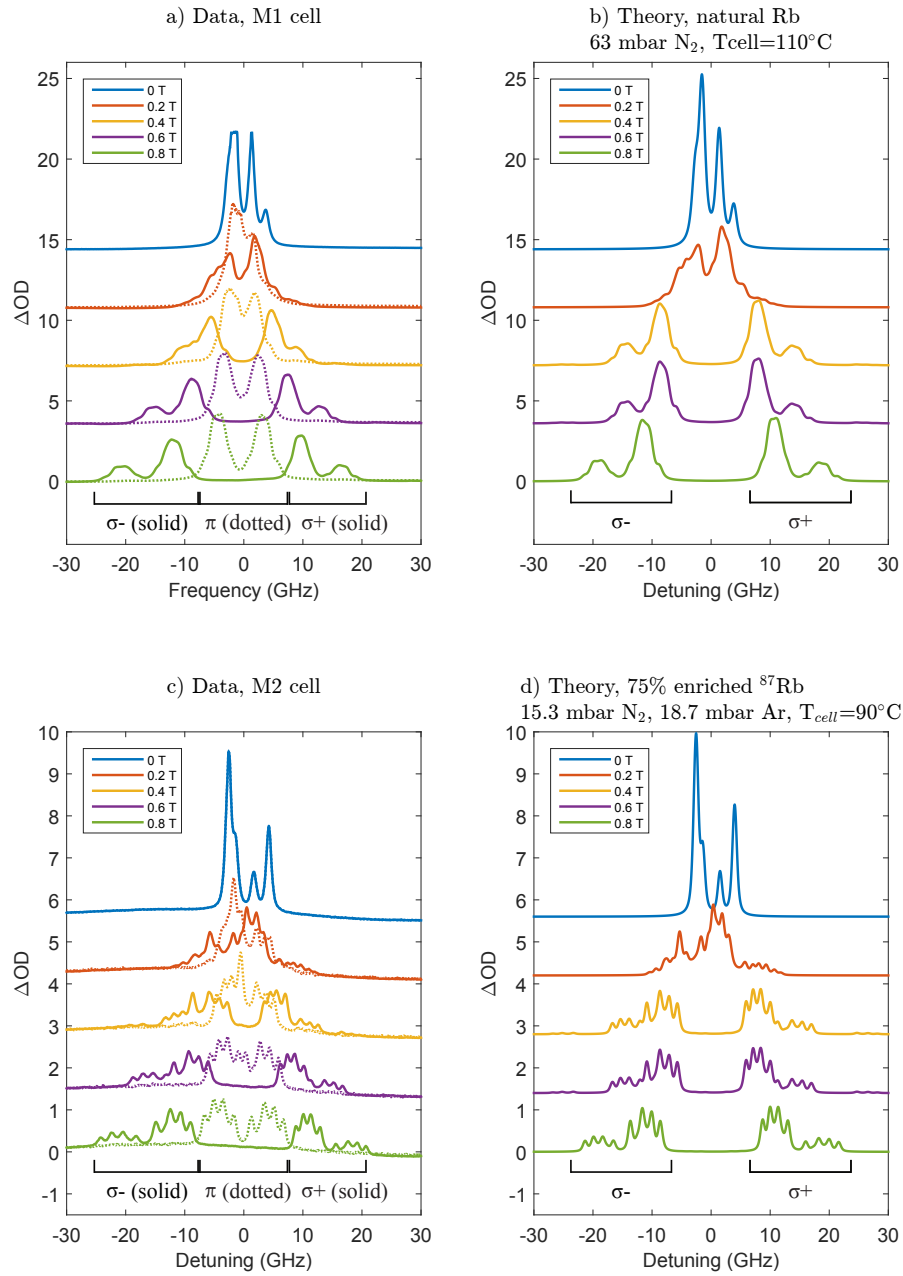


Figure 8.6: a) Calculated and b) measured optical spectra as a function of dc magnetic field in the M1 cell; c) calculated and d) measured spectra in the M2 cell. Solid lines show spectra for light 50% σ_- polarised and 50% σ_+ polarised (solid lines). Measured spectra are also shown for π polarised light (dotted lines). The spectra at different B_{dc} are vertically offset for clarity.

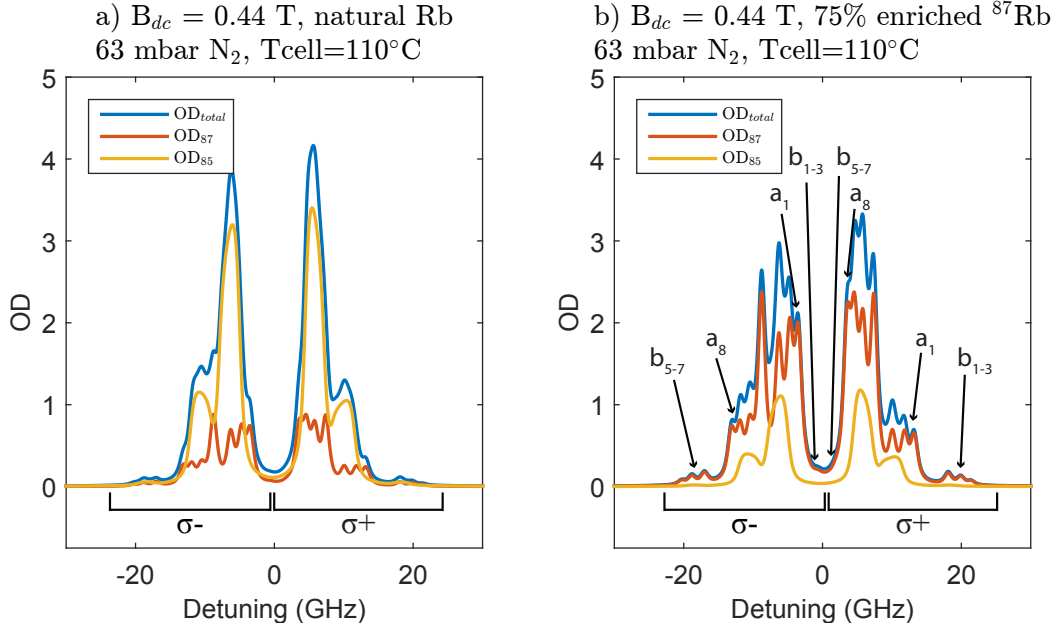


Figure 8.7: Calculated optical spectra, including the contributions from ^{87}Rb and ^{85}Rb , for a) the M1 cell and b) for the same cell but with enriched ^{87}Rb . The spectra are shown for $B_{dc} = 0.44$ T and 50/50 σ_-/σ_+ polarised light. The coupling to each of the a and b coefficient states is labelled in (b).

using π polarised light.

Figure 8.7 examines optical spectra for $B_{dc} = 0.44$ T in more detail. The spectra were calculated using ElecSus, and $B_{dc} = 0.44$ T was chosen as it was the dc field used for imaging 18 GHz microwaves in Section 8.6. Like for Figure 8.6, I calculated the spectra separately for σ_\pm transitions, assuming 100% σ_\pm polarised incident laser light, and summed the resulting absorption spectra. In order to roughly match with the experimental spectra, I then multiplied the summed spectra by a factor $\alpha = 0.5$. The contributions of ^{87}Rb and ^{85}Rb , OD_{87} and OD_{85} , are shown for both the M1 cell and for an identical cell filled with Rb enriched to 75% ^{87}Rb . The spectra show σ_- transitions on the left, and σ_+ transitions on the right. For each polarisation, there are 14 OD_{87} transitions, coupling to each of the a and b coefficient states (see Section 8.1) of the 8 ^{87}Rb hyperfine ground state levels [93]. Transitions coupling to the a states are strongest, as $a \rightarrow 1$ as B_{dc} increases. From right to left, the a transitions couple to levels $A_1 \rightarrow A_8$. There are 3 b transitions on either side of the a transitions, although the b transitions near zero-detuning in Figure 8.7 are not well-resolved⁸. The b transitions are barely visible for the vertical scale used in Figure 8.6. For coupling to $a_1 \rightarrow a_4$, the σ_+ transitions are strongest, whilst for coupling to $a_5 \rightarrow a_8$, the σ_- transitions are strongest. This is reversed for transitions

⁸There are only 6 b transitions, as the stretched states, A_4 and A_8 , are comprised of only a single $|m_I, m_J\rangle$ state.

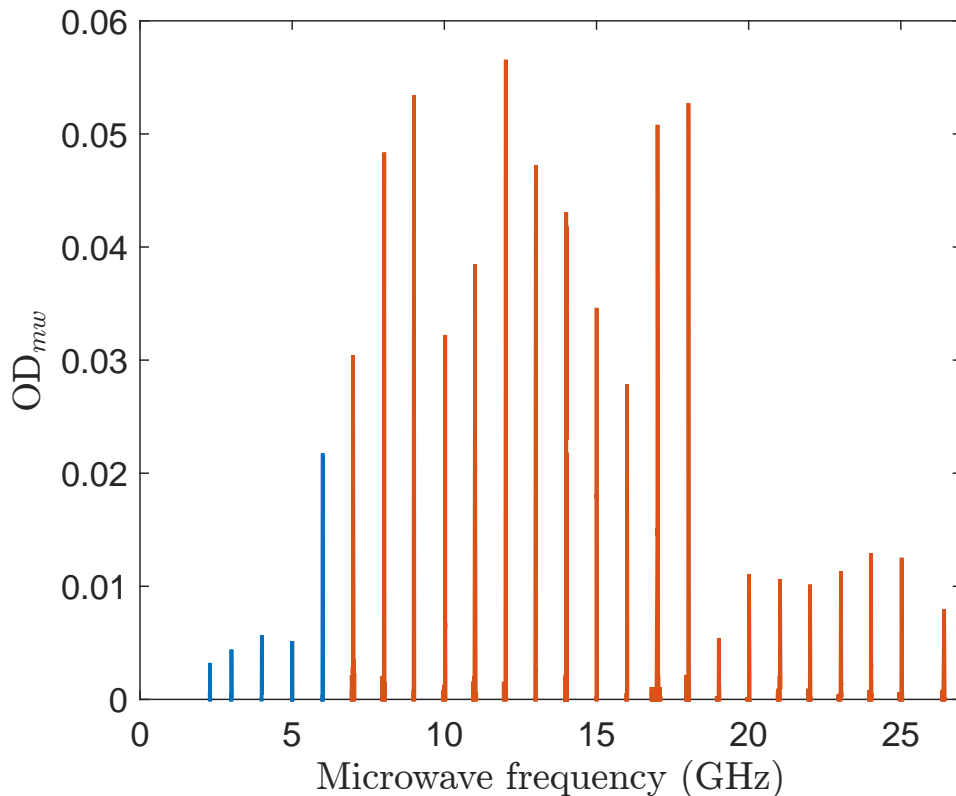


Figure 8.8: Double-resonance peaks demonstrating the detection of microwaves with frequencies ranging from 2.3 GHz to 26.4 GHz. Each peak is a single experimental run. The data was taken on both the T_{34} (blue) and T_{18} (red) transitions.

coupling to the b states.

The ^{87}Rb a transitions cover a wider frequency range than those of ^{85}Rb , due to the larger ^{87}Rb hyperfine splitting. This means that there is relatively minimal background OD due to ^{85}Rb for the transitions coupling to a_1 , a_4 , a_5 , and a_8 .

8.5 Double-Resonance Microwave Detection

As we tune the dc magnetic field, we are able to detect microwaves over a broad range of frequencies. As a demonstration, Figure 8.8 shows experimentally obtained DR peaks for microwaves spanning 2.3 GHz to 26.4 GHz (see Section 3.2.1 for a description of double-resonance spectra). Each peak represents a separate measurement in the M1 cell. Peaks in the range 7 – 26.5 GHz (red) are measured on the σ_+ T_{18} transition, whilst the peaks in the range 2 – 6 GHz (blue) are measured on the σ_- T_{34} transition. I used three different amplifiers to span the frequency range.

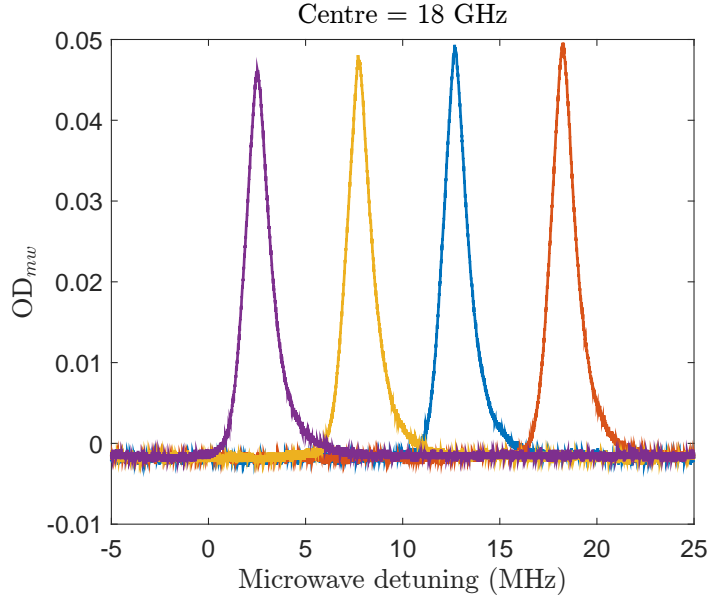


Figure 8.9: Double-resonance peaks for microwave frequencies near 18 GHz, showing how the dc magnetic field can be used to fine-tune the microwave detection frequency.

As described in Section 3.5.3, these were: amplifier 1 over the 6 – 19 GHz range; amplifier 2 over the 20 – 26.5 GHz range; and amplifier 3 over the 2 – 5 GHz range. The laser was π -polarised, with a typical intensity of $I = 5 \text{ mW/cm}^2$. The variation in peak height is primarily due to variations in the microwave amplitude and the cell temperature. The microwave amplitude varied with the output power of the amplifiers (a function of frequency), the free-space output-coupling efficiency of the microwave device used to illuminate the cell, and the coupling efficiency into the microwave cavity created by the solenoid. One of the heating lasers was misaligned for the 2 – 5 GHz measurements, reducing the signal amplitude. The decreasing strength of the T_{34} transition with increasing B_{dc} (decreasing microwave frequency) would have also reduced the DR peak amplitudes.

The lower limit on microwave frequency in Figure 8.8 was imposed by asymptotic behaviour of the T_{34} transition frequency at high B_{dc} (see Figure 8.1.b), and the upper limit was imposed by our microwave frequency generator. In general, the upper limit is likely to be given by equipment constraints, rather than the atoms themselves, such as the frequency generator or the available dc magnetic field. For the T_{45} transition, the ultimate lower limit is likely to be given by the optical resolution of the A_4 and A_5 states. The optical overlap between two states increases as the transition frequency decreases, reducing the optical pumping efficiency and the OD contrast induced by population oscillations between the states. This does not affect the Rabi (or Ramsey) oscillation frequency. The lower detection limit will therefore be given by the optical linewidth, on the order of 0.5-2 GHz, depending

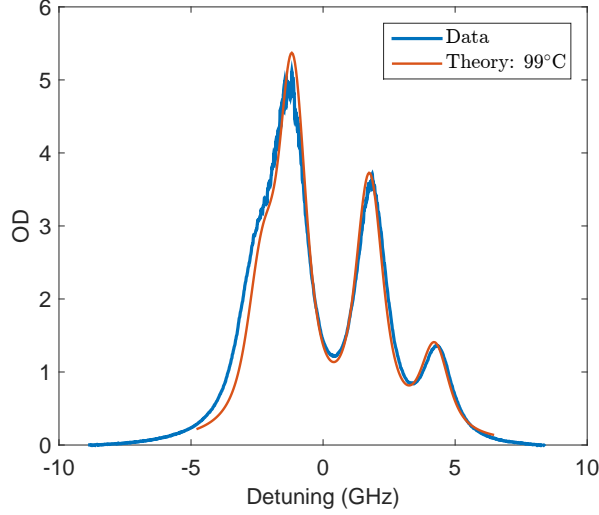


Figure 8.10: Optical absorption spectrum used to determine the cell temperature for the data presented in Figure 8.9. The data has been fit using the model described in Section 2.3, with the temperature as a free parameter.

on the buffer gas.

The dc magnetic field also allows us fine control over the microwave detection frequency, as shown in Figure 8.9. Each DR peak represents a single measurement in the M1 cell on the T_{18} transition, with the zero of the horizontal axis corresponding to a microwave frequency of 18 GHz. The laser was π -polarised, with an intensity of $I = 5 \text{ mW/cm}^2$ over its central 3 mm, measured upstream of an aperture used to reduce the beam diameter to 0.6 mm. The laser probed the approximate spatial centre of the dc magnetic field, with variations in the dc field resulting in a 1 MHz linewidth (see Figure 8.11). The cell temperature was $(99 \pm 1)^\circ\text{C}$. As shown in Figure 8.10, the temperature was obtained by fitting the OD model presented in Section 2.3 to the optical absorption spectrum measured with the solenoid turned off. I used $P_{fill} = 63 \text{ mbar}$ of N_2 , $T_{fill} = 80^\circ\text{C}$. The measured frequency axis was scaled using Gaussian fits to the spectrum to match the frequencies of the four ^{85}Rb and ^{87}Rb D_2 lines to published values [88, 89]. The discrepancies between data and theory are not explained by reasonable variations in temperature or buffer gas pressure (e.g. $\pm 5^\circ\text{C}$ or $\pm 10 \text{ mbar N}_2$), and are likely to be due to non-linearities in the scan of laser frequency as a function of time.

8.6 Microwave and DC Magnetic Field Imaging

In this section, I present images of the σ_+ component of an 18 GHz microwave field (Figure 8.11.a), and the B_{dc} field required to tune the T_{18} transition to resonance with the applied microwave field (Figure 8.11.b). Both the B_{dc} and B_{mw} data were

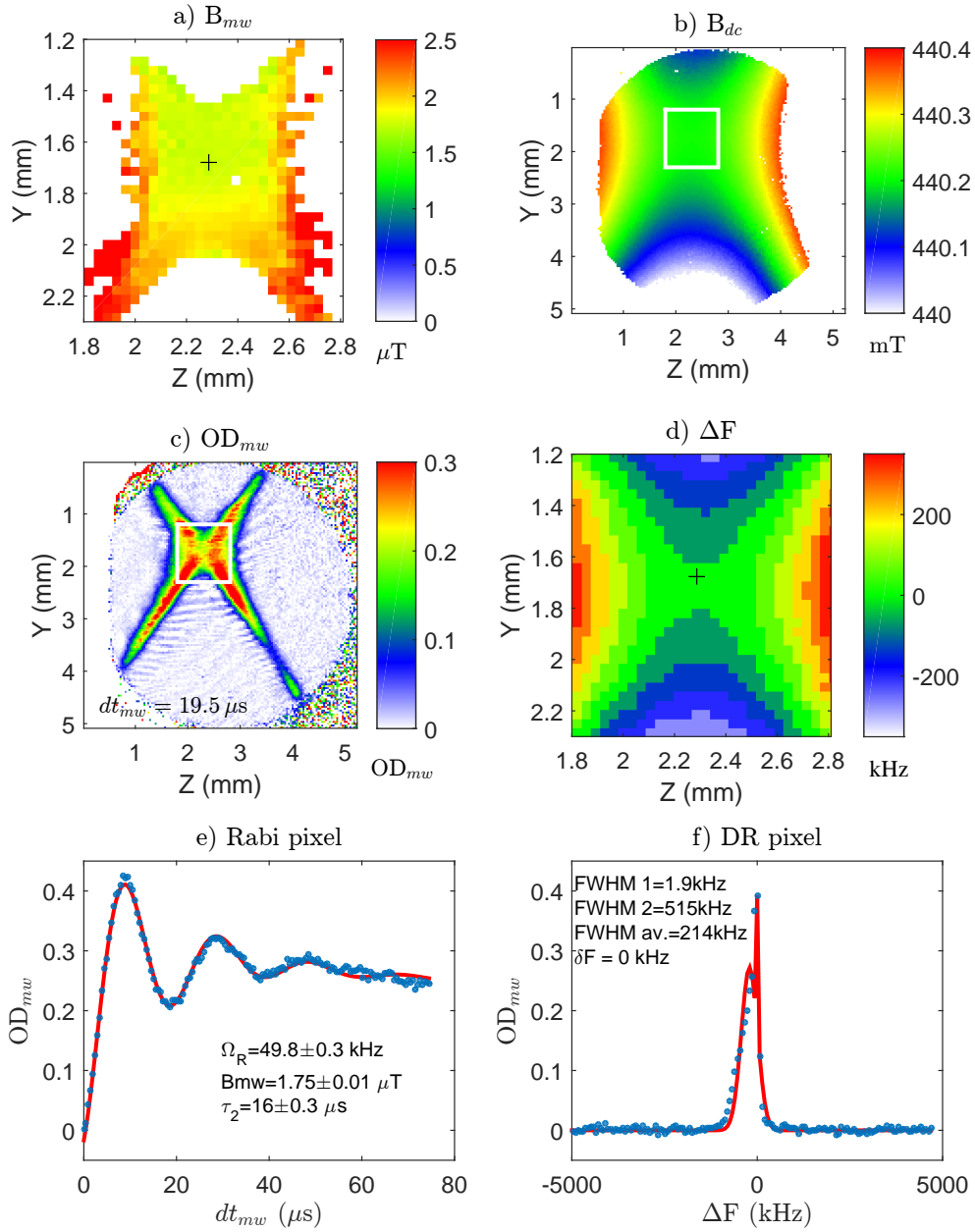


Figure 8.11: Experimentally obtained images of a) B_{mw} for an 18 GHz microwave; b) the B_{dc} field used to tune the T_{18} transition to resonance; c) OD_{mw} for a π microwave pulse in the cell centre; d) detuning of the T_{18} transition from 18.00065 GHz around the B_{dc} centre; e) an example Rabi oscillation, for the pixel marked by a cross in (a); and f) an example DR peak, for the pixel marked by a cross in (d).

taken on the T_{18} transition. The data is the average of 5 runs, with fitting performed on the averaged data. The intensity of the π -polarised laser was $I = 30 \text{ mW/cm}^2$, and the laser frequency was tuned to address the A_1 level. The length of the probe laser pulse was $dt_{probe} = 1.2 \mu\text{s}$. The change in OD due to optical pumping across the cell was measured to be $OD_{pump} = 1.0 \pm 0.1$, and the T_1 time in the cell bulk ranged from $90 \mu\text{s}$ at the top of the cell to $150 \mu\text{s}$ at the bottom (see Figure 8.13). The origin of the gradient in T_1 is unclear: it does not correspond to the 780 nm laser profile, but may be due to a temperature gradient induced by the 1500 nm heating laser or the fact that the top of the cell is open to the air. From optical absorption spectra with the solenoid turned off, the cell temperature was found to be approximately $T_{cell} = 110^\circ\text{C}$.

Figure 8.11.a shows an image of the σ_+ component of an 18 GHz microwave field in the M1 cell, with the field of view defined by the region of relatively homogeneous B_{dc} field. The zoomed-in region of the cell is marked with a white box in Figure 8.11.c, and is the same region shown in Figure 8.11.d. I used the local measured value of B_{dc} to calculate the coupling constant between the Rabi frequency and microwave amplitude, α_{18} , for each pixel. In principle, we should also use the local microwave detuning, δF , to calculate the Rabi frequency, $\Omega_R = \sqrt{\Omega^2 - \delta F^2}$. However, this proved impractical due to the 67 kHz ΔF step size (discussed below), which was larger than the observed $\Omega \approx 50 \text{ kHz}$ oscillation frequencies. The determination of α_{18} is less affected, as α_{18} is only weakly field dependent at kG dc magnetic fields (see Figure 8.3). In future measurements, a ΔF image with finer step size should be recorded immediately after the Rabi sequence. For the data presented in Figure 8.11, I used $\Omega_R = \Omega$. The transverse dimensions of the B_{mw} field of view are approximately $0.6 \times 0.6 \text{ mm}^2$. This is several times the Rb diffusion distance during a measurement. For $P_{fill} = 63 \text{ mbar N}_2$, $T_{fill} = 80^\circ\text{C}$, $T_{cell} = 110^\circ\text{C}$, we have $D = 3.3 \text{ cm/s}$. Using $\Delta x = \sqrt{2Ddt}$, the diffusion distance during the coherence time $dt = \tau_2 = 16 \mu\text{s}$ is $\Delta x = 0.1 \text{ mm}$, and the diffusion distance during the time Rabi oscillations are visible, $dt = 60 \mu\text{s}$, is $\Delta x = 0.2 \text{ mm}$. We can therefore conclude that we are indeed *imaging* the microwave field with an array of sensors (albeit a much smaller array than used in the previous Chapters).

Figure 8.11.c shows OD_{mw} , the change in OD induced by the microwave, for a microwave pulse of $dt_{mw} = 19.5 \mu\text{s}$. The microwave field in the solenoid cavity appears reasonably uniform, and the OD_{mw} image traces out a contour line of the dc magnetic field, showing the regions of the dc field where the Paschen-Back splitting brings the T_{18} transition frequency on resonance with the applied microwave. As seen in Figure 8.11.f, $dt_{mw} = 19.5 \mu\text{s}$ corresponds to a 2π microwave pulse in the centre of the B_{dc} field, which can be seen as a dip in OD_{mw} at the crossing point of the contour lines.

Figure 8.11.e shows Rabi oscillations for an example pixel at ($Z = 2.29 \text{ mm}$, $Y = 1.68 \text{ mm}$). This is marked by a cross in Figure 8.11.a, and is the same location as the example DR pixel in Figure 8.11.f. The data has been fit using

$$OD_{mw} = A + B \exp(-dt_{mw}/\tau_1) + C \exp(-dt_{mw}/\tau_2) \sin^2(\frac{1}{2}\Omega dt_{mw} + \phi), \quad (8.31)$$

where A , B , C , τ_1 , τ_2 , Ω and ϕ were fitting parameters. For ($Z = 2.29$ mm, $Y = 1.68$ mm), the oscillation frequency is $\Omega = 49.8$ kHz⁹ and the local B_{dc} gives $\alpha_{18} = 0.49$. Making the approximation $\Omega_R = \Omega$, this gives a microwave amplitude of $B_{mw} = 1.75$ μ T. The fitting uncertainty, of $\Delta B_{mw} = 10$ nT, corresponds to a sensitivity of $\delta B_{mw} = 0.1$ μ T Hz^{-1/2} over the 5×30 s = 150 s measurement time. This sensitivity is an order of magnitude better than that obtained with the ultrathin cells in Chapter 7. However, the sensor volume here is two orders of magnitude larger: $V = 0.05 \times 0.05 \times 0.14$ mm³ = 3.5×10^{-4} mm³ in Chapter 7, compared to $V = 0.1 \times 0.1 \times 2$ mm³ = 2×10^{-2} mm³ here.

The B_{dc} data was obtained by taking a pulsed DR spectrum of the cell. This gave the frequency of the T₁₈ transition across the cell, from which B_{dc} could be numerically calculated¹⁰. Although a Ramsey sequence can in principle be used to image dc fields of any magnitude, it is impractical for imaging the large variations in the solenoid field. The dynamic range of the Ramsey technique is limited by the reduction in signal strength with microwave detuning, and the difficulty in detecting the fast Ramsey oscillations associated with large detunings. The dynamic range of the DR imaging technique, on the other hand, is limited only by the number of shots in an experiment run (150 in this case), and the subsequent trade-off between the desired field resolution and dynamic range. The DR imaging sequence was the same as the Rabi imaging sequence used in Chapter 7, but the microwave pulse length was fixed at $dt_{mw} = 8.5$ μ s, and I scanned the microwave frequency between shots. The microwave pulse length was chosen to give a π pulse in the centre of the B_{dc} field (see Figure 8.11.e). For Figure 8.11, the dynamic range was chosen to cover microwave detunings over the range -5 MHz $< \Delta F < 5$ MHz, giving a step size between data points of 67 kHz. The microwave frequency was given by $F_{mw} = CF + \Delta F$, where the centre frequency of the scan was $CF = 18.00065$ GHz.

Figure 8.11.b shows an image of the B_{dc} field inside the vapor cell. The ΔF scan limits correspond to a detection range of 440 mT $< B_{dc} < 440.4$ mT. The field is saddle-shaped, rising up from the centre along the Z axis towards the solenoid cones, and dropping away from the centre along the Y axis. The variation along the X axis through the 2 mm thickness of the cell is integrated out, but from the cylindrical symmetry of the solenoid, it is reasonable to assume that the field variation along the X axis is similar to that along the Y axis. The cell is well-aligned with the centre of the X -component of B_{dc} , as the cell position was adjusted with a translation stage to minimise the DR linewidth. Gradients in B_{dc} present the primary dephasing mechanism in the cell. Although the homogeneity of the dc magnetic field across the cell is better than 10^{-3} , the variation in B_{dc} across the cell is several Gauss (1 G = 0.1 mT).

Figure 8.11.d shows δF , the detuning of the T18 transition frequency from $CF = 18.00065$ GHz, in a zoomed-in region around the centre of the B_{dc} field. This region

⁹Remember, all frequencies in this Chapter are given in units of cyclic frequency, and not angular frequency.

¹⁰I compared the measured microwave frequencies with numerically obtained eigenvalues of the Hamiltonian given by Eq. (8.1). One could also use the Breit-Rabi formula.

is marked by a white box in Figure 8.11.b. We see variation in the T18 frequency of ± 250 kHz, with a resolution of 67 kHz given by the ΔF step size.

Figure 8.11.f shows an example pixel from the centre of the B_{dc} field, at ($Z = 2.29$ mm, $Y = 1.68$ mm), marked by a cross in Figure 8.11.d. Due to the sharpness and non-Gaussian nature of the DR peak, I simply took δF to be given by the value of ΔF where OD_{mw} is largest. The resolution in δF was then given by the 67 kHz frequency step size. However, the frequency step size was too coarse to measure the width of the DR peak without fitting the data. We can estimate the FWHM by fitting two Gaussians, and taking the weighted average of their respective widths,

$$FWHM_{av} = \frac{A_1}{A_1 + A_2} FWHM_1 + \frac{A_2}{A_1 + A_2} FWHM_2, \quad (8.32)$$

where $A_{1(2)}$ and $FWHM_{1(2)}$ are the respective amplitudes and widths of the two Gaussians. At ($Z = 2.29$ mm, $Y = 1.68$ mm), we find a width of $FWHM_{av} = 214$ kHz. This is 4 times the Rabi frequency at the same location (Figure 8.11.e).

8.7 Atomic Relaxation

The dc magnetic field has a significant effect on the collisional relaxation processes in the cell. The Rb SE rate has been found to decrease by a factor of 3 in a 6 kG field [114–116]. Relaxation due to the spin rotation interaction ($\gamma(r)\mathbf{S} \cdot \mathbf{N}$) in collisions with the buffer gas is suppressed at high dc magnetic fields [86, 126], however the Carver rate ($\delta A(r)\mathbf{I} \cdot \mathbf{S}$) increases, and is able to induce T_1 relaxation.

Figure 8.12 shows measured T_1 values as a function of the applied dc magnetic field. The measurements were made using Franzen imaging sequences. The cell temperature was $T_{cell} = 100^\circ\text{C}$, as estimated from the optical absorption spectrum with the solenoid turned off. The π -polarised laser intensity was 30 mW/cm^2 , and the probe pulse duration was $dt_{probe} = 0.6 \mu\text{s}$. I measured the dc magnetic field by taking a DR spectrum of the T_{18} transition, and numerically obtaining B_{dc} from the T_{18} resonance frequency. I began measurements at $B_{dc} = 4800$ G, and adjusted the laser frequency as I decreased B_{dc} in order to maximise the DR signal, ensuring that the laser remained resonant with the A_1 level. At $B_{dc} \approx 0$, the laser was thus probing the ^{87}Rb $F = 1$ state.

The T_1 time in Figure 8.12 increases with B_{dc} , although the effect appears minimal below $B_{dc} = 1000$ G. This delayed suppression of relaxation was not seen in Ref. [114], however it is likely that our curve is nonetheless primarily due to suppression of Rb SE. The contribution of buffer gas collisions is minimal at low fields, with $\gamma_{bg} \ll \gamma_{walls}, \gamma_{SE}$ for our cell parameters, and is unlikely to change by orders of magnitude as B_{dc} is increased. As shown in Figure 8.13, there was a gradient in T_1 across the cell, with T_1 lower at the top of the cell. The T_1 values in Figure 8.12 are the averaged values in the region of the cell bulk marked by a white box in Figure 8.13. The error bars represent the standard deviation in the T_1 time over this region. There is good agreement between the exponential and $1/e$ fits.

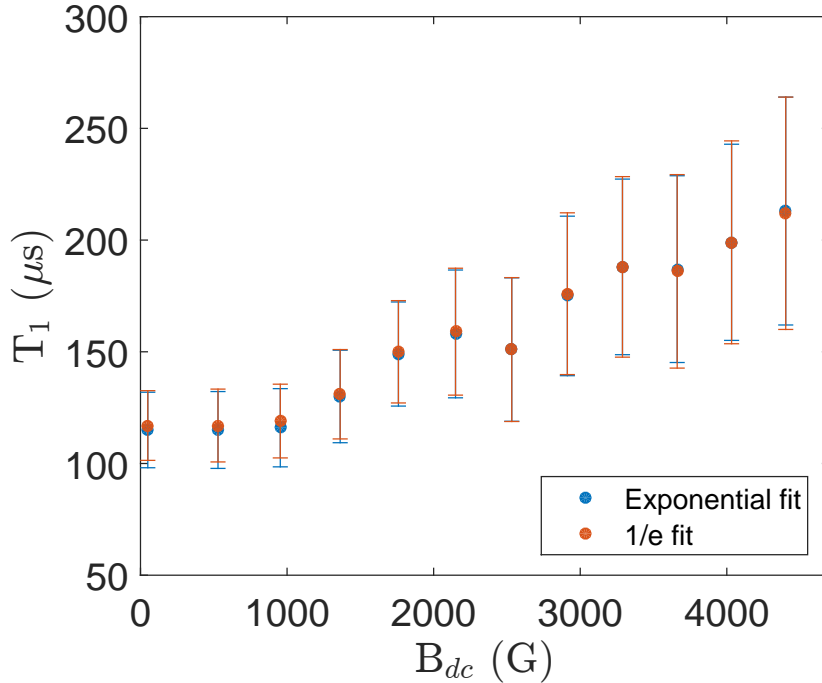


Figure 8.12: Measured T_1 time as a function of B_{dc} . The error bars are the standard deviation in the range of T_1 values seen across the cell bulk (see Figure 8.13). T_1 increases with B_{dc} , primarily due to the suppression of Rb spin-exchange collisions.

It is unclear how the changing level structure affects T_1 . Although optical pumping has been studied at high dc magnetic fields [210, 211], I am not aware of detailed, state-dependent relaxation studies. Neglecting the contribution of ^{85}Rb for a moment, T_1 at low B_{dc} is the lifetime of the population difference between the ^{87}Rb $F = 1$ and $F = 2$ states. At high B_{dc} , where the laser predominantly only interacts with the A_1 state, T_1 is the lifetime of the population depletion of A_1 . More levels are involved for intermediate fields, large optical linewidths, and when ^{85}Rb is considered. It is conceivable that the changing nature (or definition) of T_1 in these various regimes could result in some variation in the observed T_1 time, even if the underlying collisional processes remain the same.

8.8 Conclusions

In this Chapter, I presented a proof-of-principle demonstration of microwave magnetic field imaging for microwaves of any frequency, imaging an 18 GHz microwave field, and detecting microwaves from 2.3 GHz to 26.4 GHz. I also demonstrated a new, high dynamic range technique for imaging dc magnetic fields, based on a dou-

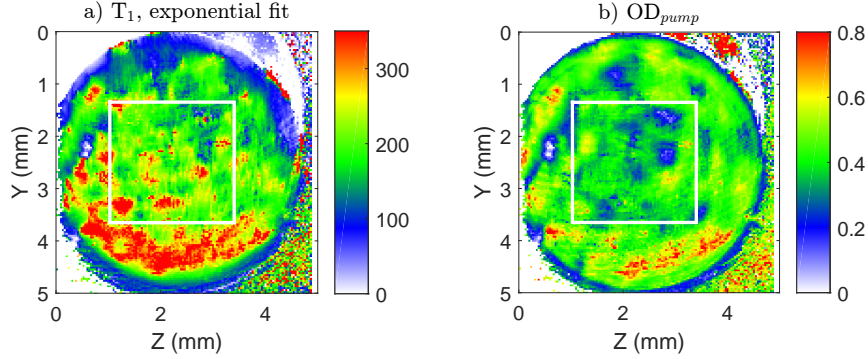


Figure 8.13: Images of a) T_1 and b) OD_{pump} at $B_{dc} = 4402$ G. T_1 is longest at the cell bottom, and shortest at the top. The white box marks the region whose averaged values are plotted in Figure 8.12.

ble resonance sequence. The ^{87}Rb σ_- and π hyperfine transitions are only available over the frequency ranges 2.2 – 9.1 GHz and 5.9 – 22.8 GHz, respectively. However, σ_+ transitions are available at all microwave frequencies, and I have shown that it is possible to completely reconstruct the vector components of the microwave magnetic field amplitude, and the relative phases between them, using only σ_+ transitions. The reconstruction requires images of B_+ with the dc magnetic field both parallel and anti-parallel to each of the X , Y , and Z axes. Given the required tesla-order field strength, orientation of the B_{dc} field is likely to present a significant future engineering challenge, and it may prove simpler to rotate the device under test and imaging optics instead (which would also require some engineering work).

The invasiveness of the large B_{dc} fields and their influence on devices under test is not yet clear, and one could imagine that for some devices, the B_{dc} fields would modify the device operation. The setup could be miniaturised by replacing the bulky solenoid with permanent rare-earth magnets [39, 212]. Tuning of the dc magnetic field strength could then be achieved by adjusting the distance of the magnets from the cell.

Chapter 9

Outlook

In this thesis, I have described the development of new techniques for imaging microwave and dc magnetic fields and atomic relaxation in alkali vapor cells. We built a microwave imaging setup with sufficient sensitivity, spatial resolution, and distance of approach to characterise real world devices at the fixed frequency of 6.8 GHz. The setup can also be used to image dc magnetic fields. Our microwave field, dc field, and relaxation imaging techniques are already being adopted by the atomic clock community for characterising the fields inside high-performance, miniaturised vapor cell atomic clocks [52]. Wider applications require a frequency tunable microwave imaging technique, with imaging above ~ 18 GHz of particular interest to industry, as microwave simulations become less reliable at high frequency. I have extended our microwave imaging well into this regime, demonstrating in a proof-of-principle setup that we are able to image microwaves at any frequency. I presented imaging of an 18 GHz microwave field, and the detection of microwaves with frequencies from 2.3 GHz to 26.4 GHz.

There are now a number of promising directions available for us to explore, which I discuss in the following sections.

Optimisation of Imaging with the Ultrathin Cells

As discussed throughout this thesis, particularly at the end of Chapter 6, there are several optimisations that can be made to our high resolution imaging setup.

A next-generation ultrathin cell should be filled with pure ^{87}Rb , and use an antirelaxation coating, most likely OTS. This would provide: longer atomic state lifetimes (T_1 and T_2), improving our field sensitivity; an increased signal-to-noise ratio; reduced sensitivity to laser frequency drifts; and the option to operate at a lower temperature for the same signal strength. Another option would be to instead use Cs, which is isotopically pure (^{133}Cs is the only stable isotope), and gives a higher vapor pressure for a given temperature. The larger (9.2 GHz) hyperfine splitting would allow for higher buffer gas pressures whilst maintaining optical resolution of the hyperfine ground states, which would provide better spatial resolution and reduced wall relaxation. Drawbacks would include the larger number of m_F states,

and the incompatibility with some of our current optics equipment.

We should move to primarily heat the cell with a laser, allowing us to reduce the heat load on the device-under-test. This is simple to achieve in a permanently sealed cell, such as the microcells used in Chapters 4 and 8. For the ultrathin cells attached to the filling station, however, laser heating of the entire cell, glass-to-metal transition, and valve is somewhat impractical. We could wrap this section in heating tape, and only optically heat the cell chamber. Subsequent generations of ultrathin cells will also be permanently sealed.

We could enhance our imaging signal by perhaps 1-2 orders of magnitude by placing the cell in a cavity or multipass cell [213–215]. Such configurations have been used with single-channel detection, but we would need to make some adaptations for CCD camera imaging. This may require the use of a low-finesse cavity with large diameter mirrors, or the use of an array of microcavities or multipass cells. Ideally, the mirror surfaces would be on the inside of the cell, to minimise loss through the cell windows. The mirror surfaces would then need to be coated with a thin protective layer, such as Al_2O_3 [213], in order to protect them from reactions with the Rb.

The ultimate spatial resolution may be obtained by constructing an array of microcells, with individual microcell dimensions on the order of, say, $5 - 20 \mu\text{m}$. The cells would be antirelaxation coated, and connected through channels (which would need to provide a reasonably good conductance). Depending on the quality of the coating, the cell may or may not require buffer gas.

Our sensitivity is severely limited by our experiment duty cycle, which is dominated by camera readout and data saving. In a 30 s experiment run, we currently take 300 images (150 actual, 150 reference) at approximately 20 fps, and then wait 15 s for data saving. Dramatic improvements are possible with a different camera and data processing techniques, such as gating of the CCD and on-chip binning, and the acquisition of 2000 images at 2500 fps has been demonstrated in ultracold atom experiments [167]. Even faster detection may be possible by replacing the CCD camera with an array of photodiodes.

An important future step will be the integration of frequency tunable imaging with the ultrathin cells and filling station. The integration will probably be best achieved through the use of permanent rare-earth magnets [39, 212].

Faraday Rotation Measurements

The best sensitivity in dc and rf vapor cell magnetometers has been achieved measuring the Faraday rotation of a far-detuned probe beam through the atomic vapor [20, 111, 214, 216]. We could also use Faraday rotation measurements, to non-destructively observe Rabi or Ramsey oscillations in real time. The experiment sequence would consist of a brief optical pumping pulse, followed by observation of coherent oscillations driven by an applied microwave. For sufficiently fast detection speeds ($10^5 - 10^6 \text{ s}^{-1}$), the Rabi oscillations could be observed in real time, and the dead-time between probing of the atoms could be effectively eliminated. The off-

resonant probe intensity could be increased to reduce the effect of photon shot noise, potentially allowing us to reach the atomic projection noise limit. To my knowledge, CCD or CMOS cameras cannot currently provide more than a few 1000 fps [167], and we would need to use a photodiode (or array of photodiodes) for detection.

Real-Time Imaging

I have found that streaming data sequences and displaying images of the OD in real time can be a useful experimental tool, for example during the alignment and parameter optimisation phase. Streaming of a Rabi sequence provides images of OD_{mw} , and thus contour lines of the microwave magnetic field. The streaming frame rate is currently limited by the image processing speed on the PC, rather than by the camera, and is currently only 0.3 Hz. This is already useful, but with the same equipment and improved programming, the frame rate could be increased above 100 Hz. With a frame rate of 24 Hz we would achieve visually ‘real time’ imaging of OD_{mw} , which would greatly help during cell-chip alignment, and could even replace the need for time-consuming reconstructions of B_{mw} for some device characterisation applications. One could envisage a characterisation station where a microwave device could be brought up to a cell, to display contour lines of the microwave magnetic field on a screen. Scanning the microwave device around over the cell would allow the user to intuitively explore the microwave field in real time. Such a process could take minutes or less, and would be ideal for characterisations and debugging ‘on the fly’.

Microwave Electrometry

The full characterisation of a microwave near field requires measurements of both the electric (E_{mw}) and magnetic (B_{mw}) components, as there is no straightforward relationship between the components. Alkali atoms in Rydberg states have proven to be excellent sensors of E_{mw} [47–49, 81, 82], and are able to detect far weaker microwave amplitudes than our B_{mw} imaging technique, as detection is performed using Rydberg electric dipole transitions, which are much stronger than the magnetic dipole transitions we use for B_{mw} detection. However, Rydberg states are relatively delicate compared to the hyperfine ground states we use for B_{mw} imaging, and are quickly destroyed in collisions with buffer gas atoms. The vapor cell requirements for B_{mw} and E_{mw} imaging would therefore seem somewhat incompatible: we require high buffer gas pressures to prevent wall relaxation and provide spatial resolution for B_{mw} imaging, but require that there is little to no buffer gas present for E_{mw} imaging. The problem could be easily solved with our ultrathin cells attached to the filling station, described in Chapter 6. With the addition of a 480 nm laser to excite Rb Rydberg states, the filling station would allow us to perform an E_{mw} measurement without buffer gas, then fill the cell with buffer gas and image B_{mw} . A filling station is the ideal setup for such a measurement of both components, as it avoids the errors that using two different cell would bring, such as cell alignment

and structural differences between the two cells.

Microwave Circuit Characterisation

Much of the drive of our microwave imaging project has been towards applications in integrated circuit (IC) characterisation. Scientific applications include the characterisation of atom chips and ion traps. There are also potentially vast industrial applications, with microwave ICs particularly important in the telecommunications sector. The trend towards ever smaller and denser chips, operating at higher frequencies, represents a significant characterisation challenge [56].

Industry is interested in characterisation techniques for non-linear devices, and devices operating at frequencies above 18 GHz. Our current high resolution setup is already of interest for non-linear devices operating at 6.8 GHz, and we have made contact with a major microwave company for collaboration, performing an early characterisation of a prototype 6.8 GHz non-linear device. An imaging system combining the high resolution and distance of approach presented in Chapter 7 with the frequency tunability presented in Chapter 8, and possibly also the E_{mw} imaging discussed above, will be a competitive solution to the characterisation problem faced by industry. Characterisation of microwave fields from 1-50 GHz should be achievable with room-temperature solenoids (which can operate to 1.6 T), and it may be possible to image fields up to 1 THz using the strongest available superconducting solenoids (35 T).

Applications in Medical Imaging

Microwave sensing and imaging (MSI) is an emerging field that has shown promise in a range of applications, including imaging of the brain for strokes and cerebral edema, breast cancer screening, bone imaging, and heart imaging [217]. Microwaves are applied to the body of interest, and features are identified through the differing permittivity and conductivity between tissue types. Microwave imaging is attractive compared to established tools such as X-ray, MRI, and CT imaging, as microwaves are non-ionising, and microwave techniques promise to be relatively cheap and portable. Breast imaging has received particular interest, due to the physical accessibility of the breast, the high signal contrast between tissue types, and the high incidence of breast cancer [218, 219].

There has been considerable effort in recent years to develop practical imaging techniques [217]. The choice of microwave frequency is a trade-off between microwave penetration and spatial resolution, and imaging is typically performed in the 0.5-10 GHz frequency band [218, 220]. The sensitivity requirements can be considerable, as microwave attenuation through the breast can result in an output signal 100 dB below the input signal. Current microwave detection systems consist of an array of microwave antennas, sensitive to E_{mw} [221]. Optimal image reconstruction requires a high sensor density, however the density is limited by cross-talk between antennas, and by their perturbations of the microwave field. Sensor calibration is

also a significant concern [217].

Atomic sensors offer an attractive alternative to antennas, either using ground state atoms to measure B_{mw} or atoms in Rydberg states to measure E_{mw} . The sensors are intrinsically calibrated, there is no cross-talk between sensors [209], and field perturbation due to the glass vapor cell is minimal compared to metallic antennas. Sufficient sensitivity may be engineered through a faster experiment duty cycle and larger vapor cells, and we have shown that atomic sensors can cover the frequency band of interest. As noted in Chapter 7, E_{mw} sensing with Rydberg atoms is able to detect much weaker microwaves than our B_{mw} imaging. Current MSI techniques only investigate E_{mw} however, and it may be that measurements of both microwave components can improve the sensitivity and specificity (i.e. diagnostic accuracy) of the technique.

Following the success of vapor cell magnetometers in diagnostic imaging of the heart [33, 34] and brain [35–38], microwave imaging with vapor cells may also prove to be an attractive medical tool. The implementation would require a long-term research collaboration with the existing MSI community, and perhaps also with the medical vapor cell magnetometer community.

Appendix A

Constants and Rb Data

Table A.1: Selected fundamental constants, from Ref. [88].

Planck's constant	h	$6.626\,068\,72(52) \times 10^{-34}$ Js
	\hbar	$1.054\,571\,596(82) \times 10^{-34}$ Js
Speed of light	c	$2.997\,924\,58 \times 10^8$ m/s
Bohr magneton	μ_B	$9.274\,009\,15(23) \times 10^{-24}$ J/T
		$h \cdot 1.399\,624\,604(35)$ MHz/G
Boltzmann's constant	k_B	$1.380\,650\,4(24) \times 10^{-23}$ J/K
Elementary charge	e	$1.602\,176\,487 \times 10^{-19}$ C
Bohr radius	a_0	$0.529\,177\,208\,59 \times 10^{-10}$ m

Table A.2: ^{87}Rb data, from Ref. [88] unless otherwise indicated.

Rel. natural abundance		27.83(2)%
Nuclear spin	I_{87}	3/2
Atomic mass	m_{87}	$1.443\,160\,648(72) \times 10^{-25}$ kg
$5^2\text{S}_{1/2}$ hyperfine constant	A_{hfs}	$h \cdot 3.417\,341\,305\,452\,15(5)$ GHz
$5^2\text{S}_{1/2}$ hyperfine splitting	ΔE_{hfs}	$h \cdot 6.834\,682\,610\,904\,312$ GHz [159]

Table A.3: ^{85}Rb data, from Ref. [89].

Rel. natural abundance		72.17(2)%
Nuclear spin	I_{85}	5/2
Atomic mass	m_{85}	$1.409\,993\,199(70) \times 10^{-25}$ kg
$5^2\text{S}_{1/2}$ hyperfine constant	A_{hfs}	$h \cdot 1.011\,910\,813\,0(20)$ GHz
$5^2\text{S}_{1/2}$ hyperfine splitting	ΔE_{hfs}	$h \cdot 3.035\,732\,439\,0(60)$ GHz

Table A.4: Rb D₂ line data, from Refs. [88, 89].

Nuclear spin g-factor	g_I	$-0.000\,995\,141\,4(10)$
$5^2S_{1/2}$ g-factor	g_J	$2.002\,331\,13(20)$
$5^2P_{3/2}$ g-factor	g_J	$1.336\,2(13)$
Wavelength (in vacuum)	λ	$780.241\,209\,686(13)$ nm
Frequency	ω_0	$384.230\,484\,468\,5(62)$ THz
Decay rate / Natural linewidth	Γ_{nat}	$38.117(11) \times 10^6 \text{ s}^{-1}$ $2\pi \cdot 6.065(9)$ MHz
Saturation Intensity $ F = 2, m_F = \pm 2\rangle \rightarrow F' = 3, m_F = \pm 3\rangle$ cycling transition (σ_{\pm} polarised light)	I_{sat}	$1.669(2)$ mW/cm ²

Appendix B

Lineshape Functions

Here, I describe the lineshape functions used in Chapter 2 to model the OD in vapor cells. The natural and collisionally broadened lineshapes are described by a Lorentzian,

$$L(\omega) = \frac{1}{\pi} \frac{2\Gamma}{(\omega - \omega_0)^2 + 4\Gamma^2}, \quad (\text{B.1})$$

where ω is the laser frequency, ω_0 is the frequency of the atomic transition, and Γ is the Lorentzian FWHM. Doppler broadening of atomic lines results in a Gaussian lineshape,

$$G(\omega) = \frac{1}{\sqrt{2\pi}\sigma} \exp\left(-\frac{(\omega - \omega_0)^2}{2\sigma^2}\right), \quad (\text{B.2})$$

where

$$\sigma = \frac{\Delta\omega}{2\sqrt{2 \ln 2}}, \quad (\text{B.3})$$

is the Gaussian r.m.s. width, and $\Delta\omega$ is the FWHM. The optical lineshape is given by a convolution of the Gaussian and Lorentzian lineshapes, known as a Voigt profile,

$$V(\omega) = \int_{-\infty}^{+\infty} G(\omega')L(\omega - \omega')d\omega'. \quad (\text{B.4})$$

The Voigt profile can also be written in terms of the complementary error function,

$$V(\omega) = \frac{1}{\sigma\sqrt{2\pi}} \Re[\exp(-z^2)\text{erfc}(-iz)], \quad (\text{B.5})$$

where $z = \frac{1}{\sigma\sqrt{2}}(\omega + i\Gamma)$, and $\text{erfc}(z)$ is defined for all complex z by

$$\text{erfc}(z) = \frac{2}{\sqrt{\pi}} \int_z^{+\infty} \exp(-t^2)dt. \quad (\text{B.6})$$

Appendix C

Angular Momentum Matrices

For transitions between hyperfine states, the angular momentum matrix elements are given by

$$I_z|I, m_I\rangle = m_I|I, m_I\rangle, \quad (\text{C.1})$$

$$J_z|J, m_J\rangle = m_J|J, m_J\rangle, \quad (\text{C.2})$$

$$I_{\pm}|I, m_I\rangle = \sqrt{(I \mp m_I)(I \pm m_I + 1)}|I, m_I \pm 1\rangle, \quad (\text{C.3})$$

$$J_{\pm}|J, m_J\rangle = \sqrt{(J \mp m_J)(J \pm m_J + 1)}|J, m_J \pm 1\rangle. \quad (\text{C.4})$$

Our definition of the Rabi frequencies (see Section 3.1.3) sets

$$I_x = \frac{1}{2}(I_+ + I_-), \quad J_x = \frac{1}{2}(J_+ + J_-), \quad (\text{C.5})$$

$$I_y = \frac{1}{2i}(I_+ - I_-), \quad J_y = \frac{1}{2i}(J_+ - J_-). \quad (\text{C.6})$$

For transitions between the ^{87}Rb $5S_{1/2}$ hyperfine states, and using the basis $\psi_1 = |m_J = 1/2, m_I = 3/2\rangle$, $\psi_2 = |m_J = 1/2, m_I = 1/2\rangle$, \dots , $\psi_8 = |m_J = -1/2, m_I = -3/2\rangle$, the explicit matrices are

$$I_z = \begin{pmatrix} 3/2 & 0 & 0 & 0 & 0 & 0 & 0 & 0 \\ 0 & 1/2 & 0 & 0 & 0 & 0 & 0 & 0 \\ 0 & 0 & -1/2 & 0 & 0 & 0 & 0 & 0 \\ 0 & 0 & 0 & -3/2 & 0 & 0 & 0 & 0 \\ 0 & 0 & 0 & 0 & 3/2 & 0 & 0 & 0 \\ 0 & 0 & 0 & 0 & 0 & 1/2 & 0 & 0 \\ 0 & 0 & 0 & 0 & 0 & 0 & -1/2 & 0 \\ 0 & 0 & 0 & 0 & 0 & 0 & 0 & -3/2 \end{pmatrix},$$

Appendix D

Hyperfine Transitions for Microwave Sensing

Here I expand upon the discussion in Section 8.1.1 for ^{87}Rb , and give the microwave transition strengths and frequencies for other alkali species.

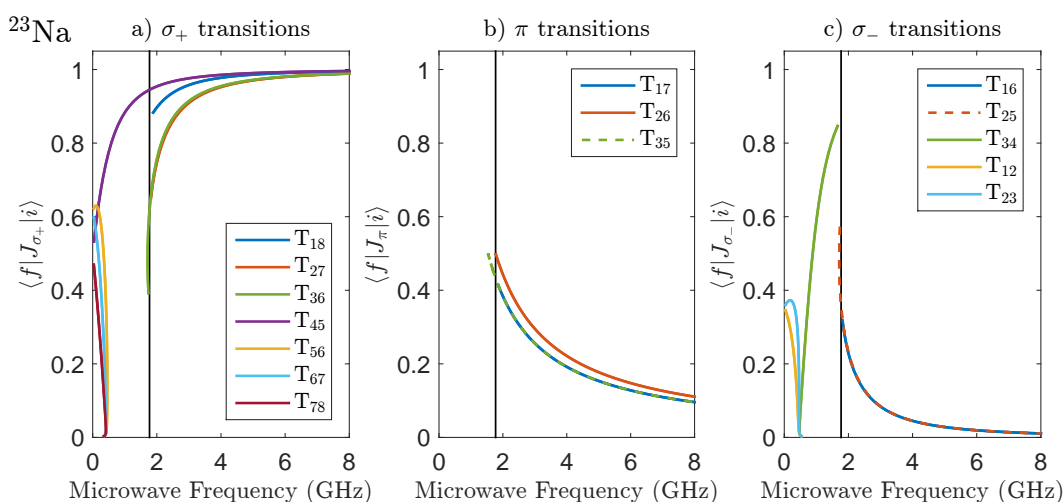


Figure D.1: Strengths of the σ_+ , π , and σ_- hyperfine transitions within the ^{23}Na $3^2S_{1/2}$ ground state, as a function of the microwave transition frequency. The black vertical line is at 1.772 GHz. Data for ^{23}Na was taken from Ref. [222].

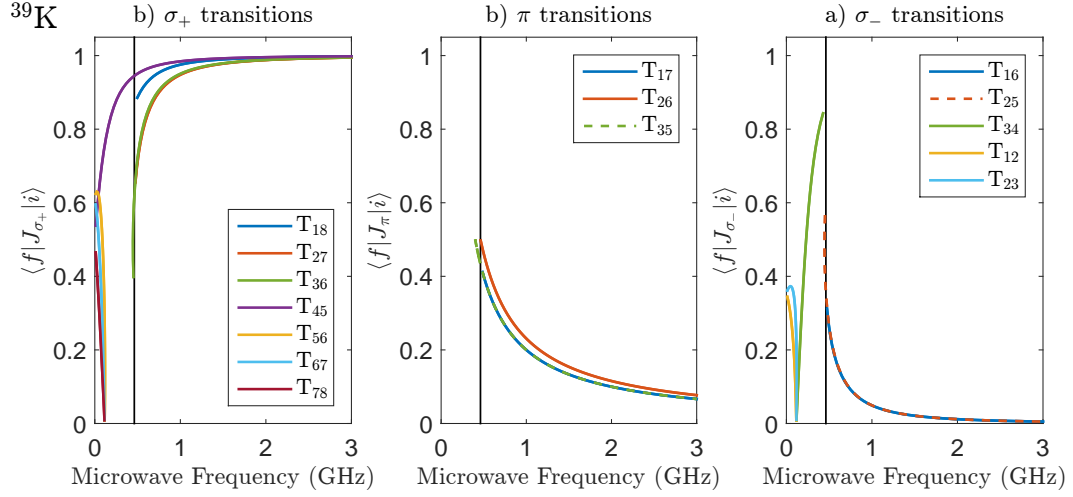


Figure D.2: Strengths of the σ_+ , π , and σ_- hyperfine transitions within the ^{39}K $4^2S_{1/2}$ ground state, as a function of of the microwave transition frequency. The black vertical line is at 0.417 GHz. Data for ^{39}K was taken from Ref. [223].

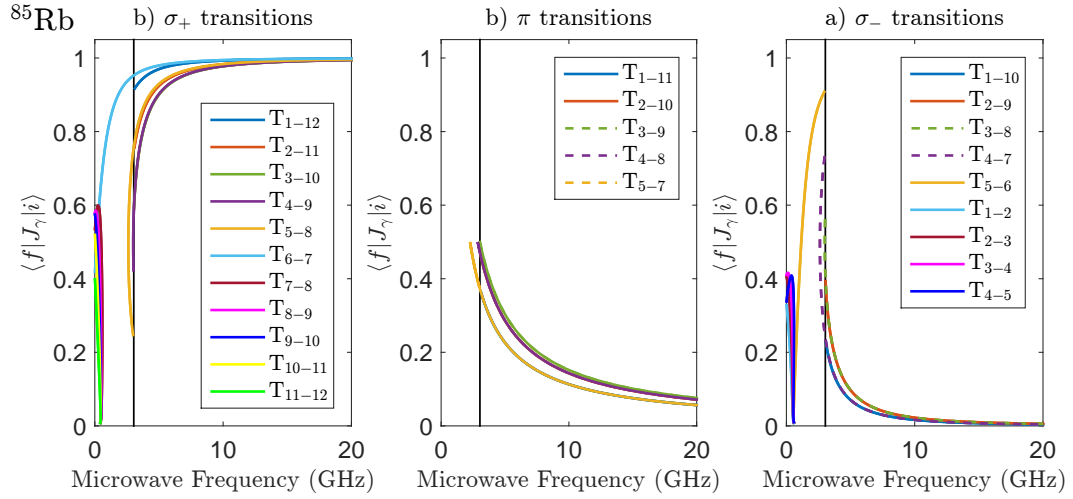


Figure D.3: Strengths of the σ_+ , π , and σ_- hyperfine transitions within the ^{85}Rb $5^2S_{1/2}$ ground state, as a function of of the microwave transition frequency. The black vertical line is at 3.036 GHz. Data for ^{85}Rb was taken from Ref. [89].

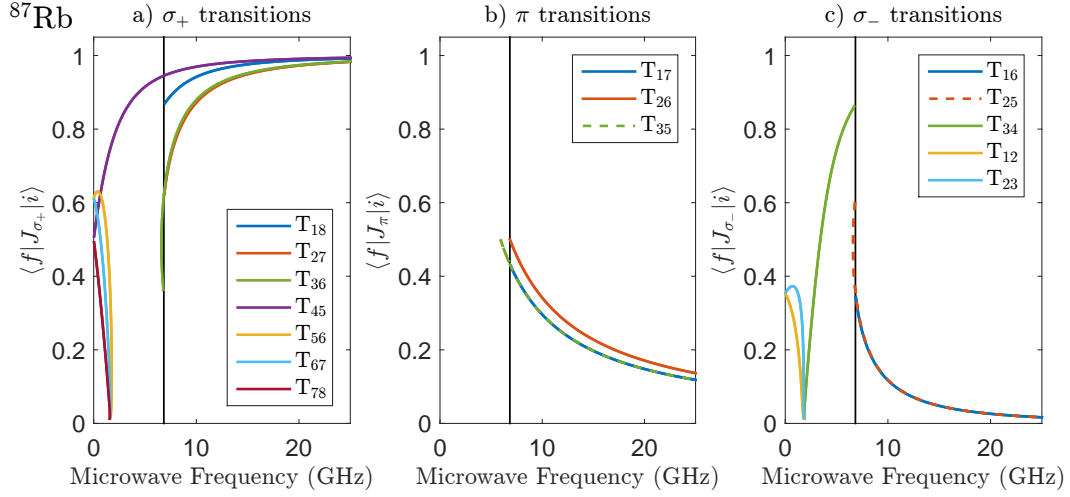


Figure D.4: Strengths of the σ_+ , π , and σ_- hyperfine transitions within the ^{87}Rb $5^2S_{1/2}$ ground state, as a function of the microwave transition frequency. The black vertical line is at 6.835 GHz. Data for ^{87}Rb was taken from Ref. [88].

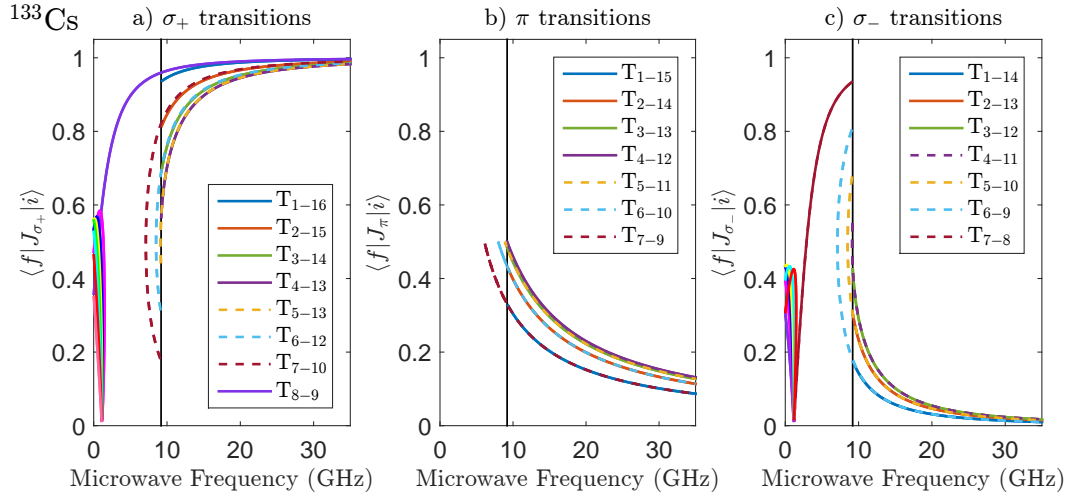


Figure D.5: Strengths of the σ_+ , π , and σ_- hyperfine transitions within the ^{133}Cs $6^2S_{1/2}$ ground state, as a function of the microwave transition frequency. The black vertical line is at 9.193 GHz. For the sake of brevity, the low-frequency transitions have been excluded from the legends. Data for ^{133}Cs was taken from Ref. [205].

Appendix E

Filling Station Operation

This appendix contains supplementary information to Chapter 6, including a more detailed description and photos of the setup, and operation instructions.

E.1 Ultrathin Cell Preparation

This section gives a step-by-step guide to preparing and installing a cell on the filling station setup. The cells are epoxied to a glass-metal transition, which is then attached to the filling station vacuum system.

- (a) Prepare the glass-metal (GM) transition¹. First, flatten and polish the end of the glass tube. It is important to keep the tube vertical at all times during grinding and polishing. We used an Al block, inserting the glass tube into a conveniently sized hole, as shown in Figure E.1.a. Apply pressure as evenly downward as possible, and trace out a figure-8 pattern on the polishing material. We began with a coarse polishing board², before moving to successively finer polishing papers³. At all stages, we used water for lubrication, and frequently wiped the surface clean of loose grit. Each stage requires 5-10 minutes of polishing. Check at the end of each stage that the polishing has been uniform. A good measure of this is the uniformity of the reflectivity of the end surface. The final surface should be mirror-like.

Once the glass has been polished smooth, clean the GM transition. First wipe off the ends and outside with a tissue wet with acetone. Then immerse the cell in acetone and clean for approximately 5 minutes in an ultrasonic bath. Rise with isopropanol, and then repeat the ultrasonic cleaning in an isopropanol bath. Rise again with isopropanol, and dry with an air gun.

- (b) Prepare the epoxy. We used a two-part epoxy⁴ which has been identified by

¹We use CF-16 to 13 mm diameter Pyrex transitions from Vaacom (T13P).

²Multidiamant, DAS 150.25, RAG 165848.00

³30 μm , 6 μm , 3 μm , 1 μm , 0.6 μm paper, from Thorlabs

⁴Epotek-377

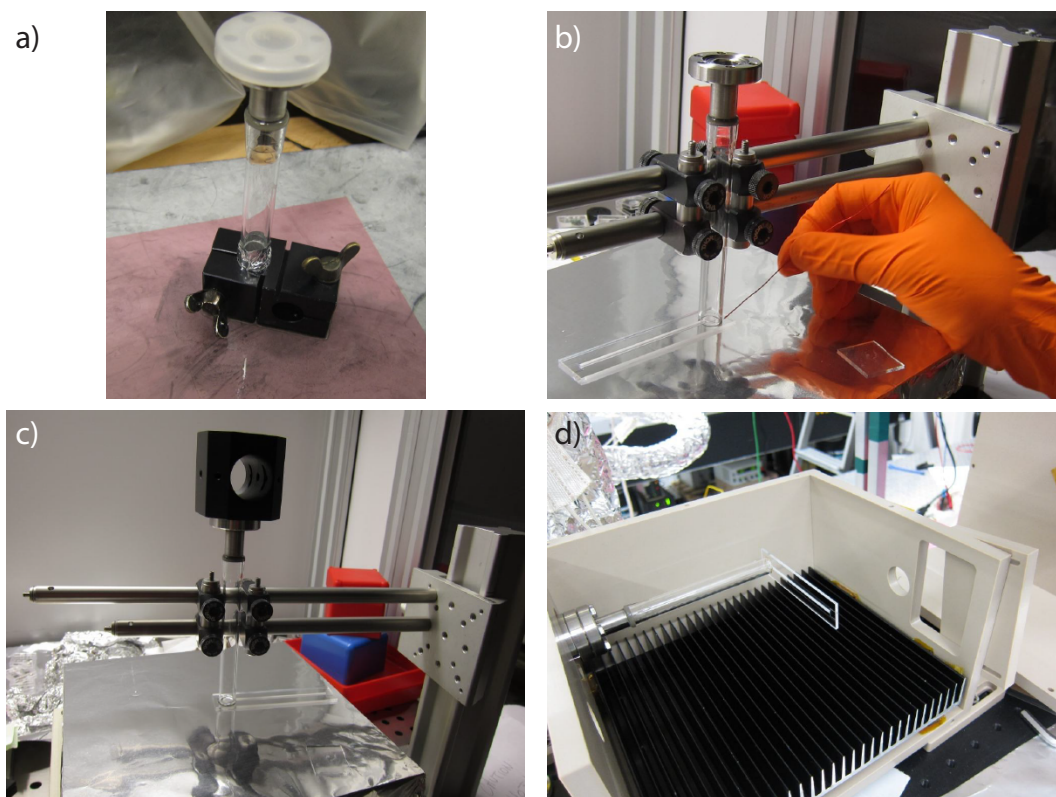


Figure E.1: Photos showing the preparation of ultrathin cells: a) Polishing the end of the GM transition to create a flat and smooth surface for bonding to the cell; b) Applying epoxy to join the cell and GM transition. The GM transition is gently held in a mounting frame, and the cell is placed on a heating platform; c) A weight is placed on top of the GM transition, applying a light pressure to the epoxy bond. The setup is then covered with Al foil (not shown), and slowly heated to set the epoxy; d) The cell and GM transition attached to the filling station.

the Pfau group in Stuttgart as being minimally affected by hot Rb vapours. Mix in equal parts, and then outgas for around 5 minutes in a (low) vacuum chamber.

- (c) Prepare the cell. It should be clean already – just double-check for bits of dust that might be on or in it.
- (d) Put the cell on to a heating plate, hole-side up. Apply epoxy to the end of the glass tube, and place it on top of the cell, with stabilising supports as shown in Figure E.1.b,c. Cover the tube and cell with Al foil, which creates a makeshift oven. Heat up to around 170°C , ramping up slowly over an hour or two. Leave it at equilibrium for another hour, and then let it slowly cool back down.

- (e) The cell and GM transition should now be bonded together and ready to attach to the filling station, as shown in Figure E.1.d. The angle of the cell can be adjusted with the help of a spirit-level before screwing the CF connection tight.

E.2 Vacuum System

The vacuum system is divided into several (partially overlapping) heating zones, as shown in Figure E.2.a. The names I have used for the various valves and other components are given in Figure E.2.b.

Figure E.3 shows photos of the filling station oven. The main heating is provided by two heating pads attached to the underside of the fins at the bottom of the oven. The two heating pads are connected in series, and are referred to as the Oven pads. There is additional heating around the glass-metal transition and the Cell Valve.

The limit on operating temperature is given by the valves, which have a long-term maximum operating temperature of 150°C, due to the Viton rubber used for the O-ring seals. Viton can survive up to 200°C for brief periods, however. The rest of the vacuum system is much more robust, with the CF connections between the vacuum components compatible with 400°C. The temperature sensors are not necessarily placed at the hottest points, and so it is safest to keep the temperatures of all sensors near the valves well below 150°C.

E.3 Rb Transfer

We introduce Rb to the vacuum system in a glass Rb ampule placed in a separate section of the vacuum system (see Figure E.2). After baking out the vacuum system at a temperature of approximately 140°C, we break the glass ampule, and transfer the Rb to the vapor cell. The Rb needs to travel from the Rb ampule, through the Central CF section, through the Cell Valve and into the cell. The Rb transport works by heating the ampule to create a large Rb vapor density, and creating a cold spot where the Rb should condense. The Central CF section should be the hottest section, in order to prevent Rb buildup there. The cell should be at room temperature: the colder the cell is, the more efficiently the Rb will transfer. The transfer takes several days, as the Rb must coat each surface with several monolayers before it is able to progress further [148].

- (a) Evacuate the system, and then close all of the valves. Double-check that the pressure gauge valve is closed. Otherwise, Rb will cover the gauge components and you will have to buy a new gauge.
- (b) Open the Pump Valve, and evacuate the central CF section. You should be able to go down to a few 10^{-8} mbar at the pump (at the time of writing, the pump pressure was 4×10^{-8} mbar with all but the Rb valve open), though a few 10^{-7} mbar is a sufficiently low pressure to proceed. If the pressure is too

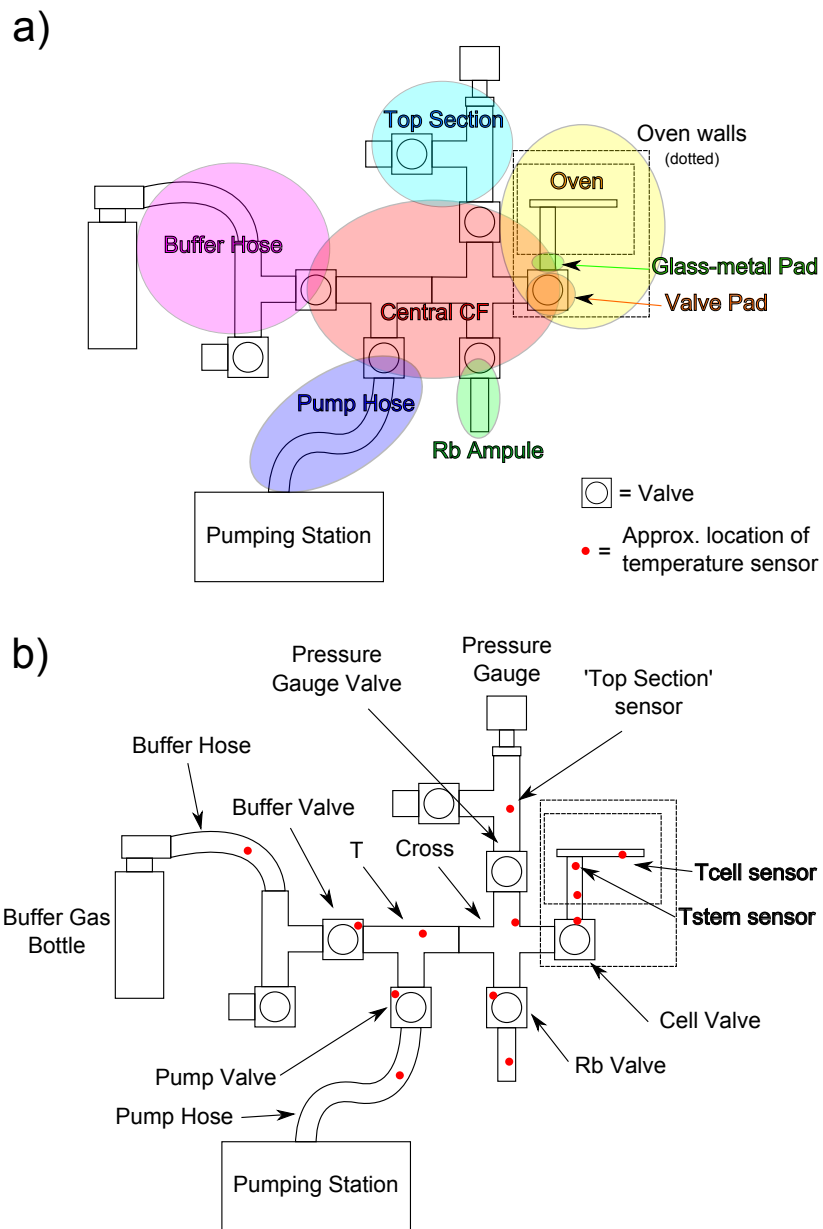


Figure E.2: Schematic diagrams of the vacuum system, showing a) the heating zones, and b) the approximate locations of temperature sensors and the names of certain pieces.

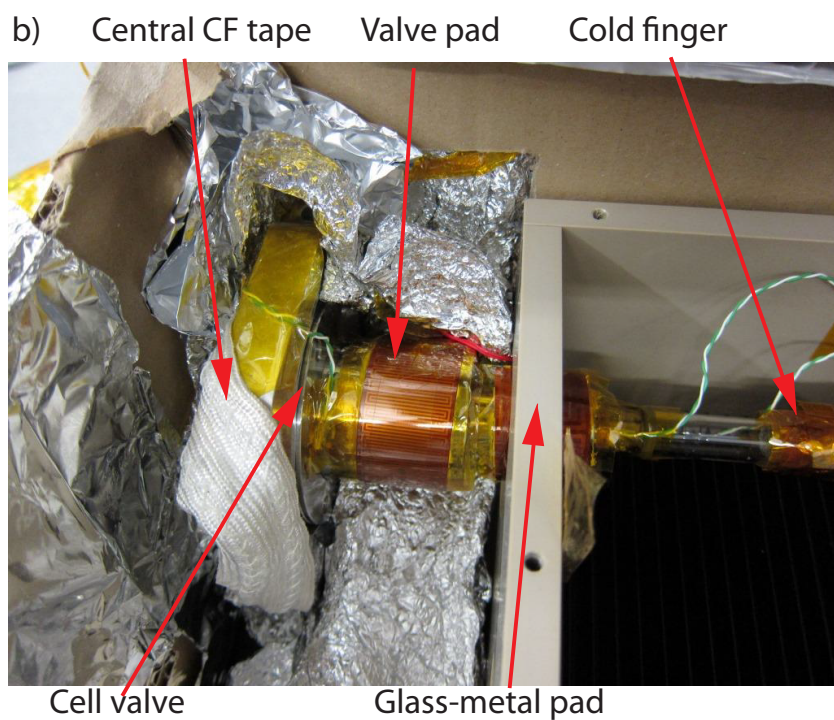
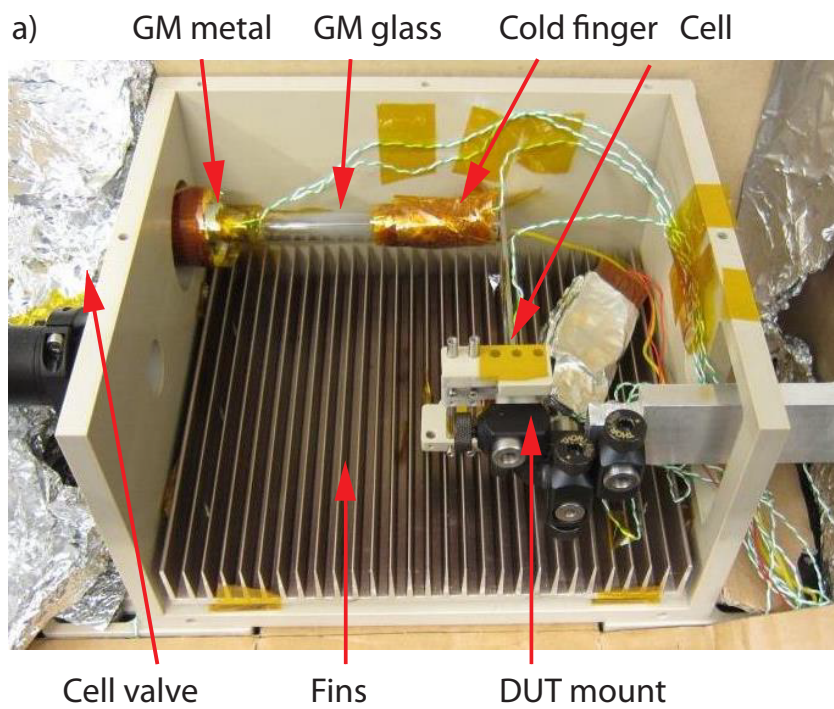


Figure E.3: Photos of a) the filling station oven; and b) a close-up of the cell valve, with heat insulation removed. The cell, DUT (device under test) mount, and various temperature control components are labelled.

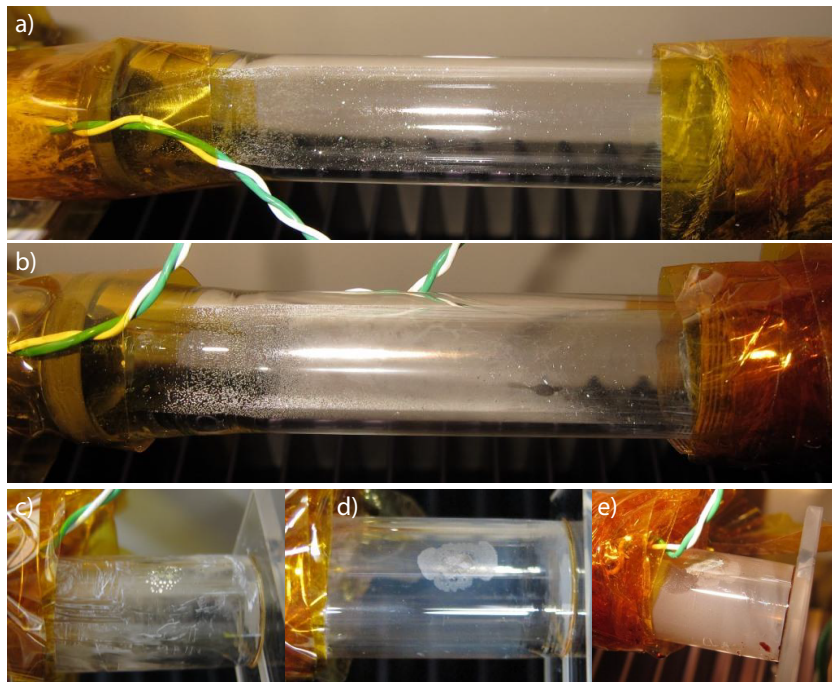


Figure E.4: Photos of the Rb transfer process and reservoir, showing a) specks of Rb appearing in the glass-metal transition during a Rb transfer; b) the white residue that appeared with the second Rb transfer; c) the Rb reservoir, consisting of macroscopic droplets of Rb formed underneath the cold finger. The white material on the surrounding glass is heat paste; d) the exhausted Rb reservoir after the cell curing process; and e) the accumulation of white residue around the Rb reservoir.

high, you can heat up the Central CF and Pump Hose sections, with only the Pump Valve open, for an extra period of baking.

- (c) Open the Rb Valve, and pump down on the Rb ampule section. You should only need to do this briefly, as the Rb itself should act as a strong getter for most contaminants/leakage into this section (except He). I generally find that the pressure at the pump jumps (briefly, for less than a minute) up to a few 10^{-6} mbar when the Rb Valve is opened.
- (d) Close the Pump Valve, and then open the Cell Valve. You should now have all valves closed, except for the Rb and Cell valves.
- (e) Now you can start heating everything up. Typical voltages and currents are given in Table E.1, and steady state temperatures in Table E.2. It is safest to increase the heating slowly in (say 2-3) stages. You should periodically check all of the temperature sensors (say once per 30 mins at the start, then less frequently after). Note that the oven and cell heating should be left off; Rb will condense best on a room temperature surface⁵.
- (f) The Rb transfer will take a few days. Just wait. After 1-2 days, you will start to see specks of Rb appear on the glass of the glass-metal transition. Once these have accumulated to a reasonable level (see Figure E.4.a), turn the heating off and wait for everything to cool down.
- (g) For the final stage of the Rb transfer, close the Cell Valve, and heat the oven up for a few hours, using the general operation heating parameters given in Table E.3. The Rb will condense on the glass underneath the cold finger, forming a reservoir. An example is shown in Figure E.4.c.

Table E.1: Typical heating settings for the filling station during a Rb transfer.

Central CF	Valve Pad	Glass-Metal Pad	Oven	Pump Hose	Buffer Hose	Top Sec.	Rb Ampule
127 V	70 V	8 V	0	115	0	55	1.0 A

Table E.2: Oven temperatures ($^{\circ}\text{C}$) in the filling station under the Rb transfer settings given in Table E.1.

Rb Valve	P. Gauge Valve	Top Sec.	Rb Ampule	Cross	Buffer Valve	Pump Valve	Buffer Hose	Pump Hose
126.5	142.3	49.6	105.0	121.0	120.6	133.1	23.5	149.3

⁵Or a cooler surface, but then you need to be particularly careful about condensation and strain due to temperature gradients.

E.4 Buffer Gas Filling

- (a) Start by ensuring there is a good vacuum in all of the system. Open all valves (except the two that open to atmosphere!), and pump down until a pressure better than a few 10^{-7} mbar is reached.
- (b) It is a good idea to also vent some buffer gas through the regulator to remove any contaminants that may have leaked in. Close all valves except the Buffer and Pump Valves. Open the buffer gas bottle, and adjust the coarse regulator valve to give a small (sub-mbar) pressure. Slowly open the needle valve, and vent gas through for a few seconds. Close the buffer gas bottle, and slowly vent all of the remaining gas in the regulator.
- (c) Now we can introduce buffer gas to the system. It is safest to first roughly find the correct pressure with the Cell Valve closed. Make sure that all of the valves, including the regulator valves are closed, with the exception of the the Buffer and Pressure Gauge Valves. Open the buffer gas bottle again, and adjust the coarse regulator valve to give ~ 100 mbar of buffer gas pressure. The exact value is not important, but it should be higher than the desired filling pressure. Slowly open the regulator needle, and increase the buffer gas pressure until the (top section) pressure gauge reads the desired pressure. It is a good idea to practice closing the valve off a few times as you increase the buffer pressure.
- (d) Once you have the desired buffer pressure in the vacuum system, open the Cell Valve. The pressure reading will fall a bit, and you can carefully add a little more buffer gas to the system if you are feeling confident. But in most situations, 1 or 2 mbar difference in buffer gas pressure will not drastically change the cell performance. Wait 5 minutes or so for things to equilibrate, and close the Cell Valve. The reading on the pressure gauge will increase as you close the valve. I used the midpoint of the open and closed values as the filling pressure.
- (e) **Double check that the cell valve is closed.**
- (f) Close all of the other valves, **including the buffer gas bottle**. The cell is now ready for use. The cell can be operated for several weeks without need for refilling (depending on the condition of the cell valve).

E.5 General Operation

For general operation of the filling station setup, we only need to heat the area around the vapor cell. Typical settings for the heating system are given in Table E.3, and the resulting temperatures in Table E.4. One thing to note is that for historical reasons, the heating tape from the Central CF section (T, Cross, Buffer-, Pump,

Cell, and Rb Valves) is partially responsible for heating the Cell Valve. This means that the heating for the central CF section also needs to be turned on when operating the oven. Otherwise, the Cell Valve will be too cold, and the Rb will condense there instead of under the cold finger.

Table E.3: Typical heating settings for the filling station under general operation.

Central CF	Valve Pad	Glass-Metal Pad	Oven	Pump Hose	Buffer Hose	Top Sec.	Rb Ampule
100 V	84 V 0.15 A	7 V 0.13 A	1.08 A	0	0	0	0

Table E.4: Oven temperatures ($^{\circ}\text{C}$) in the filling station under the general operation settings given in Table E.3.

Fins (bottom)	Fins (top)	Cell	GM metal	GM glass	Cold finger	Oven top	Cell Valve	Chip Mount
182.5	181.7	146.9	150.4	151.1	130.1	145.4	136.5	84.3

The maximum heating rate with the settings given in Table E.3 is quite slow, and the oven takes 2-3 hours to heat up. Once the system has been characterised, this means that the oven heating can simply be switched on, and left to heat up without further monitoring.

The Cell Valve should be closed at all times during operation. It is a good idea to close the other valves as well, for example to prevent dirt from the heated central CF section condensing in the unheated sections. The pumping station should be turned off, as it otherwise creates mechanical noise in the system.

E.6 Valve Damage

The cell valve developed a leak after several months of operation. As discussed in section 6.5.1, this was due to Rb degrading the Viton O-ring seal. Damaged seals may be replaced (in practice, this requires also replacing the cell), and a possible long-term solution is to instead use a valve with a copper seal. Photos of the damaged valve are shown in Figure E.5.

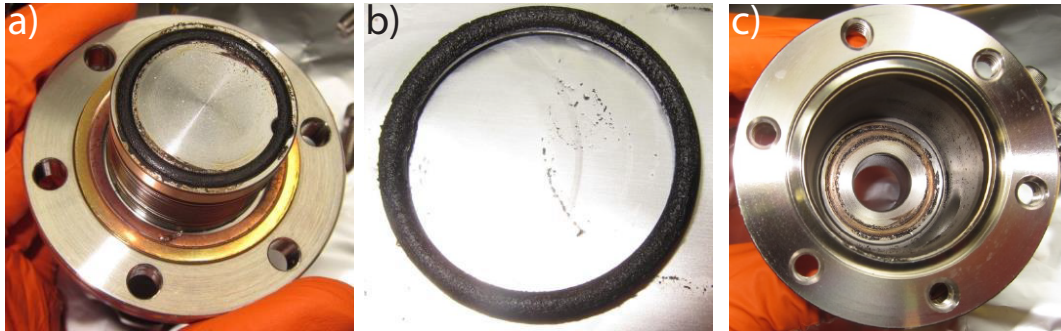


Figure E.5: Photos of the damaged cell valve, showing a) the valve actuator, with the O-ring in place; b) the O-ring after removal from the valve; and c) the brown and black markings left by the O-ring where it pressed into the valve housing to create a seal.

Appendix F

Cell Cleaning

Rb in a vapor cell will accumulate at the coldest point available to it. Ideally, this is somewhere well away from the windows, with a well-defined temperature. The cell windows are difficult to heat however, due to the need for optical access, and it is common for Rb and other contaminants to build up on them. This can be tolerated for some time, but eventually the cell windows become opaque, and must be cleaned. The build up of Rb and other contaminants is a largely reversible process, and so we can clean the cells by reversing the temperature gradient. We locally heat the cell windows, and allow the Rb and contaminants to accumulate in a new cold spot.

Figure F.1 shows the cleaning process for the microcells. Typical cleaning temperatures were $\sim 150^\circ\text{C}$. Figure F.2 shows the process for the ultrathin cells. I created a 15°C temperature gradient along the cell, and a 30°C temperature gradient between the far end of the cell and the cold finger. In order to increase the mobility of the residue, I performed the cleaning at high temperature. The far end of the cell was at 157°C , the cold-finger-end was at 143°C , and the cold finger was at 128°C .

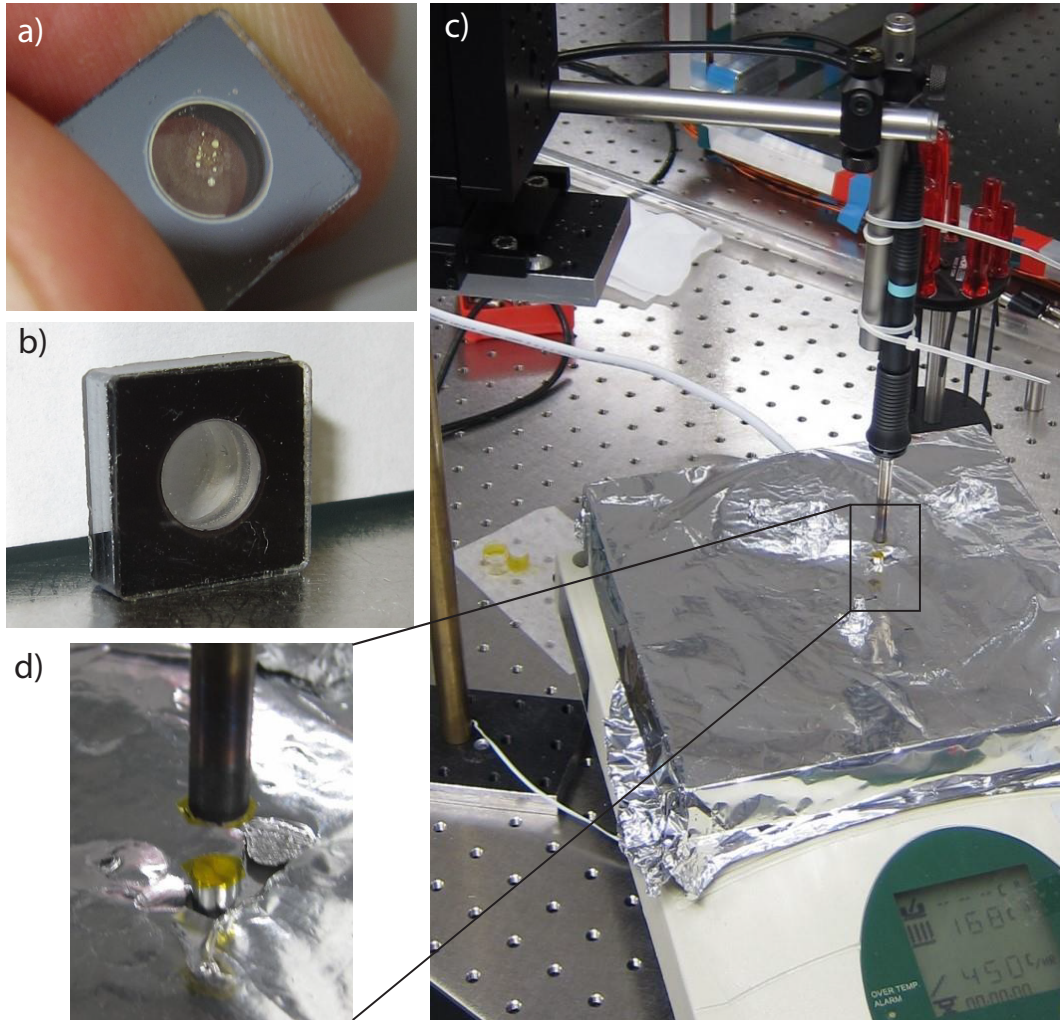


Figure F.1: Photos of the cleaning process for the microcells, showing a) the M1 cell before cleaning, with Rb and what is most likely Rb_2O on the windows; b) the M1 cell after cleaning. Most of the buildup is gone, but a faint brown layer can still be seen in the centre; c) the setup used for cleaning, which used a soldering iron with the tip screwed off and a metal cylinder on top of a heating plate to locally heat the cell windows; and d) zoomed in picture of the cylinder and soldering iron, which were covered in Kapton tape in order to avoid scratching the cell windows.

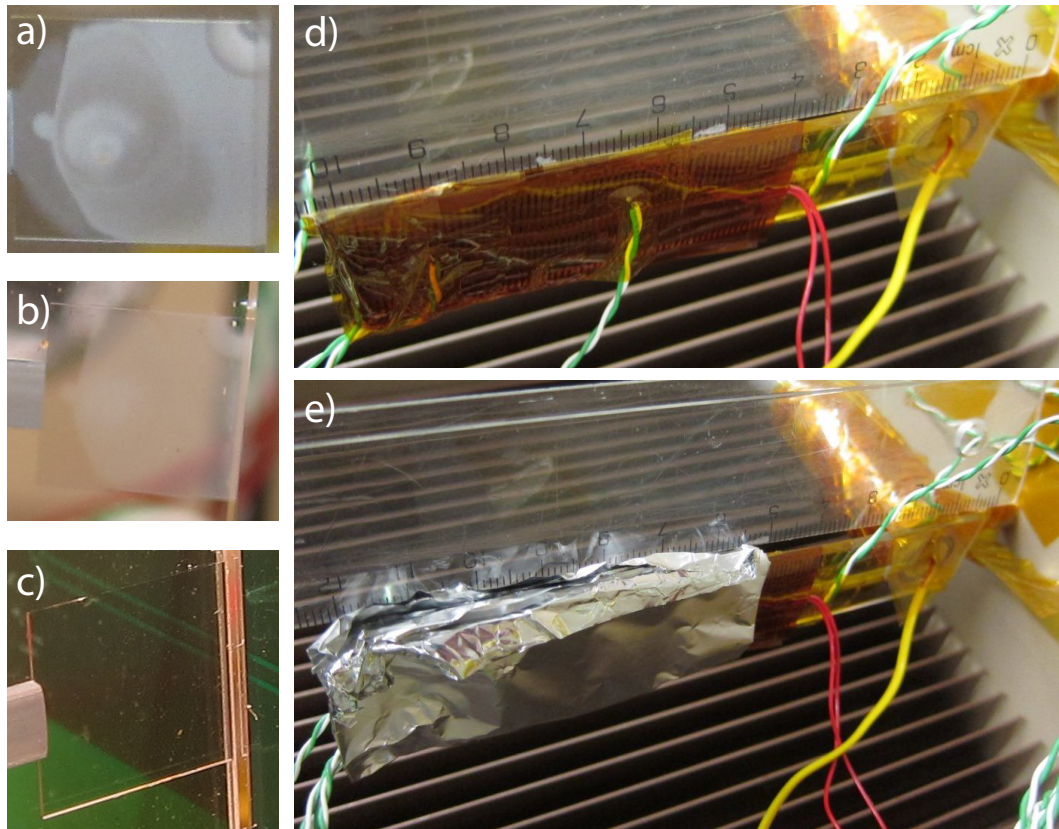


Figure F.2: Photos of the cleaning process for the ultrathin cells, showing a) the U1 cell with a large buildup of white residue on the windows; b) the U1 cell after 4.5 days of cleaning; c) the clean-as-new U1 cell after several days more of cleaning; d+e) the cleaning involved wrapping the cell with a heating pad and insulating Al foil to create a temperature gradient that drove the white residue back under the cold finger (see also Figure E.4.e).

Appendix G

How to see Rabi Oscillations

In every new setup, seeing the first Rabi oscillation is something of a process. The main obstacles are finding the right microwave frequency to drive the atomic transitions, which may have an unknown shift due to buffer gas collisions or a dc magnetic field, and obtaining microwaves with a sufficiently large amplitude to drive Rabi oscillations during the T_2 time.

Aside from the larger signal given by a thicker cell, Rabi oscillations are generally easier to see in a thin cell with high buffer gas pressures. The spatial confinement of the atoms makes it easier to ensure that the atoms see uniform dc and microwave magnetic fields over the interrogation time. Additionally, in order to see Rabi oscillations driven by a travelling microwave, the cell dimensions must be significantly smaller than the microwave wavelength (4 cm for 6.8 GHz). In larger cells, atoms at different positions in the cell will see different phases of the microwave field, will wash out phase-sensitive measurements, such as Faraday rotation. Our measurements are unaffected however, as our absorption imaging measures atomic populations, which are insensitive to the microwave phase. Cell size is less important in a microwave magnetron cavity, where the microwave phase is relatively uniform throughout the cavity.

On the other hand, as the cell thickness decreases, relaxation rates also increase, both due to wall collisions, and the increased Rb SE associated with a higher operating temperature. Larger microwave amplitudes are then required to drive Rabi oscillations within the reduced T_2 time.

The geometry around the cell is important when driving oscillations with a far field microwave. Pieces of metal and coils of wire will impose boundary conditions on the microwave, and it is possible for such items to form a crude microwave cavity. Although this can provide the benefit of amplifying the microwave, the main result is that the coupling of the microwave source into the cell region becomes strongly dependent on source position, and to some extent microwave frequency. Near field microwaves are less affected by the surrounding geometry, as the perturbing geometry is generally at a distance much larger than the near field length scales.

When attempting to see a first Rabi oscillation, it is best to start with a DR sig-

nal on an oscilloscope. It is significantly easier to optimise the DR signal, which gives feedback in real time and has a clearer response to weak or off-resonant microwaves. The first step is to find the microwave transition frequency of the atoms, which may not necessarily be known, due to uncertainties in the buffer gas pressure or dc magnetic field. This step is best performed using a microwave horn or antenna, which radiate uniform fields, rather than using a non-uniform DUT near field. Perform a scan of the microwave centre frequency (CF), with a reasonably large frequency span (ΔF). The optimal ΔF depends on the system parameters, but is perhaps 10 to 1000 times the transition linewidth. This is a relatively straightforward task for low dc magnetic fields, and all 7 DR peaks should be visible in a single frequency sweep (depending on the microwave polarisation). The microwave frequency sweep rate should not be too fast or too slow, as the signal will wash out in both regimes. I generally found a 10-50 ms sweep time worked well. Once you find a DR peak, reduce ΔF to find the resonance frequency. With a DR peak visible on the scope, the other parameters can then be optimised. These include laser intensity, polarisation, and stability, the microwave horn position, and the microwave power. The microwave source can then be replaced by the DUT, and the parameters, including DUT placement, optimised again.

In some cases, it is also extremely difficult to see a first DR signal, such as in the frequency tunable setup presented in Chapter 8. As discussed in Section 3.4.6 and Chapter 9, I have written an absorption imaging sequence that produces OD_{mw} images, i.e. contour lines of the microwave field, in quasi real time (0.3 Hz, limited by coding). I found that this was the most robust way to get a first microwave signal, and could be used to align the microwave source relative to the cell and optimise the signal. A particular advantage is that the OD_{mw} images give the shape of the resonant microwave field in the cell, showing if the microwave is only penetrating a small distance into the cell, or is only resonant with a small fraction of the atoms (due to large dc field gradients). Once the OD_{mw} images have been used to obtain a signal, the final optimisation is still best performed using the DR method described above. This is due in large part to the still relatively slow OD_{mw} image refresh rate.

Appendix H

S-Parameter Characterisations of the Demonstration Microwave Devices

Here, I present S-Parameter measurements of the three demonstration structures used in Chapter 7. The S-Parameters measure reflection (S11) and transmission (S12) signals through the two ports on the devices as a function of microwave frequency. The measurements were performed using a vector network analyser¹.

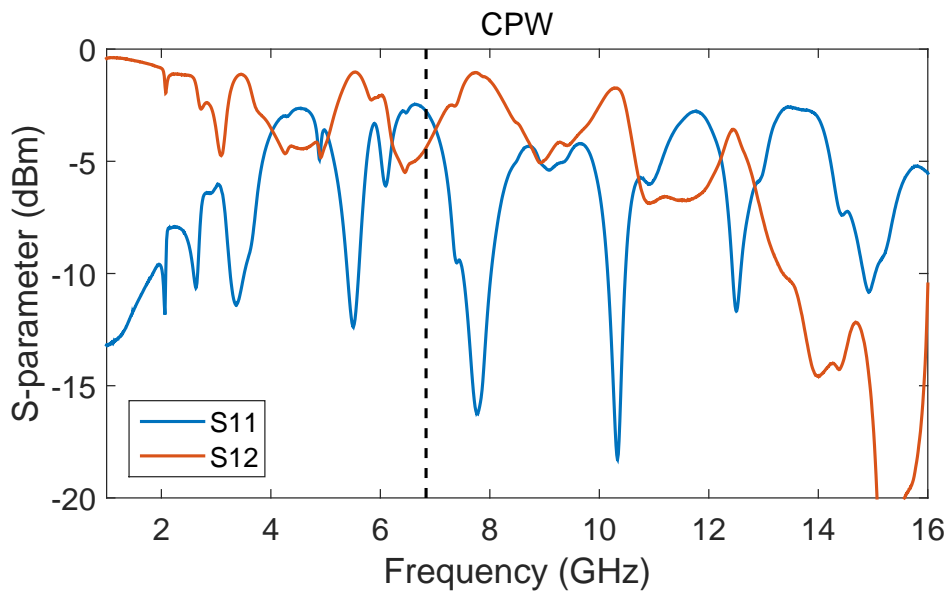


Figure H.1: S11 (reflection) and S12 (transmission) parameters for the CPW. The dotted line is at 6.835 GHz.

¹Agilent PNA N5222A.

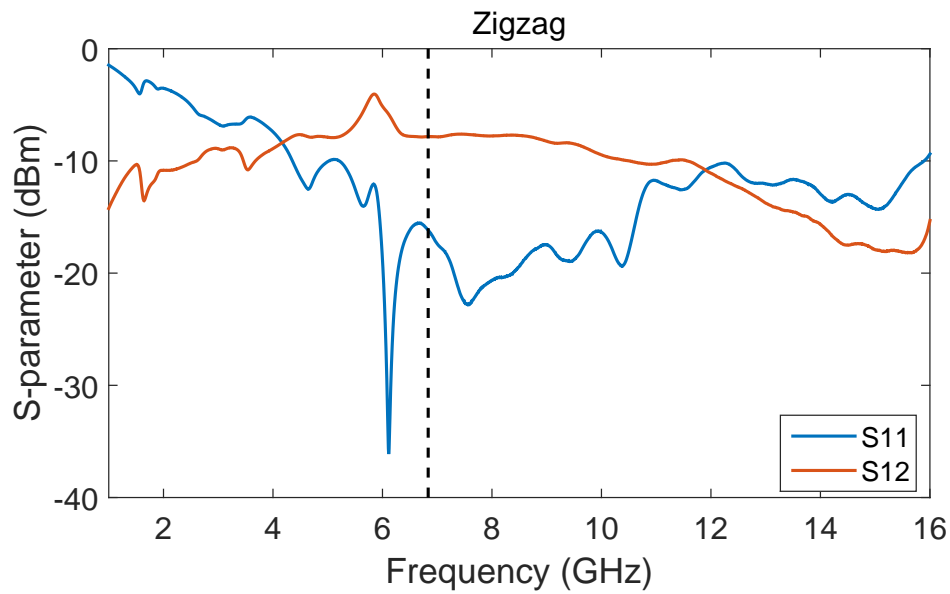


Figure H.2: S11 (reflection) and S12 (transmission) parameters for the Zigzag chip. The dotted line is at 6.835 GHz.

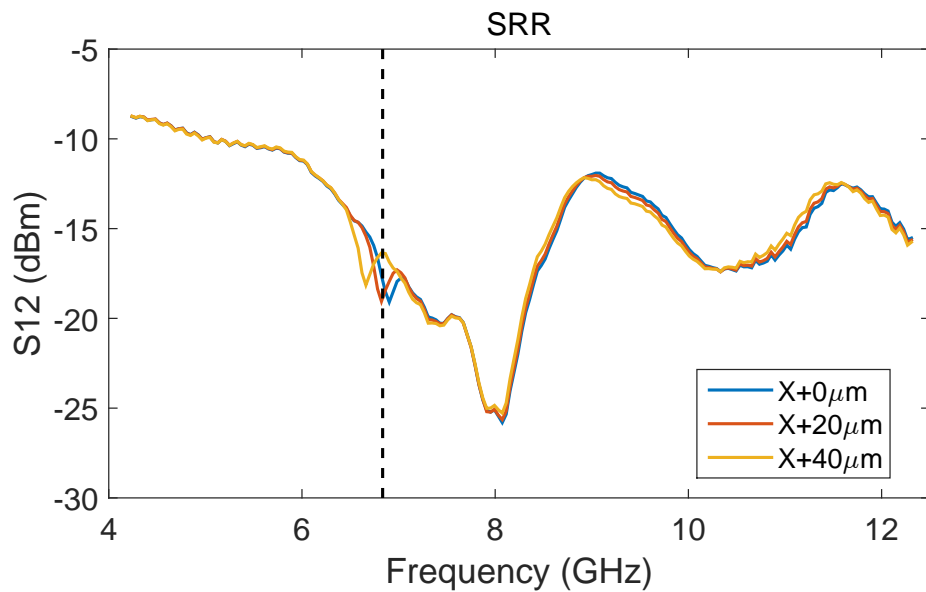


Figure H.3: S12 parameter (transmission) for the SRR. Traces are shown for different chip-cell distances, showing the tuning of the resonance peak. The variable X accounts for the fact that the absolute chip-cell distance was not measured. The dotted line is at 6.835 GHz.

Bibliography

- [1] W Franzen. Spin relaxation of optically aligned rubidium vapor. *Physical Review*, 115(4):850–856, 1959.
- [2] M. Arditi and T. R. Carver. Hyperfine Relaxation of Optically Pumped Rb⁸⁷ Atoms in Buffer Gases. *Physical Review*, 136(3A):A643, 1964.
- [3] M. A. Bouchiat and J Brossel. Relaxation of optically pumped Rb atoms on paraffin-coated walls. *Physical Review*, 147(1), 1966.
- [4] William Happer. Optical pumping. *Reviews of Modern Physics*, 44(2):169–249, 1972.
- [5] Jacques Vanier, Jean-F Simard, and Jean-S Boulanger. Relaxation and frequency shifts in the ground state of Rb⁸⁵. *Physical Review A*, 9(3):1031, 1974.
- [6] Jacques Vanier, Claude Audoin, and Adam Hilger. *The Quantum Physics of Atomic Frequency Standards*, volume 1. Adam Hilger, Bristol, 1989.
- [7] James Camparo. The Rubidium Atomic Clock and Basic Research. *Physics Today*, 60(11):33, 2007.
- [8] J. Vanier and C. Mandache. The passive optically pumped Rb frequency standard: the laser approach. *Applied Physics B*, 87(4):565–593, May 2007.
- [9] Svenja Knappe, Vishal Shah, Peter D. D. Schwindt, Leo Hollberg, John Kitching, Li-Anne Liew, and John Moreland. A microfabricated atomic clock. *Appl. Phys. Lett.*, 85(9):1460, 2004.
- [10] M Pellaton, C Affolderbach, Y Pétremand, N de Rooij, and G Mileti. Study of laser-pumped double-resonance clock signals using a microfabricated cell. *Physica Scripta*, T149:014013, May 2012.
- [11] S. Kang, M. Gharavipour, C. Affolderbach, F. Gruet, and G. Mileti. Demonstration of a high-performance pulsed optically pumped Rb clock based on a compact magnetron-type microwave cavity. *Journal of Applied Physics*, 117(10):104510, 2015.

- [12] D. Budker, W. Gawlik, D. F. Kimball, S. M. Rochester, V. V. Yashchuk, and A. Weis. Resonant nonlinear magneto-optical effects in atoms. *Reviews of Modern Physics*, 74(October):1153, 2002.
- [13] D Budker and M Romalis. Optical magnetometry. *Nature Physics*, 3:227–234, 2007.
- [14] John Kitching, Svenja Knappe, and Elizabeth A. Donley. Atomic Sensors – A Review. *IEEE Sensors Journal*, 11(9):1749–1758, September 2011.
- [15] M. V. Balabas, D. Budker, J. Kitching, P. D. D. Schwindt, and J. E. Stalnaker. Magnetometry with millimeter-scale antirelaxation-coated alkali-metal vapor cells. *Journal of the Optical Society of America B*, 23(6):1001, 2006.
- [16] Vishal Shah, Svenja Knappe, Peter D. D. Schwindt, and John Kitching. Sub-picotesla atomic magnetometry with a microfabricated vapour cell. *Nature Photonics*, 1(11):649–652, November 2007.
- [17] Peter D. D. Schwindt, Brad Lindseth, Svenja Knappe, Vishal Shah, John Kitching, and Li-Anne Liew. Chip-scale atomic magnetometer with improved sensitivity by use of the M_x technique. *Appl. Phys. Lett.*, 90(8):081102, 2007.
- [18] Theo Scholtes, Volkmar Schultze, Rob IJsselsteijn, Stefan Woetzel, and Hans-Georg Meyer. Light-shift suppression in a miniaturized M_x optically pumped Cs magnetometer array with enhanced resonance signal using off-resonant laser pumping. *Opt. Exp.*, 20(28):29217–22, December 2012.
- [19] I. Savukov, S. Seltzer, M. Romalis, and K. Sauer. Tunable Atomic Magnetometer for Detection of Radio-Frequency Magnetic Fields. *Phys. Rev. Lett.*, 95(6):063004, August 2005.
- [20] H. B. Dang, A. C. Maloof, and M. V. Romalis. Ultrahigh sensitivity magnetic field and magnetization measurements with an atomic magnetometer. *Applied Physics Letters*, 97(15):151110, 2010.
- [21] E A Donley, J L Long, T C Liebisch, E R Hodby, T A Fisher, and J Kitching. Nuclear quadrupole resonances in compact vapor cells: The crossover between the NMR and the nuclear quadrupole resonance interaction regimes. *Phys. Rev. A*, 79:013420, 2009.
- [22] S.-K. Lee, K. L. Sauer, S. J. Seltzer, O. Alem, and M. V. Romalis. Sub-femtotesla radio-frequency atomic magnetometer for detection of nuclear quadrupole resonance. *Applied Physics Letters*, 89(21):214106, 2006.
- [23] Li Yao and Shoujun Xu. Long-range, high-resolution magnetic imaging of nanoparticles. *Angewandte Chemie (International ed. in English)*, 48(31):5679–82, January 2009.

- [24] Dindi Yu, Songtham Ruangchaithaweek, Li Yao, and Shoujun Xu. Detecting molecules and cells labeled with magnetic particles using an atomic magnetometer. *Journal of Nanoparticle Research*, 14(9):1135, August 2012.
- [25] D Issadore, Y I Park, H Shao, C Min, K Lee, M Liong, R Weissleder, and H Lee. Magnetic sensing technology for molecular analyses. *Lab on a chip*, 14(14):2385–97, July 2014.
- [26] Michael V. Romalis and Hoan B. Dang. Atomic magnetometers for materials characterization. *Materials Today*, 14(6):258–262, June 2011.
- [27] Arne Wickenbrock, Sarunas Jurgilas, Albert Dow, Luca Marmugi, and Ferruccio Renzoni. Magnetic induction tomography using an all-optical ^{87}Rb atomic magnetometer. *Optics Letters*, 39(22):6367, 2014.
- [28] I. Savukov and M. Romalis. NMR Detection with an Atomic Magnetometer. *Physical Review Letters*, 94(12):123001, March 2005.
- [29] I M Savukov, V S Zotev, P L Volegov, M a Espy, a N Matlashov, J J Gomez, and R H Kraus. MRI with an atomic magnetometer suitable for practical imaging applications. *Journal of magnetic resonance (San Diego, Calif. : 1997)*, 199(2):188–91, August 2009.
- [30] I Savukov and T Karaulanov. Anatomical MRI with an atomic magnetometer. *Journal of magnetic resonance (San Diego, Calif. : 1997)*, 231:39–45, June 2013.
- [31] Shoujun Xu, Valeriy V Yashchuk, Marcus H Donaldson, Simon M Rochester, Dmitry Budker, and Alexander Pines. Magnetic resonance imaging with an optical atomic magnetometer. *Proceedings of the National Academy of Sciences of the United States of America*, 103(34):12668–71, August 2006.
- [32] Shoujun Xu, C. Crawford, Simon Rochester, Valeriy Yashchuk, Dmitry Budker, and Alexander Pines. Submillimeter-resolution magnetic resonance imaging at the Earth’s magnetic field with an atomic magnetometer. *Physical Review A*, 78(1):013404, July 2008.
- [33] G. Bison, N. Castagna, A. Hofer, P. Knowles, J.-L. Schenker, M. Kasprzak, H. Saudan, and A. Weis. A room temperature 19-channel magnetic field mapping device for cardiac signals. *Applied Physics Letters*, 95(17):173701, 2009.
- [34] Orang Alem, Tilmann H Sander, Rahul Mhaskar, John LeBlanc, Hari Eswaran, Uwe Steinhoff, Yoshio Okada, John Kitching, Lutz Trahms, and Svenja Knappe. Fetal magnetocardiography measurements with an array of microfabricated optically pumped magnetometers. *Physics in Medicine and Biology*, 60(12):4797–4811, 2015.

- [35] I Savukov and T Karaulanov. Magnetic-resonance imaging of the human brain with an atomic magnetometer. *Applied Physics Letters*, 103(4):43703, July 2013.
- [36] Cort N Johnson, P D D Schwindt, and M Weisend. Multi-sensor magnetoencephalography with atomic magnetometers. *Physics in medicine and biology*, 58(17):6065–77, September 2013.
- [37] Robert Wyllie, Matthew Kauer, Ronald T Wakai, and Thad G Walker. Optical magnetometer array for fetal magnetocardiography. *Optics letters*, 37(12):2247–9, July 2012.
- [38] Vishal K Shah and Ronald T Wakai. A compact, high performance atomic magnetometer for biomedical applications. *Physics in medicine and biology*, 58(22):8153–61, November 2013.
- [39] L Weller, KS S Kleinbach, Mark A. Zentile, S Knappe, I G Hughes, and C S Adams. Optical isolator using an atomic vapor in the hyperfine Paschen–Back regime. *Optics Letters*, 37(16):2–5, August 2012.
- [40] Mark A Zentile, Daniel J Whiting, James Keaveney, Charles S Adams, and Ifan G Hughes. Sub-GHz Faraday filter on the Cs D1 line. (2):1–4.
- [41] Matthias Widmann, Simone Portalupi, Sang-yun Lee, Peter Michler, and Ilja Gerhardt. Faraday Filtering on the Cs-D 1 -Line for Quantum Hybrid Systems. pages 1–4, 2015.
- [42] M Hosseini, B M Sparkes, G Campbell, P K Lam, and B C Buchler. High efficiency coherent optical memory with warm rubidium vapour. *Nature communications*, 2(2):174, 2011.
- [43] D. Higginbottom, B. Sparkes, M. Rancic, O. Pinel, M. Hosseini, P. Lam, and B. Buchler. Spatial-mode storage in a gradient-echo memory. *Physical Review A*, 86(2):1–10, August 2012.
- [44] K. Jensen, W. Wasilewski, H. Krauter, T. Fernholz, B. M. Nielsen, M. Owari, M. B. Plenio, a. Serafini, M. M. Wolf, and E. S. Polzik. Quantum memory for entangled continuous-variable states. *Nature Physics*, 7(1):13–16, November 2010.
- [45] P. S. Michelberger, T. F. M. Champion, M. R. Sprague, K. T. Kaczmarek, M. Barbieri, X. M. Jin, D. G. England, W. S. Kolthammer, D. J. Saunders, J. Nunn, and I. A. Walmsley. Interfacing GHz-bandwidth heralded single photons with a room-temperature Raman quantum memory. *New Journal of Physics*, 17(4):43006, 2014.
- [46] I Fescenko and A Weis. Imaging magnetic scalar potentials by laser-induced fluorescence from bright and dark atoms. *Journal of Physics D: Applied Physics*, 47(23):235001, 2014.

- [47] Jonathon A. Sedlacek, Arne Schwettmann, Harald Kübler, Robert Löw, Tilman Pfau, and James P. Shaffer. Microwave electrometry with Rydberg atoms in a vapour cell using bright atomic resonances. *Nature Physics*, 8(11):819–824, September 2012.
- [48] J Sedlacek, A Schwettmann, H. Kübler, and J. P. Shaffer. Atom Based Vector Microwave Electrometry Using Rubidium Rydberg Atoms in a Vapor Cell. *Physical Review Letters*, 111:063001, 2013.
- [49] H Q Fan, S Kumar, R Daschner, H Kübler, and J P Shaffer. Subwavelength microwave electric-field imaging using Rydberg atoms inside atomic vapor cells. *Optics Letters*, 39(10):3030–3, May 2014.
- [50] Pascal Böhi and Philipp Treutlein. Simple microwave field imaging technique using hot atomic vapor cells. *Appl. Phys. Lett.*, 101(18):181107, 2012.
- [51] Andrew Horsley, Guan-Xiang Du, Matthieu Pellaton, Christoph Affolderbach, Gaetano Mileti, and Philipp Treutlein. Imaging of relaxation times and microwave field strength in a microfabricated vapor cell. *Physical Review A*, 88(6):063407, December 2013.
- [52] Christoph Affolderbach, Guan-Xiang Du, Thejesh Bandi, Andrew Horsley, Philipp Treutlein, and Gaetano Mileti. Imaging Microwave and DC Magnetic Fields in a Vapor-Cell Rb Atomic Clock. *IEEE Transactions on Instrumentation and Measurement*, PP(99), 2015.
- [53] Andrew Horsley, Guan-Xiang Du, and Philipp Treutlein. Widefield Microwave Imaging in Alkali Vapor Cells with sub-100 μm Resolution. *arXiv*, 2015.
- [54] Pascal Böhi, Max F. Riedel, Theodor W. Hänsch, and Philipp Treutlein. Imaging of microwave fields using ultracold atoms. *Appl. Phys. Lett.*, 97(5):051101, August 2010.
- [55] A Imtiaz, Thomas Mitchell Wallis, and P Kabos. Near-Field Scanning Microwave Microscopy. *IEEE microwave magazine*, (February):52–64, 2014.
- [56] Björn T. Rosner and Daniel W. Van Der Weide. High-frequency near-field microscopy. *Review of Scientific Instruments*, 73(7):2505, 2002.
- [57] Anton Ivanov, Thejesh Bandi, Guan-Xiang Du, Andrew Horsley, Christoph Affolderbach, Philipp Treutlein, Gaetano Mileti, and Anja K. Skrivervik. Experimental and Numerical Studies of the Microwave Field Distribution in a Compact Magnetron-Type Microwave Cavity. *in proceedings of the 28th European Frequency and Time Forum (EFTF), Neuchatel, Switzerland, June 22-26 2014*, 2014.
- [58] B Deutschmann. On the effects of transient electromagnetic interference on integrated circuits. *Electronic Device Failure Analysis*, 8(4):16–24, 2006.

- [59] Tristan Dubois, Sylvie Jarrix, Annick Penarier, Philippe Nouvel, Daniel Gasquet, Laurnet Chusseau, and Bruno Azais. Near-field electromagnetic characterization and perturbation of logic circuits. *IEEE Transactions on Instrumentation and Measurement*, 57(11):2398–2404, 2008.
- [60] Thomas P Budka, Scott D Waclawik, and Gabriel M. Rebeiz. A Coaxial 0.5-18 GHz Near Electric Field Measurement System for Planar Microwave Circuits Using Integrated Probes. *IEEE Transactions on Microwave Theory and Techniques*, 44(12):2174–2184, 1996.
- [61] Selahattin Sayil, David V. Kerns, and Sherra E. Kerns. A survey of contactless measurement and testing techniques. *IEEE Potentials*, 24(1):25–28, 2005.
- [62] Selahattin Sayil, DV Kerns Jr, and SE Kerns. Comparison of contactless measurement and testing techniques to a all-silicon optical test and characterization method. *IEEE Transactions on Instrumentation and Measurement*, 54(5):2082–2089, 2005.
- [63] Yingjie Gao and Ingo Wolff. Miniature electric near-field probes for measuring 3-d fields in planar microwave circuits. *IEEE Transactions on Microwave Theory and Techniques*, 46(7):907–913, 1998.
- [64] S. K. Dutta, C. P. Vlahacos, D. E. Steinhauer, Ashfaq S. Thanawalla, B. J. Feenstra, F. C. Wellstood, Steven M. Anlage, and Harvey S Newman. Imaging microwave electric fields using a near-field scanning microwave microscope. *Applied Physics Letters*, 74(1):156–158, 1999.
- [65] R C Black, F C Wellstood, E. Dantsker, a. H. Miklich, D. Koelle, F. Ludwig, and J. Clarke. Imaging radio-frequency fields using a scanning SQUID microscope. *Applied Physics Letters*, 66(10):1267, 1995.
- [66] Pengfei Wang, Zhenheng Yuan, Pu Huang, Xing Rong, Mengqi Wang, Xiangkun Xu, Changkui Duan, Chenyong Ju, Fazhan Shi, and Jiangfeng Du. High-resolution vector microwave magnetometry based on solid-state spins in diamond. *Nature Communications*, 6:6631, 2015.
- [67] Patrick Appel, Marc Ganzhorn, Elke Neu, and Patrick Maletinsky. Nanoscale microwave imaging with a single electron spin in diamond. To be published.
- [68] D. Winkler, R. Schmitt, M. Brunner, and B. Lischke. Flexible picosecond probing of integrated circuits with chopped electron beams. *IBM Journal of Research and Development*, 34(2.3):189–203, March 1990.
- [69] Michel Vallet and Philippe Sardin. Electrical testing for failure analysis: E-beam testing. *Microelectronic engineering*, 49:157–167, 1999.
- [70] Christoph Böhm. Electric Force Microscopy: Gigahertz and Nanometer Measurement Tool. *Microelectronic Engineering*, 31:171–179, 1996.

- [71] W. Mertin. New aspects in electro-optic sampling. *Microelectronic Engineering*, 31(1-4):365–376, February 1996.
- [72] Yingjie Gao and Ingo Wolff. A new miniature magnetic field probe for measuring three-dimensional fields in planar high-frequency circuits. *IEEE Transactions on Microwave Theory and Techniques*, 44(6):911–918, 1996.
- [73] J.L. Jordan, R.N. Simons, and C.a. Zorman. Contactless radio frequency probes for high-temperature characterisation of microwave integrated circuits. *Electronics Letters*, 50(11):817–819, May 2014.
- [74] G. M. Sardi, a. Lucibello, M. Kasper, G. Gramse, E. Proietti, F. Kienberger, and R. Marcelli. Optimization of the imaging response of scanning microwave microscopy measurements. *Applied Physics Letters*, 107(3):033107, 2015.
- [75] R. C. Black, F. C. Wellstood, E. Dantsker, a. H. Miklich, D. T. Nemeth, D. Koelle, F. Ludwig, and J. Clarke. Microwave microscopy using a superconducting quantum interference device. *Applied Physics Letters*, 99(1995):99, 1995.
- [76] Vladimir V Talanov, Nesco M Lettsome Jr, Valery Borzenets, Nicolas Gagliolo, Alfred B Cawthorne, and Antonio Orozco. A scanning SQUID microscope with 200 MHz bandwidth. *Superconductor Science and Technology*, 27(4):044032, 2014.
- [77] T Zelder, B Geck, I Rolfes, and H Eul. Radio Science contactless vector network analysis with varying transmission line geometries. *Advances in Radio Science*, 6:19–25, 2008.
- [78] R. P. Frueholz and J. C. Camparo. Microwave field strength measurement in a rubidium clock cavity via adiabatic rapid passage. *Journal of Applied Physics*, 57(1985):704–708, 1985.
- [79] J. Camparo. Atomic Stabilization of Electromagnetic Field Strength Using Rabi Resonances. *Physical Review Letters*, 80(2):222–225, 1998.
- [80] Moto Kinoshita, Kazuhiro Shimaoka, and Yozo Shimada. Optimization of the atomic candle signal for the precise measurement of microwave power. *IEEE Transactions on Instrumentation and Measurement*, 62(6):1807–1813, 2013.
- [81] CL Holloway and JA Gordon. Sub-Wavelength Imaging and Field Mapping via EIT and Autler-Townes Splitting In Rydberg Atoms. *Applied Physics Letters*, 104:244102, 2014.
- [82] CL Holloway and JA Gordon. Broadband Rydberg Atom-Based Electric-Field Probe: From Self-Calibrated Measurements to Sub-Wavelength Imaging. *arXiv preprint arXiv: . . .*, (1):1–12, 2014.

- [83] Ronald A Ginley. Traceability for Microwave Power Measurements : Past , Present , and Future. *Wireless and Microwave Technology Conference (WAMI-CON), 2015 IEEE 16th Annual*, (2), 2015.
- [84] Dmitry Budker, Derek F. Jackson Kimball, and David P. DeMille, editors. *Atomic Physics: An Exploration through Problems and Solutions*. Oxford University Press, Oxford, 2008.
- [85] Marcus Auzinsh, Dmitry Budker, and Simon M. Rochester. *Optically Polarised Atoms*. Oxford University Press, Oxford, 2010.
- [86] William Happer, Yuan-Yu Jau, and Thad Walker. *Optically Pumped Atoms*. Wiley-VCH, Weinheim, 2010.
- [87] Dmitry Budker and Derek F. Jackson Kimball, editors. *Optical Magnetometry*. Cambridge University Press, Cambridge, 2013.
- [88] Daniel Adam Steck. Rubidium 87 D Line Data. available online at <http://steck.us/alkalidata> (revision 2.1.4, 23 December 2010).
- [89] Daniel Adam Steck. Rubidium 85 D Line Data. available online at <http://steck.us/alkalidata> (revision 2.1.4, 23 December 2010).
- [90] Mark A. Zentile, James Keaveney, Lee Weller, Daniel J. Whiting, Charles S. Adams, and Ifan G. Hughes. ElecSus: A program to calculate the electric susceptibility of an atomic ensemble. *Computer Physics Communications*, 189:162–174, 2015.
- [91] Paul Siddons, Charles S Adams, Chang Ge, and Ifan G Hughes. Absolute absorption on rubidium D lines: comparison between theory and experiment. *Journal of Physics B: Atomic, Molecular and Optical Physics*, 41(15):155004, August 2008.
- [92] Lee Weller, Robert J Bettles, Paul Siddons, Charles S Adams, and Ifan G Hughes. Absolute absorption on the rubidium D1 line including resonant dipole–dipole interactions. *Journal of Physics B: Atomic, Molecular and Optical Physics*, 44(19):195006, October 2011.
- [93] Lee Weller, Kathrin S Kleinbach, Mark A Zentile, Svenja Knappe, Charles S Adams, and Ifan G Hughes. Absolute absorption and dispersion of a rubidium vapour in the hyperfine Paschen–Back regime. *Journal of Physics B: Atomic, Molecular and Optical Physics*, 45(21):215005, November 2012.
- [94] Lee Weller. Absolute Absorption and Dispersion in a Thermal Rb Vapour at High Densities and High Magnetic Fields. *PhD Thesis, Durham University*, 2013.
- [95] Ben E. Sherlock and Ifan G. Hughes. How weak is a weak probe in laser spectroscopy? *American Journal of Physics*, 77(2):111, 2009.

- [96] Christopher J. Foot. *Atomic Physics*. Oxford University Press Inc., New York, 2005.
- [97] Harold J. Metcalf and Peter van der Straten. *Laser Cooling and Trapping*. Springer-Verlag, New York, 1999.
- [98] M. Rosenberry, J. Reyes, D. Tupa, and T. Gay. Radiation trapping in rubidium optical pumping at low buffer-gas pressures. *Physical Review A*, 75(2):023401, February 2007.
- [99] Martine Chevrollier. Radiation trapping and Lévy flights in atomic vapours: an introductory review. *Contemporary Physics*, 53(3):227–239, May 2012.
- [100] D. K. Walter, W. M. Griffith, and W. Happer. Energy transport in high-density spin-exchange optical pumping cells. *Physical Review Letters*, 86(15):3264–3267, 2001.
- [101] S. J. Seltzer. Developments in Alkali-Metal Atomic Magnetometry. *PhD Thesis, Princeton University*, 2008.
- [102] Andreas F. Molisch and Bernhard P. Oehry. *Radiation Trapping in Atomic Vapours*. Oxford University Press, Oxford, UK, 1998.
- [103] E. S. Hrycyszyn and L. Krause. Inelastic collisions between excited alkali atoms and molecules. VII. Sensitized fluorescence and quenching in mixtures of rubidium with H₂, HD, D₂, N₂, CH₄, CD₄, C₂H₄, and C₂H₆. *Canadian Journal of Physics*, 48(22):2761–2768, 1970.
- [104] Salvatore Micalizio, Aldo Godone, Filippo Levi, and Claudio Calosso. Pulsed optically pumped Rb87 vapor cell frequency standard: A multilevel approach. *Physical Review A*, 79(1):013403, January 2009.
- [105] R P Frueholz and C H Volk. Analysis of Dicke narrowing in wall-coated and buffer-gas-filled atomic storage cells, 1999.
- [106] J. Keaveney, A. Sargsyan, U. Krohn, I. Hughes, D. Sarkisyan, and C. Adams. Cooperative Lamb Shift in an Atomic Vapor Layer of Nanometer Thickness. *Physical Review Letters*, 108(17):1–5, April 2012.
- [107] N. P. Wells, T. U. Driskell, and J. C. Camparo. Kr-collision shift of the Rb D1 transition: The isoclinic point and precision optical spectroscopy. *Physical Review A - Atomic, Molecular, and Optical Physics*, 89(5):1–6, 2014.
- [108] J F Kielkopf. Predicted alkali collision broadening by noble gases based on semiempirical potentials. *Journal of Physics B: Atomic and Molecular Physics*, 9(17):L547–L550, 1976.

- [109] DJ Croucher and JL Clark. Total collision cross sections and van der Waals constants for alkali atom interactions with atoms and non-reactive diatomic molecules at thermal energies. *Journal of Physics B: Atom. Molec. Phys.*, 603:603–623, 1969.
- [110] DK Walter, WM Griffith, and W Happer. Magnetic slowing down of spin relaxation due to binary collisions of alkali-metal atoms with buffer-gas atoms. *Phys. Rev. Lett.*, 88:2–5, 2002.
- [111] J. Allred, R. Lyman, T. Kornack, and M. Romalis. High-Sensitivity Atomic Magnetometer Unaffected by Spin-Exchange Relaxation. *Physical Review Letters*, 89(13):130801, September 2002.
- [112] A. Ben-Amar Baranga, S. Appelt, M. Romalis, C. Erickson, A. Young, G. Cates, and W. Happer. Polarization of ^3He by Spin Exchange with Optically Pumped Rb and K Vapors. *Physical Review Letters*, 80(13):2801–2804, March 1998.
- [113] S. Brattke, U. Kallmann, and W.-D. Hartmann. Coherent dark states of rubidium 87 in a buffer gas using pulsed laser light. *The European Physical Journal D*, 3(2):159–161, August 1998.
- [114] S. Kadlecsek, L. Anderson, and T. Walker. Field Dependence of Spin Relaxation in a Dense Rb Vapor. *Physical Review Letters*, 80:5512–5515, 1998.
- [115] C. J. Erickson, D. Levron, W. Happer, S. Kadlecsek, B. Chann, L. W. Anderson, and T. G. Walker. Spin relaxation resonances due to the spin-axis interaction in dense rubidium and cesium vapor. *Physical Review Letters*, 85:4237–4240, 2000.
- [116] S. Kadlecsek, T. Walker, D. K. Walter, C. Erickson, and W. Happer. Spin-axis relaxation in spin-exchange collisions of alkali atoms. *Physical Review A*, 63:052717, 2001.
- [117] Jacques Vanier. Relaxation in Rubidium-87 and the Rubidium Maser. *Physical Review*, 168(1):129–149, 1968.
- [118] HM Gibbs and RJ Hull. Spin-Exchange Cross Sections for $\text{Rb}^{87}\text{-Rb}^{87}$ and $\text{Rb}^{87}\text{-Cs}^{133}$ Collisions. *Physical Review*, 153(1), 1967.
- [119] NW Ressler, RH Sands, and TE Stark. Measurement of Spin-Exchange Cross Sections for Cs^{133} , Rb^{87} , Rb^{85} , K^{39} , and Na^{23} . *Physical Review*, 184(1), 1969.
- [120] A. Korver, R. Wyllie, B. Lancor, and T. G. Walker. Suppression of spin-exchange relaxation using pulsed parametric resonance. *Physical Review Letters*, 111(July):1–5, 2013.
- [121] Thad G. Walker and William Happer. Spin-exchange optical pumping of noble-gas nuclei. *Reviews of Modern Physics*, 69(2):629–642, 1997.

- [122] Brian Patton. NMR Studies of Angular Momentum Transfer and Nuclear Spin Relaxation. *PhD Thesis, Princeton University*, 2007.
- [123] Rajat K. Ghosh. Spin Exchange Optical Pumping of Neon and its Applications. *PhD Thesis, Princeton University*, 2009.
- [124] Or Katz, Or Peleg, and Ofer Firstenberg. Coherent coupling of alkali atoms by random collisions. pages 1–5, 2015.
- [125] Rikio Kondo, Satoshi Tojo, Takashi Fujimoto, and Masahiro Hasuo. Shift and broadening in attenuated total reflection spectra of the hyperfine-structure-resolved D2 line of dense rubidium vapor. *Physical Review A - Atomic, Molecular, and Optical Physics*, 73(6):1–7, 2006.
- [126] J. C. Camparo. Semiempirical theory of Carver rates in alkali/noble-gas systems. *Journal of Chemical Physics*, 126(2007), 2007.
- [127] B. H. McGuyer. Hyperfine-frequency shifts of alkali-metal atoms during long-range collisions. *Physical Review A - Atomic, Molecular, and Optical Physics*, 87(5):1–5, 2013.
- [128] M. Huang, J. G. Coffey, and J. C. Camparo. Rb87 hyperfine-transition dephasing in mixed buffer-gas systems. *Physical Review A - Atomic, Molecular, and Optical Physics*, 75:1–8, 2007.
- [129] F. Gong, Y.-Y. Jau, and W. Happer. Nonlinear Pressure Shifts of ^{87}Rb and ^{133}Cs in Ar and Kr. *2008 IEEE International Frequency Control Symposium*, 233002(June):1–4, 2008.
- [130] B. H. McGuyer, T. Xia, Y. Y. Jau, and W. Happer. Hyperfine frequencies of ^{87}Rb and ^{133}Cs atoms in Xe gas. *Physical Review A - Atomic, Molecular, and Optical Physics*, 84(3):1–4, 2011.
- [131] B. Bean and R. Lambert. Temperature dependence of hyperfine density shifts. III. ^{23}Na , ^{39}K , and ^{85}Rb in He, Ne, Ar, and N_2 . *Physical Review A*, 12(4):1498–1502, 1975.
- [132] B. Bean and R. Lambert. Temperature dependence of hyperfine density shifts. IV. ^{23}Na , ^{39}K , and ^{85}Rb in He, Ne, Ar, and N_2 at low temperatures, 1976.
- [133] Olga Kozlova, Stéphane Guérandel, and Emeric De Clercq. Temperature and pressure shift of the Cs clock transition in the presence of buffer gases: Ne, N_2 , Ar. *Physical Review A - Atomic, Molecular, and Optical Physics*, 83(6):1–9, 2011.
- [134] K. Dorenburg, M. Gladisch, and G. zu Putlitz. Hyperfine structure density shift coefficients for K, Rb and Cs at high buffer gas densities. *Zeitschrift für Physik A Atoms and Nuclei*, 289(2):145–149, 1979.

- [135] P. J. Oredo, Y. Y. Jau, A. B. Post, N. N. Kuzma, and W. Happer. Buffer-gas-induced shift and broadening of hyperfine resonances in alkali-metal vapors. *Physical Review A - Atomic, Molecular, and Optical Physics*, 69(December 2003):042716–1, 2004.
- [136] J. Vanier, R. Kunski, N. Cyr, J. Y. Savard, and M. Têtu. On hyperfine frequency shifts caused by buffer gases: Application to the optically pumped passive rubidium frequency standard. *Journal of Applied Physics*, 53(8):5387, 1982.
- [137] M. V. Romalis, E. Miron, and G. D. Cates. Pressure broadening of Rb D 1 and D 2 lines by ^3He , ^4He , N_2 , and Xe: Line cores and near wings. 56(6), 1997.
- [138] Matthew D. Rotondaro and Glen P. Perram. Collisional broadening and shift of the rubidium d1 and d2 lines by rare gases, H_2 , D_2 , N_2 and CF_4 . *Journal of Quantitative Spectroscopy and Radiative Transfer*, 57(4):497–507, 1997.
- [139] A. H. Couture, T. B. Clegg, and B. Driehuys. Pressure shifts and broadening of the Cs D1 and D2 lines by He, N_2 , and Xe at densities used for optical pumping and spin exchange polarization. *Journal of Applied Physics*, 104(9):0–6, 2008.
- [140] Greg A. Pitz, Douglas E. Wertepny, and Glen P. Perram. Pressure broadening and shift of the cesium D_1 transition by the noble gases and N_2 , H_2 , HD, D_2 , CH_4 , C_2H_6 , CF_4 , and ^3He . *Physical Review A*, 80(6):1–8, 2009.
- [141] Kelly A. Kluttz, Todd D. Averett, and Brian A. Wolin. Pressure broadening and frequency shift of the D1 and D 2 lines of Rb and K in the presence of ^3He and N_2 . *Physical Review A - Atomic, Molecular, and Optical Physics*, 87(3):3–7, 2013.
- [142] Fei Gong. New Physics And Technology For Spin-Polarized Alkali-Metal Atoms. *PhD Thesis, Princeton University*, 2008.
- [143] Stefan Grafström and Dieter Suter. Interaction of spin-polarized atoms with a surface studied by optical-reflection spectroscopy. *Phys. Rev. A*, 54(3):2169, September 1996.
- [144] K. Zhao, M. Schaden, and Z. Wu. Method for Measuring the Dwell Time of Spin-Polarized Rb Atoms on Coated Pyrex Glass Surfaces Using Light Shift. *Physical Review Letters*, 103(7):073201, August 2009.
- [145] Eric P. Corsini, Todor Karaulanov, Mikhail Balabas, and Dmitry Budker. Hyperfine frequency shift and Zeeman relaxation in alkali-metal-vapor cells with antirelaxation alkene coating. *Physical Review A*, 87(2):022901, February 2013.
- [146] R. J. McNeal, R. Bersohn, M. Dorfman, and R. A. Bernheim. Optical Pumping and Chemical Reactions. *Journal of Chemical Physics*, 40(6):1678, 1964.

- [147] J. C. Camparo, R. P. Frueholz, and B. Jaduszliwer. Alkali reactions with wall coating materials used in atomic resonance cells. *Journal of Applied Physics*, 62(1987):676–681, 1987.
- [148] J. Ma, A. Kishinevski, Y.-Y. Jau, C. Reuter, and W. Happer. Modification of glass cell walls by rubidium vapor. *Physical Review A*, 79(4):042905, April 2009.
- [149] H.N. De Freitas, M. Oria, and M. Chevrollier. Spectroscopy of cesium atoms adsorbing and desorbing at a dielectric surface. *Applied Physics B: Lasers and Optics*, 75(6-7):703–709, November 2002.
- [150] I. Nelson and T. Walker. Rb-Xe spin relaxation in dilute Xe mixtures. *Physical Review A*, 65(1):1–6, 2001.
- [151] Radoslaw Chrapkiewicz, Wojciech Wasilewski, and Czeslaw Radzewicz. How to measure diffusional decoherence in multimode Rubidium vapor memories? *Optics Communications*, 317:1–6, 2014.
- [152] Kiyoshi Ishikawa and Tsutomu Yabuzaki. Diffusion coefficient and sublevel coherence of Rb atoms in N₂ buffer gas. *Phys. Rev. A*, 62(6):065401, November 2000.
- [153] FA Franz and CE Sooriamoorthi. Spin relaxation within the 6²P_{1/2} and 6²S_{1/2} states of cesium measured by white-light optical pumping. *Physical Review A*, 10(1), 1974.
- [154] M. Balabas, T. Karaulanov, M. Ledbetter, and D. Budker. Polarized Alkali-Metal Vapor with Minute-Long Transverse Spin-Relaxation Time. *Physical Review Letters*, 105(7):070801, August 2010.
- [155] S. J. Seltzer and M. V. Romalis. High-temperature alkali vapor cells with antirelaxation surface coatings. *Journal of Applied Physics*, 106(11):114905, 2009.
- [156] R Straessle, Matthieu Pellaton, Y. Petremand, D. Briand, Christoph Affolderbach, Gaetano Miletì, and N. F. de Rooji. Low-Temperature Indium Hermetic Sealing of Alkali Vapor-Cells for Chip-Scale Atomic Clocks. *Proceedings of the IEEE International Conference on Microelectronics*, (February):361–364, 2012.
- [157] Pascal Böhi. Coherent manipulation of ultracold atoms with microwave near-fields. *PhD Thesis, Max-Planck Institute for Quantum Optics*, 2010.
- [158] TR Gentile, BJ Hughey, Daniel Kleppner, and TW Ducas. Experimental study of one-and two-photon Rabi oscillations. *Phys. Rev. A*, 40(9):5103, 1989.
- [159] J Guéna, M Abgrall, A Clairon, and S Bize. Contributing to TAI with a secondary representation of the SI second. *Metrologia*, 51(1):108, 2014.

- [160] Norman Ramsey. *Molecular beams*. Oxford University Press, Oxford, 1956.
- [161] T. P. Crowley, E. A. Donley, and T. P. Heavner. Quantum-based microwave power measurements: Proof-of-concept experiment. *Review of Scientific Instruments*, 75(8):2575–2580, 2004.
- [162] David C Paulusse, Nelson L Rowell, and Alain Michaud. Accuracy of an Atomic Microwave Power Standard. *IEEE Transactions on Instrumentation and Measurement*, 54(2):692–695, 2005.
- [163] W Ketterle, DS Durfee, and DM Stamper-Kurn. *Making, probing and understanding Bose-Einstein condensates*, in *Bose-Einstein condensation in atomic gases, Proceedings of the International School of Physics “Enrico Fermi”, Course CXL*. IOS Press, Amsterdam, 1996.
- [164] EW Streed, Andreas Jechow, Benjamin G. Norton, and David Kielpinski. Absorption imaging of a single atom. *Nature Communications*, 3(1):933, 2012.
- [165] J Estève, C Gross, A Weller, S Giovanazzi, and M K Oberthaler. Squeezing and entanglement in a Bose-Einstein condensate. *Nature*, 455(7217):1216–1219, October 2008.
- [166] Andrew Horsley, Guan-Xiang Du, Matthieu Pellaton, Christoph Affolderbach, Gaetano Mileti, and Philipp Treutlein. Spatially Resolved Measurement of Relaxation Times in a Microfabricated Vapor Cell. *Proceedings of the 2013 Joint IEEE-UFFC, EFTF and PFM Symposium*, pages 575–578, 2013.
- [167] Miroslav Gajdacz, Poul L. Pedersen, Troels Mørch, Andrew J. Hilliard, Jan Arlt, and Jacob F. Sherson. Non-destructive Faraday imaging of dynamically controlled ultracold atoms. *Review of Scientific Instruments*, 84(8):083105, 2013.
- [168] Caspar F. Ockeloen. Quantum Metrology with a Scanning Probe Atom Interferometer. *PhD Thesis, University of Basel*, 2014.
- [169] L Ricci, M Weidermueller, T Esslinger, A Hemmerich, C Zimmermann, V Vuletic, W Koenig, and T W Haensch. A compact grating-stabilized diode laser system for atomic physics. *Optics Communications*, 117:541–549, 1995.
- [170] X. Baillard, A. Gauguet, S. Bize, P. Lemonde, Ph. Laurent, A. Clairon, and P. Rosenbusch. Interference-filter-stabilized external-cavity diode lasers. *Optics Communications*, 266(2):609–613, October 2006.
- [171] M. Harris, C. Adams, S. Cornish, I. McLeod, E. Tarleton, and I. Hughes. Polarization spectroscopy in rubidium and cesium. *Physical Review A*, 73(6):062509, June 2006.
- [172] K. Zhao and Z. Wu. Mapping surfaces using regionally specific hyperfine polarization. *Physical Review A*, 70(1):010901, July 2004.

- [173] K. Zhao and Z. Wu. Regionally specific hyperfine polarization of Rb atoms in the vicinity ($\sim 10^{-5}$ cm) of surfaces. *Physical Review A*, 71(1):012902, January 2005.
- [174] M. Schaden, K. Zhao, and Z. Wu. Effects of diffusion and surface interactions on the line shape of electron paramagnetic resonances in the presence of a magnetic field gradient. *Physical Review A*, 76(6):062502, December 2007.
- [175] K. F. Zhao and Z. Wu. Evanescent wave magnetometers with ultrathin ($\sim 100\mu\text{m}$) cells. *Applied Physics Letters*, 93(10):101101, 2008.
- [176] Emily Ulanski and Zhen Wu. Measurement of dwell times of spin polarized rubidium atoms on octadecyltrichlorosilane- and paraffin-coated surfaces. *Applied Physics Letters*, 98(20):201115, 2011.
- [177] J. Di Francesco, F. Gruet, C. Schori, C. Affolderbach, R. Matthey, G. Mileti, Y. Salvadé, Y. Petremand, and N. De Rooij. Evaluation of the frequency stability of a VCSEL locked to a micro-fabricated Rubidium vapour cell. *Proceedings SPIE Vol. 7720*, pages 77201T–77201T–9, April 2010.
- [178] Gaetano Mileti, I. Ruedi, and H. Schweda. Line Inhomogeneity Effects and Power Shift in Miniaturized Rubidium Frequency Standards. *Proc. 6th European Frequency and Time Forum*, pages 515–519, 1992.
- [179] S. Knappe. *MEMS atomic clocks*, in: *Comprehensive Microsystems*, volume 3. Elsevier, Amsterdam, 2007.
- [180] D Giel, G Hinz, D Nettels, and A Weis. Diffusion of Cs atoms in Ne buffer gas measured by optical magnetic resonance tomography. *Optics Express*, 6(13):251–6, June 2000.
- [181] Salvatore Micalizio, Aldo Godone, Claudio Calosso, Filippo Levi, Christoph Affolderbach, and Florian Gruet. Pulsed optically pumped rubidium clock with high frequency-stability performance. *IEEE Transactions on Ultrasonics, Ferroelectrics, and Frequency Control*, 59(3):457–62, March 2012.
- [182] Christoph Affolderbach, Fabien Droz, and Gaetano Mileti. Experimental Demonstration of a Compact and Gas Cell Atomic Frequency Standard. *IEEE Transactions on Instrumentation and Measurement*, 55(2):429–435, 2006.
- [183] T. Bandi, C. Affolderbach, C.E. Calosso, and G. Mileti. High-performance laser-pumped rubidium frequency standard for satellite navigation. *Electronic Letters*, 47(12):698–699, March 2011.
- [184] Thejesh Bandi. Double-Resonance Studies on Compact, High-Performance Rubidium Cell Frequency Standards. *PhD Thesis, Laboratoire Temps-Fréquence, Institut de Physique, Université de Neuchâtel*, 2013.

- [185] Thejesh Bandi, Christoph Affolderbach, Camillo Stefanucci, Francesco Merli, Anja K Skrivervik, and Gaetano Mileti. Compact High-Performance Continuous-Wave Double-Resonance Rubidium Standard With $1.4 \times 10^{-13} \tau^{-1/2}$ Stability. *IEEE Transactions on Ultrasonics, Ferroelectrics, and Frequency Control*, 61(11):1769–1778, 2014.
- [186] Camillo Stefanucci, Thejesh Bandi, Francesco Merli, Matthieu Pellaton, Christoph Affolderbach, Gaetano Mileti, and Anja K Skrivervik. Compact microwave cavity for high performance rubidium frequency standards. *The Review of Scientific Instruments*, 83(10):104706, October 2012.
- [187] R. Lutwak, D. Emmons, W. Riley, and R.M. Garvey. The chip-scale atomic clock-coherent population trapping vs. conventional interrogation. *Proceedings of the 34th Annual Precise Time and Time Interval (PTTI) Meeting*, pages 539–550, 2003.
- [188] A. Risley, S. Jarvis, and J. Vanier. The dependence of frequency upon microwave power of wall-coated and buffer-gas-filled gas cell Rb87 frequency standards. *Journal of Applied Physics*, 51(9):4571–4576, 1980.
- [189] Ingo Wolff. *Coplanar Microwave Integrated Circuits*. John Wiley & Sons, Inc., Hoboken, New Jersey, 2006.
- [190] Eimutis Juzeliunas. Advances in detection of magnetic fields induced by electrochemical reactions—a review. *Journal of Solid State Electrochemistry*, 11(6):791–798, September 2006.
- [191] Gonzalo E. Gallo, John S. Popovics, and Patrick L. Chapman. Corrosion monitoring of metals. *European Journal of Environmental and Civil Engineering*, 15(4):633–647, January 2011.
- [192] Gonzalo E. Gallo and John S. Popovics. Monitoring active corrosion of metals in natural environments with magnetometry. *Corrosion Science*, 63:1–4, October 2012.
- [193] Shoujun Xu, Simon M. Rochester, Valeriy V. Yashchuk, Marcus H. Donaldson, and Dmitry Budker. Construction and applications of an atomic magnetic gradiometer based on nonlinear magneto-optical rotation. *Review of Scientific Instruments*, 77(8):083106, 2006.
- [194] Elad Harel, Leif Schröder, and Shoujun Xu. Novel detection schemes of nuclear magnetic resonance and magnetic resonance imaging: applications from analytical chemistry to molecular sensors. *Annual review of analytical chemistry (Palo Alto, Calif.)*, 1:133–63, January 2008.
- [195] Li Yao, Andrew C Jamison, and Shoujun Xu. Scanning imaging of magnetic nanoparticles for quantitative molecular imaging. *Angewandte Chemie (International ed. in English)*, 49(41):7493–6, October 2010.

- [196] Li Yao, Yuhong Wang, and Shoujun Xu. Label-free microRNA detection based on exchange-induced remnant magnetization. *Chemical communications (Cambridge, England)*, 49(45):5183–5, June 2013.
- [197] N. Wells, T. Driskell, and J. Camparo. ^{87}Rb Isoclinic Point Thermometry. *Proceedings of the 2015 Joint Conference of the IEEE International Frequency Control Symposium and European Frequency and Time Forum*, pages 25–32, 2015.
- [198] K. Kitagami, K. Hosumi, K. Goto, and A. Hatakeyama. Quantitative measurements of light-induced desorption of rubidium atoms from quartz substrates. *Physical Review A*, 85(6):062901, June 2012.
- [199] C.H. Volk, R.P. Frueholz, T.C. English, T.J. Lynch, and W.J. Riley. Lifetime and Reliability of Rubidium Discharge Lamps for Use in Atomic Frequency Standards. *38th Annual Symposium on Frequency Control*, 1984.
- [200] R.A. Cook and R.P. Frueholz. An improved rubidium consumption model for discharge lamps used in rubidium frequency standards. *Proceedings of the 42nd Annual Frequency Control Symposium, 1988.*, 1988.
- [201] C M Klimcak, M Huang, and J C Camparo. Alkali Metal Consumption by Discharge Lamps Fabricated from GE-180 Aluminosilicate Glass. *Proceedings of the 2015 Joint Conference of the IEEE International Frequency Control Symposium and European Frequency and Time Forum*, pages 180–187, 2015.
- [202] Z. Wu, W. Happer, M. Kitano, and J. Daniels. Experimental studies of wall interactions of adsorbed spin-polarized ^{131}Xe nuclei. *Physical Review A*, 42(5):2774, 1990.
- [203] J. A. Rushton, M. Aldous, and M. D. Himsworth. Contributed Review: The feasibility of a fully miniaturized magneto-optical trap for portable ultracold quantum technology. *Review of Scientific Instruments*, 85(12):121501, 2014.
- [204] Bernardo Jaduszliwer, Michael Huang, and James C Camparo. Buffer Gas Consumption in Rubidium Discharge Lamps. *Proceedings of the 2015 Joint Conference of the IEEE International Frequency Control Symposium and European Frequency and Time Forum*, pages 37–46, 2015.
- [205] Daniel Adam Steck. Cesium D Line Data. available online at <http://steck.us/alkalidata> (revision 2.1.4, 23 December 2010).
- [206] E. Alexandrov, M. Balabas, D. Budker, D. English, D. Kimball, C.-H. Li, and V. Yashchuk. Light-induced desorption of alkali-metal atoms from paraffin coating. *Physical Review A*, 66(4):042903, October 2002.
- [207] A. Baranga, S. Appelt, C. Erickson, A. Young, and W. Happer. Alkali-metal-atom polarization imaging in high-pressure optical-pumping cells. *Physical Review A*, 58(3):2282–2294, September 1998.

- [208] Philipp Treutlein. Coherent manipulation of ultracold atoms on atom chips. *PhD Thesis, Max-Planck Institute for Quantum Optics*, 2008.
- [209] R. Mhaskar, S. Knappe, and J. Kitching. A low-power, high-sensitivity micro-machined optical magnetometer. *Applied Physics Letters*, 101(24):5–8, 2012.
- [210] B. Olsen, B. Patton, Y.-Y. Jau, and W. Happer. Optical pumping and spectroscopy of Cs vapor at high magnetic field. *Physical Review A*, 84(6):063410, December 2011.
- [211] Ben Andrew Olsen. Optical Pumping and Spectroscopy of Alkali Vapors in Magnetic Fields. *PhD Thesis, Princeton University*, 2011.
- [212] Mark A Zentile, Rebecca Andrews, Lee Weller, Svenja Knappe, Charles S Adams, and Ifan G Hughes. The hyperfine Paschen–Back Faraday effect. *Journal of Physics B: Atomic, Molecular and Optical Physics*, 47(7):075005, 2014.
- [213] S. Li, P. Vachaspati, D. Sheng, N. Dural, and M. V. Romalis. Optical rotation in excess of 100 rad generated by Rb vapor in a multipass cell. *Physical Review A - Atomic, Molecular, and Optical Physics*, 84(6):1–4, 2011.
- [214] D. Sheng, S. Li, N. Dural, and M. Romalis. Subfemtotesla Scalar Atomic Magnetometry Using Multipass Cells. *Physical Review Letters*, 110(16):160802, April 2013.
- [215] Heng Shen. Spin squeezing and entanglement with room temperature atoms for quantum sensing and communication. *PhD Thesis, University of Copenhagen*, (December), 2014.
- [216] I K Kominis, T W Kornack, J C Allred, and M V Romalis. A subfemtotesla multichannel atomic magnetometer. *Nature*, 422(6932):596–9, April 2003.
- [217] Rohit Chandra, Huiyuan Zhou, Ilanko Balasingham, Senior Member, and Ram M Narayanan. On the Opportunities and Challenges in Microwave Medical Sensing and Imaging. *IEEE Transactions on Biomedical Engineering*, 62(7):1667–1682, 2015.
- [218] Elise C Fear, Susan C Hagness, Paul M Meaney, Michal Okoniewski, and Maria A Stuchly. Enhancing Breast Tumor Detection with Near-Field Imaging. *Microwave Magazine, IEEE*, 3(March):48–56, 2002.
- [219] Natalia Nikolova. Microwave Imaging for Breast Cancer. *IEEE Microwave Magazine*, 12(7):78–94, 2011.
- [220] Nikola Petrović. Measurement System for Microwave Imaging Towards a Biomedical Application. *PhD Thesis, Maelardalen University*, 2014.

- [221] John P Stang. A 3D Active Microwave Imaging System for Breast Cancer Screening. *PhD Thesis, Duke University*, 2008.
- [222] Daniel Adam Steck. Sodium D Line Data. available online at <http://steck.us/alkalidata> (revision 2.1.4, 23 December 2010).
- [223] T G Tiecke. Properties of Potassium, 2010. available online at http://staff.science.uva.nl/walraven/walraven/Publications_files/PotassiumProperties.pdf.